

UC San Diego

UC San Diego Electronic Theses and Dissertations

Title

High-Speed Hybrid Silicon-Lithium Niobate Electro-Optic Modulators & Related Technologies

Permalink

<https://escholarship.org/uc/item/3vj7v7zp>

Author

Weigel, Peter Orlando

Publication Date

2018

Peer reviewed|Thesis/dissertation

UNIVERSITY OF CALIFORNIA SAN DIEGO

**High-Speed Hybrid Silicon-Lithium Niobate Electro-Optic Modulators
& Related Technologies**

A dissertation submitted in partial satisfaction of the
requirements for the degree
Doctor of Philosophy

in

Electrical Engineering (Photonics)

by

Peter O. Weigel

Committee in charge:

Professor Shayan Mookherjea, Chair
Professor Joseph Ford
Professor James Friend
Professor George Papen
Professor Stojan Radic
Professor Gabriel Rebeiz

2018

Copyright
Peter O. Weigel, 2018
All rights reserved.

The dissertation of Peter O. Weigel is approved, and it is acceptable in quality and form for publication on microfilm and electronically:

Chair

University of California San Diego

2018

DEDICATION

To my parents, for supporting my education throughout my entire life, even when
it took me three thousand miles away.

This work is also dedicated to my friend Shane, who departed this world far too
soon. All my successes are shared with him.

EPIGRAPH

Give me a place to stand, and I shall move the world.

–Archimedes (from *The Library of History of Diodorus Siculus*, Fragments of Book XXVI, as translated by F. R. Walton in *Loeb Classical Library* (1957) Vol. XI)

TABLE OF CONTENTS

Signature Page	iii
Dedication	iv
Epigraph	v
Table of Contents	vi
List of Figures	x
List of Tables	xvi
Acknowledgements	xvii
Vita	xx
Abstract of the Dissertation	xxii
Chapter 1 Theory of Electro-Optic Modulators	1
1.1 Introduction	1
1.2 Lithium Niobate & the Pockels Effect	2
1.2.1 Voltage-Length Product in LN MZMs	5
1.2.2 Electro-Optic Bandwidth Theory for a Traveling Wave Mach-Zehnder Modulator	9
1.3 Silicon & the Plasma Dispersion Effect	13
Bibliography	15
Chapter 2 Design of Hybrid Electro-Optic Modulators	16
2.1 Introduction	16
2.2 Hybrid Si-LN Optical Mode Design	17
2.2.1 Optical Mode for the Electro-Optic Modulator	19
2.2.2 Optical Mode for Si Waveguide Applications	20
2.2.3 Optical Mode for the Edge Coupler	21
2.2.4 Bonding Markers & Electrode Markers	23
2.3 Full Optical Design of the EOM	23
2.4 Design of the Electrical Lines	24
2.4.1 EOM Region	25
2.4.2 Electrical Bends	26
2.4.3 Electrical Pads	26
Bibliography	27

Chapter 3	A Process Design Kit for Hybrid Si-LiNbO ₃ Devices	28
	3.1 Introduction	28
	3.2 Technology Summary	29
	3.2.1 Features of the Technology	29
	3.3 Design Tools	31
	3.4 Process Outline	32
	3.5 Design Rules for the Hybrid Si-LN Platform	34
	3.5.1 Non-Hybrid Si Components	34
	3.5.2 Hybrid Si-LN Components	35
	3.6 Static Library Components	38
	3.6.1 Edge Coupling Taper	39
	3.6.2 Thin-Si Waveguide	39
	3.6.3 Thin-Si Spline Bends	39
	3.6.4 Thin-Si 3-dB Directional Coupler	41
	3.6.5 Mach-Zehnder Interferometer	44
	3.6.6 Hybrid Si-LN Taper	45
	3.6.7 Hybrid Si-LN Waveguide	46
	3.6.8 Hybrid Si-LN Electro-Optic Phase Shifter	47
	3.6.9 Coplanar Waveguide Transmission Line	47
	3.7 Acknowledgments	50
	Bibliography	50
Chapter 4	Fabrication of Hybrid Electro-Optic Devices	51
	4.1 Introduction	51
	4.2 Film-on-Insulator Wafers	51
	4.3 SOI Patterning & Oxide Polishing	53
	4.4 Bonding Theory	55
	4.4.1 Types of Bonds	55
	4.5 Reducing Thermal Stress in Heterogeneous Bonded Materials	58
	4.6 Handle Removal	68
	4.7 Metallization	69
	4.8 Acknowledgments	70
	Bibliography	70
Chapter 5	All-Optical Hybrid Silicon-Lithium Niobate Devices	75
	5.1 Introduction	75
	5.2 Hybrid Modes and Mode-Transition Tapers	78
	5.3 Waveguides, Directional Couplers and Photonic Circuits	83
	5.4 Discussion and Analysis	85
	5.5 Acknowledgments	89
	Bibliography	89

Chapter 6	Characterization of Hybrid Electro-Optic Modulators	92
	6.1 Introduction	92
	6.2 Optical Characterization of an Electro-Optic Modulator	92
	6.2.1 Optical Transmission through an Electro-Optic Modulator	94
	6.2.2 Propagation Loss	95
	6.2.3 Spline Bending Loss	96
	6.2.4 Method to Optimize Optical Polarization State	97
	6.3 Electrical Characterization of an Electro-Optic Modulator	98
	6.3.1 Lossy Transmission Line Theory	100
	6.3.2 Electrical Extraction from VNA Measurements	103
	6.3.3 Measuring $V_{\pi}L$	104
	6.3.4 Low Frequency Electro-Optic Response	105
	6.3.5 High Frequency Electro-Optic Response	105
	6.4 Electro-Optic Characterization of an Electro-Optic Modulator	106
	6.4.1 Fabrication	107
	6.4.2 Electro-Optic Mach-Zehnder Modulator Design	109
	6.4.3 Electro-Optic Measurements	110
	6.5 Conclusion	114
	6.6 Acknowledgments	115
	Bibliography	115
Chapter 7	Second Harmonic Generation in Hybrid Waveguides	118
	7.1 Introduction	118
	7.2 Optical Second-Harmonic Generation	119
	7.2.1 Derivation of Power at the Generated Second Harmonic Frequency	119
	7.3 Design of Folded Hybrid Silicon Carbide-Lithium Niobate Waveguides	
	for Efficient Second Harmonic Generation	128
	7.3.1 A Brief Background of Integrated Photonic Circuits and Nonlin-	
	ear Optics in LN	129
	7.3.2 Overview of the Proposed Structure	131
	7.3.3 Additional Theory of the Nonlinear Interaction Region	133
	7.3.4 Silicon Carbide-Lithium Niobate Second Harmonic Generation	
	Design	135
	7.3.5 Impact of Variations of Design Parameters	136
	7.3.6 Loss and Disorder	137
	7.3.7 Bent Hybrid Waveguide Region	139
	7.3.8 Effective Mode Area (A_{eff})	142
	7.3.9 Lithium Niobate Confinement Factor (LNCF)	143
	7.4 Concluding Thoughts	144
	7.5 Acknowledgments	146
	Bibliography	146

Appendix A	149
A.1 Alternative $V_{\pi}L$ Derivation	149
A.2 Deriving the Electro-Optic Response from Coupled Mode Theory	151
Bibliography	156

LIST OF FIGURES

Figure 1.1:	Top view of a standard MZM in the push-pull configuration, meaning the two arms of the MZM have (ideally) equal and opposite electro-optic phase shifts ($\Delta\phi =$ the total phase shift of the device). Gray lines represent the optical waveguides, gold boxes represent the electrical lines (“electrodes”)...	2
Figure 1.2:	$V_{\pi}L$ is evaluated versus: n_{eff} (a), G (b), and Γ_{mo} (c).	9
Figure 1.3:	Circuit model showing where the electro-optic modulator fits between the signal generator (with applied voltage V_a and internal impedance of Z_G) and the load impedance Z_L . The voltage along the modulator is $V_m(z)$, which varies along the length of the EOM.	12
Figure 1.4:	The results shown in this figure are simulated 3-dBe electrical bandwidth values, in GHz, based on Equation 1.23. a Assumes perfect index matching ($\Delta n = 0$) and perfect impedance matching ($Z_G = Z_0 = Z_L = 50 \Omega$). Each curve represents a different electrical conductor loss...	13
Figure 2.1:	a A schematic representation of the hybrid Si-LN EOM cross-section in the push-pull configuration. Material labels are provided below the image, and material dimensions are as follows: h_{Si} = Si waveguide height; w_{Si} = Si waveguide width; h_{sub} = height of SOI substrate...	18
Figure 2.2:	Simulated $LNCF$ (a) and A_{eff} (b) for combinations of w_{Si} and h_{LN} , with $h_{Si} = 150$ nm.	20
Figure 2.3:	a Optical mode with $w_{Si} = 650$ nm, $h_{LN} = 600$ nm, and $h_{Si} = 150$ nm, under the LN film. b Same mode as a, but outside of the LN region. c Top view of the transition from the EOM mode (narrow 320 nm wide Si waveguide, left side), to a wide Si-LN waveguide, and finally to a wide all-Si mode.	21
Figure 2.4:	a Simulation of power transmission of an edge coupler between a lensed tapered fiber with MFD = 2.5 μm and a Si waveguide of height 150 nm surrounded by SiO_2 . The maximum power coupling is 89% for a Si width of 220 nm. b Logarithmic plot of the normalized electric field component...	22
Figure 2.5:	a GDS layout of EOM chip with arrays of alignment markers for electrode mask alignment and LN bonding alignment. b Edge-to-edge alignment is when the chip marker (black) and the mask marker (gray) are designed to align at the edge. This allows for high precision alignment, since both markers are visible.	23
Figure 2.6:	Top view of the full EOM layout. DC = directional coupler, PLD = path-length difference.	24
Figure 2.7:	This is the GDS layout of a portion of the electrical lines, shown in white on a black background. The ground lines are expanded at the pads to ensure that the probes can make contact, and the signal line is left unaltered for minimal reflections.	26
Figure 3.1:	a Linear waveguide taper optical transmission simulation in MODE. b Directional coupler waveguide optical simulation in FDTD. c Direct current (DC) electric-field simulation in DEVICE. d Circuit simulation of electro-optic modulator in INTERCONNECT.	31

Figure 3.2:	Cross-section after bonding and thermal anneal. Each layer's thickness is given, along with resistivity values for the Si handles.	34
Figure 3.3:	Cross-section after the full fabrication process. Each layer's thickness is given, along with resistivity values for the Si handles.	35
Figure 3.4:	a Minimum edge waveguide spacing. b Maximum Si waveguide width. c Minimum spline bend radius.	35
Figure 3.5:	a Linear plot of a simulated hybrid mode. $w_{Si} = 320$ nm and $h_{LN} = 600$ nm. The first and second rows of plots are x , y , and z components of the E- and H-fields, respectively. The third row of plots, labeled S_x , S_y , and S_z , are components of the time-average instantaneous Poynting vector.	36
Figure 3.6:	Log plot of a simulated hybrid optical mode when $w_{Si} = 200$ nm and $h_{LN} = 900$ nm, i.e. one of the gray boxes in the upper right corner of Table. 3.2. In this case, the E_x , H_y , and H_z components are nearly slab modes, while the E_y , E_z , and H_x components are non-zero.	38
Figure 3.7:	a Top view of optimized input/output waveguide taper. Taper length L_{taper} is varied from $10 \mu\text{m}$ to $500 \mu\text{m}$ in MODE Solutions. b Plot of edge taper transmission versus taper length at $\lambda = 1550$ nm for the taper in a	39
Figure 3.8:	Simulation of E_{norm} (the norm of all three E-field components) of the non-hybrid mode. Since E_y and E_z are so small for this TE-like mode, $E_{norm} \approx E_x$. $w_{Si} = 650$ nm. As with all Si waveguides in this document, $h_{Si} = 150$ nm.	40
Figure 3.9:	Cubic spline curve with knots P_0 and P_3 , and control points P_1 and P_2	40
Figure 3.10:	a 90° spline bend with knots P_0 and P_3 , and control points P_1 and P_2 . b Cubic spline waveguide 90° bend with width w_{Si} and characteristic length L_c . L_c is measured from the middle of the input waveguide to the edge of the output waveguide (or vice versa).	41
Figure 3.11:	a Cubic spline S bend. b Cubic spline waveguide S bend with width w_{Si} , lateral offset L_x , and longitudinal length L_y	42
Figure 3.12:	Generic directional coupler. L_{coup} is the straight-section coupling length, and L_{ex} is the additional coupling length in the region that angles away from the straight region. The coupling matrix comes from section 6.2.2 in [4].	42
Figure 3.13:	a GDS layout of a symmetric directional coupler. $L_{coup} = 50 \mu\text{m}$, $L_{ex} = 40 \mu\text{m}$ of 90° spline bends, the gap in the straight region is 280 nm, and each waveguide has a width of 650 nm. b Coupling coefficient $ \kappa ^2$ for the coupler in a as a function of wavelength.	43
Figure 3.14:	a Schematic of an asymmetric directional coupler. Coupling occurs most strongly in section L_2 , less strongly in sections L_1 and L_3 , and not at all in section L_4 . b This plot shows the transmission through C and D for an input in B. Total transmission is around 98% across the full wavelength range...	44
Figure 3.15:	Top view of an MZI structure. Black lines represent waveguides and the path-length difference on the top arm is highlighted in yellow. Each $50/50$ splitter is either a symmetric DC or an asymmetric DC (there are other types of WG-based splitters, but they are not part of this design kit).	45

Figure 3.16:	a E_x field of optical mode in hybrid Si-LN region with wide ($w_{Si} = 650$ nm) Si. b Narrow ($w_{Si} = 320$ nm) Si. c Top view of hybrid Si-LN taper. The taper is in the Si ridge layer, and LN film is bonded over the entire area. d Plot of transmission versus taper length.	45
Figure 3.17:	a Plot of simulated effective mode area (left axis, black circles) and LNCF (right axis, red circles). b Plot of simulated effective index (left axis, black circles) and group index (right axis, red squares). The dashed vertical blue line in each part shows where the mode we chose to use sits.	47
Figure 3.18:	3D depiction of the final cross-section from Fig. 3.3, but for the single Si waveguide of a hybrid Si-LN EO phase shifter. Only the straight section of the PS is shown here. Each layer's thickness is given, along with resistivity values for the Si handles. The EO PS has length "L."	48
Figure 3.19:	Plot of (3.4) when varying: a Characteristic impedance Z_0 , with $\Delta n = 0.10$ and $\alpha_{RF} = 1$ dB/(cm-GHz ^{1/2}); b RF losses α_{RF} , with $Z_0 = Z_G = Z_L = 50 \Omega$ and $\Delta n = 0.10$; and c RF-to-optical index difference Δn , with $Z_0 = Z_G = Z_L = 50 \Omega$ and $\alpha_{RF} = 1$ dB/(cm-GHz ^{1/2}). $L = 1$ cm for all simulations.	49
Figure 4.1:	The basic crystal ion slicing process is depicted in four steps: a The first wafer (W1) is ion-implanted. b W1 is bonded to the second wafer (W2), comprised of some handle material covered with a thin, smooth insulator material. c The bonded stack is heated until W1 cracks off ("slicing")...	52
Figure 4.2:	a A standard 220 nm SOI wafer from SOITEC is thinned to 150 nm with RIE. b Photoresist is spun on the wafer and patterned with DUV lithography. c RIE is used to etch the photoresist pattern into the thin Si layer. d Approximately 1 μ m of oxide is deposited via HDP CVD onto the patterned wafer.	54
Figure 4.3:	a SEM image of an over-polished waveguide. The measured value of only 20 nm is 130 nm below the targeted thickness, and is too thin to guide light. b Wafer map of oxide thickness over Si features after CMP and wet etch in optimized process flow (Fig. 4.2f).	54
Figure 4.4:	a The thin-film stack used in hybrid photonic devices based on silicon-on-insulator (SOI) and lithium niobate-on-insulator (LNOI). b A simplified bulk LN-BCB-Si bonded structure used in the calculations shown in Fig. 4.5.	59
Figure 4.5:	a Calculated maximum stresses in the upper-handle layer (LN or Si) of the complete thin-film stack and the simplified LN-BCB-Si stack shown in Fig. 4.4. Stress along each axis of the LN handle is nearly identical for the full stack and for the simplified stack, suggesting that the details...	62
Figure 4.6:	Depiction of LNOI with a Si handle, after implantation and before splitting off the bulk LN.	63
Figure 4.7:	a through e show camera images of 1 cm \times 1 cm pieces of LN or LNOI that were bonded to bulk Si pieces of a similar size through a 1 μ m BCB layer. a is bulk LN, b is LNOI with a LN handle, and c through e are LNOI with a Si handle, which has been removed by dry-etching...	64

Figure 4.8:	Energy-dispersive x-ray (EDX) spectrum analysis. The left plot is of a Si-backed LNOI sample from the manufacturer, and the right plot is of a LN film bonded through BCB to bulk Si. These two samples exhibit similar spectra, indicating a similarity in material properties.	66
Figure 4.9:	a The patterned SOI sample, bonded to a 4.2 mm × 16 mm film of LN through a thin BCB layer. b A zoomed in image of a corner of the bonded region. c The specific device we measure, magnified from a with sections of unchanging straight waveguide removed for visual convenience.	67
Figure 4.10:	a Wafer cross-section as received from Sandia National Laboratories, as depicted in Fig. 4.2f. b Bond the LN-on-insulator (LNOI) die (from a NanoLN wafer) to an SOI die, singulated from the Sandia wafer. c Remove the handle (SiO ₂ and substrate) from the LN film after bonding.	68
Figure 5.1:	Hybrid LN-Si photonic circuits. a Silicon photonic components were fabricated using deep ultraviolet (DUV) lithography. Singulated dies (size: 25 mm × 16 mm) were bonded to diced pieces (size: 21 mm × 17 mm) of an unpatterned Lithium Niobate (LN)-on-insulator wafer.	77
Figure 5.2:	Waveguide modes. a Calculated hybrid optical mode profiles for different Si rib widths. The panels show the magnitude of the electric field in the TE polarization, with the E-field vector oriented along the crystal axis. As the Si rib width w decreases, the modal effective index (n_{eff}) decreases...	79
Figure 5.3:	Adiabatic mode transition. a Gradual linear reduction of the Si rib width to transition between cross-sections A and B. b Numerical calculations of the modal effective index versus waveguide width, with yellow circles indicating the initial and final points of the taper.	81
Figure 5.4:	Waveguide characterization. a Transmission measurements of test structures consisting of 650 nm wide Si waveguides with SiO ₂ cladding (labeled ‘Si/SiO ₂ ’). b Transmission versus length of waveguides and bends (paper-clip structures)...	83
Figure 5.5:	Hybrid Si-LN optical circuit. a Optical microscope image of an interferometric hybrid Si-LN circuit which uses both waveguide cross-sections (C.S.) A and B, four adiabatic transitions (Transition) in each lightpath, two directional couplers (D.C.), and twenty 90-degree bends in each lightpath.	86
Figure 5.6:	Si/SiO₂ Mach-Zehnder interferometer (MZI). a An SiO ₂ -clad Si photonic MZI was fabricated on the same chip but outside the bonded LN region. The input-output waveguides pass under the LN bonded region and emerge on the other facet of the chip.	88
Figure 6.1:	a Schematic of the EOM (not to scale, not showing electrodes), including two 3-dB directional couplers (DC) and a waveguide segment for path-length difference (PLD). Three optical waveguide modes are used, labeled as A, B, and C.	93

Figure 6.2:	a Optical transmission through EOM device with greater than 15 dB extinction ratio across the entire measured wavelength range of 1525 nm to 1575 nm. b Pictorial representation of optical setup. SM = single mode, PM = polarization maintaining, and L/T = lensed/tapered.	94
Figure 6.3:	Transmission for various waveguide lengths at $\lambda = 1550$ nm is shown for the all-Si mode (a , Mode A) and the Si-LN mode (b , Mode C). Propagation loss is significantly lower for the hybrid, narrow-Si mode, at only 0.64 dB/cm compared with 1.34 dB/cm for the all-Si mode...	95
Figure 6.4:	a Measured (circles) spline bending loss for various characteristic lengths (L_c) at $\lambda = 1550$ nm. Lines represent linear fits of transmission measurements for a number of devices with varying amounts of quarter-circle spline bends.	97
Figure 6.5:	a Scattering matrix representation of a two-port electrical network. b ABCD matrix representation of a two-port electrical network. c Circuit schematic for a long, lossy transmission line of length d . R, L, C, and G are the per unit length series resistance, series inductance, shunt capacitance...	100
Figure 6.6:	a Measured electrical S-parameters of the EOM's coplanar-waveguide transmission line. b Left y-axis: extracted microwave phase index n_m and microwave loss α_m (units of dB/cm). Right y-axis: characteristic impedance Z_c (Ω).	103
Figure 6.7:	A plot of optical power versus applied dc voltage. The dc voltage supply is a Keithley 2420. Device length is 5 mm. ER = extinction ratio. Fitting was performed in MATLAB.	105
Figure 6.8:	a Experimental setup for low frequency modulation response. PD = photodetector. Red arrows represent the optical signal, black arrows represent the electrical signal. b Measured response of a low frequency EOM from 100 MHz up to 6 GHz (the limit of the VNA).	106
Figure 6.9:	a Thin film x-cut lithium-niobate (LN) on insulator dies were bonded at room temperature to segmented dies of a patterned and planarized silicon-on-insulator (SOI) wafer which contained fabricated silicon photonic waveguide circuits. No etching or patterning of the LN film was performed.	108
Figure 6.10:	a Normalized optical transmission of the Mach-Zehnder interferometric electro-optic Modulator (MZM), versus dc voltage at optical wavelength = 1560 nm. Fitted $V_\pi L = 6.7$ V.cm for device length $L = 0.5$ cm.	111
Figure 6.11:	Measured electro-optic response up to 106 GHz.	113
Figure 7.1:	Measured n and k curves of PECVD amorphous SiC.	132
Figure 7.2:	a Cross-section of hybrid SiC-LN waveguide. b Top view of our proposed structure, consisting of a quasi-phase matched region (the "PPLN" section), an adiabatic taper to convert the SiC width from a narrow rib to a wide rib, and two 90° spline bends to wrap the SiC back around into the PPLN section.	133
Figure 7.3:	a Sweep of η_0 versus SiC width for SiC heights of 100 nm, 150 nm, 200 nm, and 250 nm. b Mode pictures for $w_{SiC} = 120$ nm and $h_{SiC} = 250$ nm for the SH mode (top) and FH mode (bottom).	135
Figure 7.4:	How the phase matching FH wavelength shifts as a function of w_{SiC} , h_{SiC} , h_{LN} , and temperature is shown in a , b , c , and d , respectively.	136

Figure 7.5:	Simulated P_{SH} when loss is added to the model (a) and when duty cycle error is added to the model (b) . In both cases, the input power (P_{FH}) is 10 mW and the nonlinear interaction length is assumed to be 1 cm. In b , each curve represents a different RMS poling period error, from 0 nm (no error) to 250 nm.	138
Figure 7.6:	a Top view of the 180° bend, plus tapers and additional straight waveguides (“Str.”), connecting adjacent QPM NLO sections. The phase along the structure is tracked in b to ensure that an integer multiple of $\Delta k = 2\pi$ rad. occurs at the output of the bend. c Plot of device area A_D versus L_c	139
Figure 7.7:	Simulated spline bending losses for the SH and FH waves are shown in parts a and b , respectively. Losses are significantly lower for the SH wave because of its reduced mode size. Simulated taper losses are shown in part c for both SH and FH waves.	141
Figure 7.8:	Sweep of A_{eff} versus SiC width at $\lambda = 775$ nm (part a) and $\lambda = 1550$ nm (part b) for SiC heights of 100 nm, 150 nm, 200 nm, and 250 nm. c and d show mode pictures for $w_{SiC} = 250$ nm and $h_{SiC} = 250$ nm (part c) and $w_{SiC} = 150$ nm and $h_{SiC} = 250$ nm (part d) for the SH mode (top) and the FH mode (bottom).	143
Figure 7.9:	Sweep of LNCF versus SiC width at $\lambda = 775$ nm (part a) and $\lambda = 1550$ nm (part b) for SiC heights of 100 nm, 150 nm, 200 nm, and 250 nm. c and d show mode pictures for $w_{SiC} = 100$ nm and $h_{SiC} = 100$ nm (part c) and $w_{SiC} = 200$ nm and $h_{SiC} = 100$ nm (part d) for the SH mode (top) and the FH mode (bottom).	145

LIST OF TABLES

Table 3.1:	Process outline to fabricate hybrid Si-LN devices (active and passive).	32
Table 3.2:	Table of acceptable combinations of values for Si width and LN thickness. In the upper right of the table, one or more of the field components (E_x , E_y , E_z , H_x , H_y , or H_z) has coupled into the LN slab. In the lower section of the table, TE_2 exists and can couple with TE_0	36
Table 4.1:	Material properties of all materials used in our numerical calculations of thermally-induced stress. All data is taken at room temperature. E is the modulus of elasticity, and α is the coefficient of thermal expansion (CTE). x , y , and z are used to denote the crystal axes of anisotropic LN.	60
Table 7.1:	Fitted parameters of the Tauc-Lorentz model for our PECVD SiC film. See [17] for more details on the Tauc-Lorentz model.	132

ACKNOWLEDGEMENTS

I would like to thank my adviser, Shayan Mookherjea, for overseeing this thesis work. He knows better than anyone the struggles I have suffered and the successes I have enjoyed over the years. I can not thank him enough for his support and tutelage during my graduate studies.

I would also like to thank all of my co-authors for their assistance throughout this experience. The Sandia team led by Anthony Lentine has been nothing short of superb. There is no doubt that this work would never have been anything more than an amalgamation of simulations if not for the efforts of Anthony and others. In particular, I would like to thank Douglas Trotter for patiently answering all of my fabrication-related questions, even when it meant getting pulled into an unexpected Friday afternoon conference call. Sri Sriram and Vincent Stenger at Srico, Inc., thank you for allowing me to spend a few weeks at your headquarters in Ohio. There's really nothing quite as impressive as seeing how a small business makes beautiful products. To my collaborators here at UC San Diego: thank you for the (sometimes long) talks about high-speed electrical measurements and components, and for sharing equipment, sometimes the day before a deadline. More than once. Cooper Levy, Kelvin Fang, and Hasan Al-Rubaye – I would still be staring at noisy 6 GHz VNA measurements if not for your help.

To the group members who guided me in my early years, I owe you a debt I can never repay. Ryan Aguinaldo developed many of the early simulation techniques for this project before I joined the research group, and freely offered his time and expertise to get me started. I cherish our meandering, sometimes even circular, discussions on the meaning of Maxwell's equations. Marc Savanier's knowledge of nonlinear optical theory and fabrication experience were invaluable throughout the course of this research. It was truly an honor to work alongside him. And of course I would be remiss not to mention Ranjeet Kumar and Jun Rong Ong for their constant willingness to see me succeed and to help where they could (as well as the not-so-infrequent outing to Buffalo Wild Wings whenever Ranjeet decided he wasn't vegetarian for a day).

Of course, this acknowledgments section would be incomplete without mentioning the efforts of Jie Zhao, another PhD student in our research group. Jie's tireless efforts, particularly in

the clean room, have gotten us through many a tight deadline. I look forward to seeing her own thesis work progress over the next couple of years.

Chapter 3, in part, is a reprint of the material as it appears in Conference on Lasers and Electro-Optics (CLEO) 2017. Peter O. Weigel and Shayan Mookherjea, paper JTU5A.126. The dissertation author, together with his adviser, led the research efforts for this work and co-authored the paper.

Section 4.5 of Chapter 4, in full, is a reprint of the material as it appears in Optical Materials 2017. Peter O. Weigel & Shayan Mookherjea, Optical Materials Vol. 66, 605-610 and in Conference on Lasers and Electro-Optics (CLEO) 2017. Peter O. Weigel and Shayan Mookherjea, paper. SM3K.1. The dissertation author, together with his adviser, led the research efforts for this work and co-authored the papers.

Chapter 5, in part, is a reprint of the material as it appears in Scientific Reports 2016. Peter O. Weigel, Marc Savanier, Christopher T. DeRose, Andrew T. Pomerene, Andrew L. Starbuck, Anthony L. Lentine, Vincent Stenger & Shayan Mookherjea, Scientific Reports **6**, 22301. The dissertation author, together with his adviser, led the research efforts for this work and co-authored the paper.

Chapter 6, in part, is currently being prepared for submission for publication of the material. Peter O. Weigel, Jie Zhao, Kelvin Fang, Hasan Al-Rubaye, Douglas Trotter, Dana Hood, John Mudrick, Christina Dallo, Andrew T. Pomerene, Andrew L. Starbuck, Christopher T. DeRose, Anthony L. Lentine, Gabriel Rebeiz and Shayan Mookherjea. Portions of Chapter 6 are reprinted from Conference on Lasers and Electro-Optics (CLEO) 2018. Peter O. Weigel, Jie Zhao, Douglas Trotter, Dana Hood, John Mudrick, Christina Dallo, Andrew T. Pomerene, Andrew L. Starbuck, Christopher T. DeRose, Anthony L. Lentine and Shayan Mookherjea, paper SF2I.4. The dissertation author, together with his adviser, led the research efforts for this work and co-authored the papers.

Chapter 7, in part, is a reprint of the material as it appears in Journal of the Optical Society B 2018. Peter O. Weigel & Shayan Mookherjea, JOSA B 35(3), 593-600 and in Conference on Lasers and Electro-Optics (CLEO) 2017. Peter O. Weigel, Marc Savanier and Shayan Mookherjea,

paper SW4M.5. The dissertation author, together with his adviser, led the research efforts for this work and co-authored the papers.

VITA

- 2013 B.S. in Electrical Engineering *summa cum laude*, Lehigh University
- 2014 M.S. in Electrical Engineering, University of California San Diego
- 2018 Ph.D. in Electrical Engineering (Photonics), University of California San Diego

PUBLICATIONS

Peter O. Weigel, Jie Zhao, Kelvin Fang, Hasan Al-Rubaye, Douglas Trotter, Dana Hood, John Mudrick, Christina Dallo, Andrew T. Pomerene, Andrew L. Starbuck, Christopher T. DeRose, Anthony L. Lentine, Gabriel Rebeiz and Shayan Mookherjea, “Bonded Thin Film Lithium Niobate Modulator on a Silicon Photonics Platform Exceeding 100 GHz Bandwidth,” *Manuscript under review*.

Peter O. Weigel, Jie Zhao, Douglas Trotter, Dana Hood, John Mudrick, Christina Dallo, Andrew T. Pomerene, Andrew L. Starbuck, Christopher T. DeRose, Anthony L. Lentine and Shayan Mookherjea, “Foundry-compatible Hybrid Silicon / Lithium Niobate Electro-Optic Modulator,” in *Conference on Lasers and Electro-Optics (CLEO)*, paper SF2I.4 (2018).

Peter O. Weigel and Shayan Mookherjea, “Design of folded hybrid silicon carbide-lithium niobate waveguides for efficient second-harmonic generation,” *Journal of the Optical Society B* 35(3), 593-600 (2018).

Peter O. Weigel, Marc Savanier and Shayan Mookherjea, “Hybrid Lithium Niobate Waveguide for Efficient Quasi-Phase-Matched Optical Frequency Conversion,” in *Conference on Lasers and Electro-Optics (CLEO)*, paper SW4M.5 (2017).

Peter O. Weigel and Shayan Mookherjea, “Process Design Kit and Modulator Simulations for Hybrid Silicon-Lithium Niobate Integrated Optics,” in *Conference on Lasers and Electro-Optics (CLEO)*, paper JTU5A.126 (2017).

Peter O. Weigel and Shayan Mookherjea, “Hybrid Silicon / Lithium Niobate Waveguide Micro-chips Stable to 300°C,” in *Conference on Lasers and Electro-Optics (CLEO)*, paper SM3K.1 (2017).

Peter O. Weigel and Shayan Mookherjea, “Reducing the thermal stress in a heterogeneous material stack for large-area hybrid optical silicon-lithium niobate waveguide micro-chips,” *Optical Materials* Vol. 66, 605-610 (2017).

Peter O. Weigel, Marc Savanier, Christopher T. DeRose, Andrew T. Pomerene, Andrew L. Starbuck, Anthony L. Lentine, Vincent Stenger and Shayan Mookherjea, “Lightwave circuits in lithium niobate through hybrid waveguides with silicon photonics,” *Scientific Reports* 6, 22301 (2016).

Marc Savanier, Peter O. Weigel and Shayan Mookherjea, “Proposal and analysis of a hybrid silicon photonic-lithium niobate waveguide for difference frequency generation,” *Optics Communications* 356, 330-335 (2015).

Ryan Aguinaldo, Peter Weigel, Hannah Grant, Christopher DeRose, Anthony Lentine, Andrew Pomerene, Andrew Starbuck and Shayan Mookherjea, “Characterization of a silicon-photonics multi-wavelength power monitor,” in *Optical Interconnects Conference*, 139-140 (2014).

Ryan Aguinaldo, Peter Weigel, Hannah Grant, Christopher DeRose, Anthony Lentine, Andrew Pomerene, Andrew Starbuck, Andre Tkacenko and Shayan Mookherjea, “A silicon photonic channelized spectrum monitor for UCSD’s multi-wavelength ring network,” in *Conference on Lasers and Electro-Optics (CLEO)*, paper STu1G.4 (2014).

ABSTRACT OF THE DISSERTATION

**High-Speed Hybrid Silicon-Lithium Niobate Electro-Optic Modulators
& Related Technologies**

by

Peter O. Weigel

Doctor of Philosophy in Electrical Engineering (Photonics)

University of California San Diego, 2018

Professor Shayan Mookherjea, Chair

Electro-optic modulators (EOMs) serve as a technological pillar of the modern telecommunications industry. Without these devices, which convert electrical data into optical data through one of several physical phenomena (depending on the specific technology), telecommunications channels would be severely bandwidth-limited, particularly within data centers. To meet the ever-increasing bandwidth demands of the industry, either more EOMs are necessary (resulting in higher power requirements) or higher bandwidth EOM technology must be developed. This thesis discusses the theory, design, fabrication, and characterization of foundry-compatible hybrid silicon-lithium niobate (Si-LN) electro-optic modulators integrated on a wafer platform, a new technology with potentially far-reaching applications.

By bonding a thin film of ion-sliced LN crystal, which retains the crystal properties of bulk LN, to silicon waveguides in the Mach-Zehnder modulator configuration, it is theoretically possible to exceed the bandwidth limitations of all-Si modulators without abandoning the scalable, dense silicon-on-insulator (SOI) platform. These hybrid devices make use of the favorable linear electro-optic Pockels effect of LN while using the high-index Si waveguide to reduce the optical mode area, so that low-voltage, high-bandwidth devices can be realized. This thesis focuses on developing broadband EOMs with cutoff frequencies beyond 100 GHz. Developing this technology on an SOI wafer platform fabricated via photolithography in a foundry facility presents a realistic path towards next-generation high-speed, low-power integrated EOMs.

Chapter 1

Theory of Electro-Optic Modulators

1.1 Introduction

In its most basic form, an electro-optic modulator (EOM) is a device that converts electrical data into optical data by, in some way, imprinting an electrical waveform onto the phase of an optical laser beam (i.e., “modulation”). The EOM in this simple form is known as a phase modulator, but more often the phase modulator is a component in an interferometric structure such as the Mach-Zehnder interferometer (MZI) shown in Fig. 1.1a, where the phase modulation in each arm of the structure is used to cause interference, effectively modulating the optical intensity. When used in this layout, the EOM is called an intensity modulator and the layout is termed a Mach-Zehnder modulator (MZM), the electrically active form of the MZI.

While free space, table-top EOMs can be built with bulk components, because of size, weight, and power limitations, integrated EOMs have been an area of research since the 1970s [1]. This chapter will discuss general EOM theory, particularly for integrated lithium niobate (LiNbO_3 or LN) EOMs which use the Pockels effect. Silicon (Si) EOMs based on the plasma dispersion effect will also be discussed.

All devices considered for the remainder of this chapter are assumed to be in the MZM configuration.

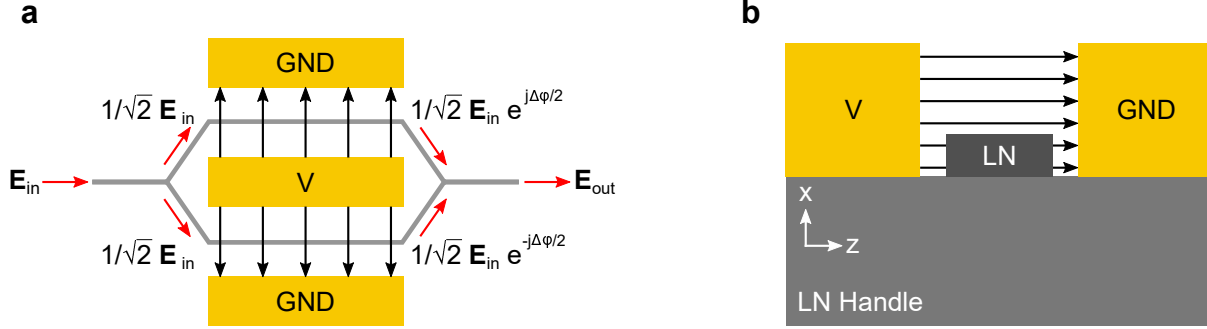


Figure 1.1: **a** Top view of a standard MZM in the push-pull configuration, meaning the two arms of the MZM have (ideally) equal and opposite electro-optic phase shifts ($\Delta\phi$ = the total phase shift of the device). Gray lines represent the optical waveguides, gold boxes represent the electrical lines (“electrodes”), red arrows represent the flow of light, and black arrows represent electric field lines. ‘GND’ = ground, ‘V’ = applied voltage, and \mathbf{E}_{in} is the electric field component of the input optical wave. **b** A cross-section of a single arm of the MZM, where the waveguiding region is defined by an etched ridge of LN on a bulk LN handle.

1.2 Lithium Niobate & the Pockels Effect

Before discussing *how* lithium niobate is useful, it is first helpful to explain *why* lithium niobate is useful. Lithium Niobate (LN) is a birefringent crystal, which means it has a different refractive index depending upon the polarization and direction of propagation of light through the crystal. In particular, LN displays negative uniaxial birefringence, meaning only the z axis (also known as the crystal axis) has a different refractive index (uniaxial), but it is a lower value than the refractive index along the x and y crystal axes (negative). The refractive index along the z axis is called the extraordinary refractive index (n_e) and the refractive index along x and y is called the ordinary refractive index (n_o).

Additionally, the LN crystal can be cut into a wafer form in different ways. Each type of cut of wafer is defined by the axis of the crystal that is perpendicular to the wafer surface. For example, a z -cut LN crystal will have the z crystal axis perpendicular to the surface of the crystal, while an x -cut LN crystal will have the z axis parallel to the surface of the crystal. Because of these properties, LN lacks inversion symmetry to its crystal lattice.¹

¹Though of less interest to this thesis, LN is also piezoelectric (generates charge when put under mechanical stress, useful for acoustic wave generation) and pyroelectric (generates charge when put under thermal stress, useful as a thermal transducer) [2].

Crystals which lack inversion symmetry are classified generally as “non-centrosymmetric” and display the Pockels effect, also known as the linear electro-optic effect, where a shift in the crystal’s refractive index is observed under the application of an electric field. As a brief proof of this effect (see [3] for more details), we shall start by considering an index ellipsoid in the (x, y, z) coordinate system:

$$\frac{x^2}{n_x^2} + \frac{y^2}{n_y^2} + \frac{z^2}{n_z^2} = 1. \quad (1.1)$$

Here n_i is the material’s refractive index along each of the principle dielectric axes, x , y , and z . As mentioned earlier, the Pockels effect is a change in a material’s refractive index as a function of an applied electric field:²

$$\Delta \left(\frac{1}{n^2} \right)_{ij} \equiv r_{ijk} E_k \quad (1.2)$$

where r_{ijk} is the linear electro-optic tensor, and E_k is the k th component of the applied electric field. k can represent any of the three principal axes (x, y , or z). Under the application of an electric field as per Equation (1.2) (i.e. adding Equation (1.2) to Equation (1.1)) results in

$$\begin{aligned} \left(\frac{1}{n_x^2} + r_{11k} E_k \right) x^2 + \left(\frac{1}{n_y^2} + r_{22k} E_k \right) y^2 + \left(\frac{1}{n_z^2} + r_{33k} E_k \right) z^2 \\ + 2xyr_{12k} E_k + 2yzr_{23k} E_k + 2zxr_{13k} E_k = 1. \end{aligned} \quad (1.3)$$

Equation (1.3) assumes that $r_{ijk} = r_{jik}$, which is valid when considering high purity non-active crystals. Voigt index contraction is next used to simplify (1.3), where 1 = (11) = (xx), 2 = (22) = (yy), 3 = (33) = (zz), 4 = (23) = (32) = (yz) = (zy), 5 = (13) = (31) = (xz) = (zy), and 6 = (12) = (21) = (xy) = (yx). This convention is only for convenience, as it reduces the number of independent electro-optic coefficients from 27 to 18. Using this contraction in matrix form, Equation (1.2) becomes

²Physically, this is caused by a slight shift in the crystal lattice.

$$\begin{bmatrix} \Delta(1/n^2)_1 \\ \Delta(1/n^2)_2 \\ \Delta(1/n^2)_3 \\ \Delta(1/n^2)_4 \\ \Delta(1/n^2)_5 \\ \Delta(1/n^2)_6 \end{bmatrix} = \begin{bmatrix} r_{11} & r_{12} & r_{13} \\ r_{21} & r_{22} & r_{23} \\ r_{31} & r_{32} & r_{33} \\ r_{41} & r_{42} & r_{43} \\ r_{51} & r_{52} & r_{53} \\ r_{61} & r_{62} & r_{63} \end{bmatrix} \begin{bmatrix} E_x \\ E_y \\ E_z \end{bmatrix} \quad (1.4)$$

Equation (1.4) is valid for any crystalline material that meets the aforementioned symmetry criteria. Non-centrosymmetric crystals, such as crystalline Si, have an electro-optic tensor that looks like this:

$$r_{Si} = \begin{bmatrix} 0 & 0 & 0 \\ 0 & 0 & 0 \\ 0 & 0 & 0 \\ 0 & 0 & 0 \\ 0 & 0 & 0 \\ 0 & 0 & 0 \end{bmatrix} \quad (1.5)$$

which is what one should expect, considering that non-centrosymmetric materials contain an inversion symmetry. Of more interest is the electro-optic tensor for LN, which falls under the 3m crystal symmetry class [2]:

$$r_{LN} = \begin{bmatrix} 0 & -r_{22} & r_{13} \\ 0 & r_{22} & r_{13} \\ 0 & 0 & r_{33} \\ 0 & r_{42} & 0 \\ r_{42} & 0 & 0 \\ -r_{22} & 0 & 0 \end{bmatrix} . \quad (1.6)$$

Precise material properties vary depending on the composition of the LN crystal (e.g. Li⁺ percentage) as well as crystal purity and the wavelength of operation, but as a rough estimate, $r_{22} = 3.4$ pm/V, $r_{13} = 8.6$ pm/V, $r_{42} = r_{51} = 26$ pm/V, and $r_{33} = 31$ pm/V at a wavelength of 633 nm [3, 2]. Larger r_{ij} values correspond to a stronger Pockels effect. The advantage of LN, in addition to its ability to be formed into high purity crystalline wafers from a melt (as opposed to being grown in a reactor, where uniformity, repeatability, and growth rate are concerns), is that applying an electric field along the crystal's z axis results in non-zero values to only $\Delta(1/n^2)_1$, $\Delta(1/n^2)_2$, and $\Delta(1/n^2)_3$ in Equation (1.4). Of particular interest is $\Delta(1/n^2)_3$, because it is proportional to r_{33} , the largest electro-optic coefficient in LN. Since this index shift is occurring along the z axis of the crystal (see Equation (1.3)) – the same direction the electric field is being applied along – an optical wave polarized along this crystal axis will respond to the material index shift with a (linearly) proportional phase shift.³ This physical effect is at the root of all electro-optic devices built using LN.

1.2.1 Voltage-Length Product in LN MZMs

The voltage-length product, or $V_\pi L$, is a popular figure of merit used to describe the inverse relationship between the voltage required to modulate the output optical intensity of an MZM from a maximum to a minimum by applying a π phase shift (V_π) and the physical length of the modulation region (L). This definition will vary depending on the effect used for modulation. For MZMs based on the Pockels effect, $V_\pi L$ can be derived from general electromagnetic theory.

We begin by considering an MZM with the top view and cross-section of Fig. 1.1. For such a structure, the optical mode exists primarily in the LN ridge region, though some exponential tails of the mode exist in the surrounding cladding region (typically air or silicon dioxide) which does not display the Pockels effect. In this case, we must be careful when calculating $V_\pi L$ to only consider that portion of the mode which is in the LN and polarized along the proper crystal axis. For this derivation, we will assume the optical wave is well polarized along the z axis so that only the LN

³It's worth mentioning that the $\Delta(1/n^2)_1$ and $\Delta(1/n^2)_2$ terms, which are non-zero and proportional to r_{13} when an electric field is applied along the crystal's z axis, result in changes to the material index in the x and y crystal axes.

material index shift associated with r_{33} needs to be considered.⁴

We begin with the wave equation for an optical field [4]:

$$\nabla_t \mathbf{E}_o + [n^2 k_0^2 - \beta_{\text{eff}}^2] \mathbf{E}_o = 0, \quad (1.7)$$

where n is the material index, $k_0 = 2\pi/\lambda_0$ is the free-space wavenumber, λ_0 is the free-space wavelength, $\beta_{\text{eff}} = 2\pi n_{\text{eff}}/\lambda_0$ is the optical mode's propagation constant, and $\mathbf{E}_o \propto \exp^{j(\beta_{\text{eff}}y - \omega t)} \hat{z}$. Equation (1.7) is the unperturbed wave equation, i.e. without any voltage. When a voltage is applied, the LN material index changes by Δn . In that case, n^2 becomes $(n+\Delta n)^2 = n^2 + \Delta n^2 + 2n\Delta n \approx n^2 + 2n\Delta n$, where the approximation is valid because $\Delta n \ll n$. Similarly, β_{eff}^2 becomes $(\beta_{\text{eff}} + \Delta\beta_{\text{eff}})^2 \approx \beta_{\text{eff}}^2 + 2\beta_{\text{eff}}\Delta\beta_{\text{eff}}$.

When a voltage is applied, the optical field is perturbed and the wave equation becomes

$$\nabla_t \mathbf{E}'_o + [(n^2 + 2n\Delta n)k_0^2 - (\beta_{\text{eff}}^2 + 2\beta_{\text{eff}}\Delta\beta_{\text{eff}})] \mathbf{E}'_o = 0. \quad (1.8)$$

Assuming that the perturbed field $\mathbf{E}'_o \approx \mathbf{E}_o$, we can substitute Equation (1.7) into Equation (1.8), multiply both sides by \mathbf{E}_o^* , and arrive at

$$[2n\Delta n k_0^2 - 2\beta_{\text{eff}}\Delta\beta_{\text{eff}}] |\mathbf{E}_o|^2 = 0. \quad (1.9)$$

The electro-optic effect takes place over all space in the transverse domain, which is accounted for by integrating over the x,z plane:

$$\int \int_{-\infty}^{\infty} [2n(x,z)\Delta n(x,z)k_0^2 - 2\beta_{\text{eff}}\Delta\beta_{\text{eff}}] |E_o(x,z)|^2 dx dz = 0. \quad (1.10)$$

With some rearrangement of Equation (1.10), and keeping in mind that $\beta_{\text{eff}} = 2\pi n_{\text{eff}}/\lambda_0$, we arrive at:

⁴In principle, each of the index shifts caused by a z -oriented applied electric field can be evaluated separately, considering that they are orthogonal to one another. However, in most practical cases the polarization fraction of a well-designed guided mode will be >99% and along the z axis, so effects due to r_{13} (which is nearly four times smaller than r_{33}) along the x and y crystal axes will be negligible.

$$\Delta n_{\text{eff}} = \frac{1}{n_{\text{eff}}} \frac{\int \int_{LN} n(x,z) \Delta n(x,z) |E_o(x,z)|^2 dx dz}{\int \int_{\infty} |E_o(x,z)|^2 dx dz}, \quad (1.11)$$

$n(x,z)$ and $\Delta n(x,z)$ correspond to the *material* refractive index and refractive index change, respectively, at each point (x,z) . Since $\Delta n(x,z)$, which is due to the Pockels effect, equals zero outside of the LN film, the integral in the numerator is only taken over the LN. The refractive index of LN is well known, as is the change in refractive index of LN under an applied voltage [3]:

$$\Delta n_e \approx -\frac{1}{2} n_e^3 r_{33} E_{RF}. \quad (1.12)$$

Δn_e is the change in the extraordinary refractive index of LN when introduced to an external electric field E_{RF} , where ‘RF’ stands for ‘radio frequency’ and is commonly used to denote high frequency alternating current (ac) electrical signals. Here we are only considering the change in the extraordinary axis because the optical mode is TE-like in x -cut LN, meaning that the optical mode is almost entirely polarized along the crystal axis of LN and sees only the extraordinary refractive index, n_e . n_e is the extraordinary refractive index of LN when no electric field is applied, r_{33} is the previously defined largest component of the linear electro-optic tensor r_{ijk} , and E_{RF} is the applied electric field along the crystal (z) axis to utilize the r_{33} electro-optic coefficient.

By substituting Equation (1.12) into Equation (1.11) and denoting $n(x,z) = n_e$, we have

$$\Delta n_{\text{eff}} = \frac{-n_e^4 r_{33}}{2n_{\text{eff}}} \frac{\int \int_{LN} |E_o(x,z)|^2 E_{RF}(x,z) dx dz}{\int \int_{\infty} |E_o(x,z)|^2 dx dz}. \quad (1.13)$$

The integral in the numerator of Equation (1.13) can be normalized to a uniform field by substituting E_{RF} with $\frac{V_A}{G} \frac{G}{V_A} E_{RF}$ in Equation (1.13):

$$\Delta n_{\text{eff}} = \frac{-n_e^4 r_{33} V_A}{2n_{\text{eff}} G} \frac{G \int \int_{LN} |E_o(x,z)|^2 E_{RF}(x,z) dx dz}{V_A \int \int_{\infty} |E_o(x,z)|^2 dx dz}, \quad (1.14)$$

or, more succinctly:

$$\Delta n_{\text{eff}} = \frac{-n_e^4 r_{33} V_A}{2n_{\text{eff}} G} \Gamma_{mo}, \quad (1.15)$$

where

$$\Gamma_{mo} = \frac{G \int \int_{LN} |E_o(x, z)|^2 E_{RF}(x, z) dx dz}{V_A \int \int_{\infty} |E_o(x, z)|^2 dx dz} \quad (1.16)$$

is the normalized overlap between the optical and electrical fields in the $x-z$ plane, and has a maximum value of 1 when the applied field is entirely uniform, as in the case of an ideal parallel-plate configuration.

The phase of an unperturbed optical wave is $\phi = \beta_{\text{eff}} z = \frac{2\pi n_{\text{eff}} z}{\lambda_0}$. When the optical field is perturbed by an applied electric field, the optical phase becomes $\phi + \Delta\phi = \frac{2\pi(n_{\text{eff}} + \Delta n_{\text{eff}})z}{\lambda_0}$. If we assume that the upper ground electrode of Fig. 1.1a is not present, then the electric field is only applied along the lower optical waveguide and the phase difference between the left and right waveguides at the y-junction combiner of the EOM is $\Delta\phi = \frac{2\pi \Delta n_{\text{eff}} z}{\lambda_0}$. When we substitute Equation (1.15) into this expression for $\Delta\phi$, we get

$$\Delta\phi = -\frac{n_e^4 r_{33} \pi V_A z}{n_{\text{eff}} \lambda_0 G} \Gamma_{mo}. \quad (1.17)$$

The half wave voltage-length product $V_{\pi} L$ is the voltage required to achieve a phase shift of $\pm\pi$ radians multiplied by the length of the device. If we set $\Delta\phi = -\pi$, $z = L$ (the length of the electro-optic interaction region), and call $V_A = V_{\pi}$, we can derive an expression for the half wave voltage-length product for a thin film LN-based EOM:

$$V_{\pi} L = \frac{n_{\text{eff}} \lambda_0 G}{n_e^4 r_{33} \Gamma_{mo}}. \quad (1.18)$$

Equation (1.18) reduces to the traditional expression (Equation (9a) in [5]) when $n_{\text{eff}} = n_e$ and the integrals in Γ_{mo} are taken over the entire cross-section domain, not just the LN ridge. These are practical assumptions for titanium indiffused LN (Ti:LiNbO₃) modulators.

Equation (1.18) is analyzed in Fig. 1.2, where each of the three variables (n_{eff} , G , and Γ_{mo}) is swept through a reasonable range of values in the non push-pull configuration (in the push-pull configuration – such as in Fig. 1.1a – all $V_{\pi}L$ values would simply be divided by 2).

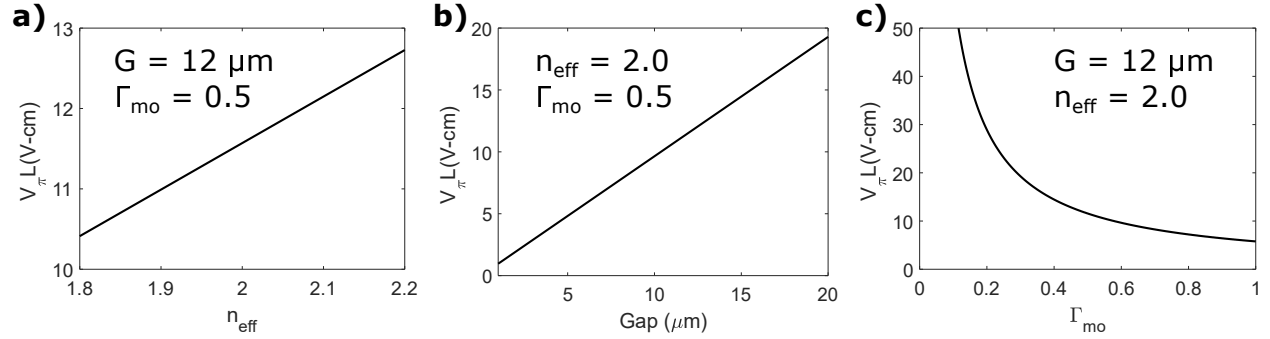


Figure 1.2: $V_{\pi}L$ is evaluated versus: n_{eff} (a), G (b), and Γ_{mo} (c).

Of interest to a designer is the theoretical limitation for this type of structure. In the theoretical limit, $\Gamma_{mo} = 1$ and $V_{\pi}L = 2.41 \cdot 10^5 \cdot n_{\text{eff}}G$ (V-cm) at $\lambda_0 = 1550$ nm. In bulk LN devices the limitation on the electrode gap is the width of the optical mode (as well as electrical losses which affect modulation bandwidth limitations, but we will not consider those here). Lastly, if $\Gamma_{mo} = 1$ and the optical mode is well confined in the LN ridge region, then it's unlikely n_{eff} will be much lower than 2.10, since the majority of the mode will reside in the LN and not the lower-index cladding.

In this “best-case” scenario ($G = 1 \mu\text{m}$ and $n_{\text{eff}} = 2.10$), $V_{\pi}L = 0.5$ (V-cm) in the non push-pull configuration, and $V_{\pi}L = 0.25$ (V-cm) in the push-pull configuration. This is a reasonable estimate of the limitation on $V_{\pi}L$ when the EOM is optimized solely for $V_{\pi}L$ minimization (this ignores optical loss limitations and fabrication limitations, such as the finite width of the LN ridge).

1.2.2 Electro-Optic Bandwidth Theory for a Traveling Wave Mach-Zehnder Modulator

The 3-dB bandwidth of an electro-optic modulator is a metric used to describe the device's working frequency range. An MZM designed with straight electrical lines displays a low-pass frequency response, and the frequency point where the response drops to 3-dB below its dc value is called its 3-dB bandwidth.

There are, however, two different definitions of 3-dB bandwidth commonly used when discussing electro-optic modulators. Perhaps unsurprisingly, these are the electrical 3-dB bandwidth and the optical 3-dB bandwidth. To understand the differences between these two bandwidths, some discussion of the device's response is required. First, consider the basic definition of the modulator's response described in the previous paragraph:

$$m(\omega) = \left| \frac{P_o(\omega)}{P_o(0)} \right|. \quad (1.19)$$

Here, P_o is the *optical* output power, modulated with an electrical signal at frequency ω . Because of its low pass characteristics, the response of the MZM is defined as the ratio of P_o at ω Hz to P_o at 0 Hz. In dB, this becomes the optical modulation response $m_o(\omega)$:

$$m_o(\omega) = 10 \log_{10}(m(\omega)) = 10 \log_{10} \left(\left| \frac{P_o(\omega)}{P_o(0)} \right| \right). \quad (1.20)$$

However, the modulated laser is detected through a photodetector, which has a responsivity R (units of amps per watt) and outputs an electrical current proportional to optical power, so that

$$m(\omega) = \left| \frac{RP_o(\omega)}{RP_o(0)} \right| = \left| \frac{I_e(\omega)}{I_e(0)} \right| \quad (1.21)$$

where I_e is the electrical current out of the photodetector. In this case, the electrical bandwidth is defined with respect to the electrical power P_e measured out of the photodetector:⁵

$$m_e(\omega) = 10 \log_{10} \left(\left| \frac{P_e(\omega)}{P_e(0)} \right| \right) = 10 \log_{10} \left(\left| \frac{I_e^2(\omega)}{I_e^2(0)} \right| \right) = 20 \log_{10} \left(\left| \frac{I_e(\omega)}{I_e(0)} \right| \right) = 20 \log_{10} \left(\left| \frac{P_o(\omega)}{P_o(0)} \right| \right), \quad (1.22)$$

where $m_e(\omega)$ is the electrical modulation response. From Equations (1.20) and (1.22), it is clear that $m_e(\omega)|_{dB_e} = 2m_o(\omega)|_{dB_o}$. For distinction, units of 'dBe' are used for the electrical response and units of 'dBo' are used for the optical response. When defining the 3-dB bandwidth, the optical

⁵Electrical power is proportional to current squared.

3-dB bandwidth will be the 6-dB electrical bandwidth. Both definitions are used in the literature, sometimes ambiguously.

The complete derivation of the small signal frequency response $m(\omega)$ of a traveling-wave MZM (that is, one in which the wavelength of the electrical wave is taken into account) is described quite thoroughly in [4], and will not be included here. The final expression for the modulation response of a modulator with coplanar waveguide electrodes, from [4], is:

$$m(\omega) = \frac{R_L + R_G}{R_L} \left| \frac{Z_{in}}{Z_{in} + Z_G} \right| \left| \frac{(Z_L + Z_0)F_{u+} + (Z_L - Z_0)F_{u-}}{(Z_L + Z_0)\exp(\gamma_m L) + (Z_L - Z_0)\exp(-\gamma_m L)} \right| \quad (1.23)$$

where R_L is the load resistance, R_G is the generator resistance, Z_{in} is the device's electrical input impedance, Z_G is the generator impedance, Z_0 is the characteristic impedance of the EOM for its electrical TEM mode,⁶ $F_{u\pm} = (1 - \exp(u_{\pm}))/u_{\pm}$, $u_{\pm} = \pm\alpha_m L + j(\omega/c)(\pm n_m - n_o)L$, $\gamma_m = \alpha_m + j\omega n_m/c$, L is the electro-optic interaction length, α_m is the electrical propagation loss, c is the speed of light in vacuum ($c = 299,792,458$ m/s), n_m is the electrical mode's effective index, and n_o is the optical mode's group index. A circuit model of a traveling-wave electro-optic modulator is shown in Fig. 1.3, and Z_{in} is defined as:

$$Z_{in} = Z_0 \frac{Z_L + Z_0 \tanh(\gamma_m L)}{Z_0 + Z_L \tanh(\gamma_m L)} \quad (1.24)$$

By analyzing Equation (1.23), it can be seen that three aspects of the device need to be considered. First, the device must be impedance matched. Ideally, the device is designed so that $Z_0 = Z_G = Z_L$. Z_G is usually 50Ω , so Z_0 tends to be designed for 50Ω . Second, the electrical and optical indices must be as close to one another as possible. This means the electrical wave should propagate along the transmission line with the same (or close to the same) velocity as the optical wave. Here there tends to be some confusion over whether or not to use the phase velocity or group velocity of each wave. Because there is only one frequency component being considered,

⁶For these structures, the RF mode is a TEM mode, so a characteristic impedance can be defined.

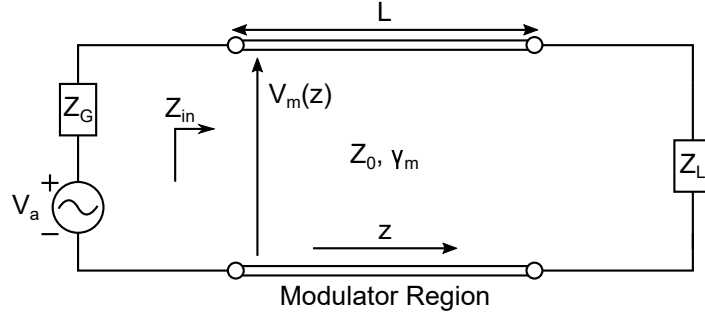


Figure 1.3: Circuit model showing where the electro-optic modulator fits between the signal generator (with applied voltage V_a and internal impedance of Z_G) and the load impedance Z_L . The voltage along the modulator is $V_m(z)$, which varies along the length of the EOM.

the electrical phase index and group index are identical and either can be used. Furthermore, in a well-designed EOM the electrical mode is highly non-dispersive, so that electrical phase index and group index are nearly identical. However, the optical mode's group index should be used, not its phase index. While a single wavelength of light is entering the EOM device, as soon as modulation occurs, optical sidebands are generated around the wavelength of the input laser beam, caused by the interaction of the laser light with the electrical signal. Third and lastly, the device's electrical propagation loss must be kept as low as possible.

From Equation (1.23), it is clear that there is a relationship between the length and bandwidth of the device. In particular, each of the three parameters described in the previous paragraph will have some effect on the device's bandwidth, but how significant that effect is depends on the length of the device. These relationships are explored in Fig. 1.4, where electrical loss, index mismatch, and impedance mismatch are varied in order to show the limitations of the traveling-wave MZM structure. Curiously, in the case of an impedance mismatched device where $Z_0 > Z_G = Z_L$ (as in Fig. 1.4c), the bandwidth actually improves for a device length L , though the frequency response is much noisier and will result in undesired reflections that could damage some external electronics [4].

From Fig. 1.4, it is clear that even a device with no index or impedance mismatch and minimal electrical loss ($\alpha_{cond} = 0.2 \text{ dB}/[\text{cm-GHz}^{1/2}]$), the solid curve in Fig. 1.4a) is limited to less than a 50 GHz electrical bandwidth for a device length of 5 cm or longer. A typical bulk LN

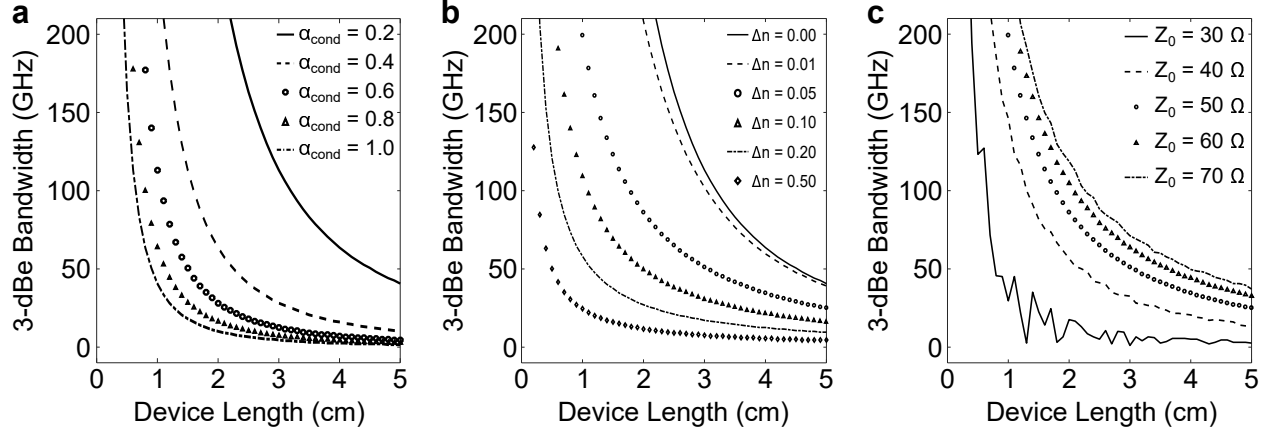


Figure 1.4: The results shown in this figure are simulated 3-dBe electrical bandwidth values, in GHz, based on Equation 1.23. **a** Assumes perfect index matching ($\Delta n = 0$) and perfect impedance matching ($Z_G = Z_0 = Z_L = 50 \Omega$). Each curve represents a different electrical conductor loss (α_{cond} , the only significant source of electrical loss at high frequencies for a well-designed device), in units of dB/[cm-GHz^{1/2}]. **b** Different index matching values are shown for $\alpha_{cond} = 0.2$ dB/[cm-GHz^{1/2}] and perfect impedance matching. $\Delta n = n_m - n_o$. **c** In this case, $\alpha_{cond} = 0.2$ dB/[cm-GHz^{1/2}], $\Delta n = 0.05$, and different values of Z_0 are plotted, assuming $Z_G = Z_L = 50 \Omega$.

EOM device, however, has a $V_\pi L$ on the order of 10 V-cm in the push-pull configuration. In that case, to achieve even $V_\pi = 5$ V, the device would have to be 2 cm long. For $V_\pi = 1$ V, L would have to equal 10 cm, in which case the electrical bandwidth will never approach 50 GHz, much less 100 GHz or beyond. The fundamental limitation to higher bandwidth, practical EOMs, is the typically very large $V_\pi L$ factor for bulk LN devices. With a low enough $V_\pi L$, there is enough margin of error to engineer the structure for high bandwidth.

A more in-depth analysis of the limitations on Pockels-based MZM devices is included in the next chapter, where the hybrid Si-LN EOM that is the main subject of this thesis work will be introduced.

1.3 Silicon & the Plasma Dispersion Effect

Although this thesis focuses on devices which utilize the Pockels effect, the plasma dispersion effect (also known as the free carrier dispersion effect) in silicon is briefly mentioned because of its recent widespread use in Si-based integrated optical circuits.

Unlike the Pockels effect, the plasma dispersion effect in silicon is a change in refractive index (n) and absorption (α) as a function of the change in dopants (electrons or holes). This effect was first observed experimentally by Soref and Bennett in 1987 [6], and for $\lambda = 1.55 \mu\text{m}$ is expressed quantitatively as [7]:

$$\Delta n = \Delta n_e + \Delta n_h = -8.8 \times 10^{-22} \Delta N_e - 8.5 \times 10^{-18} (\Delta N_h)^{0.8} \quad (1.25)$$

$$\Delta \alpha = \Delta \alpha_e + \Delta \alpha_h = -8.5 \times 10^{-18} \Delta N_e + 6.0 \times 10^{-18} \Delta N_h \quad (1.26)$$

for the change in Si refractive index (Δn) and Si absorption ($\Delta \alpha$). The subscript ‘e’ is used to represent changes (in either n or α) due to free electron carrier concentration, while ‘h’ is used for free hole carrier concentrations. For example, Δn_e is the change in Si refractive index due to free electrons. ΔN_e and ΔN_h are the change in electron and hole carrier concentrations, respectively.

A Si MZM can be designed with the same optical and electrical circuitry as shown for the simple MZM of Fig. 1.1a, except that the phase shift $\Delta\phi/2$ in each arm will be due to physical movement of carriers in or out of the optical waveguide. Whether charges are moving into or out of the optical region when an electric field is applied defines the type of modulator. If charges are moving into the waveguide region under the application of an electric field, it is termed a carrier injection MZM and the device is forward biased; conversely, if charges are moving out of the waveguide region under the application of an electric field then it is termed a carrier depletion MZM and the device is reverse biased.

Si MZMs have recently reached electrical bandwidths as high as 50 GHz [8]. However, this appears to be approaching the bandwidth limitation of Si MZMs, which are around 60 GHz [9, 10]. In addition to bandwidth, loss, power consumption, and device footprint are of concern as well. A useful figure of merit is the voltage-loss product, obtained by multiplying $V_\pi L$ by the device propagation loss (in dB/cm) to arrive at a figure of merit with units of V-dB. Although the reference is a few years old at this point, the comparisons made in Table 1 of [11] are useful to

understand the limitations of Si modulators: reducing voltage increases optical propagation loss, and any reasonably effective Si MZM device has propagation loss values on the order of tens of dB/cm. While Si MZMs are attractive for their ability to be easily integrated into foundry processes, their potential for high-bandwidth, large-scale applications are severely limited by the intrinsic loss associated with doping silicon waveguides.

Bibliography

- [1] Kaminow I, Ramaswamy V, Schmidt R, Turner E. Lithium niobate ridge waveguide modulator. *Applied Physics Letters*. 1974;24(12):622–624.
- [2] Weis R, Gaylord T. Lithium niobate: summary of physical properties and crystal structure. *Applied Physics A*. 1985;37(4):191–203.
- [3] Yariv A, Yeh P. *Photonics: optical electronics in modern communications*. Oxford Univ.; 2006.
- [4] Ghione G. *Semiconductor devices for high-speed optoelectronics*. Cambridge University Press; 2009.
- [5] Alferness RC. Waveguide electrooptic modulators. *IEEE Transactions on Microwave Theory Techniques*. 1982;30:1121–1137.
- [6] Soref R, Bennett B. Electrooptical effects in silicon. *IEEE journal of quantum electronics*. 1987;23(1):123–129.
- [7] Reed GT. *Silicon photonics: the state of the art*. John Wiley & Sons; 2008.
- [8] Sun J, Sakib M, Driscoll J, Kumar R, Jayatilleka H, Chetrit Y, et al. A 128 Gb/s PAM4 Silicon Microring Modulator. In: *Optical Fiber Communication Conference*. Optical Society of America; 2018. p. Th4A–7.
- [9] Gardes F, Reed G, Emerson N, Png C. A sub-micron depletion-type photonic modulator in silicon on insulator. *Optics Express*. 2005;13(22):8845–8854.
- [10] Li ZY, Xu DX, McKinnon WR, Janz S, Schmid JH, Cheben P, et al. Silicon waveguide modulator based on carrier depletion in periodically interleaved PN junctions. *Optics express*. 2009;17(18):15947–15958.
- [11] Gill D, Green W, Assefa S, Rosenberg J, Barwicz T, Shank S, et al. A figure of merit-based electrooptic Mach-Zehnder modulator link penalty estimate protocol. *arXiv preprint arXiv:12112419*. 2012;.

Chapter 2

Design of Hybrid Electro-Optic Modulators

2.1 Introduction

The main focus of this thesis work is on hybrid silicon-lithium niobate (Si-LN) electro-optic modulators (EOMs), the cross-section of which is shown in Fig. 2.1a in the push-pull configuration.¹ The concept of the design is to use the high-index Si rib waveguide (refractive index around 3.5 for wavelength (λ) around 1550 nm) to provide the optical mode with some horizontal confinement so that it remains a guided mode while performing the actual electro-optic modulation in the thin LN film, which assists the Si rib with vertical modal confinement. The LN film is not etched or sawn to avoid complicated fabrication steps that are less likely to be adopted by foundries, as well as to maximize optical transmission. Unlike all-Si EOMs, no electro-optic modulation is performed in the Si layer in this hybrid EOM. Instead, the Pockels effect in LN is used for modulation. Unlike the carrier dispersion effect in Si, the Pockels effect theoretically allows for extremely broadband devices while maintaining low optical propagation loss [1]. Indeed, state-of-the-art, research-grade, all-LN EOMs have reached 70 GHz electrical bandwidth in the past [2], though precise LN etching was required and the $V_{\pi}L$ was around 10 V-cm (about as low a $V_{\pi}L$ as all-LN EOMs can achieve

¹An EOM in the Mach-Zender configuration described in the previous chapter can modulate either one or both arms of the device; when both arms are modulated, a phase of $\pi/2$ and $-\pi/2$ are imparted on each of the arms, respectively, and voltage required a total phase shift $\Delta\phi$ is cut in half. This is called the push-pull configuration.

while still reaching high bandwidths).

All-Si EOMs, on the other hand, have reached as high as 50 GHz electrical bandwidth in depletion mode with $V_{\pi}L = 0.6$ V-cm, but with an optical propagation loss of 188 dB/cm in the active region and an extinction ratio of only 5.3 dB (LN EOMs, almost universally, have 20 dB or greater extinction ratio). This bandwidth appears to be at or close to the upper limit of Si-based EOMs [3, 4]. Of course, these limitations are well known to the Si photonics community. For years, the challenges to creating better Si modulators have been mainly fabrication-based, i.e. optimizing dopant concentrations and waveguide placement. Certainly, clever Si EOM designs have advanced the field significantly over the years [5], but device and fabrication optimization appear to be close to their limits.

By leveraging the high-accuracy and wafer-scale foundry fabrication of silicon-on-insulator (SOI) devices and integrating thin films of LN with such technology, it is possible to reduce the voltage limitations of traditional all-LN EOMs without sacrificing optical propagation loss or extinction ratio. By using an SOI substrate, wafer-scale Si-LN processing becomes a possibility with all the potential benefits that modern CMOS fabrication has to offer. Additionally, by using a well-defined Si rib below the LN film, extra design parameters are introduced to the device that were not available to all-LN device designers of the past. These extra parameters, discussed below, allow for precise bandwidth tuning without losing the low voltage and optical loss afforded by the hybrid design.

2.2 Hybrid Si-LN Optical Mode Design

The hybrid Si-LN optical mode is in some ways a two-material core waveguide, except the second material (LN) is quasi-infinite in width. This means the waveguide must be carefully designed to maximize light in the LN region (where the electro-optic Pockels effect takes place) without decoupling entirely from the Si waveguide core. An example of a well-designed optical mode is provided in Fig. 2.1b, where the LN confinement factor ($LNCF$ – the percentage of the

optical mode that is horizontally polarized and in the LN region) is 81% and the effective mode area (A_{eff}) is only $1.3 \mu\text{m}^2$. In this case, the mode is not monotonic because the Si waveguide is narrower than the wavelength in Si (approximately 440 nm), so the mode cannot fit in the Si rib and must expand outwards into the nearby SiO_2 and LN regions. This behavior is not observed in weakly guided waveguides, such as fibers and bulk crystals.

$LNCF$ is defined as

$$LNCF = \frac{\int_{-\infty}^{+\infty} \int_{-h_{LN}}^0 |\mathbf{S}_y|^2 dx dz}{\int_{-\infty}^{+\infty} \int_{-\infty}^{+\infty} |\bar{\mathbf{S}}|^2 dx dz} \cdot 100 \quad [\%], \quad (2.1)$$

where h_{LN} is the LN thickness. A_{eff} is defined as

$$A_{\text{eff}} = \frac{(\int_{-\infty}^{+\infty} |\mathbf{E}|^2 dA)^2}{\int_{-\infty}^{+\infty} |\mathbf{E}|^4 dA} \quad [\text{m}^2]. \quad (2.2)$$

where \mathbf{S} is the total time-averaged Poynting vector, \mathbf{S}_y is the time-average Poynting vector parallel to the propagation axis y and \mathbf{E} is the vectorized electric field component of the optical mode.

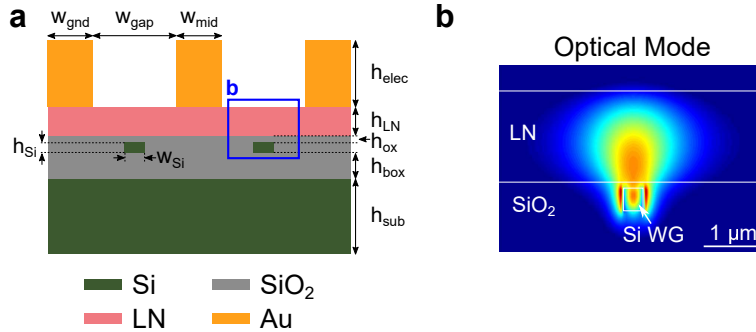


Figure 2.1: **a** A cartoon of what the hybrid Si-LN EOM cross-section should look like in the push-pull configuration. Material labels are provided below the image, and material dimensions are as follows: h_{Si} = Si waveguide height; w_{Si} = Si waveguide width; h_{sub} = height of SOI substrate; h_{box} = height of buried oxide layer; h_{ox} = height of oxide between Si waveguides and LN film; h_{LN} = height of LN film; h_{elec} = height of electrical lines; w_{gap} = gap width between ground planes and signal line; w_{mid} = width of signal line; w_{gnd} = width of ground planes. **b** Simulated Si-LN optical mode in the hybrid region. $LNCF = 81\%$ and $A_{\text{eff}} = 1.3 \mu\text{m}^2$. The region simulated in **b** is highlighted in **a** with a blue box.

To arrive at the mode design of Fig. 2.1b, it helps to first decide upon the Si layer thickness

(h_{Si} in Fig. 2.1a) to use. Too thick of a Si layer could result in multi-mode waveguides, as well as a poor *LNCF* figure of merit; and although A_{eff} will be quite low as a result, only a small percentage of the optical mode will be modulated. On the other hand, if the Si layer is too thin, it will not be useful for on-chip optical routing since tight bends will be highly lossy, and even straight waveguide propagation losses may be excessive. Additionally, a Si thickness should be chosen so that the optical mode location can be adjusted between the Si region and the LN region by changing as few design parameters as possible. With modern foundry photolithography it is quite simple to fabricate variations in the width of features, but not in their heights. For this reason, all hybrid waveguide designs should be designed with a single Si layer thickness, a single LN film thickness, and a variable Si width. This means h_{Si} must be chosen so that a change in the Si width can accommodate both a high *LNCF* cross-section as well as a low *LNCF* cross-section. For this work, a Si layer thickness of 150 nm was chosen.

The next step in the design process is to choose a Si width that is best for operation in the hybrid region of the device. The goal of this hybrid Si-LN platform is not only to make efficient broadband EOMs — it is also to integrate LN-based technologies onto SOI wafers. To do so requires that standard Si waveguides can be used in conjunction with hybrid Si-LN devices. Therefore, several Si widths must be used, depending on the application.

2.2.1 Optical Mode for the Electro-Optic Modulator

The optical mode of Fig. 2.1b is used in the hybrid EOM. This choice is informed by tracking *LNCF* and A_{eff} of the optical mode, and finding a Si width that maximizes *LNCF* (so as much of the light as possible is affected by the Pockels effect) without increasing A_{eff} to the point where the optical signal gets absorbed by the metal lines. Because of the dependency of these parameters on the LN film thickness (h_{LN}), w_{Si} and h_{LN} are chosen concurrently. Simulations of *LNCF* and A_{eff} versus w_{Si} for various h_{LN} choices are shown in Fig.2.2. In the case where h_{LN} is very thick (1000 nm), the mode area becomes very sensitive to Si waveguide width. Going from a w_{Si} of 400 nm to 300 nm results in a five times growth in A_{eff} . Since fabrication error in waveguide

dimensions can be as large as ± 15 nm, this is too sensitive to be useful. Furthermore, such a sensitive cross-section is too difficult to control by simply varying the Si rib width.

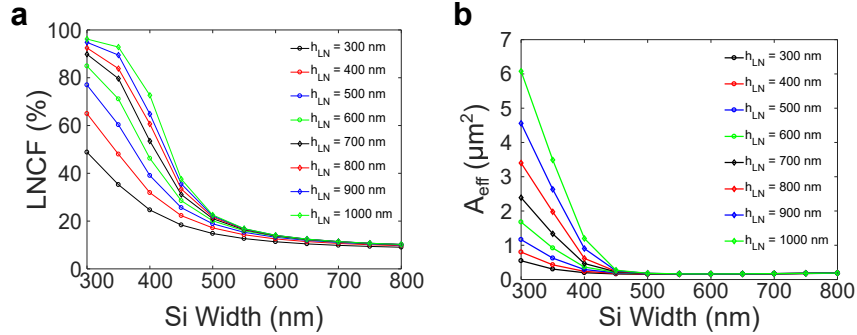


Figure 2.2: Simulated $LNCF$ (a) and A_{eff} (b) for combinations of w_{Si} and h_{LN} , with $h_{Si} = 150$ nm.

On the other hand, too thin a LN film (300 nm in Fig. 2.2) does not allow for a high $LNCF$, limiting the electro-optic Pockels effect.² The dimensions $w_{Si} = 320$ nm and $h_{LN} = 600$ nm were chosen to achieve the optical mode of Fig. 2.1b. During device fabrication (discussed in detail later on in this thesis), a chemical-mechanical planarization (CMP) step is performed on a layer of silicon dioxide (SiO_2) deposited over the Si waveguides, before attaching the LN film. For this reason, an 80 nm SiO_2 layer is placed between the Si waveguides and the LN film in Fig. 2.1b to account for the CMP tolerance of ± 50 nm. The group index of this optical mode is approximately $n_g = 2.3$.

2.2.2 Optical Mode for Si Waveguide Applications

Although one of the primary innovations of this thesis lies in the design of the hybrid Si-LN waveguide in the electro-optic modulator, an important benefit of using this waveguiding platform is its versatility. By adiabatically tapering the 320 nm wide Si waveguide in the EOM up to 650 nm, the optical mode becomes heavily confined in the Si waveguide, as is common with all-Si devices, in which case passive as well as active all-Si devices can be realized, on the same platform as the hybrid Si-LN EOM. Transitioning from the hybrid Si-LN EOM to the all-Si waveguide is done by

²This approach is a rough estimate to understanding the effect of physical parameters on $LNCF$ and A_{eff} , which in turn will partially determine $V_{\pi}L$. Once a few physical parameters are determined (either by intelligent choice or fabrication limitations), it becomes more straightforward to optimize the device for low $V_{\pi}L$, high bandwidth, or any other figure of merit.

first tapering the Si waveguide from 320 nm to 650 nm with a linear taper, and then crossing from the LN region into the non-LN region.

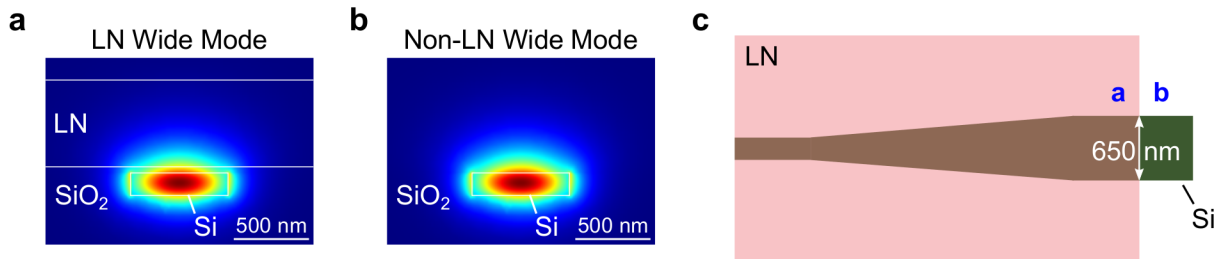


Figure 2.3: **a** Optical mode with $w_{Si} = 650$ nm, $h_{LN} = 600$ nm, and $h_{Si} = 150$ nm, under the LN film. **b** Same mode as **a**, but outside of the LN region. **c** Top view of the transition from the EOM mode (narrow 320 nm wide Si waveguide, left side), to a wide Si-LN waveguide, and finally to a wide all-Si mode. The last two modes, shown in **a** and **b**, are denoted by **a** and **b** in the figure, respectively.

By tapering to a wide waveguide first, reflections and scattering due to the LN interface are minimized. For the design of Fig. 2.3, there is a simulated loss of 0.1 dB when transitioning from the LN region to the non-LN region. The mode of Fig. 2.3b is used for on-chip optical circuitry that does not require the LN film, which can potentially include active devices in doped Si. The 650 nm Si width is chosen because it is quite wide, which helps to confine the light in the Si region, but is not wide enough to support higher-order optical modes which may couple into the fundamental TE mode shown here.

2.2.3 Optical Mode for the Edge Coupler

A final optical mode cross-section is required for proper design of this device, and that is the optical mode of the edge coupler. Edge couplers are commonly used for photonic integrated circuits to couple light from a fiber onto a waveguide by bringing the fiber right up against the edge of the chip. However, since Si is a high-index material, modes in Si waveguides tend to be very small when compared to fiber modes. A well-known strategy for coupling efficiently from a high-index contrast waveguide, such as a Si core surrounded by low-index SiO₂, into an optical fiber is to reduce the width of the waveguide to below the wavelength of light. This causes the optical mode to become much larger than the waveguide core. With careful design, the waveguide mode can be

engineered to closely match the width and shape of the fiber mode [6]. However, because this hybrid Si-LN device is fabricated on a foundry wafer using photolithography, the minimum feature size is limited by the photolithography tool. For most modern foundries, this feature size limit tends to be 180 nm. For standard 220 nm-thick Si waveguides, this results in suboptimal waveguide modes that are smaller than the fiber mode. In the case of the 150 nm-thick Si waveguides described in this thesis, and assuming an input/output fiber with a mode field diameter (MFD) of $2.5 \mu\text{m}$ (typical for a lensed tapered fiber from Oz Optics, Ltd.), the simulated overlap between the fiber mode and the waveguide mode is shown in Fig. 2.4a for a range of Si widths, and assuming $\lambda = 1550 \text{ nm}$. The best edge coupling occurs when the silicon width is 220 nm, with a simulated transmission loss of approximately 0.5 dB (per edge coupler, for a total of 1 dB per device).

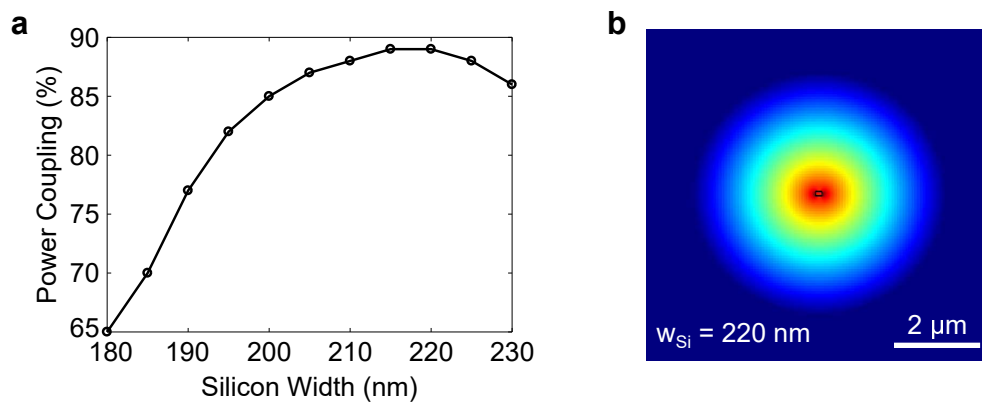


Figure 2.4: **a** Simulation of power transmission of an edge coupler between a lensed tapered fiber with $\text{MFD} = 2.5 \mu\text{m}$ and a Si waveguide of height 150 nm surrounded by SiO_2 . The maximum power coupling is 89% for a Si width of 220 nm. **b** Logarithmic plot of the normalized electric field component of the optical mode for the optimum Si width of 220 nm. The first five orders of magnitude are shown, with red representing the highest field strength and dark blue representing the weakest field strength.

The simulated plot in Fig. 2.4a reaches a maximum transmission below 100% not because of a fabrication-limited Si width, but because of an intrinsic mismatch between the optical fiber – whose mode has a two-dimensional Gaussian shape – and the waveguide. Other researchers have made improvements on the edge coupler in recent years by shaping the optical mode at the waveguide’s output [7, 8], but this typically requires electron beam lithography, custom-made fibers, multi-material waveguide stacks, or some combination of the three.

2.2.4 Bonding Markers & Electrode Markers

Though not directly part of the EOM design, markers are added to the silicon layer to assist with visual alignment of the LN film during bonding and for alignment during fabrication of the electrical lines. In this case, rectangular markers are used for electrode alignment and square markers are used for bonding alignment. Edge-to-edge marker alignment with mask markers (Fig. 2.5b) is preferable to marker-over-marker alignment (Fig. 2.5c); edge-to-edge marker alignment ensures a high level of precision since the mask and chip markers are always visible during alignment, even if one layer is slightly out of focus.

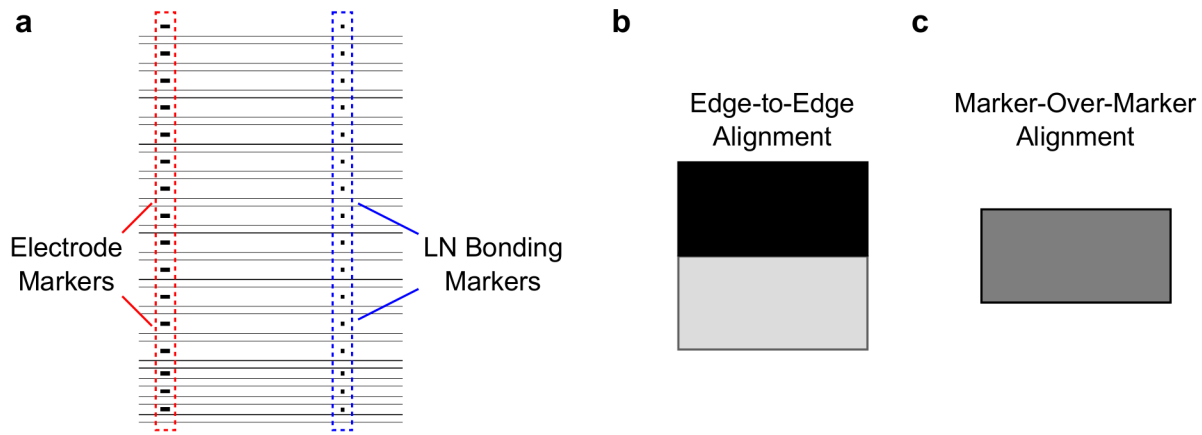


Figure 2.5: **a** GDS layout of EOM chip with arrays of alignment markers for electrode mask alignment and LN bonding alignment. **b** Edge-to-edge alignment is when the chip marker (black) and the mask marker (gray) are designed to align at the edge. This allows for high precision alignment, since both markers are visible. **c** Marker-over-marker alignment is when the chip marker and mask marker are designed to align directly over one another. This is a less accurate alignment scheme, since one alignment marker covers the other, the depth of focus of the microscope objective distorts the true alignment.

2.3 Full Optical Design of the EOM

Using the mode designs of Section 2.2, a full EOM in the Mach-Zehnder configuration can be designed, with Si tapers and bends used to convert between mode types and to adjust waveguide separation where necessary. The full hybrid EOM concept is shown in Fig. 2.6. The placement

of the LN film is not arbitrary: the edge of the LN film must be placed over the wide Si region to minimize reflection and scattering loss when going from the non-LN region into the LN region.

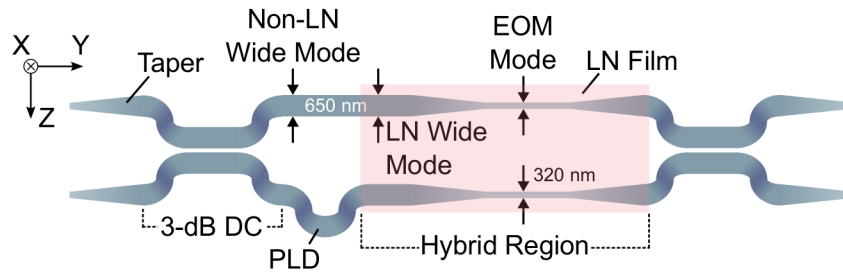


Figure 2.6: Top view of the full EOM layout. DC = directional coupler, PLD = path-length difference.

Directional couplers are used to split the input light into both arms of the EOM and then split again at the output. The DCs should be 50/50 splitters (3-dB) to achieve the highest possible device extinction ratio. High precision Si foundry processes enables accurate fabrication of DCs. Y-junctions are not used because of their sub-resolution fabrication requirements. An extra path length is included in one arm of the EOM so that the device can be tuned by changing the wavelength of operation instead of having to apply a dc bias voltage, which would require either a high-frequency bias tee or separate electrical lines and probes for the dc bias.

2.4 Design of the Electrical Lines

As mentioned previously, the electrical lines are designed so that the EOM is in the push-pull configuration. This requires coplanar waveguide (CPW) electrodes, meaning that a signal line is evenly placed between two ground planes, with the hybrid waveguides halfway between each ground plane and the signal plane, as in Fig. 2.1a. The advantage of the hybrid Si-LN EOM design is that the optical mode can be optimized separately from the electrical mode, since each mode has its own set of geometrical components that are mostly unrelated. While the optical modes of Section 2.2 were designed by varying the height and width of the Si waveguide and the height of the LN film, the electrical mode in the EOM is designed by adjusting the height and width of the ground planes and signal line, as well as the gap between the ground and signal. The only overlap

of design parameters between the optical and electrical modes is the gap between the electrical lines; if w_{gap} is too small then optical transmission will suffer. This is why it is important that A_{eff} for the optical mode is kept as small as possible, particularly since $V_{\pi}L$ is strongly affected by w_{gap} .

2.4.1 EOM Region

As discussed in the previous chapter, the electro-optic bandwidth is limited by three factors: characteristic impedance mismatch, index mismatch, and excessive electrical losses. All three of these factors must be taken into account when designing the electrical lines. Fortunately, characteristic impedance (Z_c), electrical index (n_m) and electrical losses (α_m) can all be derived from a single mode simulation, similar to the mode simulations used for optical modes but at electrical frequencies. Characteristic impedance can be calculated from current (I) and power (P):

$$Z_c = 2 \frac{P}{|I|^2}, \quad (2.3)$$

both of which can be calculated from a mode simulation, while n_m and α_m can be obtained directly from the eigenvalue of the simulated mode [9].

An important consideration during electrical line design is that of the metal thickness, material, and deposition/growth method. Metal thicknesses beyond 1 or 2 micrometers require electroplating, and as electrodes become thicker it is more likely their sidewalls will be slanted, depending on the photoresist used. Several types of electrical lines, of different materials, are experimented with in this work.

Additionally, the SOI substrate material should be carefully chosen when designing high frequency devices. A low resistivity (high conductivity) Si handle will add loss to the electrical mode. In this work, both a low resistivity and a high resistivity handle were used, but the high frequency EOM was designed with a high resistivity Si handle in mind.

2.4.2 Electrical Bends

Although the EOM is a straight device, it is much easier and more practical to make electrical contact at 90° to where optical contact is made. While characterizing the device, this is to avoid electrical probe arms and optical fiber mounts from coming into contact, but even for a packaged device this is typically desirable for the end user, who will want to connect electrical lines without disturbing the relatively delicate and permanently connected optical fibers.

As a general rule of thumb, 90° electrical bends should have a radius at least three times that of the width of the signal line. Too large of a bend will result in unnecessary electrical propagation losses, and too small of a bend could result in high-frequency rolloff in the device's frequency response. To be safe, electrical designs in this thesis use a bend radius five times greater than the signal line width.

2.4.3 Electrical Pads

Electrical contact is made at electrical pads, which should be designed to minimize reflections and additional loss. Reflections are minimized by maintaining a constant characteristic impedance. This is achieved by leaving the signal line at a constant width, and increasing the ground plane width to ensure that a wide variety of probe spacings can be accommodated (see Fig. 2.7).

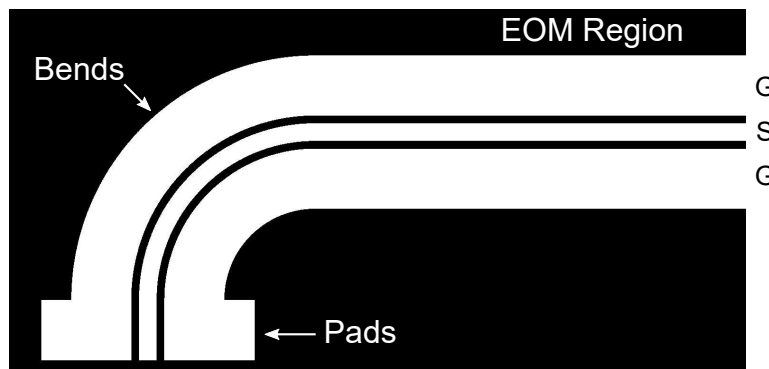


Figure 2.7: This is the GDS layout of a portion of the electrical lines, shown in white on a black background. The ground lines are expanded at the pads to ensure that the probes can make contact, and the signal line is left unaltered for minimal reflections.

Bibliography

- [1] Chang WS. RF photonic technology in optical fiber links. Cambridge University Press; 2007.
- [2] Noguchi K, Mitomi O, Miyazawa H. Millimeter-wave Ti: LiNbO₃ optical modulators. *Journal of Lightwave Technology*. 1998;16(4):615.
- [3] Reed GT, Mashanovich GZ, Gardes FY, Nedeljkovic M, Hu Y, Thomson DJ, et al. Recent breakthroughs in carrier depletion based silicon optical modulators. *Nanophotonics*. 2014;3(4-5):229–245.
- [4] Gardes F, Reed G, Emerson N, Png C. A sub-micron depletion-type photonic modulator in silicon on insulator. *Optics Express*. 2005;13(22):8845–8854.
- [5] Reed GT. *Silicon photonics: the state of the art*. John Wiley & Sons; 2008.
- [6] Almeida VR, Panepucci RR, Lipson M. Nanotaper for compact mode conversion. *Optics letters*. 2003;28(15):1302–1304.
- [7] Wood M, Sun P, Reano RM. Compact cantilever couplers for low-loss fiber coupling to silicon photonic integrated circuits. *Optics Express*. 2012;20(1):164–172.
- [8] Chen L, Doerr CR, Chen YK, Liow TY. Low-Loss and Broadband Cantilever Couplers Between Standard Cleaved Fibers and High-Index-Contrast Si₃N₄ or Si Waveguides. *IEEE Photonics Technology Letters*. 2010;22(23):1744–1746.
- [9] Toney JE. *Multiphysics Modeling of Electro-Optic Devices*. Comsol 2011. 2011;.

Chapter 3

A Process Design Kit for Hybrid Si-LiNbO₃ Devices

3.1 Introduction

Modern CMOS circuit designers use process design kits (PDKs), generally supplied by foundries, to design their electrical circuits. A typical PDK will include, at a minimum, a design rules manual outlining how components should be designed to adhere to the foundry's capabilities. PDKs can also include a component library so that the designer does not need to run in-depth physical simulations, and can instead work at the circuit level. Because of this, there is a lower barrier to entry of CMOS circuit design. Additionally, designs are completed faster and at a lower cost. The optical circuit community would be wise to follow this model, and indeed several members of the community have begun to do so (as is evident from the list of proprietary component libraries in PhoeniX's OptoDesign software, as well as the PDK recently made available by Analog Photonics, LLC through the AIM Photonics program [1]).

In the pursuit of simplifying the photonic circuit design process, parameterized cells (P-cells) of hybrid silicon-lithium niobate (Si-LN) components in Lumerical's INTERCONNECT software have been created. A "P-cell" is a table of S-parameters (that can be optical, electrical, or even

electro-optical) for a given component with a certain geometry. A simple embedded waveguide, for example, has a width and a height. The P-cell for that waveguide will have pre-simulated width and height parameters built into a table (the S parameters), and when the user changes the width and/or height of the waveguide, the P-cell will respond accordingly. In this way, a single component designer can simulate vast combinations of devices, and package the results into “black boxes” that can be used by optical circuit designers in e.g. Lumerical’s INTERCONNECT software. This has two benefits: it prevents circuit designers from having to dedicate effort to time-consuming physical simulations, and it naturally leads to a set of design rules for the circuit designer to follow, not unlike the design rules used by CMOS circuit designers (such as waveguide spacing, minimum bending radii, dopant levels, etc.).

While the individual P-cells developed over the course of this research are not included in this thesis, the design rules manual for the hybrid Si-LN optical circuit platform is provided in this chapter, including explanations and simulation data of the various components developed for this unique hybrid silicon-lithium niobate optical platform.

3.2 Technology Summary

This document is a design manual for hybrid silicon-lithium niobate integrated optical components. Primary applications of this technology are Pockels effect electro-optic modulators and $\chi^{(2)}$ nonlinear optical devices. This document contains a description of the technology, a fabrication process overview, design rules, and a variety of library components that can be implemented in Lumerical’s circuit simulation tool, Interconnect. Additionally, sample MATLAB scripts are provided for GDS design.

3.2.1 Features of the Technology

The approach taken with this technology is to focus on bonding dies of SOI to dies of LNOI. The reasons for this are three-fold: 1) To minimize the use of expensive LNOI material; 2) To

better match the smaller LNOI wafer (3 in.) to the larger SOI wafer (>6 in.); and 3) To utilize both standalone Si and hybrid Si-LN optical circuitry on the same die.

To enable and accommodate a hybrid optical mode, the Si waveguide layer on the SOI is set at 150 nm. This value is assumed throughout the remainder of this document. Optical circuit components are designed by adjusting other parameters, such as the width of the Si waveguides and the thickness of the LN (lithium niobate, LiNbO_3) film.

3.3 Design Tools

The simulations in this document were carried out in Lumerical’s four software packages: FDTD Solutions, Mode Solutions, DEVICE, and INTERCONNECT. FDTD solves Maxwell’s equations in 3D or 2D, MODE provides a full waveguide design environment with various solvers, and DEVICE is a multiphysics environment for modeling charge and heat transport. INTERCONNECT is a circuit-level simulation tool that allows for high-level circuit simulations.

FDTD Solutions, MODE Solutions, and DEVICE were used to simulate individual components across different combinations of geometries. The results of those simulations were stored in files accessible by models in INTERCONNECT. Those sorts of models are known as “parameterized cells,” or “PCells” for short. Because in-depth simulations across a wide range of parameter values have already been performed and uploaded into INTERCONNECT via the PCells, a designer can simply change a component’s physical dimensions in INTERCONNECT to instantly and automatically adjust the dependent properties (such as S-parameters or modal effective index) of that component.

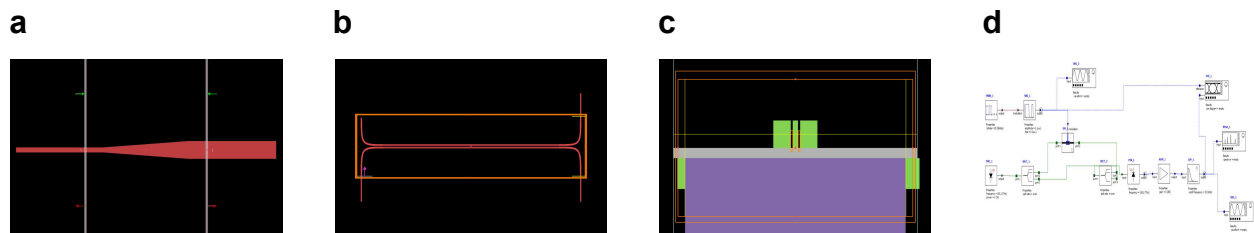


Figure 3.1: **a** Linear waveguide taper optical transmission simulation in MODE. **b** Directional coupler waveguide optical simulation in FDTD. **c** Direct current (DC) electric-field simulation in DEVICE. **d** Circuit simulation of electro-optic modulator in INTERCONNECT.

3.4 Process Outline

The structures designed in this document are reliant upon a series of processing steps which are outlined in Table 3.1 below.

Table 3.1: Process outline to fabricate hybrid Si-LN devices (active and passive).

Process Step	Details	Options
1a) Starting SOI Wafer	250 nm 1-0-0 p-type SOI with 3 μm BOX	FZ high resistivity handle wafer
1b) Starting LNOI Wafer	600 nm LNOI with 2 μm BOX	Si or LiNbO ₃ handle, film thickness from 300 nm to 1 μm .
2) SOI Thinning	80 nm etch of Si layer to 170 nm	
3) SOI Oxidation	20 nm oxidation of Si layer to 150 nm final thickness	
4) Si Layer Definition	Pattern Si layer	
5) Oxide Deposition	SiO ₂ PECVD deposition	
6) CMP	Chemical-mechanical polish of deposited oxide with final target thickness of 190 nm (40 nm thicker than Si layer)	
7) Clean SOI and LNOI	5 min. megasonic in: a) acetone bath; b) IPA bath. Follow with 15 min. in RCA-1 bath.	
8) PSA	Plasma surface activation in PVA TePla PS100: 30 sec./150 W, SOI and LNOI.	
9) Post-PSA Water Bath	Place SOI and LNOI in DI-water bath for 5 min.	
10) Bond	Dry, align, and contact SOI and LNOI surfaces to be bonded. Apply uniform pressure (<150 kPa).	If bonding manually, apply pressure first in center to initiate bond before pressuring edges of bond region.

Table 3.1: Process outline to fabricate hybrid Si-LN devices (active and passive), continued.

Process Step	Details	Options
11) Thermal Anneal	200°C/2 hours on a hot plate. Requires that SOI and LNOI materials have identical or similar material properties (coefficient of thermal expansion and modulus of elasticity).	Alternative heating methods can work as well.
12) Oxide deposition	2 μm SiO ₂ PECVD deposition	
13) BB 220 Coating	Protect exposed Si features and SOI handle with two coats of BB 220. Soft bake: 80°C/3 min., 180°C/3 min., 220°C/5 min.	
14) SiO ₂ Removal	HF etch: 2 sec.	BOE etch: 20 min.
15) XeF ₂ Etching	Xactix: 2.0 mT/15 sec. per cycle/200 cycles	
16) SiO ₂ Removal	HF etch: 2 sec.	BOE etch: 20 min.
17) Ti/Au Evaporation	E-beam evaporation: 10 nm Ti, 50 nm Au	Thicker Au is acceptable but unnecessary
18) Spin-on AZ P4620	AZ P4260: 2000 rpm/40 sec.	
19) Au Electrode Definition	Pattern AZ P4620 with electrode mask	
20) Electroplate	Electroplate Au: 10 mA/20 min./8 μm	Other combinations of current and electroplating time are possible.
21) Remove Excess Material	Remove AZ P4620 and seed layer of Ti/Au that has not been electroplated.	

Fig. 3.2 shows the cross-section after bonding and thermal anneal but before handle removal. This sort of structure is useful for hybrid Si-LN optics. Fig. 3.3 shows the cross-section after handle removal and metallization. This fully-fabricated structure is used for electro-optic devices, where it is necessary to remove the upper handle in order to bring the metal lines close enough to allow the electrical field to interact with the optical field.

Si Handle Wafer						390 μm < 0.05 $\Omega\text{-cm}$
CVD Oxide						2 μm
LiNbO ₃						0.600 μm
CVD Oxide						0.040 μm
CVD Oxide	Si		Si		Si	0.150 μm
Buried Oxide						3 μm
Si Handle Wafer						650 μm >1000 $\Omega\text{-cm}$

Figure 3.2: Cross-section after bonding and thermal anneal. Each layer's thickness is given, along with resistivity values for the Si handles.

3.5 Design Rules for the Hybrid Si-LN Platform

This section details the design rules/suggestions for components in the hybrid Si-LN platform. These rules are based upon limitations of the components rather than limitations of the lithography process. Lithographic capabilities are dependent upon the foundry used for fabrication.

Please note that all design rules assume an optical signal within the wavelength range [1500,1600] nm and a Si thickness of 150 nm.

3.5.1 Non-Hybrid Si Components

Standard Si photonic circuitry (that is, optical waveguides in Si surrounded by SiO₂) is used for things like coupling on and off the chip, splitting/combining light, and propagating light. To avoid undesired results, such as unintentional waveguide coupling and excessive loss, the following design rules should be observed:

1. Edge waveguide spacing of 40 μm .
2. Maximum width of 900 nm.
3. Minimum spline characteristic length (analogous to bend radius) of 10 μm .

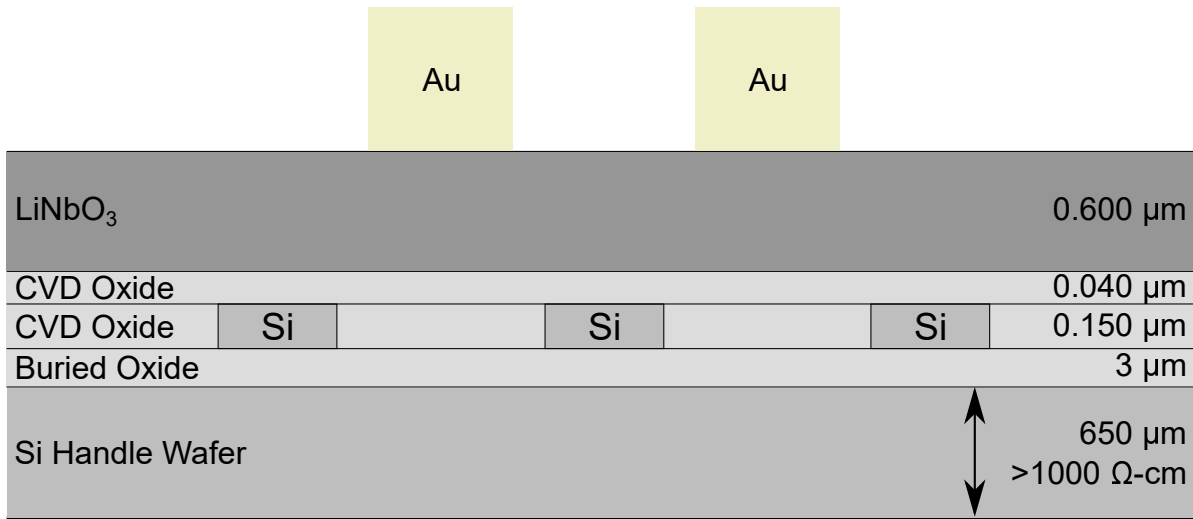


Figure 3.3: Cross-section after the full fabrication process. Each layer's thickness is given, along with resistivity values for the Si handles.

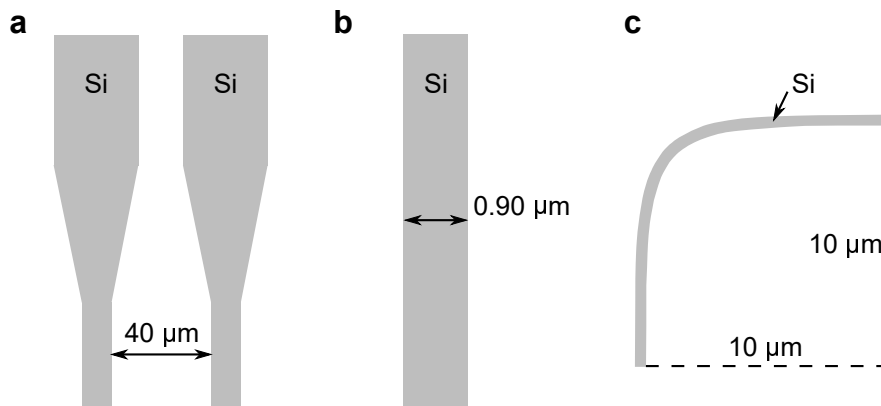


Figure 3.4: **a** Minimum edge waveguide spacing. **b** Maximum Si waveguide width. **c** Minimum spline bend radius.

3.5.2 Hybrid Si-LN Components

The hybrid section of this platform takes advantage of the fact that the indices of (anisotropic) LiNbO₃ (LN) are higher than the index of SiO₂. In such a scenario the optical mode resides in the Si and LN regions of the cross-section more so than in the SiO₂ in the substrate and lateral regions. A simulation of this optical mode is shown in Fig. 3.5 for a Si width of 320 nm and a LN height of 600 nm. Not every possible combination of Si width (w_{Si}) and LN height (h_{LN}) will result in an acceptable hybrid mode. If the LN is too thick and the Si is too narrow, a slab mode will propagate in the LN film. Alternatively, if the Si is too wide then higher order modes will propagate

and interact with the fundamental TE_0 mode of interest. A listing of acceptable geometries for this cross-section is provided in Table 3.2. Gray boxes are w_{Si}/h_{LN} combinations that are unacceptable, while white boxes represent acceptable w_{Si}/h_{LN} combinations.

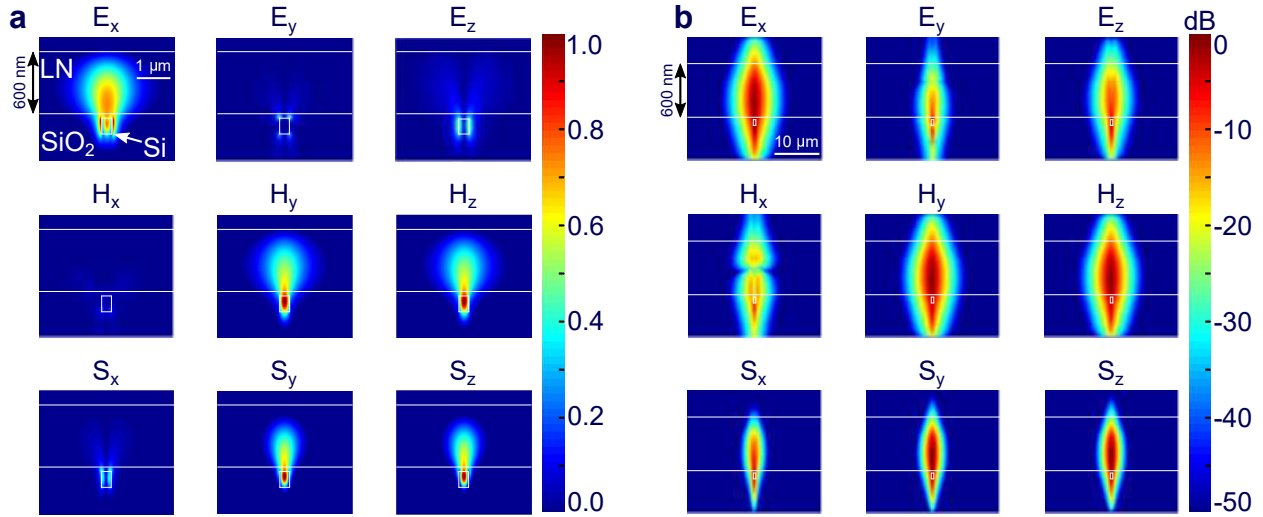


Figure 3.5: **a** Linear plot of a simulated hybrid mode. $w_{Si} = 320$ nm and $h_{LN} = 600$ nm. The first and second rows of plots are x, y , and z components of the E- and H-fields, respectively. The third row of plots, labeled S_x, S_y , and S_z , are components of the time-average instantaneous Poynting vector. **b** Log plot of Fig. 3.5a. Because this is the TE_0 mode, it is very nearly TE-polarized (E_y, E_z , and H_x are close to zero; this is more obvious in the linear plot shown in Fig. 3.5a). Part **b** of this figure is provided in dB for comparison with Fig. 3.6. Scale bars are given in the E_x plots.

Table 3.2: Table of acceptable combinations of values for Si width and LN thickness. In the upper right of the table, one or more of the field components (E_x, E_y, E_z, H_x, H_y , or H_z) has coupled into the LN slab. In the lower section of the table, TE_2 exists and can couple with TE_0 . TE_2 exists at a narrower Si width (900 nm) in the non-hybrid region.

w_{Si} (nm) \ h_{LN} (nm)	300	400	500	600	700	800	900
200	Yes	Yes	No	No	No	No	No
250	Yes	Yes	Yes	Yes	Yes	No	No
300	Yes	Yes	Yes	Yes	Yes	Yes	No
350	Yes	Yes	Yes	Yes	Yes	Yes	No

Table 3.2: Table of acceptable combinations of values for Si width and LN thickness. In the upper right of the table, one or more of the field components (E_x , E_y , E_z , H_x , H_y , or H_z) has coupled into the LN slab. In the lower section of the table, TE_2 exists and can couple with TE_0 . TE_2 exists at a narrower Si width (900 nm) in the non-hybrid region, continued.

w_{Si} (nm) \ h_{LN} (nm)	300	400	500	600	700	800	900
400	Yes						
450	Yes						
⋮	⋮	⋮	⋮	⋮	⋮	⋮	⋮
900	Yes						
950	No	Yes	Yes	Yes	Yes	Yes	Yes
1000	No	No	Yes	Yes	Yes	Yes	Yes
1050	No	No	Yes	Yes	Yes	Yes	Yes
1100	No	No	No	Yes	Yes	Yes	Yes
1150	No	No	No	No	No	Yes	Yes
1200	No	No	No	No	No	Yes	Yes
1250	No	No	No	No	No	Yes	Yes
1300	No	No	No	No	No	No	Yes
1350	No	No	No	No	No	No	Yes
1400	No						

The reasons why certain combinations of w_{Si} and h_{LN} are unacceptable for waveguiding go back to the index of refraction for each material in the cross-section. Silicon has a higher index than either the ordinary or the extraordinary index of LN ($n_{Si} \approx 3.47$, $n_{LN} \approx 2.21, 2.14$). When the Si waveguide below the LN slab (Fig. 3.2 and Fig. 3.3) becomes too narrow, the optical mode is no longer laterally confined by the Si waveguide and becomes a slab mode. Particular field

components can behave as higher order slab modes, like E_y , E_z , and H_x in Fig. 3.6. This is why certain combinations of w_{Si} and h_{LN} are gray in the upper right of Table 3.2. Conversely, the lower left of Table 3.2 is grayed to mark the scenario where the Si waveguide is wide enough to support the higher order TE_{20} mode, which can couple with TE_{00} and act as a source of optical loss.

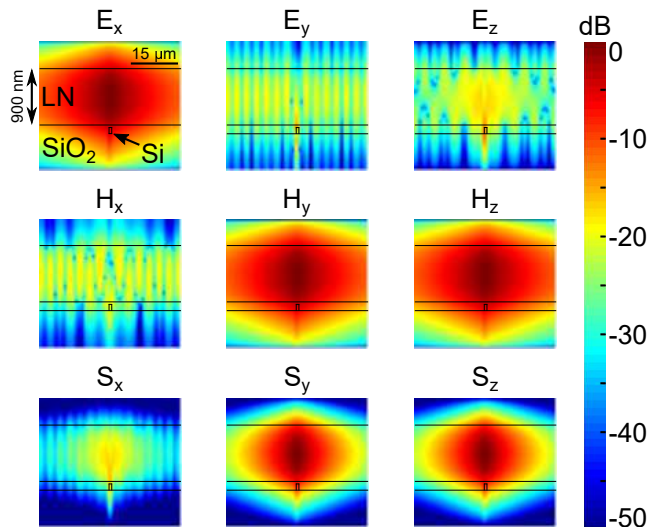


Figure 3.6: Log plot of a simulated hybrid optical mode when $w_{\text{Si}} = 200 \text{ nm}$ and $h_{\text{LN}} = 900 \text{ nm}$, i.e. one of the gray boxes in the upper right corner of Table. 3.2. In this case, the E_x , H_y , and H_z components are nearly slab modes, while the E_y , E_z , and H_x components are non-zero. This is in contrast to the well-behaved mode in Fig. 3.5.

3.6 Static Library Components

We have developed several static library components for use in Lumerical’s INTERCONNECT circuit-level simulation software. Each component is “static” in the sense that it has fixed values for all physical parameters, which results in dependent data like effective index and coupling coefficient changing only with wavelength. This is in contrast to the following section, which discusses parameterized cells (PCells) with variable input physical parameters and therefore variable parameters of interest (effective index, coupling coefficient, etc).

It is in this section that each component is described in detail, using optimized physical values for a Si thickness of 150 nm.

3.6.1 Edge Coupling Taper

We use linear tapers as edge couplers to couple from an off-chip fiber into the thin-silicon platform. These linear tapers start at a width of 205 nm and end at a width of 650 nm, the nominal waveguide width for this platform. The top view of this structure is shown in Fig. 3.7a. After simulating taper loss for these width values as a function of taper length in Fig. 3.7b, we decided to set the taper length to 200 μm . This assumes 3 μm of SiO_2 below the Si waveguide, and 2 μm of SiO_2 above the Si waveguide.

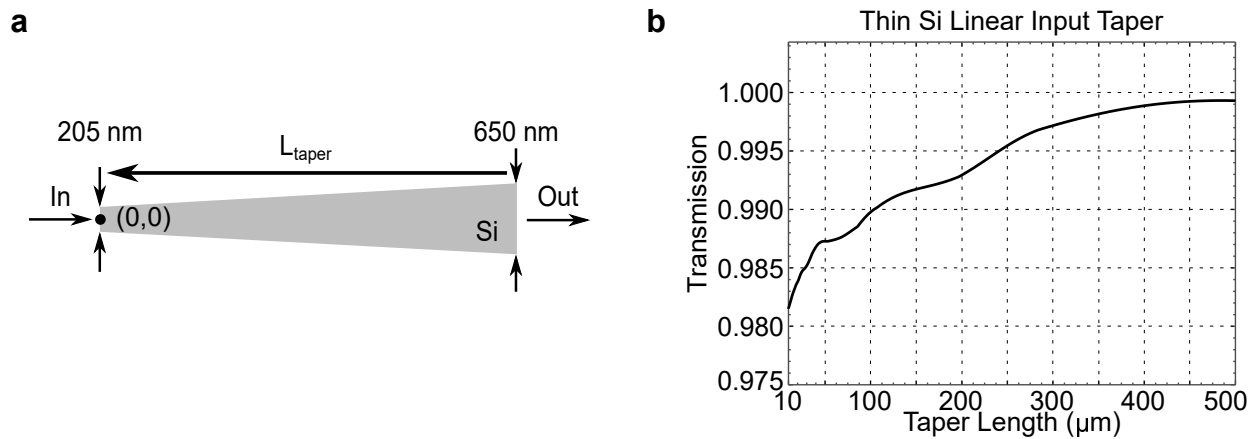


Figure 3.7: **a** Top view of optimized input/output waveguide taper. Taper length L_{taper} is varied from 10 μm to 500 μm in MODE Solutions. **b** Plot of edge taper transmission versus taper length at $\lambda = 1550 \text{ nm}$ for the taper in **a**.

3.6.2 Thin-Si Waveguide

Routing light from the edge of the chip to the bonded region is done with a simple buried channel waveguide of high-index Si ($n_{\text{Si}} \approx 3.47$) surrounded by low-index SiO_2 ($n_{\text{SiO}_2} \approx 1.44$). We use a Si width of 650 nm for these thin-Si waveguides. At $\lambda = 1550 \text{ nm}$, $n_{\text{neff}} = 2.29$.

3.6.3 Thin-Si Spline Bends

We use cubic spline curves (also known as cubic Bézier curves) to create our waveguide bends. A cubic spline curve is known to be the smoothest of all functions (though not necessarily the

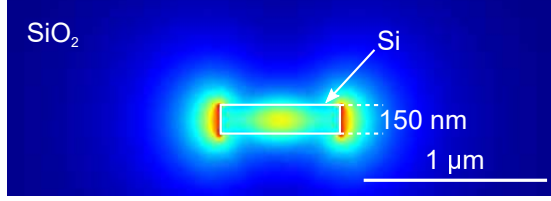


Figure 3.8: Simulation of E_{norm} (the norm of all three E-field components) of the non-hybrid mode. Since E_y and E_z are so small for this TE-like mode, $E_{\text{norm}} \approx E_x$. $w_{\text{Si}} = 650$ nm. As with all Si waveguides in this document, $h_{\text{Si}} = 150$ nm.

most space-efficient) [?], and for this reason is a popular choice in waveguide design to minimize bending losses [3]. The functional form of the cubic spline curve that we use is as follows:

$$\mathbf{S}(t) = (1-t)^3\mathbf{P}_0 + 3(1-t)^2t\mathbf{P}_1 + 3(1-t)t^2\mathbf{P}_2 + t^3\mathbf{P}_3, \quad 0 \leq t \leq 1 \quad (3.1)$$

\mathbf{P}_0 and \mathbf{P}_3 are knots – the starting and ending points of the curve – while \mathbf{P}_1 and \mathbf{P}_2 are control points; that is, points that define the shape of the curve. Each point \mathbf{P}_i has an x- and a y-coordinate to describe its location, and in practice (3.1) is broken down into its spatial components when generating a spline curve. An example of a random spline curve is shown in Fig. 3.9.

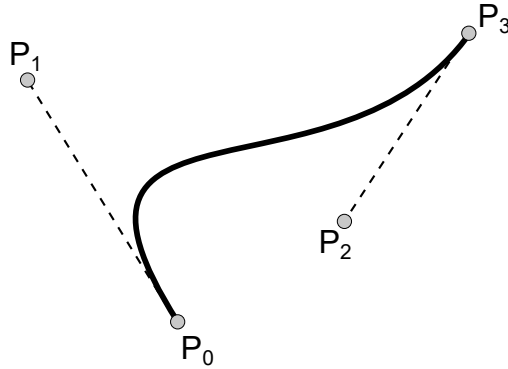


Figure 3.9: Cubic spline curve with knots \mathbf{P}_0 and \mathbf{P}_3 , and control points \mathbf{P}_1 and \mathbf{P}_2 .

90° Bends

If \mathbf{P}_1 and \mathbf{P}_2 are set equal to each other and are arranged to form a right triangle with \mathbf{P}_0 and \mathbf{P}_3 , as shown in Fig. 3.10a, then the spline curve becomes a 90° spline bend. When two such 90° spline bends are generated next to one another, offset by some distance w_{Si} , and connected at their

endpoints, a 90° spline waveguide bend is created. A simple 90° spline bend is shown in Fig. 3.10a, and a 90° spline waveguide bend is shown in Fig.3.10b. Bending loss simulations were carried out in FDTD Solutions for a constant waveguide width w_{Si} of 650 nm. The results are shown in Fig. 3.10c.

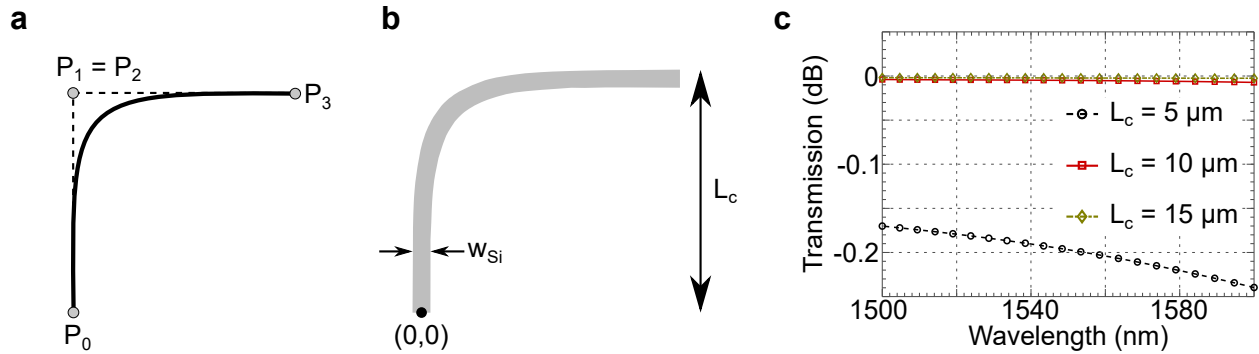


Figure 3.10: **a** 90° spline bend with knots P_0 and P_3 , and control points P_1 and P_2 . **b** Cubic spline waveguide 90° bend with width w_{Si} and characteristic length L_c . L_c is measured from the middle of the input waveguide to the edge of the output waveguide (or vice versa). **c** FDTD simulation of 90° waveguide bend of various characteristic lengths, L_c , for the waveguide shown in Fig. 3.8. For $L_c \geq 10 \mu m$, simulated bending loss is insignificant across the 1500 nm - 1600 nm range of interest.

S Bends

If the optical signal needs to be offset laterally, an S bend can be used. We construct S bends using the spline curve by placing the control points as shown in Fig. 3.11, where the vertical distance from P_0 to P_1 and P_2 is one-half the vertical distance from P_0 to P_3 . P_1 and P_0 share the same x-coordinate, as do P_2 and P_3 . The S bend is characterized by its lateral offset L_x and its longitudinal length L_y .

3.6.4 Thin-Si 3-dB Directional Coupler

The components discussed so far can be put to use as pieces of larger components, such as directional couplers. A directional coupler is created when two (or more) waveguides come into close enough proximity of one another for their evanescent fields to interact, resulting in a weak “coupling” of energy between the waveguides. A simple schematic of such a device is given in

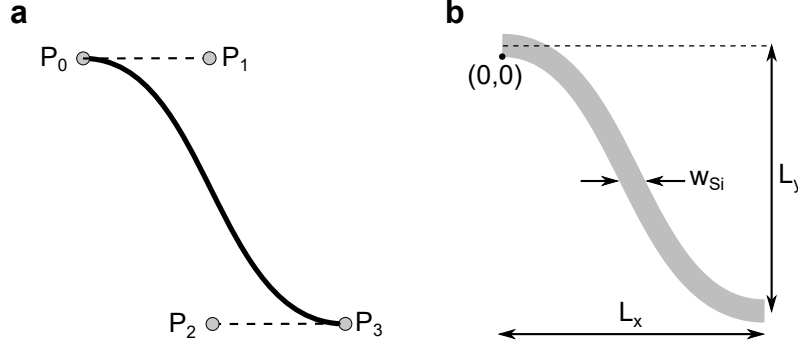


Figure 3.11: **a** Cubic spline S bend. **b** Cubic spline waveguide S bend with width w_{si} , lateral offset L_x , and longitudinal length L_y .

Fig. 3.12. Our directional couplers were designed to split input energy evenly, such that an input in one of the two input ports (A and B in Fig. 3.12) would split evenly into both output ports (C and D in Fig. 3.12). This is known as a 3-dB directional coupler.

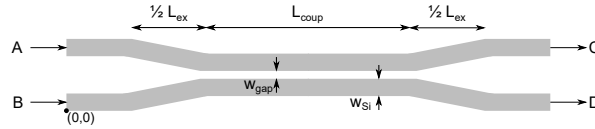


Figure 3.12: Generic directional coupler. L_{coup} is the straight-section coupling length, and L_{ex} is the additional coupling length in the region that angles away from the straight region. The coupling matrix comes from section 6.2.2 in [4].

Coupling from the inputs to the outputs of a directional coupler can be calculated by matrix multiplication (assuming that A, B, C, and D are electric field components). Considering the inputs and outputs of Fig. 3.12, we have the following equation [4]:

$$\begin{bmatrix} C \\ D \end{bmatrix} = \begin{bmatrix} t & i\kappa \\ i\kappa & t \end{bmatrix} \begin{bmatrix} A \\ B \end{bmatrix} \quad (3.2)$$

where t and κ are taken to be real, and $|t|^2 + |\kappa|^2 = 1$. A 3-dB directional coupler (that is, one which splits half of its input light intensity out each of the two outputs, assuming a single input) is one where the coupling coefficient $|\kappa|^2 = 0.5$.

Symmetric Directional Coupler

Fig. 3.13a shows the GDS layout of a symmetric directional coupler. $L_{\text{coup}} = 50 \mu\text{m}$ and $L_{\text{ex}} = 40 \mu\text{m}$ ($L_c = 10 \mu\text{m}$ for each of the 90° spline bends). Referring to the dimensions shown in Fig. 3.12, $w_{\text{gap}} = 280 \text{ nm}$ and $w_{\text{Si}} = 650 \text{ nm}$. A plot of wavelength-dependent $|\kappa|^2$ is shown in Fig. 3.13b.

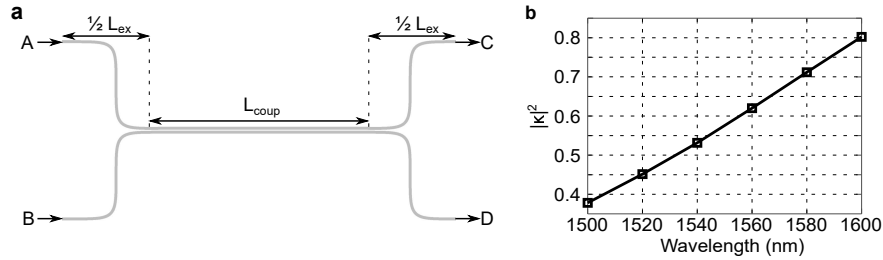


Figure 3.13: **a** GDS layout of a symmetric directional coupler. $L_{\text{coup}} = 50 \mu\text{m}$, $L_{\text{ex}} = 40 \mu\text{m}$ of 90° spline bends, the gap in the straight region is 280 nm, and each waveguide has a width of 650 nm. **b** Coupling coefficient $|\kappa|^2$ for the coupler in **a** as a function of wavelength.

Asymmetric Directional Coupler

The symmetric directional coupler in the previous section has one considerable drawback: it varies strongly with wavelength. From Fig. 3.13b, $|\kappa|^2$ changes by more than 0.4 over the range of $\lambda = [1500, 1600] \text{ nm}$. Many, if not nearly all, practical applications of a directional coupler require a constant coupling coefficient over a wide range of wavelength values. One way to do this is to make the coupling length ($L_{\text{Lcoup}} + L_{\text{ex}}$) very short, but then $|\kappa|^2$ is much too low for most applications. A better design path is to make an asymmetric directional coupler [5]. This sort of design accounts for varying wavelengths by tapering the width of one of the waveguides in the straight coupling section. When this is done correctly, broadband coupling can be achieved. Fig. 3.14a shows the design of an asymmetric directional coupler, and Fig. 3.14b presents simulated results of the coupling coefficient from FDTD Solutions for the structure of Fig. 3.14a.

Referencing the variables in Fig. 3.14a, $w_1 = 650 \text{ nm}$, $w_2 = 400 \text{ nm}$, $w_3 = 300 \text{ nm}$, $w_g = 280 \text{ nm}$, $L_1 = L_3 = L_4 = 30 \mu\text{m}$, and $L_2 = 325 \mu\text{m}$. All Si features are 150 nm thick.

There is some wavelength dependency in the output of this asymmetric directional coupler –

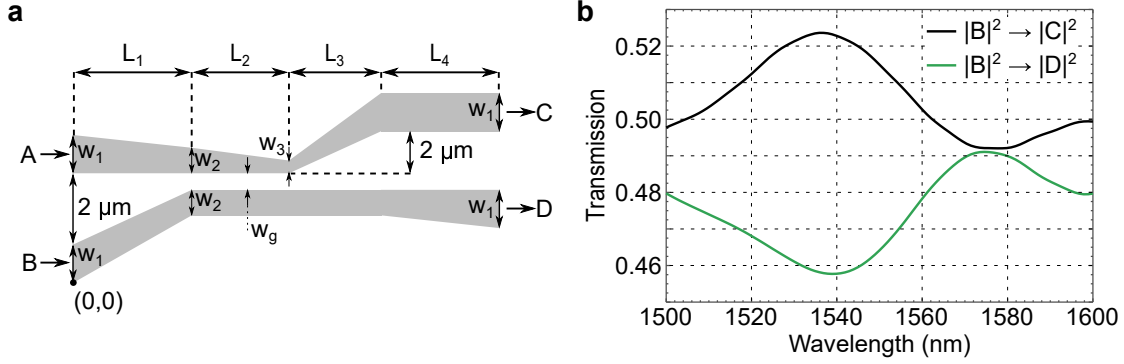


Figure 3.14: **a** Schematic of an asymmetric directional coupler. Coupling occurs most strongly in section L_2 , less strongly in sections L_1 and L_3 , and not at all in section L_4 . **b** This plot shows the transmission through C and D for an input in B. Total transmission is around 98% across the full wavelength range shown. Power splitting from $|B|^2$ to $|C|^2$ and $|D|^2$ is nearly independent of wavelength.

assuming B as the input – but it is much less significant than with the standard directional coupler of the previous section. Across this same wavelength range, $|\Delta\kappa|^2 \approx 0.4$ ($|\Delta\kappa|^2$ is the change in $|\kappa|^2$ across the [1500,1600] nm wavelength range) for the standard directional coupler. For this asymmetric directional coupler, $\Delta|\kappa|^2 \approx 0.06$, a factor of 7 improvement. The drawback to using the asymmetric directional coupler is that it is about seven times longer than the symmetric directional coupler. This trade-off between the two structures should be evaluated by the designer.

3.6.5 Mach-Zehnder Interferometer

A Mach-Zehnder interferometer (MZI) can be made in a waveguide structure by splitting light and then recombining it, either with or without a passive path-length difference (PLD) between the two arms of the structure. A top view of a path-length imbalanced MZI is shown in Fig. 3.15. A PLD MZI uses non-hybrid Si tapers to couple on and off the chip, non-hybrid Si WGs, either a symmetric or an asymmetric DC as the splitter, and either hybrid waveguides or non-hybrid waveguides in the path-length difference section.

The PDK developed for this hybrid Si-LN platform includes an optical MZI component that can be simulated in Lumerical’s INTERCONNECT software.

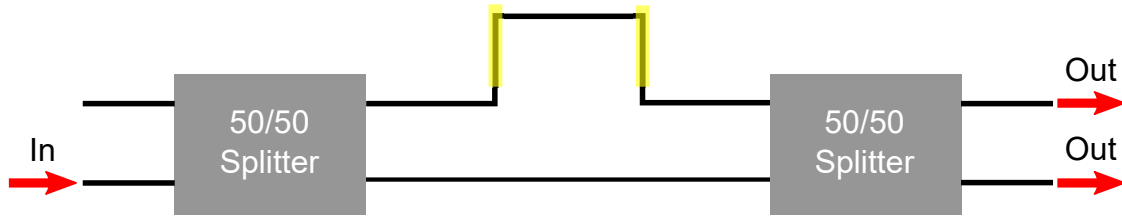


Figure 3.15: Top view of an MZI structure. Black lines represent waveguides and the path-length difference on the top arm is highlighted in yellow. Each 50/50 splitter is either a symmetric DC or an asymmetric DC (there are other types of WG-based splitters, but they are not part of this design kit).

3.6.6 Hybrid Si-LN Taper

Linear tapers were discussed in Section 3.6.1 to be used as edge couplers to couple light from an input fiber to the chip, or from the chip to an output fiber. A similar taper concept is used in the hybrid region of the chip to convert light from the optical mode of Fig. 3.16a to that of Fig. 3.16b.

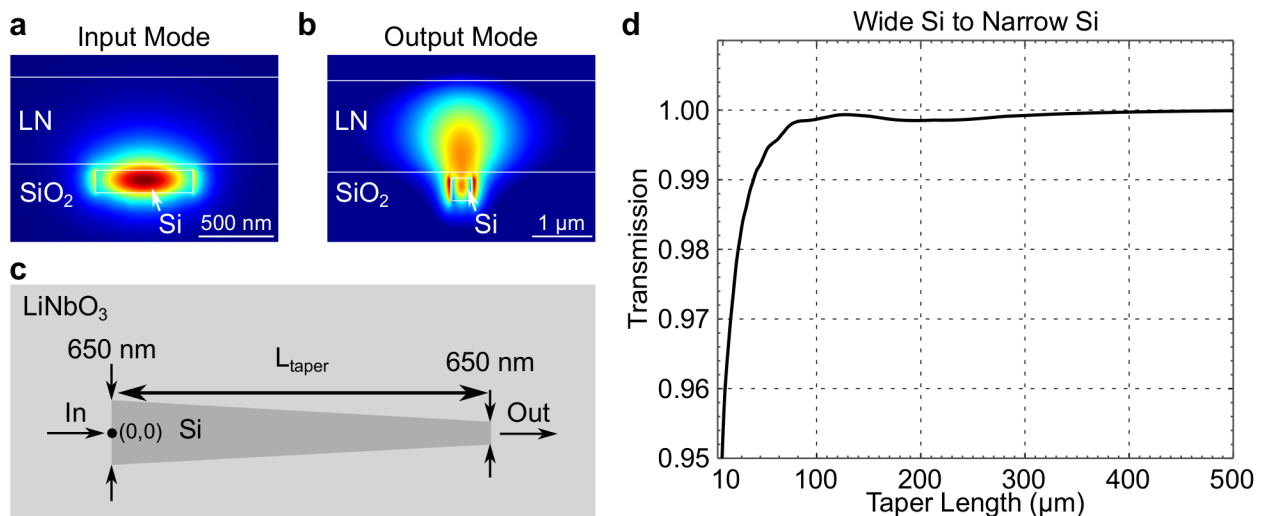


Figure 3.16: **a** E_x field of optical mode in hybrid Ssi-LN region with wide ($w_{Si} = 650$ nm) Si. **b** Narrow ($w_{Si} = 320$ nm) Si. **c** Top view of hybrid Si-LN taper. The taper is in the Si ridge layer, and LN film is bonded over the entire area. **d** Plot of transmission versus taper length. The final taper design uses a taper length $L_{tap} = 200$ μm .

This taper is what allows the hybrid Si-LN platform to be so versatile. By reducing the width of the Si ridge, the fraction of the optical mode in the LN film increases. This is because LN (the cover material) has a higher index of refraction than SiO₂ (the substrate material). As the

Si waveguide width is reduced, less light is confined by the Si, despite its higher index, because its width is smaller than one wavelength in silicon (≈ 447 nm). If the Si were embedded in SiO_2 , then the evanescent fields would spread equally into the cover and substrate. Since the cover has a higher index, as well as a non-infinite thickness, the mode's evanescent fields spread deeper into the LN cover and are vertically confined by the upper edge of the LN film. Horizontal confinement is maintained by the sidewalls of the Si ridge waveguide, and thus this hybrid Si-LN platform is capable of guiding a mode that exists in both the Si and LN regions. Proper design of this hybrid linear taper results in a useful hybrid mode.

Simulations of this taper were performed in MODE Solutions using the EME solver to analyze the hybrid linear taper, whose top view is shown in Fig. 3.16c where $w_1 = 650$ nm and $w_2 = 320$ nm (these are the input and output taper widths, respectively). In this component, the linear taper is made in the Si ridge layer and LN thin film ($h_{\text{LN}} = 600$ nm) is bonded over the entire taper region. Taper losses become negligible beyond a taper length L_{taper} of $100 \mu\text{m}$ (Fig. 3.16d). We chose $L_{\text{taper}} = 200 \mu\text{m}$ for our final design's taper length.

3.6.7 Hybrid Si-LN Waveguide

Once the hybrid waveguide is tapered down to the desired width (in this case, that is $w_{\text{Si}} = 320$ nm), it can be used in hybrid optical designs. A plot of E_x for this mode is shown in Fig. 3.16b. This waveguide is designed so that as much of the optical mode sits in the LN region as possible, without allowing the mode to decouple from the Si rib waveguide. A plot of mode area and LN confinement factor (LNCF) is provided in Fig. 3.17. LNCF is defined as the percentage of power traveling along the hybrid waveguide that is produced by the TE component of the mode:

$$\text{LNCF} = \frac{\int_{\text{LN}} (\mathbf{E}_x \mathbf{H}_y^*) dx dy}{\int_{-\infty}^{\infty} (\mathbf{E}_x \mathbf{H}_y^* - \mathbf{E}_y \mathbf{H}_x^*) dx dy} \quad (3.3)$$

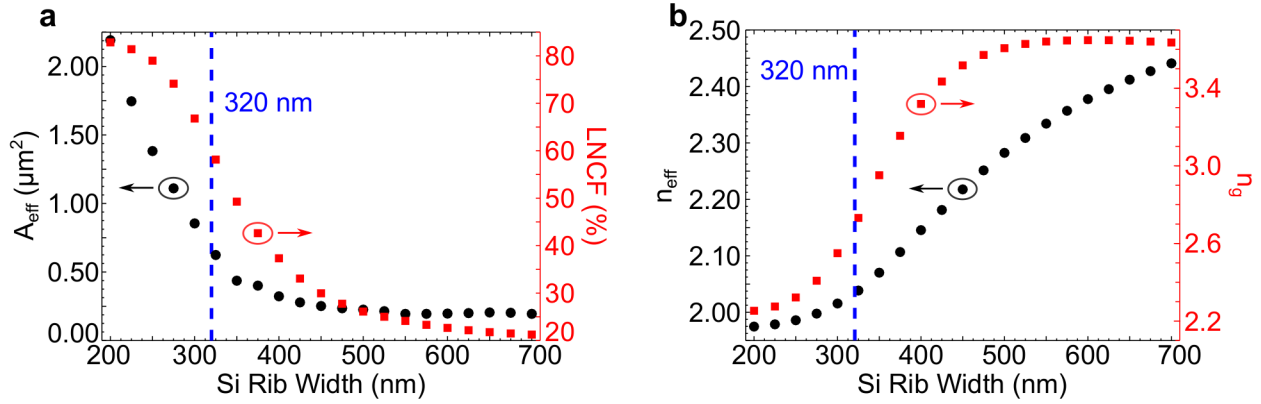


Figure 3.17: **a** Plot of simulated effective mode area (left axis, black circles) and LNCf (right axis, red circles). **b** Plot of simulated effective index (left axis, black circles) and group index (right axis, red squares). The dashed vertical blue line in each part shows where the mode chosen to use sits. $A_{\text{eff}} = 0.67 \mu\text{m}^2$, LNCf = 60%, $n_{\text{eff}} = 2.04$, and $n_g = 2.73$.

3.6.8 Hybrid Si-LN Electro-Optic Phase Shifter

A single hybrid Si-LN waveguide from Section 3.6.7 can be made into a high-speed electro-optic (EO) phase shifter (PS) by launching a radio-frequency (abbreviated as RF, accounts for the frequency range of several kHz to 300 GHz) wave down a transmission line that runs parallel to the hybrid waveguide. The transmission line must be physically close to the hybrid waveguide – on the order of micrometers – to maximize the overlap of the RF and optical electric fields. A typical cross-section for this structure, using x -cut LN and a coplanar waveguide (CPW) structure for the transmission line, is shown in Fig. 3.18.

3.6.9 Coplanar Waveguide Transmission Line

The lumped element model for circuit elements is valid only when the RF frequency $f_{\text{RF}} \ll \frac{c}{nd}$, where c is the speed of light, n is the phase index of the RF mode in the circuit element, and d is the length of the element. As an example, consider a fairly typical phase index of 2.2 in a 10 cm element; in such a scenario, an element with an operating frequency well below 1.4 GHz can be treated as a lumped element and, in the case of electro-optic devices, is generally treated as an RC-limited low-pass filter.

The hybrid EO devices discussed in this work are designed with high speed (tens to hundreds

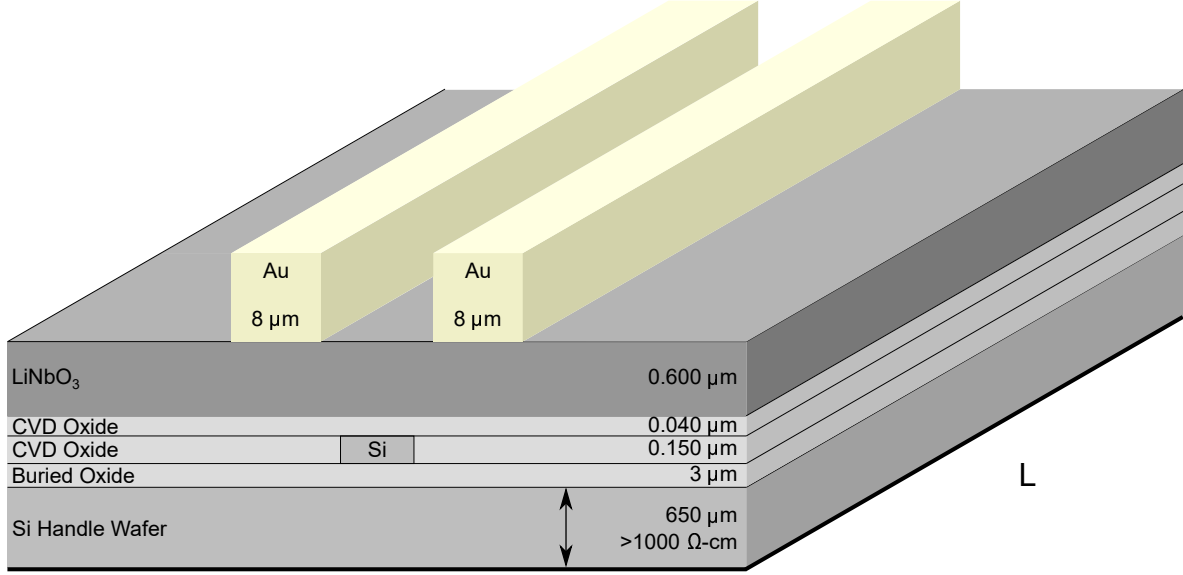


Figure 3.18: 3D depiction of the final cross-section from Fig. 3.3, but for the single Si waveguide of a hybrid Si-LN EO phase shifter. Only the straight section of the PS is shown here. Each layer's thickness is given, along with resistivity values for the Si handles. The EO PS has length “L.”

of GHz) in mind, in which case the lumped element model is invalid and is replaced with a traveling wave transmission line model [6]:

$$m(\omega) = \left| \frac{\Delta\phi(\omega)}{\Delta\phi(0)} \right| = \frac{R_L + R_G}{R_L} \cdot \left| \frac{Z_{in}}{Z_{in} + Z_G} \right| \cdot \left| \frac{(Z_L + Z_0)F(u_+) + (Z_L - Z_0)F(u_-)}{(Z_L + Z_0)e^{\gamma_m L} + (Z_L - Z_0)e^{-\gamma_m L}} \right|, \quad (3.4)$$

where $m(\omega)$ is the normalized modulation response, $F(u_{\pm}) = \frac{1-e^{u_{\pm}}}{u_{\pm}}$, and $u_{\pm} = j(\pm\beta_m - \beta_o)L \pm \alpha_m L = \pm\alpha_m L + j\frac{\omega}{c}(\pm n_m - n_o)L$. R_L is the load resistance, R_G is the source resistance, and Z_{in} is the RF input impedance of the loaded transmission line, defined as:

$$Z_{in} = Z_0 \frac{Z_L + Z_0 \tanh(\gamma_m L)}{Z_0 + Z_L \tanh(\gamma_m L)}. \quad (3.5)$$

Z_G in (3.4) is the source impedance (typically this will be $Z_G = R_G = 50 \Omega$). Z_L is the load impedance, Z_0 is the characteristic impedance of the transmission line, $\gamma_m = \alpha_m + j\beta_m$ is the complex RF propagation constant, α_m is the RF attenuation coefficient in cm^{-1} , β_m is the phase constant (also in cm^{-1}), n_m is the RF phase index, n_o is the optical group index, and L is the

interaction length along which the RF and optical modes interact. An additional term $\Delta n = n_m - n_o$ is defined for convenience and future use.

From (3.4), the following are evident:

1. Δn must be made as small as possible;
2. α_m must be minimized;
3. Z_L and Z_0 should be made equal, if possible.

Each of these design conditions is investigated separately in Fig. 3.19a-c, and a more in-depth analysis is given in [6]. For the purposes of design optimization, what is important to know is that these three conditions limit electro-optic bandwidth. Note that in Fig. 3.19, RF losses are given in terms of per $(\text{GHz})^{1/2}$. This is because in a well-fabricated electro-optic modulator, RF losses are dominated by conductor losses, which scale with the square root of frequency. By using units of $\text{dB}/(\text{cm-GHz}^{1/2})$, a single loss value can be used to describe losses across a range of frequencies. In the hybrid Si-LN modulator, this assumption is fairly accurate as long as the Si substrate has a (relatively high) resistivity of at least $1000 \Omega\text{-cm}$.

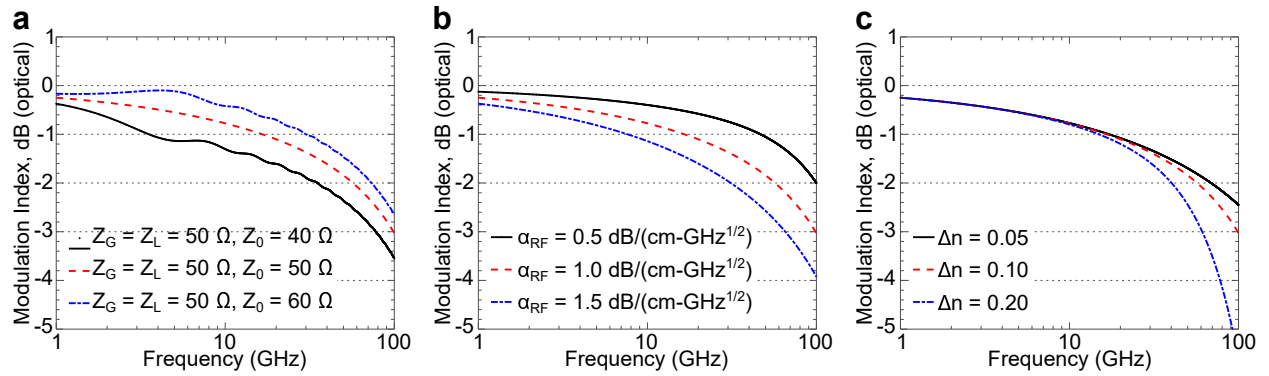


Figure 3.19: Plot of (3.4) when varying: **a** Characteristic impedance Z_0 , with $\Delta n = 0.10$ and $\alpha_{\text{RF}} = 1 \text{ dB}/(\text{cm-GHz}^{1/2})$; **b** RF losses α_{RF} , with $Z_0 = Z_G = Z_L = 50 \Omega$ and $\Delta n = 0.10$; and **c** RF-to-optical index difference Δn , with $Z_0 = Z_G = Z_L = 50 \Omega$ and $\alpha_{\text{RF}} = 1 \text{ dB}/(\text{cm-GHz}^{1/2})$. $L = 1 \text{ cm}$ for all simulations.

3.7 Acknowledgments

Chapter 3, in part, is a reprint of the material as it appears in Conference on Lasers and Electro-Optics (CLEO) 2017. Peter O. Weigel and Shayan Mookherjea, paper JTU5A.126. The dissertation author, together with his adviser, led the research efforts for this work and co-authored the paper.

Bibliography

- [1] Timurdogan E, Su Z, Poulton C, Byrd MJ, Xin S, Shiue RJ, et al. AIM Process Design Kit (AIMPDKv2. 0): Silicon Photonics Passive and Active Component Libraries on a 300mm Wafer. In: Optical Fiber Communication Conference. Optical Society of America; 2018. p. M3F-1.
- [2] Farin G. Curves and surfaces for computer-aided geometric design: a practical guide. Academic Press; 1992. Print.
- [3] Bogaerts W, et al. Compact single-mode silicon hybrid rib/strip waveguide with adiabatic bends. IEEE Photonics Journal. 2011;3(3):422-432.
- [4] Aguinaldo RF. Silicon Photonics with Applications to Data Center Networks. University of California San Diego; 2014.
- [5] DeRose CT, Watts M, Young RW, Trotter DC, Nielson GN, Zortman W, et al. Low power and broadband 2 x 2 silicon thermo-optic switch. In: Optical Fiber Communication Conference. Optical Society of America; 2011. p. OThM3.
- [6] Ghione G. Semiconductor devices for high-speed optoelectronics. Cambridge University Press; 2009. Print.

Chapter 4

Fabrication of Hybrid Electro-Optic Devices

4.1 Introduction

Fabrication of this device was performed at two locations. First, 150 mm silicon-on-insulator (SOI) wafers from SOITEC, Inc. were fabricated at Sandia National Laboratories in Albuquerque, New Mexico with standard foundry processing techniques (i.e. photolithography, reactive ion etching, silicon oxidation, etc.) as well as a chemical-mechanical planarization (CMP) step for <1 nm surface roughness. Wafer dicing/edge polishing, LiNbO_3 (LN) film bonding and handle removal, and metallization were performed at UC San Diego. Details of these fabrication efforts are detailed in this chapter.

4.2 Film-on-Insulator Wafers

Modern silicon photonics is built not on bulk silicon wafers, but on silicon-on-insulator (SOI) wafers. Modern SOI wafers are a sub-class of “film-on-insulator” wafers produced by the Smart-Cut process (also known as crystal ion slicing, or CIS), first patented in 1994 by Michel Bruel [1]. This process, depicted in Fig. 4.1, implants a bulk wafer with ions of a certain type (though typically hydrogen or helium) at a particular energy, chosen so that the ions reach a desired mean depth into the material (Fig. 4.1a). That bulk, implanted wafer is then bonded to another

wafer (the second wafer can theoretically be any material as long as it is smooth and flat enough for bonding; bonding is discussed in detail in Section 4.4) and heated until the implanted ions expand until they cause the first wafer to crack along the implanted layer (Fig. 4.1b-c). A final polishing step is performed, and what results is a wafer comprised of a thin film of crystalline material – with the same material properties as its bulk wafer form [2, 3, 4, 5] – bonded to (usually) an insulator such as silicon dioxide (SiO₂) on some bulk material handle (Fig. 4.1d).

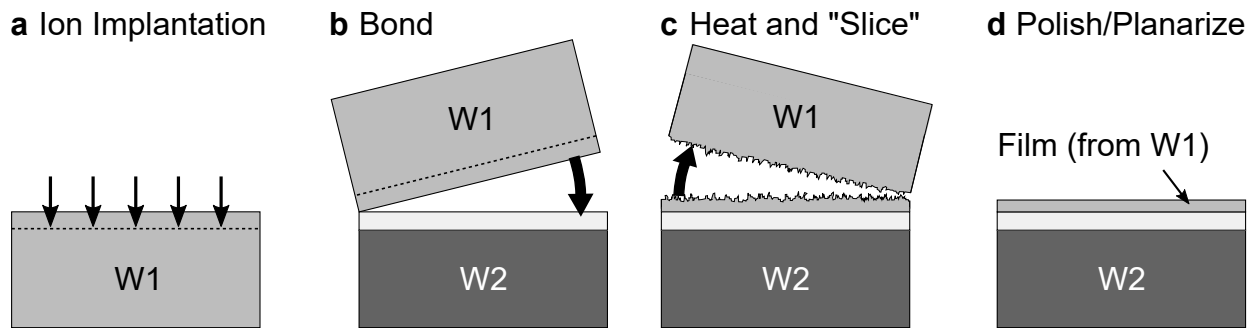


Figure 4.1: The basic crystal ion slicing process is depicted in four steps: **a** The first wafer (W1) is ion-implanted. **b** W1 is bonded to the second wafer (W2), comprised of some handle material covered with a thin, smooth insulator material. **c** The bonded stack is heated until W1 cracks off (“slicing”), leaving a thin rough layer of crystalline material. **d** Polish and planarize the thin crystal layer.

Film-on-insulator wafers have been used in guided-wave optics since they were invented [6]. They feature thin, crystalline films that can be selectively patterned to form small waveguides with high mode confinement and low loss. SOI wafers in particular are attractive as a guided-wave material for several reasons, a few of which are listed here: silicon waveguides can potentially be integrated with CMOS technology, though this requires a CMOS foundry to develop a fabrication process which accounts for optical waveguides; silicon has a high index (approximately 3.5) in the telecommunications windows above $\lambda = 1.15 \mu\text{m}$ (its bandgap), which is useful for densely packed photonic circuits; as a semiconductor, silicon can be p or n doped to create useful structures, including *p-i-n* waveguides with uses as heaters, switches, and modulators [7, 8, 9].

More recently, research into LN films-on-insulator (LNOI) has emerged due to the availability of commercial LNOI (NanoLN, Jinan Jingzheng Electronics Co. Ltd.). LN was the guided-wave material of choice until the mid to late 90s [10], when SOI wafers started to become available and

a large portion of the field moved towards developing optics on SOI (now commonly called Si photonics). However, (bulk) LN remains one of the most ubiquitous materials in the industry, and is still used for electro-optic devices worldwide. With the emergence of readily available LNOI wafers, there is renewed interest in LN photonics [11].

The fabrication in this chapter begins with an SOI wafer from SOITEC and an *x*-cut LNOI wafer from NanoLN. Both wafers are polished to <1 nm surface roughness and <20 μm flatness at their respective fabrication facilities.

4.3 SOI Patterning & Oxide Polishing

SOI patterning was performed at Sandia National Laboratories on standard 220 nm-thick Si on a 3 μm SiO_2 layer. The Si layer was thinned down to 150 nm via reactive ion etching (RIE, “dry” etching) before Si patterning was performed using wafer-scale deep ultraviolet (DUV) photolithography and RIE, followed by high-density plasma chemical-vapor deposition (HDP CVD) of approximately 1 μm of SiO_2 . A chemical-mechanical planarization/polishing (CMP) process was developed at Sandia to bring the SiO_2 thickness down to around 350-400 nm with low surface roughness and good flatness. Further oxide thinning was performed with a highly diluted hydrofluoric (HF) acid etch – 100 parts aqueous ammonium fluoride (NH_4F , 40%) to 1 part aqueous HF (49%) – to reduce the oxide thickness even further. This process flow is shown in Fig. 4.2.

However, the initial fabrication efforts did not incorporate a wet etch step after CMP. This resulted in over-polishing of the wafers, to the point where sections of the Si waveguides were too thin to propagate light; in some cases, the Si waveguides disappeared entirely. By targeting a thicker oxide layer with CMP and then slowly etching down to the desired thickness, bondable devices could be fabricated. An oxide map of a properly polished and wet etched wafer is presented in Fig. 4.3b. Negative values indicate where the oxide thickness is below the top surface of the patterned thin Si layer. From Fig. 4.3b it is clear that wafer flatness after CMP can be improved, though individual dies were typically flat enough for bonding. Surface roughness was consistently

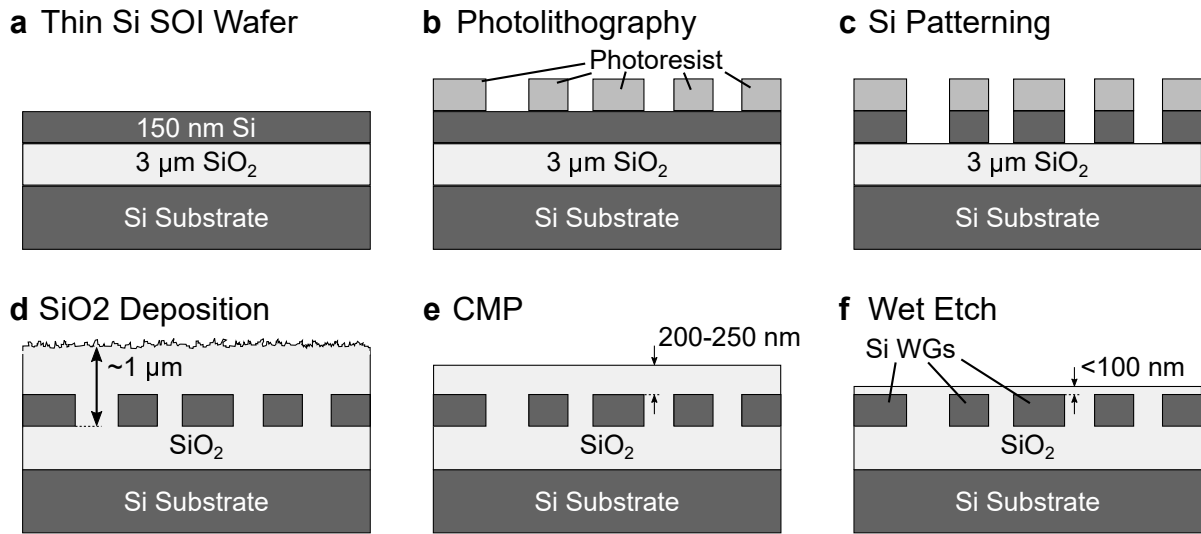


Figure 4.2: **a** A standard 220 nm SOI wafer from SOITEC is thinned to 150 nm with RIE. **b** Photoresist is spun on the wafer and patterned with DUV lithography. **c** RIE is used to etch the photoresist pattern into the thin Si layer. **d** Approximately 1 μm of oxide is deposited via HDP CVD onto the patterned wafer. **e** A CMP recipe, customized for this fabrication process, is used to bring the oxide thickness to several hundred nanometers. **f** A diluted HF wet etch is used to further reduce the oxide thickness. WG = waveguide.

low enough for bonding (<1 nm rms). Fig. 4.3c shows a properly fabricated SOI wafer, as delivered to UCSD from Sandia.

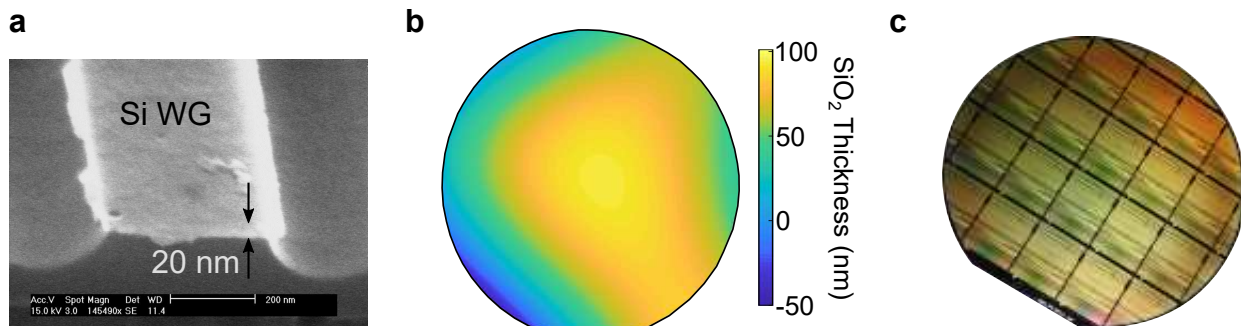


Figure 4.3: **a** SEM image of an over-polished waveguide. The measured value of only 20 nm is 130 nm below the targeted thickness, and is too thin to guide light. **b** Wafer map of oxide thickness over Si features after CMP and wet etch in optimized process flow (Fig. 4.2f). As is typical with first-attempt wafer CMP processes, wafer flatness is not yet ideal. This can be improved with optimization efforts. **c** Fully fabricated 150 mm SOI wafer from Sandia, corresponding to the wafer map of **b**.

4.4 Bonding Theory

Bonding, as its name implies, is the process of bringing two materials into contact in such a way that they remain in contact after external forces are removed. While bonding is used colloquially to describe everyday adhesives, such as glue and tape, in the context of this work the word “bonding” refers to the action of bringing two planar, smooth surfaces into contact and being held together by various intermolecular forces, namely Van der Waals forces (including hydrogen bonds, also known as dipole-dipole bonds) and covalent bonds [12]. Under the correct conditions – to be discussed in this section – large surfaces of dissimilar materials can be brought into contact and remain bonded, despite changes in stress caused by sudden temperature variations.

4.4.1 Types of Bonds

The different types of bonds used in this thesis are defined as follows:

Direct Bonding: Room-temperature bonding between the two materials of interest; uses van der Waals forces

Fusion Bonding: Covalent bonding between the two materials of interest; can be done at room temperature under the right conditions [16], but typically requires a thermal annealing process [12]

Adhesive/Indirect Bonding: Using an adhesive layer between the two materials of interest during bonding

These bond types are not mutually exclusive; it is possible to have a direct fusion bond, an adhesive direct bond, or even an adhesive fusion bond.

Direct Bonds & Fusion Bonds

A direct bond is one in which two materials are physically placed in close enough proximity (on the order of angstroms) for intermolecular forces to bind them to one another after external forces are removed. Direct bonding was first observed by Sir Isaac Newton, though he had no concept of “bonding” at the time; in reference to two pieces of polished glass coming into contact,

he described it as a “central black spot” at the point of “optical contact” [13]. Newton’s name still bears relevance to the science of bonding, as the colored rings surrounding a bonded spot are commonly called Newton rings.

There are different definitions of direct bonds and fusion bonds throughout the literature, where in some cases the only attributed distinction between the two is the temperature at which the bonding occurs [13]. This is not technically correct. Instead, the type of intermolecular bond defines whether the materials are direct bonded or fusion bonded. A fusion bond is one in which two materials are joined by chemical bonds, while a direct bond is simply two materials held together by van der Waals forces.

Direct bonding became a subject of great interest for the semiconductor and Si photonics communities (amongst others) after Bruel’s 1994 patent of the Smart-Cut process [1]. Direct bonding via the Smart-Cut process quickly accelerated from a research curiosity to a mainstream industry practice. In the silicon photonics community, for example, nearly all silicon-on-insulator (SOI) wafers are purchased from SOITEC, Inc., as opposed to being fabricated separately at each laboratory or institution.

These intermolecular forces are typically van der Waals [12], though much stronger covalent bonding at room temperature is possible in vacuum with plasma surface activation (PSA) [16]. However, due to the versatility of bonding by hand, particularly with small dies of varying sizes, all bonding discussed in this thesis was performed at room temperature and pressure.

Adhesive Bonds

An adhesive bond is similar in some ways to a direct bond, in that some direct contact, often at room temperature, occurs. However, the two layers desired to be bonded are not brought into direct contact. Instead, at least one of them is coated with a thin adhesive before bonding and then curing. In some cases, a partial cure precedes the bonding step. Adhesive bonding is advantageous due to the physical properties of adhesives – namely, they tend to be in liquid or gel form before being cured, so that typically strict bonding requirements such as low surface roughness and good

flatness become much less severe. The downsides to adhesive bonding are the separation between the two materials being bonded, and aging/thermal limits of the adhesive material.

Practical Considerations during Bonding

This thesis deals with all three types of bonding discussed previously. The adhesive used in this thesis is benzocyclobutene, or BCB (many other types of adhesives can be used for bonding, depending on the application [14]). BCB is a polymer commercially available in an aqueous form that can be spin coated onto wafers or dies and subsequently hardened through a thermal annealing process (i.e. curing). However, BCB has some thickness to it (though while in solution it can be diluted so that a cured film has a thickness below 50 nm [15]), which may not be suitable for certain applications. And like all polymers, BCB has a limited thermal budget (glass transition temperature $T_g < 350^\circ\text{C}$) and can degrade over time. The primary advantage to using BCB and polymers like it is the reduction in bonding fabrication challenges, particularly at the wafer scale where the spin-coated BCB layer can be made extremely uniform in place of a wafer polishing process [15].

If the fabrication challenges associated with unassisted direct bonding can be overcome, it is generally the most preferred form of bonding; direct bonds can be performed at room temperature and annealed to form fusion bonds, which can be as strong as covalent bonds in a homogeneous crystal with the proper annealing process and surface conditions [12], and require no polymer adhesive interlayer material. Particularly for high purity crystalline wafers, direct bonding is attractive for both its robustness and cleanliness. That being said, direct bonding requires pristine surface quality of the two wafers being bonded – even a single particle can ruin an entire wafer bond if the particle is unfortunately large – as well as low surface roughness and very good flatness across the wafer to ensure that the full wafer is bonded.

4.5 Reducing Thermal Stress in Heterogeneous Bonded Materials

Despite advances in the last decade or so in silicon photonics, lithium niobate continues to find uses in advanced areas of integrated photonics due to its favorable nonlinear properties and low propagation loss [17, 18, 19, 20]. Recently, researchers have been studying hybrid integrated photonic devices in which silicon-on-insulator (SOI) is bonded to lithium-niobate-on-insulator (LNOI), creating single-mode hybrid waveguides with sub-micron cross-sectional dimensions [21, 22, 23, 24, 25, 26]. Bonded materials are sometimes subject to additional fabrication steps, for example, to pattern waveguides [27], and such processing generates stress in the layers due to a difference in coefficients of thermal expansion (CTEs) between the different materials and can cause irreversible damage. Similar to the work done earlier in bonding laser material to SOI [28, 29], it is important to identify the parameters and properties of the inter-layer bonding material, such as benzocyclobutene (BCB), to mitigate the stresses [30, 14, 15, 31, 32].

The approach to hybrid SOI-LNOI devices we study here is to bond a SOI chip (diced from SOI wafers from Soitec, Inc., and patterned using a standard silicon photonics foundry process) to an LNOI chip (LNOI from NanoLN Jinan Jingzheng Electronics Co. Ltd.) which has a thin layer of LN crystal, an SiO₂ buffer layer and a LN or Si handle [25]. A typical cross-section of a LNOI-SOI bonded chip is shown in Fig. 4.4. The chips are initially brought into contact at room temperature, and then the bond is strengthened by a thermal anneal. Compared to other approaches, such as those based on etched or deposited thin films [33, 34, 35], the advantage of this approach is that both the Si and LN thin film layers are crystalline and of high quality, which may benefit device performance and enable opto-electronic functionality.

However, if this stack is directly bonded and the LNOI has a LN handle, it can only be held together at room-temperature by weak hydrogen bonds. We have found that the stack debonds when the temperature is raised to about 70-80°C. Researchers who have studied direct bonding of bulk Si and LN under optimum conditions have found that the two materials either debond or

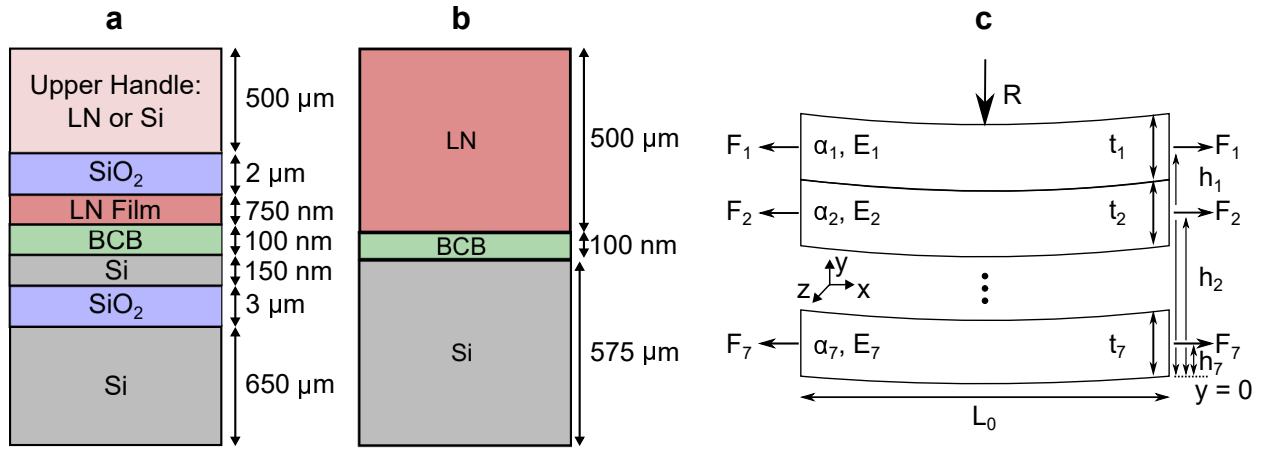


Figure 4.4: **a** The thin-film stack used in hybrid photonic devices based on silicon-on-insulator (SOI) and lithium niobate-on-insulator (LNOI). **b** A simplified bulk LN-BCB-Si bonded structure used in the calculations shown in Fig. 4.5. **c** A schematic drawing of the bonded stack, labeling the dimensions and axial forces used in equations (4.1)-(4.4).

crack by 150°C [16, 36]. It may be hypothesized that debonding of Si and LN, two materials with substantially different properties (see Table 1), can be mitigated by using a layer of amorphous, low-optical-loss adhesive, such as benzocyclobutene (BCB, cyclotene 3022-35 resin from The DOW Chemical Company). BCB has a high bond strength and thermal stability, but has a high thermal resistance and a low refractive index that is substantially different from that of either Si or LN. Calculations show that in order to maintain a hybrid optical mode similar to that of the directly-bonded case, the BCB layer must be no more than 100 nm thicker than the SOI patterned features; however, thin layers of BCB may not be sufficient to mitigate the built-up stresses. In studies of bonded III-V-to-SOI materials, BCB layer thicknesses of 50 nm have been used [15].

After thorough cleaning of a SOI chip and a LNOI chip, a layer of BCB was spun onto the Si chip; some of the chips used a BCB thickness of 300 nm (the summation of the height of the SOI features and the calculated 100 nm separation between SOI and LN), whereas other chips used a thickness of $1\ \mu\text{m}$. The chips were partially cured at 180°C for 45 minutes before being manually aligned, bonded and hard-baked for 14 hours at 190°C . By placing a weight over the chips, a force of 9.8 N was applied over a bonded area of $1\ \text{cm} \times 1\ \text{cm}$ during the hard-bake process.

Contrary to intuition, the thickness of the BCB layer did not play a role in managing thermal stress. We observed that LNOI with a LN handle cracked or debonded by the end of the hard

bake, regardless of BCB thickness. However, if the LNOI stack was based on a Si handle, the bonded films did not crack or separate. This experimental observation is discussed using a simple computational model and supported by further test experiments on test (bulk Si) samples.

We use a strain model which accounts for self-induced thermal strain (since the materials will experience strain as temperature changes), stack-induced thermal strain (i.e., thermal strain due to a mismatch in CTEs of materials held together in the stack), and bending-induced thermal strain (a difference in CTEs causes a bonded stack to bend, resulting in an additional expansion or contraction of the layers in the stack) based on the seminal theory outlined in [37].

Table 4.1: Material properties of all materials used in our numerical calculations of thermally-induced stress. All data is taken at room temperature. E is the modulus of elasticity, and α is the coefficient of thermal expansion (CTE). x , y , and z are used to denote the crystal axes of anisotropic LN.

Material	E (GPa)	α (10^{-6}-K^{-1})
Si	130[38]	2.6[39]
LN, z	199[40, 41]	3.4[42]
LN, y	173[40, 41]	13.4[42]
LN, x	173[40, 41]	13.4[42]
SiO ₂	75[43]	1.0[43]
BCB	2.9[44]	52[45]

A schematic of the structure is shown in Fig. 4.4c, and consists of seven layers, each with a different axial force, and a common bending radius R . We require eight equations to solve for the total strain in each of the seven layers. The width of each cross-section is not shown, but it is assumed that they are all 1 cm, the nominal width of the test pieces used in this study. α_i is the CTE for the i -th layer, E_i is the modulus of elasticity for the i -th layer, and t_i is the thickness of the i -th layer, where $i = 1, 2, \dots, 7$. The CTEs and moduli of elasticity at room temperature are provided in Table 7.1. The moduli of elasticity in anisotropic LN were recalculated from the stiffness tensor of [40]. Calculating a modulus of elasticity from a stiffness tensor is discussed in [41]. We assume all materials operate in the elastic regime, governed by Hooke's law: $\sigma = E\epsilon$, and

that there is no slip between bonded layers (i.e., two adjacent layers will stretch equally at their shared boundary). Additionally, we assume that the radius of curvature R is much larger than the sum of the thicknesses of all layers, and that the length L_0 of the stack is much smaller than R , so that the small-angle approximation [$\tan(\theta) \approx \theta$] is valid. Under these assumptions, the equation for the strain in the i -th layer is:

$$\epsilon_i = \alpha_i \Delta T + \frac{F_i}{E_i A_i} + \frac{t_i}{2R}. \quad (4.1)$$

We solve the following equations for the eight variables F_i and R ,

$$\sum_{i=1}^{i=7} F_i = 0, \quad (4.2)$$

$$\sum_{i=1}^{i=7} h_i F_i = \frac{1}{R} \sum_{i=1}^{i=7} E_i I_i, \quad (4.3)$$

$$\alpha_j \Delta T + \frac{F_j}{E_j A_j} + \frac{t_j}{2R} = \alpha_{j+1} \Delta T + \frac{F_{j+1}}{E_{j+1} A_{j+1}} - \frac{t_{j+1}}{2R}, \quad (4.4)$$

(4.2) is the sum of thermally-induced axial forces, (4.3) is the sum of moments caused by those forces, and (4.4) comes from the equality of strain at each boundary between layers, so that $j = 1, \dots, 6$ (because there are six boundaries between the seven layers). We assume there are no external forces. I_i is the area moment of inertia of each layer ($i = 1, \dots, 7$): $I_i = wt_i^3/12$, where w is the width of the stack. $\Delta T = T_f - T_0$, where T_f is the final temperature and T_0 is the initial temperature at which bonding occurs, and $A_i = t_i w_i$ is the area of the cross-section of the i -th layer. h_i is the distance from $y = 0$ to the point of application of F_i . This is depicted in Fig. 4.4c.

We numerically solved for this set of equations for the seven-layer structure shown in Fig. 4.4a for both a LN upper handle and a Si upper handle. Our calculations for the stress are shown in Fig. 4.5a, where stress is calculated from Hooke's law. Since LN is anisotropic and has different material properties along different crystal axes, we ran the simulation for z-axis LN as well as for y-axis LN (x-axis stress will be the same as y-axis stress in LN, see Table 7.1), assuming

the LN film had the same orientation as the LN handle. As we expected, z-axis stresses were much lower than y-axis stresses for each LNOI handle material, simply because the CTE along the z-axis of LN is much closer to the CTE of Si than is the CTE along the y-axis of LN (from Table 7.1).

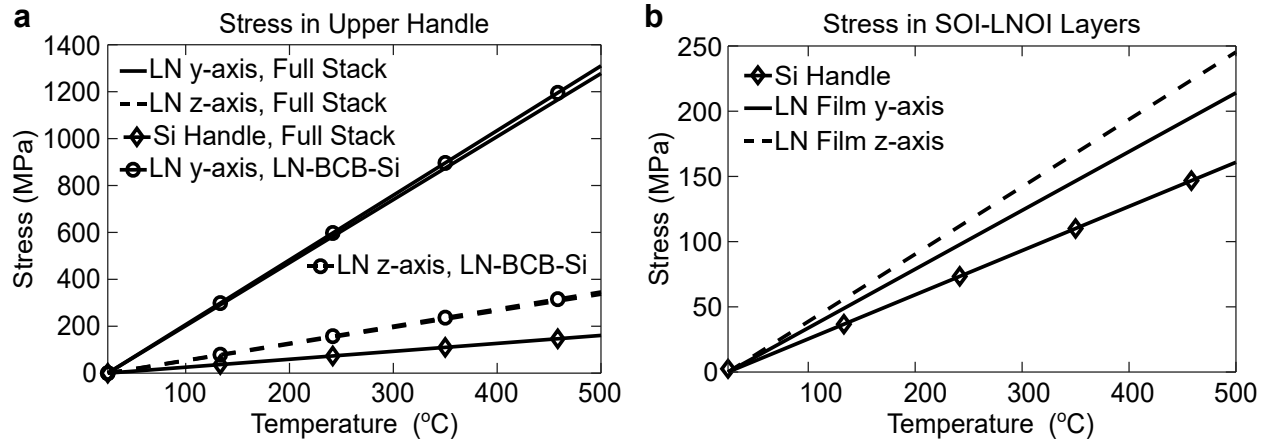


Figure 4.5: **a** Calculated maximum stresses in the upper-handle layer (LN or Si) of the complete thin-film stack and the simplified LN-BCB-Si stack shown in Fig. 4.4. Stress along each axis of the LN handle is nearly identical for the full stack and for the simplified stack, suggesting that the details of the thin films in the full stack have little bearing on the thermal stress in the upper handle layer. **b** Thermal stress in the LN film of SOI-LNOI with a Si upper handle. Si upper handle stress is also provided. z-axis LN stress is slightly higher than y-axis LN stress because the modulus of elasticity is higher for the z-axis than the y-axis of LN. The strain in the LN film is almost identical along both axes.

The numerical calculations suggest that the principal limitation in SOI-LNOI bonded stability is not the thickness of the BCB layer between the two materials as we had originally hypothesized, but, instead, whether or not the SOI handle (Si) and LNOI handle (LN or Si) are similar. To confirm this, we also studied a simpler stack, consisting of (bulk) Si and LN pieces, shown in Fig. 4.4b. Calculations shown in Fig. 4.5a nearly overlap the results of SOI-LNOI bonding along the respective LN axes, suggesting that the thermal stresses are indeed similar to the SOI-LNOI case. Experimentally, we attempted to bond a bulk piece of Si to a bulk piece of LN through a BCB layer (Fig. 4.4b), and found that the bulk LN cracked at a relatively low temperature, regardless of the BCB thickness.

A material stack of particular interest is that of Fig. 4.6. This stack consists of a bulk piece of Si coated with a relatively thin (1 μm) layer of deposited SiO_2 , bonded to a bulk piece of LN that

has been implanted to a desired depth with a certain species of ions (often either H^+ or He^+). This material stack is significant because it is the precursor to the LNOI with a Si handle that we use in this work. To go from Fig. 4.6 to a piece of LNOI, one must heat the material stack of Fig. 4.6 to at least 200°C , at which point the bulk LN splits apart at the implanted layer, leaving a thin film of LN bonded to the Si/SiO₂ substrate [46, 34]. Yet as we established above, bonding bulk Si to bulk LN and raising the temperature over 150°C results in thermally-damaged LN.

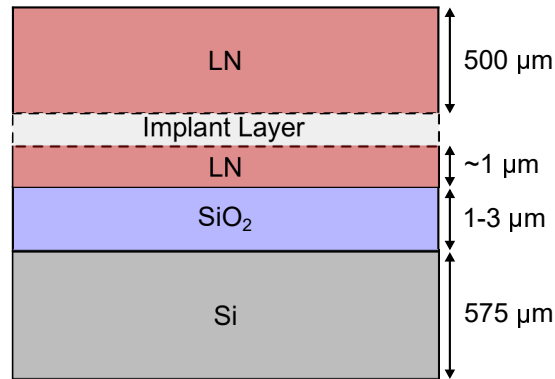


Figure 4.6: Depiction of LNOI with a Si handle, after implantation and before splitting off the bulk LN.

Here, an explanation as to why implanted bulk LN bonded to bulk Si does not crack at high temperatures is provided. The common implant species for crystal-ion slicing are H^+ and He^+ ions, which are light elements that exist as gases at room temperature. When enough of these ions are implanted into the bulk LN, they will behave as tiny pockets of gas, allowing the LN to expand and slip at that layer as temperature is increased. With rising temperature, the ions will become more energetic and eventually form a single gas bubble. At this point the LN bulk is separated from the LN film by the aggregated ions, and the LN splits [47]. Because the LN can slip and deform slightly at the implant layer, thermal stress does not build up as it would if the LN were not implanted, and the materials are left intact. The resulting LNOI can then be used for hybrid device fabrication.

The required fabrication processes hybrid SOI-LNOI devices include patterning, etching, and metalization, to name a few, which often raise (or cycle) the temperature of the stack. The benchmark studies of Takagi et al. [36] show that bulk Si-LN bonded at room temperature (without any intermediate layer) cracks around 150°C . Our results with BCB-assisted bonding show that this

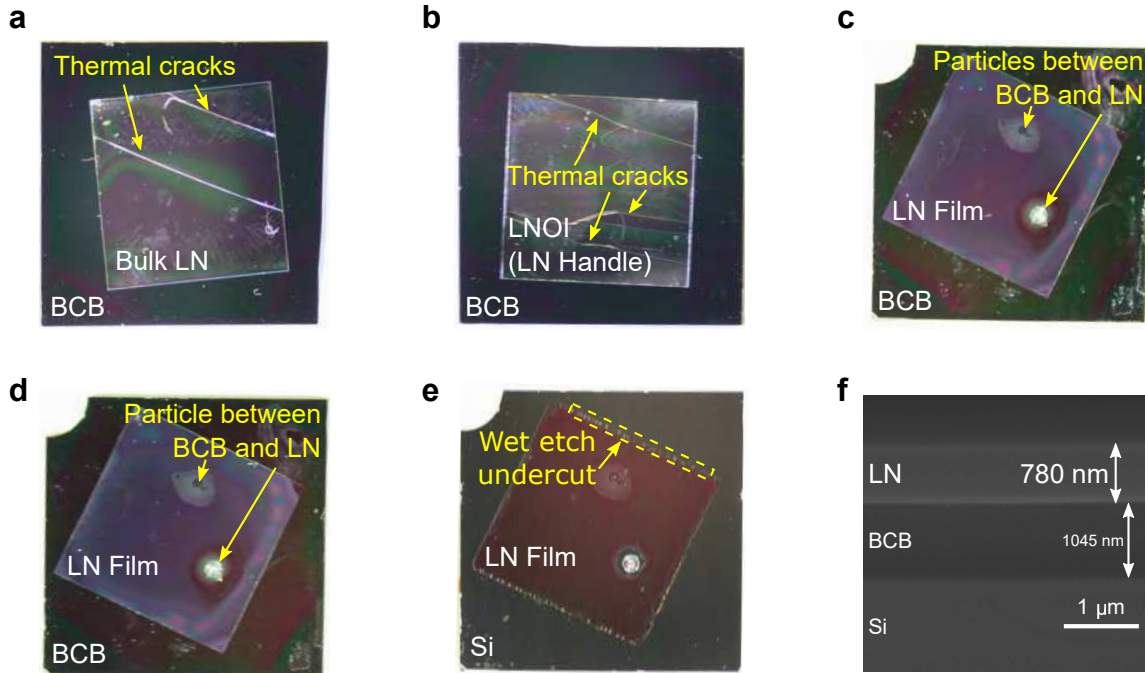


Figure 4.7: **a** through **e** show camera images of $1\text{ cm} \times 1\text{ cm}$ pieces of LN or LNOI which were bonded to bulk Si pieces of a similar size through a $1\ \mu\text{m}$ BCB layer. **a** is bulk LN, **b** is LNOI with a LN handle, and **c** through **e** are LNOI with a Si handle, which has been removed by dry-etching (note that the SiO_2 layer is still on the LN film in **c** and **d**). **c** shows the chip after substrate removal. **d** shows the same chip after 10 thermal cycles between room temperature and 300°C . **e** shows the chip after the protective SiO_2 and surrounding BCB have been removed by respective HF and Piranha acid baths. A cross-section SEM image of **e** taken at an angle of 52° from the vertical axis is presented in **f**, showing the $\sim 1\ \mu\text{m}$ thick BCB layer bonding a 780 nm thick film of LN to a bulk Si substrate.

temperature budget can be substantially exceeded. We bonded bulk Si chips to bulk LN [Fig. 4.7a], LNOI with a LN handle [Fig. 4.7b], and LNOI with a Si handle [Fig. 4.7c, handle removed]. The first two cracked in several places below 190°C , but the third did not crack during bonding or in the tested temperature range, which went up to 300°C .

The chip was further processed by extended XeF_2 dry etching to remove the Si handle from the LNOI side, i.e., the topmost layer in Fig. 4.4a. This chip therefore has a thin film of LN bonded via BCB to Si, and is accessible from the top side for further processing (e.g., poling or lithography on the LN film). Unfortunately, in our university clean room, we were not able to achieve a completely particle-free bonding process, and, despite scrupulous attempts at cleaning, a couple of dust particles were trapped beneath the LN layer, as indicated in Fig. 4.7c-e; however,

these particles did not affect the results discussed here. We cycled the chip 10 times between room temperature and 300°C without cracking, as shown by a visual comparison between Fig. 4.7c and d. Because the substrate of the chip is Si, there is no undesired pyroelectric effect during thermal cycling, as there would be with bulk LN (particularly Z-cut bulk LN).

It is conjectured that an even higher temperature budget may be achieved. Assuming that cracks first occur, in this configuration, along the y -axis (which is a reasonable assumption, since the thermal stress is much greater along the y -axis than the z -axis), our model estimates a maximum stress of approximately 340 MPa from Fig. 4.5a. Stress in the LN film of a bonded SOI-LNOI stack with an upper handle of Si is shown in Fig. 4.5b, and does not reach the failure point of 340 MPa until well over 500°C. The highest temperature our stack can withstand is thus set by the BCB layer, which has a glass transition temperature of approximately 360°C when fully cured. Experimentally, we did not exceed 300°C to avoid the BCB glass transition temperature.

The SiO₂ layer and surrounding BCB were then removed – Fig. 4.7 – for EDX (energy-dispersive x-ray) spectrum analysis. Results of the EDX measurement are shown in Fig. 4.8. BCB on bulk Si peaks primarily in the ranges of carbon and oxygen, while our BCB-bonded LN film on bulk Si (Fig. 4.7c-e) peaks in the range of oxygen, with a smaller peak at niobium. The spectrum of Si-backed LNOI (a manufacturer-provided sample with known properties [48]) is nearly identical to our BCB-bonded sample. This indicates that the LN crystal film has not deteriorated after the 300°C thermal cycling or the preceding bonding and handle removal.

Transferring LN films from one handle to another, without damaging the LN crystal, is an important accomplishment for the advancement of hybrid silicon-lithium niobate photonics, as commercially available 3-inch wafers of LNOI can be transferred to any SOI-based photonic chip to create hybrid photonic circuits. An alternative approach to developing hybrid waveguides is to ion slice small pieces of LN and place the pieces on the patterned silicon substrate for bonding [50]. The approach we have taken avoids having to handle delicate LN pieces without a supporting handle, and allows for larger area, regularly-sized (e.g., rectangular) LN films to be bonded.

Using the knowledge gained from our research into thermal stress of a bonded stack, we

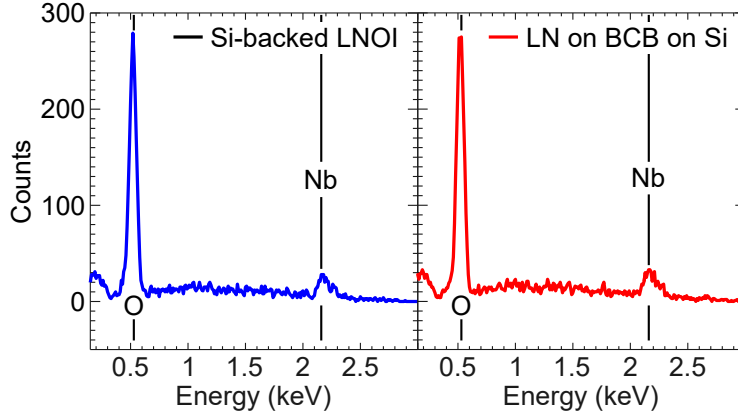


Figure 4.8: Energy-dispersive x-ray (EDX) spectrum analysis. The left plot is of a Si-backed LNOI sample from the manufacturer, and the right plot is of a LN film bonded through BCB to bulk Si. These two samples exhibit similar spectra, indicating a similarity in material properties. Oxygen and niobium spectral indicators are well known and have been documented [49].

were able to transfer a LN film to a patterned SOI chip over a significant area – in this case $4.2 \text{ mm} \times 16 \text{ mm}$ – to create a large hybrid region covering a couple dozen devices shown in Fig. 4.9a. After the film transfer and bonding, we deposited $1 \mu\text{m}$ of PECVD SiO_2 at 300°C to improve optical coupling on- and off-chip through tapered silicon waveguides. We investigated one of the devices in the bonded hybrid region of the chip – a 50/50 Y-splitter in silicon with waveguides that taper down to 320 nm from 650 nm , propagate for 5 mm , then taper up to 650 nm before recombining in a 50/50 Y-recombiner – which is shown in Fig. 4.9c. The mode transitions from the bonded region to the unbonded region (the transition into the bonded region is shown in Fig. 4.9a but not in (c)) and is followed by an S-bend comprised of two $25 \mu\text{m}$ quarter-circle bends to offset the output from the input; this prevents light from coupling directly from the input fiber into the output fiber without passing through the waveguide.

After subtracting fiber losses and fiber-to-chip coupling loss, we measured the insertion loss through this device to be 10.2 dB over a total chip length of 26 mm , comparable to the measured losses of [25]. This includes two transitions from a non-bonded silicon waveguide to a bonded Si-LN waveguide, two 50/50 Y-junctions (shown with IR imaging in Fig. 4.9d-e, taken with a Xenics XEVA-566 infrared camera through a $10\times$ Mitutoyo microscope objective), and a 5 mm hybrid propagation section, between the Y-junctions, where the silicon strip narrows down from a

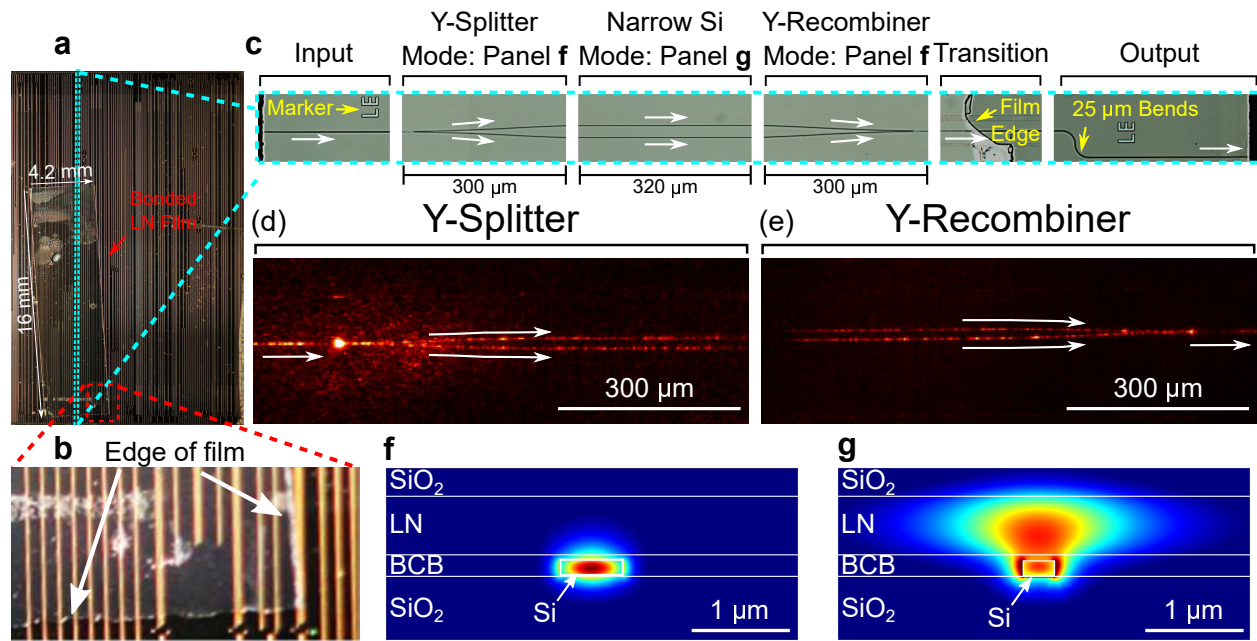


Figure 4.9: **a** The patterned SOI sample, bonded to a 4.2 mm \times 16 mm film of LN through a thin BCB layer. **b** A zoomed in image of a corner of the bonded region. **c** The specific device we measure, magnified from **a** with sections of unchanging straight waveguide removed for visual convenience. The transition out of the bonded region is shown before the output, and white arrows indicate the direction of optical propagation through the waveguide. **d** and **e** are top-down infrared images of 1550 nm light passing through the Y-splitter and Y-recombiner, respectively. These pictures were taken with a Xenics XEVA-566 infrared camera through a 10x Mitutoyo microscope objective. **f** and **g** show the simulated electric fields of the modes in the 650 nm and 320 nm wide silicon strips.

width of 650 nm to 320 nm. Simulations of the modes in the 650 nm and 320 nm wide silicon strips are shown in Fig. 4.9f and g, respectively. While these losses are higher than those seen in all-LN thin ridge structures [51], we are far from full optimization of our process.

This work shows that whereas certain types of bonded Si-LN stacks cannot be heated to elevated temperatures without damage, 1 μ m thick BCB-assisted bonding of thin films of LN on a Si handle, which matches the Si handle of the SOI chips, can withstand elevated temperatures of at least 300°C over multiple heat-and-cool cycles, allowing for further fabrication processes to be performed. We have shown that we can transfer a pre-fabricated LN film from a simple LNOI platform to a patterned SOI chip, with little to no damage to the LN film, over a sizable area, and deposit PECVD SiO₂ at 300°C without disturbing the LN film. In particular, we observe optical transmission through a hybrid Si-LN waveguide that goes through a 50/50 Y-splitter and

then a Y-recombiner, an optical structure that can be used to make electro-optic and thermo-optic chip-scale devices. This is promising for the continued development of hybrid Si-LN technologies with thin crystalline device layers.

4.6 Handle Removal

In order to fabricate a full hybrid Si-LN electro-optic modulator, further processing is required after bonding and annealing. As alluded to in Section 4.5, the LN film's handle must be removed in order to fabricate electrodes close enough to the LN film for any observable electro-optic effect to occur. The general process flow is shown in Fig. 4.10.

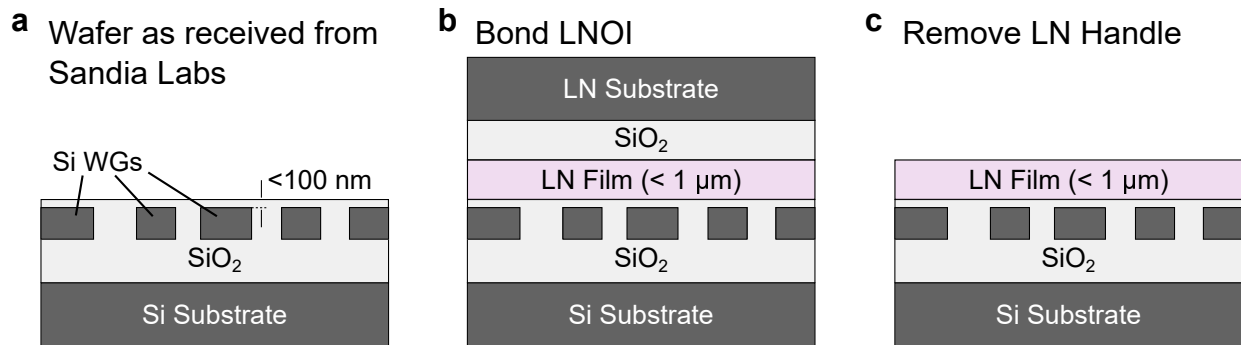


Figure 4.10: **a** Wafer cross-section as received from Sandia National Laboratories, as depicted in Fig. 4.2f. **b** Bond the LN-on-insulator (LNOI) die (from a NanoLN wafer) to an SOI die, singulated from the Sandia wafer. **c** Remove the handle (SiO₂ and substrate) from the LN film after bonding.

Wafer handle removal has become more commonplace over the last decade or so, thanks in large part to the the microelectromechanical systems (MEMS) community. Due to this recent interest in wafer handle removal and wafer-scale thin film transfer, some manufacturers have begun to offer temporary bonding agents specifically designed to transfer thin films from one handle to another. In this work, an adhesive called BrewerBond 220 (BB220) was purchased from BrewerScience, Inc. BB220 has the consistency of liquid wax, and can be spin coated onto a sample before curing and temporary bonding. Also, like wax bonding, BB220 can be cooled to room temperature to harden after an initial cure, and then softened again at higher temperatures to slide debond the transferred

film from its original substrate.

However, the most important aspect of BB220 in this work is its ability to withstand hydrofluoric (HF) wet etching and XeF₂ dry etching. To remove the LN handle, which was chosen to be Si for its reduced thermal mismatch and easy removal (Section 4.5) a LNOI die was bonded to an SOI die. Next, the sample was coated with BB220 everywhere except the Si backside of the LNOI, which was removed with a deep XeF₂ etch in a Xactic isotropic etcher. This was followed by an HF etch to remove the 2 μm SiO₂ layer between the LN and the Si handle. Finally, the BB220 was removed in a toluene-based solvent. At this stage in the fabrication process, the sample was ready for electrode fabrication.

4.7 Metallization

The metallization process was performed after handle removal as the final step in the fabrication process of the hybrid Si-LN EOM. First, a seed layer of 5 nm Cr and 60 nm Au was deposited in an e-beam evaporator. After seed layer deposition, a thick 10 μm positive photoresist was spin coated onto the sample and lithographically etched to expose metal where the electrical lines were needed, as well as an open rectangle at the edge of the sample.

To form the electrical lines, the exposed sample was electroplated in a homemade non-cyanide gold electroplating bath. The sample was clipped into place on the exposed rectangle at the edge of the chip; potential current density concerns were mitigated by the flat Au seed layer across the entire sample below the photoresist. Despite the homemade electroplating setup, relatively repeatable electroplating results were possible by carefully monitoring the electroplating bath temperature, homogeneity, current, time, and electrode thickness during electroplating. Currents between 3 mA and 10 mA were used during device fabrication.

Afterwards, the photoresist was removed in acetone and the Cr/Au seed layer components were removed in their respective wet etchants.

4.8 Acknowledgments

Section 4.5 of Chapter 4, in full, is a reprint of the material as it appears in Optical Materials 2017. Peter O. Weigel & Shayan Mookherjea, Optical Materials Vol. 66, 605-610 and in Conference on Lasers and Electro-Optics (CLEO) 2017. Peter O. Weigel and Shayan Mookherjea, paper. SM3K.1. The dissertation author, together with his adviser, led the research efforts for this work and co-authored the papers.

Bibliography

- [1] Michel Bruel. Process for the production of thin semiconductor material films, December 20 1994. US Patent 5,374,564.
- [2] M Levy, RM Osgood Jr, R Liu, LE Cross, GS Cargill III, A Kumar, and H Bakhru. Fabrication of single-crystal lithium niobate films by crystal ion slicing. *Applied Physics Letters*, 73(16):2293–2295, 1998.
- [3] AM Radojevic, M Levy, H Kwak, and RM Osgood Jr. Strong nonlinear optical response in epitaxial liftoff single-crystal linbo 3 films. *Applied physics letters*, 75(19):2888–2890, 1999.
- [4] Tarek A Ramadan, M Levy, and RM Osgood Jr. Electro-optic modulation in crystal-ion-sliced z-cut linbo 3 thin films. *Applied Physics Letters*, 76(11):1407–1409, 2000.
- [5] T Izuhara, I-L Gheorma, RM Osgood Jr, AN Roy, H Bakhru, Yiheli M Tesfu, and ME Reeves. Single-crystal barium titanate thin films by ion slicing. *Applied physics letters*, 82(4):616–618, 2003.
- [6] Lionel C Kimerling. Silicon microphotonics. *Applied Surface Science*, 159:8–13, 2000.
- [7] Qianfan Xu, Bradley Schmidt, Sameer Pradhan, and Michal Lipson. Micrometre-scale silicon electro-optic modulator. *nature*, 435(7040):325, 2005.
- [8] Ryan Aguinaldo, Alex Forencich, Christopher DeRose, Anthony Lentine, Douglas C Trotter, Yeshaiahu Fainman, George Porter, George Papen, and Shayan Mookherjea. Wideband silicon-photonics thermo-optic switch in a wavelength-division multiplexed ring network. *Optics express*, 22(7):8205–8218, 2014.
- [9] JDB Bradley, PE Jessop, and AP Knights. Silicon waveguide-integrated optical power monitor with enhanced sensitivity at 1550 nm. *Applied Physics Letters*, 86(24):241103, 2005.
- [10] M Lawrence. Lithium niobate integrated optics. *Reports on Progress in Physics*, 56(3):363, 1993.

- [11] ScienceDaily. Now entering, lithium niobate valley: Reserachers demonstrate high-quality optical microstructures using lithium niobate. Online. www.sciencedaily.com/releases/2017/12/171221133650.htm.
- [12] Thomas Plach, K Hingerl, S Tollabimazraehno, G Hesser, V Dragoi, and M Wimplinger. Mechanisms for room temperature direct wafer bonding. *Journal of Applied Physics*, 113(9):094905, 2013.
- [13] Marin Alexe and Ulrich Gösele. *Wafer bonding: applications and technology*. Springer Science & Business Media, 2004.
- [14] Frank Niklaus, Göran Stemme, J-Q Lu, and RJ Gutmann. Adhesive wafer bonding. *Journal of applied physics*, 99(3):2, 2006.
- [15] Shahram Keyvaninia, Muhammad Muneeb, Stevan Stanković, PJ Van Veldhoven, Dries Van Thourhout, and Günther Roelkens. Ultra-thin dvs-bcb adhesive bonding of iii-v wafers, dies and multiple dies to a patterned silicon-on-insulator substrate. *Optical Materials Express*, 3(1):35–46, 2013.
- [16] Hideki Takagi, Ryutaro Maeda, Naoe Hosoda, and Tadatomo Suga. Room-temperature bonding of lithium niobate and silicon wafers by argon-beam surface activation. *Applied physics letters*, 74(16):2387–2389, 1999.
- [17] Stephan Krapick, Benjamin Brecht, Harald Herrmann, Viktor Quiring, and Christine Silberhorn. On-chip generation of photon-triplet states. *Optics express*, 24(3):2836–2849, 2016.
- [18] F Thomas, S Heidmann, M De Mengin, N Courjal, G Ulliac, A Morand, P Benech, E Le Coarer, and G Martin. First results in near and mid ir lithium niobate-based integrated optics interferometer based on swifts-lippmann concept. *Journal of Lightwave Technology*, 32(22):3736–3742, 2014.
- [19] Ian W Frank, Jeremy Moore, James K Douglas, Ryan Camacho, and Matt Eichenfield. Entangled photon generation in lithium niobate microdisk resonators through spontaneous parametric down conversion. In *Lasers and Electro-Optics (CLEO), 2016 Conference on*, pages 1–2. IEEE, 2016.
- [20] Abu Thomas, Mackenzie A VanCamp, Andrew Fraine, and Alexander V Sergienko. Low-noise quantum frequency conversion in titanium-diffused lithium niobate waveguide. In *Frontiers in Optics*, pages FTh1D–4. Optical Society of America, 2015.
- [21] MMR Howlader, T Suga, and MJ Kim. Room temperature bonding of silicon and lithium niobate. *Applied physics letters*, 89(3):031914, 2006.
- [22] Yoo Seung Lee, Gun-Duk Kim, Woo-Ju Kim, Sang-Shin Lee, Wan-Gyu Lee, and William H Steier. Hybrid si-linbo 3 microring electro-optically tunable resonators for active photonic devices. *Optics letters*, 36(7):1119–1121, 2011.

- [23] Idan Bakish, Ran Califa, Tali Ilovitsh, Vlada Artel, Georg Winzer, Karsten Voigt, Lars Zimmermann, Eyal Shekel, Chaim Sukenik, and Avi Zadok. Voltage-induced phase shift in a hybrid linbo₃-on-silicon mach-zehnder interferometer. In *Integrated Photonics Research, Silicon and Nanophotonics*, pages IW4A–2. Optical Society of America, 2013.
- [24] Li Chen, Qiang Xu, Michael G Wood, and Ronald M Reano. Hybrid silicon and lithium niobate electro-optical ring modulator. *Optica*, 1(2):112–118, 2014.
- [25] Peter O Weigel, Marc Savanier, Christopher T DeRose, Andrew T Pomerene, Andrew L Starbuck, Anthony L Lentine, Vincent Stenger, and Shayan Mookherjea. Lightwave circuits in lithium niobate through hybrid waveguides with silicon photonics. *Scientific reports*, 6:22301, 2016.
- [26] W Qiu, M-P Bernal, A Ndao, C Guyot, NM Hameed, N Courjal, H Maillotte, and FI Baida. Analysis of ultra-compact waveguide modes in thin film lithium niobate. *Applied Physics B*, 118(2):261–267, 2015.
- [27] Martin F Volk, Sergiy Suntsov, Christian E Rüter, and Detlef Kip. Low loss ridge waveguides in lithium niobate thin films by optical grade diamond blade dicing. *Optics express*, 24(2):1386–1391, 2016.
- [28] Günther Roelkens, Dries Van Thourhout, and Roel Baets. Ultra-thin benzocyclobutene bonding of iii-v dies onto soi substrate. *Electronics Letters*, 41(9):561–562, 2005.
- [29] Alexander W Fang, Hyundai Park, Oded Cohen, Richard Jones, Mario J Paniccia, and John E Bowers. Electrically pumped hybrid alginas-silicon evanescent laser. *Optics express*, 14(20):9203–9210, 2006.
- [30] J Almerico, S Ross, P Werbaneth, J Yang, and P Garrou. Plasma etching of thick bcb polymer films for flip chip bonding of hybrid compound semiconductor-silicon devices. *Tegal Crop*, 2001.
- [31] Cheng-Ta Ko and Kuan-Neng Chen. Wafer-level bonding/stacking technology for 3d integration. *Microelectronics reliability*, 50(4):481–488, 2010.
- [32] JJ McMahon, E Chan, SH Lee, RJ Gutmann, and J-Q Lu. Bonding interfaces in wafer-level metal/adhesive bonded 3d integration. In *Electronic Components and Technology Conference, 2008. ECTC 2008. 58th*, pages 871–878. IEEE, 2008.
- [33] Jong-Gul Yoon and Kun Kim. Growth of highly textured linbo₃ thin film on si with mgo buffer layer through the sol-gel process. *Applied physics letters*, 68(18):2523–2525, 1996.
- [34] Payam Rabiei, Jichi Ma, Saeed Khan, Jeff Chiles, and Sasan Fathpour. Heterogeneous lithium niobate photonics on silicon substrates. *Optics express*, 21(21):25573–25581, 2013.
- [35] Shuang Li, Lutong Cai, Yiwen Wang, Yunpeng Jiang, and Hui Hu. Waveguides consisting of single-crystal lithium niobate thin film and oxidized titanium stripe. *Optics express*, 23(19):24212–24219, 2015.

- [36] Hideki Takagi, Ryutaro Maeda, and Tadatomo Suga. Room-temperature wafer bonding of Si to LiNbO₃, LiTaO₃ and Ga₂O₃ by Ar-beam surface activation. *Journal of Micromechanics and Microengineering*, 11(4):348, 2001.
- [37] Stephen Timoshenko. Analysis of bi-metal thermostats. *JOSA*, 11(3):233–255, 1925.
- [38] Matthew A Hopcroft, William D Nix, and Thomas W Kenny. What is the young's modulus of silicon? *Journal of microelectromechanical systems*, 19(2):229–238, 2010.
- [39] CA Swenson. Recommended values for the thermal expansivity of silicon from 0 to 1000 K. *Journal of physical and chemical reference data*, 12(2):179–182, 1983.
- [40] RS Weis and TK Gaylord. Lithium niobate: summary of physical properties and crystal structure. *Applied Physics A*, 37(4):191–203, 1985.
- [41] Allan F Bower. *Applied mechanics of solids*. CRC press, 2009.
- [42] F Pignatiello, M De Rosa, P Ferraro, S Grilli, P De Natale, A Arie, and S De Nicola. Measurement of the thermal expansion coefficients of ferroelectric crystals by a moiré interferometer. *Optics Communications*, 277(1):14–18, 2007.
- [43] Jie-Hua Zhao, Todd Ryan, Paul S Ho, Andrew J McKerrow, and Wei-Yan Shih. Measurement of elastic modulus, poisson ratio, and coefficient of thermal expansion of on-wafer submicron films. *Journal of applied physics*, 85(9):6421–6424, 1999.
- [44] AJG Strandjord, RH Heistand, JN Bremmer, PE Garrou, and TG Tessier. A photosensitive-bcb on laminate technology (mcm-1d). In *Electronic Components and Technology Conference, 1994. Proceedings., 44th*, pages 374–386. IEEE, 1994.
- [45] Michael E Mills, Paul Townsend, Dan Castillo, Steve Martin, and Albert Achen. Benzocyclobutene (dvs-bcb) polymer as an interlayer dielectric (ild) material. *Microelectronic Engineering*, 33(1-4):327–334, 1997.
- [46] Gorazd Poberaj, Hui Hu, Wolfgang Sohler, and Peter Guenter. Lithium niobate on insulator (InOI) for micro-phonic devices. *Laser & photonics reviews*, 6(4):488–503, 2012.
- [47] B Aspar, H Moriceau, E Jalaguier, C Lagahe, A Soubie, B Biasse, AM Papon, A Claverie, J Grisolia, G Benassayag, et al. The generic nature of the smart-cut® process for thin film transfer. *Journal of Electronic Materials*, 30(7):834–840, 2001.
- [48] Lutong Cai, Yun Kang, and Hui Hu. Electric-optical property of the proton exchanged phase modulator in single-crystal lithium niobate thin film. *Optics express*, 24(5):4640–4647, 2016.
- [49] Jill Chastain, Roger C King, and J Moulder. *Handbook of X-ray photoelectron spectroscopy: a reference book of standard spectra for identification and interpretation of XPS data*. Physical Electronics Division, Perkin-Elmer Corporation Eden Prairie, Minnesota, 1992.
- [50] Li Chen, Jonathan Nagy, and Ronald M Reano. Patterned ion-sliced lithium niobate for hybrid photonic integration on silicon. *Optical Materials Express*, 6(7):2460–2467, 2016.

- [51] Arnaud Gerthoffer, Clément Guyot, Wentao Qiu, Abdoulaye Ndao, Maria-Pilar Bernal, and Nadège Courjal. Strong reduction of propagation losses in linbo3 ridge waveguides. *Optical Materials*, 38:37–41, 2014.

Chapter 5

All-Optical Hybrid Silicon-Lithium Niobate Devices

5.1 Introduction

Lithium Niobate (LN) was once considered the most promising of materials for integrated optics [1], but despite a rich set of properties, the technology of LN integrated optics has not evolved as much as integrated optics in III-V semiconductors and silicon (Si) photonics [2, 3]. Although high performance stand-alone LN devices have been shown [4, 5] and a technique of ion-sliced thin-film LN has been developed [6, 7, 8], the technology of LN integrated optics has continued to rely on traditional waveguide fabrication techniques based on ion-exchange [9], diffusion and serial writing [10] or mechanical sawing [11, 12], all of which are very different from the modern lithographic techniques and foundry processing available in Si or III-V photonics.

To address this problem, we develop an approach to developing hybrid waveguides in LN based on a two-material core cross-section, consisting of few-hundred nanometer single-crystal thin films of Si and LN bonded face-to-face. We used manufacturer-provided Si-on-insulator and LN-on-insulator wafers which have a SiO₂ cladding layer which is a few microns thick, and a handle material (Si and LN, respectively) for the substrate which is several hundred microns thick.

We first pattern all features required for waveguiding in the Si wafer using deep ultraviolet (DUV) lithography (see Methods section). This allows much finer features to be patterned than is possible in LN (which has previously constrained LN waveguides to be multi-moded [13]). Since LN is not a CMOS-compatible material and is not processed in CMOS foundries, we developed designs which allow all the waveguiding circuitry to be defined in Si, requiring only a single back-end process step of bonding LN to form the functional chip. DUV lithographic fabrication of Si photonic features is more precise, scalable and manufacturable than the traditional waveguide-fabrication techniques in LN, and the LN layer can be left as an unpatterned slab that is then bonded to the patterned Si [14]. By not patterning, etching or sawing LN, its material properties are kept pristine [15].

Fig. 5.1 shows images of a bonded chip whose dimensions are that of a typical field size of a stepper projection DUV lithography system (few centimeters squared). Upon bonding, a hybrid waveguide is formed, in which the geometric dimensions of the Si features and LN film dictate how the optical mode is distributed between the Si and LN layers. Techniques have been developed in the past decade for bonding LN of various orientations to Si wafers without incurring thermal stress mismatches [16, 17, 18, 19, 20, 21]. Bonding achieves much higher quality and better optical properties than growth of LN on Si using sol-gel processes [22] or chemical vapor deposition [23]. We directly bonded the LN chip to the Si chip i.e., without any intervening polymeric ‘glue’ layer as used in some approaches [13, 24], thus permitting the maximum control over the mode distribution.

As will be discussed below, light propagates mainly in the silicon layer in certain sections of the layout, and primarily in the LN layer where desired, and makes transitions between the two layers at several locations while remaining in the transverse-electric (TE) polarized single-mode regime, which is highly desirable for Si photonics. Thus, we can also design devices that are outside the Si-LN bonded region and behave entirely like conventional Si photonics. In this way, the technology for Si photonics can be leveraged to enhance LN integrated optics, and vice versa.

The main advantages of this approach are: (a) the requirements on LN fabrication are reduced to a minimum, i.e., a single bonding step to the manufacturer-supplied wafer after all silicon patterning has been completed (etching LN is possible [25, 26] but is technologically less mature

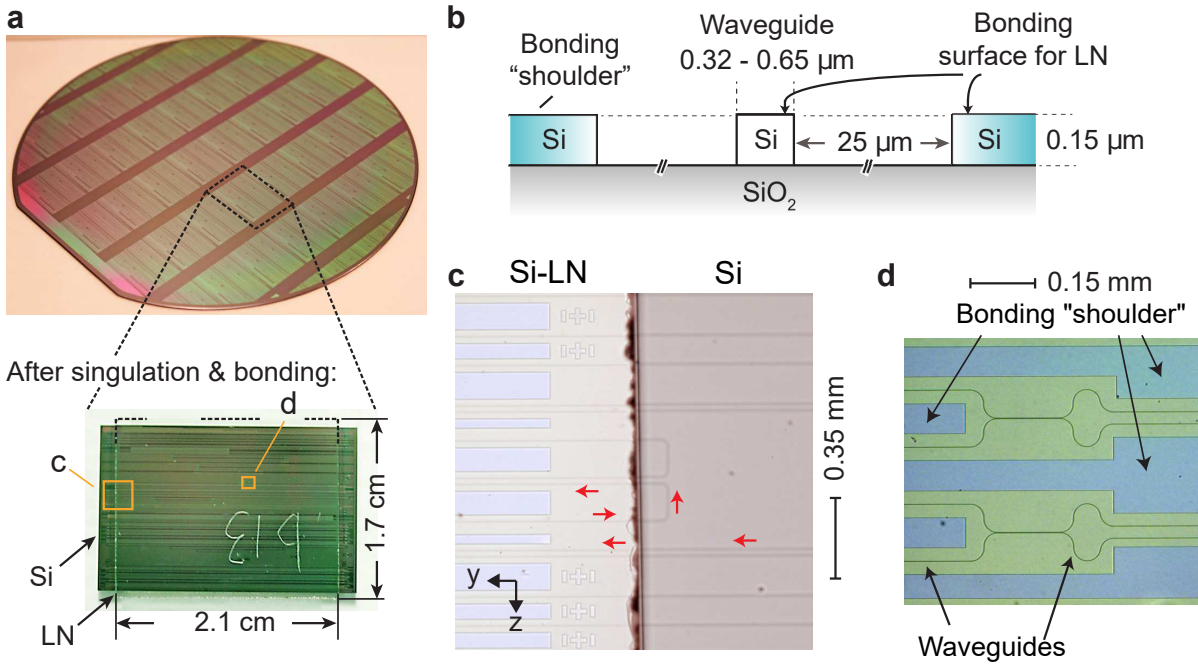


Figure 5.1: Hybrid LN-Si photonic circuits. **a** Silicon photonic components were fabricated using deep ultraviolet (DUV) lithography. Singulated dies (size: 25 mm × 16 mm) were bonded to diced pieces (size: 21 mm × 17 mm) of an unpatterned Lithium Niobate (LN)-on-insulator wafer. This particular LN chip was labeled ‘b13’ by scratch marks on the LN substrate (0.5 mm thick, opposite to the bonded surface). **b** Schematic of the cross-section showing how waveguides and bonding “shoulders,” which are at the same height as the waveguides, are conveniently formed in one lithographic etch step on the Si wafer. **c** Optical microscope image showing waveguides transitioning between the portion of the hybrid chip which is not covered by LN (i.e., conventional SiO₂-clad Si photonic waveguides), and that which is bonded to LN (and uses hybrid waveguides). Arrows colored red indicate the back-and-forth direction of light propagation in certain representative sections. **d** Optical components can be defined in the SiO₂-clad Si section, or in the LN-Si bonded section.

than etching Si, which is available in every foundry process); and (b) both the cross-sectional mode area and the length of components are greatly reduced, compared to traditional LN ion-exchanged or diffused waveguides, allowing complex circuits to be realized in a small area. The tradeoffs are that: (a) the bonding step should be performed at a low temperature since Si and LN have different coefficients of thermal expansion, and (b) the resulting hybrid modes have a higher refractive index dispersion compared to low-index contrast (e.g., doped-glass) integrated optics, and thus, components will be optimized for a desired vacuum wavelength range, e.g., the telecommunications band around 1550 nm.

5.2 Hybrid Modes and Mode-Transition Tapers

The dimensions of the Si features and LN film determine what fraction of the optical mode resides in Si and in LN. Two distinct waveguide cross-sections, labeled ‘A’ and ‘B’, are selected, as shown in Fig. 5.2a, and used in the microchip layout. These cross-sections vary only in the width of the Si structures, which allows for convenient fabrication in a single step of lithography. The numerical values of the widths and heights chosen here are suitable for wavelengths between 1530 nm and 1565 nm (i.e., the telecommunications C-band).

Cross-section A consists of 650 nm wide and 150 nm tall Si features, bonded to LN. The lowest-order mode of the waveguide is quasi-TE-polarized and is similar to the quasi-TE₀ mode in conventional silicon photonics (see Fig. 5.2a). Wider waveguides are close to becoming multimoded, which is undesirable. A waveguide using cross-section A can transition from an SiO₂-clad silicon photonic section to the bonded Si-LN region, as shown in Fig. 5.1c, with less than -0.3 dB loss calculated by numerical simulation (Lumerical software package). We have not experimentally confirmed the mode-transition loss at this time. As shown by Fig. 5.2b, waveguides using cross-section A can support compact bends with radii of 3-5 μm without incurring bending losses higher than that of a standard rib waveguide (650 nm \times 220 nm surrounded by SiO₂, labeled ‘Si/SiO₂’ in Fig. 5.2b) with a radius of 0.5-1 μm .

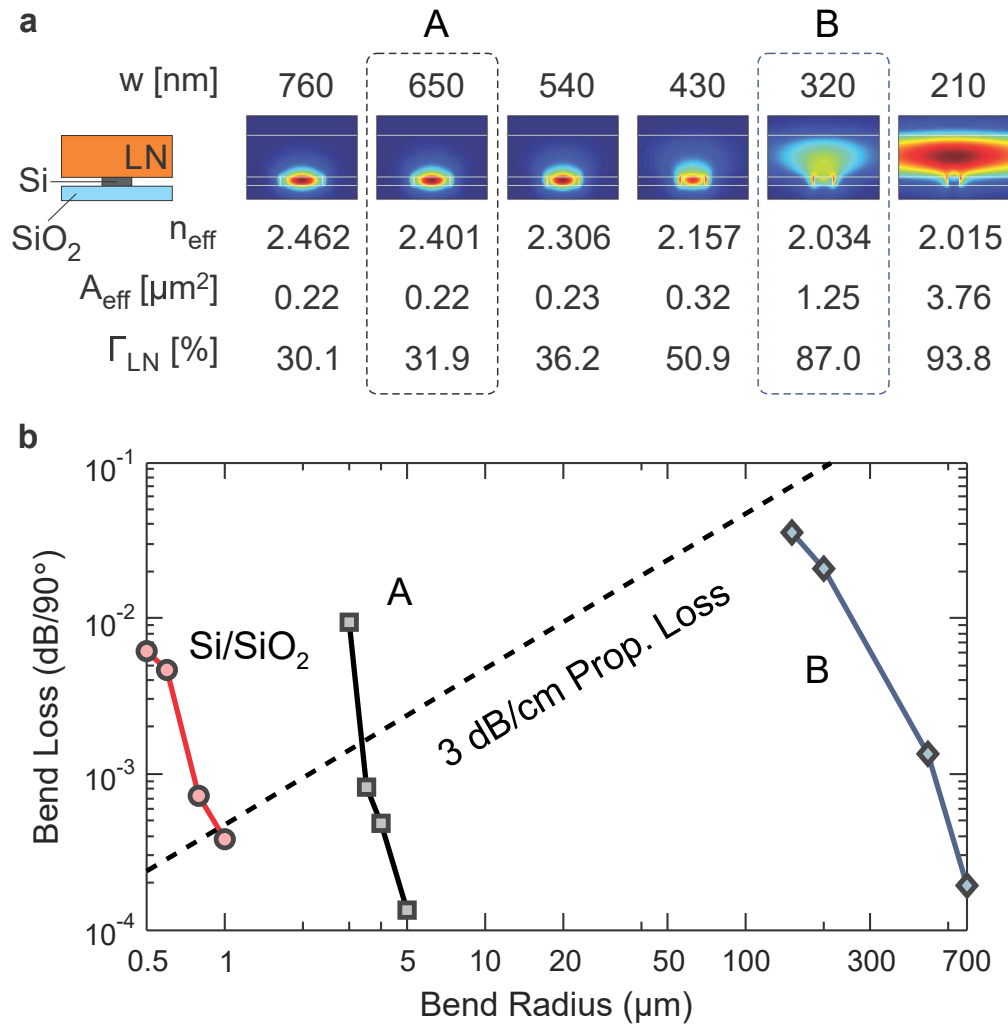


Figure 5.2: Waveguide modes. **a** Calculated hybrid optical mode profiles for different Si rib widths. The panels show the magnitude of the electric field in the TE polarization, with the E-field vector oriented along the crystal axis. As the Si rib width w decreases, the modal effective index (n_{eff}) decreases, the effective area (A_{eff}) increases, and the fraction of light in LN (Γ_{LN}) also increases. The dotted boxes indicate the two cross-sectional designs ('A' and 'B') used in the chip. **b** The calculated bending loss of the 'A' cross-sectional mode is much lower than that of the 'B' mode, and is not too different from the waveguides used in silicon photonics (labeled as 'Si/SiO₂'). Therefore, 'A' is used for bends and compact routing, and 'B' is used in straight waveguide sections when most of the light should "see" LN. The dashed line labeled '3 dB/cm Prop. Loss' represents the propagation loss at all bend radii for a propagation loss of 3 dB/cm to give an idea of practical minimum losses for bent waveguides.

Cross-section B consists of 320 nm wide Si features at the same height as cross-section A. With an air upper cladding, this waveguide is unable to support a waveguide mode by itself, and thus requires the bonded LN layer to support a well-defined mode at C-band wavelengths. Cross-section B cannot be used for compact low-loss bends (see Fig. 5.2b). Instead, it is used when we want the light to interact with the crystal properties of LN; otherwise, cross-section A is used to route light on the hybrid chip. Therefore, it is desirable to maximize the fraction of light in LN for the mode in cross-section B. The confinement factor is defined as follows: $\Gamma_{\text{LN}} = \text{Re}[\iint_{\text{LN}}(\mathbf{E} \times \mathbf{H}^* \cdot \hat{y}) dA'] / \text{Re}[\iint(\mathbf{E} \times \mathbf{H}^* \cdot \hat{y}) dA]$, where \hat{y} is the direction of light propagation and the range of integration in the integral in the numerator is restricted to the LN region. In waveguides using cross-section A, $\Gamma_{\text{LN}} \approx 32\%$ whereas in waveguides using cross-section B, $\Gamma_{\text{LN}} \approx 87\%$. The transition between the two cross-sections is discussed below.

A modified version of cross-section A, in which SiO_2 replaces LN as the upper cladding, is used outside the LN bonded region to demonstrate all-Si components made on the same platform and at the same device level. Another cross-section with a reduced Si width of 180 nm is used for couplers at the edge of the Si chip, as is commonly used in Si photonics [27], and can also be fabricated in the same step.

All these waveguide shapes are simple rectangles without relying on slots, tilted sidewalls or other difficult-to-fabricate shapes. There is no patterning in the LN layer which eliminates many of the challenges faced in the past [13]. Conceptually, the waveguide structure is similar to that of the strip-loaded waveguide film studied in the 1970's [28], but scaled to the sub-micron regime. The modal area of cross-section A ($0.22 \mu\text{m}^2$) is, in fact, smaller, and that of cross-section B ($1.25 \mu\text{m}^2$) is only slightly larger, than those of the smallest-area waveguides reported in LN, fabricated by the ion-milling technique [29].

As shown in Fig. 5.1d, large rectangular areas were defined in the Si device layer at distances of about $30 \mu\text{m}$ from the waveguide edge. These “bonding pads” between the Si and LN chips are far from the waveguide core and serve no optical purpose, but instead provide a large surface area for bonding. They are precisely at the same height as the Si rib features, since they are

formed in the same lithographic step. They are similar to “dummy fill” features inserted to assist in chemical-mechanical polishing, but without a fragmented pattern. The etched trenches between the Si ribs and the bonding pads not only provide optical confinement but may assist in bonding by defining convenient outgassing channels, and for local stress relaxation.

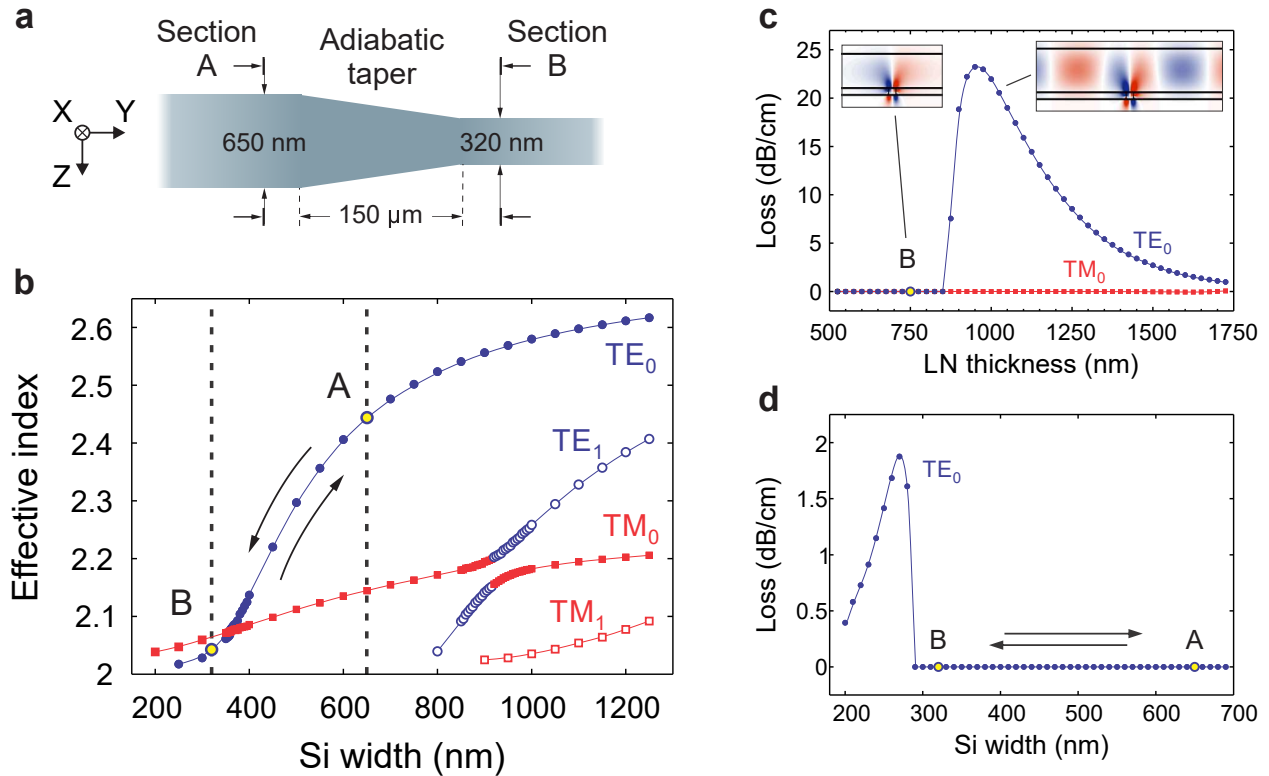


Figure 5.3: Adiabatic mode transition. **a** Gradual linear reduction of the Si rib width to transition between cross-sections A and B. **b** Numerical calculations of the modal effective index versus waveguide width, with yellow circles indicating the initial and final points of the taper. The TE-polarized mode does not hybridize with, or convert into, the TM-polarized mode in the taper. **c** Plot of simulated propagation losses for cross-section B with a varying LN film thickness. (Inset: E_x component of the fundamental TE₀ mode, (left) bound for cross-section B, i.e., 750 nm LN; and (right) leaky for 1000 nm thick LN.) The losses decrease as the mode approaches a TE slab mode. **d** Plot of simulated propagation losses for our hybrid geometry (150 nm tall Si, 750 nm thick LN) with a varying Si width. Similar to **c**, losses increase suddenly when the x-component of the E-field is no longer confined, and then decrease as the mode approaches a TE slab mode.

Along the direction of light propagation, adiabatic tapered transitions were defined in the Si layer (see Fig. 5.3a) as a linear change in the Si rib width over a distance of 150 μm. The quasi-TE-polarized mode TE₀ has the highest effective refractive index in cross-section A (and is used extensively in conventional Si photonic waveguides, which are wider than they are tall [30]).

In cross-section B, it is actually the quasi-TM-polarized mode TM_0 which has the higher refractive index. This is due to both the anisotropic properties of LN (LN has a lower material index along the z-axis) and the low index lateral air cladding on either side of the Si. However, the taper-induced coupling between these modes is zero to first order because the electric field of the former is a symmetric mode, and that of the latter is an anti-symmetric mode [31]. Thus, we are able to draw the waveguide down to a narrow width that pushes a very large fraction of the light into LN while maintaining its state of polarization all the way from the feeder waveguides. For the Si rib widths used in this design, the higher-order quasi-TE polarized mode (labeled TE_1 in Fig. 5.3b) is not guided; however, by using wider Si rib widths, tapers can couple between this anti-symmetric mode and the TM_0 mode, which may be useful for polarization rotators etc. Thus, compared to other hybrid Si-LN structures [26, 20, 32], our design achieves the highest TE-polarized (lowest-order) mode-fraction in LN while also providing a pathway for integration to Si photonics by first coupling light into cross-section A (which is similar to a traditional Si photonics cross-section), and then transitioning into cross-section B adiabatically. Attempting to couple from an external input to the quasi-TE mode in cross-section B would render the device very susceptible to roughness and bending losses, because it is not the fundamental mode. Widening the Si waveguide effectively pulls the light back into Si again, and, because it remains in the TE-polarization, allows for the benefits that have been realized by Si-only waveguides, such as tight bends and compact directional couplers, among others.

Another important consideration is that the propagation loss of a hybrid mode can increase significantly due to lack of transverse confinement, if the LN thickness falls within a range of values, depending upon the Si rib dimensions, at which one of the vectorial field components becomes slab-like (in the LN region). This effect, studied and measured in standard rib waveguides [33], has recently been highlighted for quasi-TE modes in x-cut LN proton exchanged channel waveguides [34]. Similarly, in our configuration, it originates from the $TE \leftrightarrow TM$ mode coupling at the Si strip boundaries. Quasi-TE mode leakage then occurs when the modal effective index becomes smaller than that of the TM slab mode in LN, i.e., when the minor TM-polarized field is no longer a bound

mode and propagates in the LN planar waveguide. Due to the LN birefringence, this condition cannot be met for the quasi-TM modes which is therefore immune to leakage. This is shown in Fig. 5.3c: for LN thicknesses between 850 nm and 1750 nm (not used in our present design), the propagation loss would be significantly higher than at other thicknesses. A similar behavior is observed when the width of the Si region is reduced and the LN thickness is fixed, as in Fig. 5.3d.

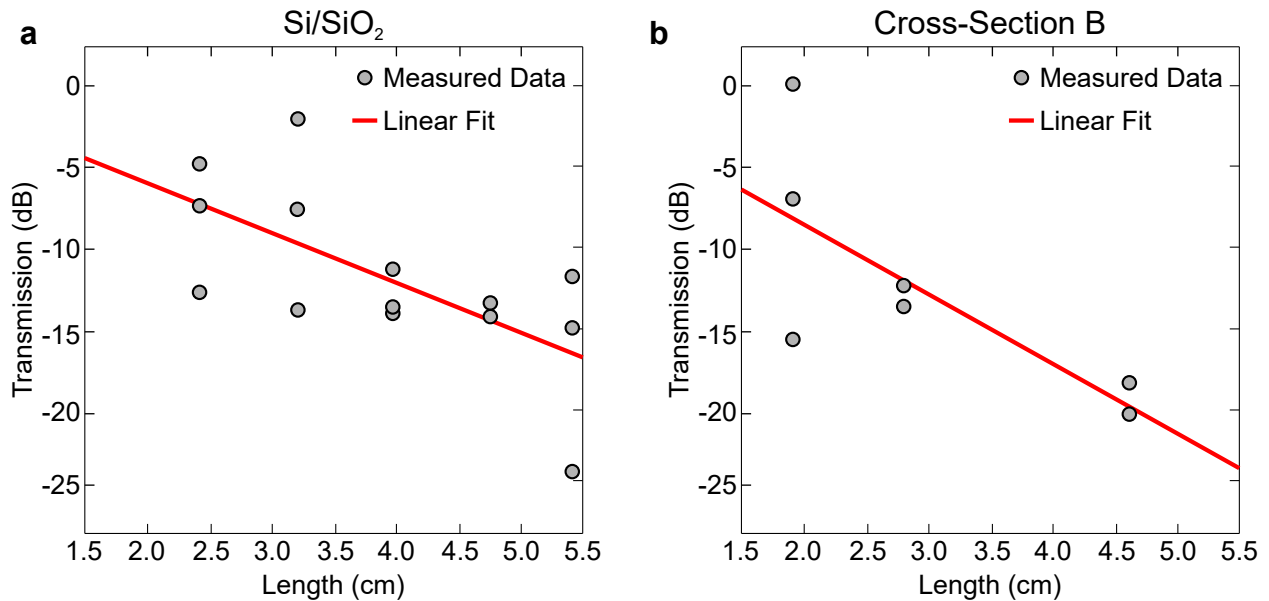


Figure 5.4: Waveguide characterization. **a** Transmission measurements of test structures consisting of 650 nm wide Si waveguides with SiO₂ cladding (labeled ‘Si/SiO₂’). **b** Transmission versus length of waveguides and bends (paper-clip structures) at the wavelength of 1.55 μm for mode cross-section ‘B’ in the straight sections and cross-section ‘A’ in the semi-circular bends (labeled ‘Cross-section B’). In both **a** and **b**, the numerical fit is shown by the solid lines. The y-axes are normalized to be 0 dB for 0 cm length waveguides.

5.3 Waveguides, Directional Couplers and Photonic Circuits

Photonic circuits can be assembled from the basic building blocks of waveguides and directional couplers. Hybrid waveguides of lengths between 1.8 cm and 4.6 cm were fabricated with the majority of the length consisting of waveguides using cross-section B. Cross-section A was used at the semi-circular bends, in order to fit the longer waveguides into a compact footprint using “paperclip” structures. The longest waveguide involves 10 transitions between cross-sections A and

B. Since the edge facets were roughly diced and not polished, the fiber-to-chip insertion loss was high (about 9.5 dB without index-matching liquid) and non-uniform. As shown in Fig. 5.4b, by measuring transmission versus length across several chips, we were able to build up an ensemble of measurements from which a propagation loss of 4.3 ± 2.1 dB/cm was extracted at 1550 nm wavelength with only minor changes across the wavelength range 1530 nm to 1570 nm. At this time, we are unable to separate the bending loss from the straight waveguide propagation loss, but the former is expected to be very small based on the large bending radius of 25 μm . Numerical simulations reported in Fig. 5.2b suggest that the bending loss should drop to less than 0.001 dB per 90° bend for bending radius greater than 3 μm using cross-section A.

By way of comparison, the propagation loss of the same Si waveguides with 3 μm SiO_2 top-cladding (rather than LN) was measured to be 3.1 ± 2.1 dB/cm in Fig. 5.4a, indicating that bonding and incorporation of LN as the top cladding did not significantly worsen the propagation characteristics. In fact, the propagation loss is similar to that measured in rib Si photonic waveguides [30] despite the thinner Si layer in our structures.

The loss values in these hybrid Si-LN waveguides using cross-section B are significantly lower than other reported values, e.g., 16 dB/cm in etched thin-film LN waveguides [13] and 6–10 dB/cm in thin-film LN waveguides (660 nm thickness, not too different from the 750 nm thickness used here) with oxidized titanium stripe [35]. Although the loss is still an order-of-magnitude higher than that of traditional in-diffused waveguides which have a much larger mode area, our circuits are also more than an order-of-magnitude more compact. Furthermore, we expect that with improved Si waveguide fabrication (e.g., roughness reduction), and filling of the air pockets on the lateral sides of the Si rib with a low-optical-loss gap-fill dielectric material, the overall propagation loss will decrease down to around 1 dB/cm.

Directional couplers were defined by lithography in the Si layer, but act on the hybrid mode using cross-section A, with a gap of 0.4 μm between the waveguide edges. The typical length was only 150 μm , compared to a typical length of about 5 mm for directional couplers with diffused or ion-exchanged waveguides. Because the mode in cross-section A resides primarily in Si, there

was no measurable crosstalk at milliwatt power levels, unlike the traditional waveguide LN devices which are susceptible to photorefractive artifacts [36, 37]. However, long-term (> 1 day) tests have not yet been performed since the chips are not fully packaged and we rely on manually-adjusted fiber coupling to the silicon waveguides.

Optical circuits can be designed if two fundamental parameters are known: the optical (modal, i.e., “effective”) refractive index of a waveguide, which determines the rate of accumulation of optical phase with distance, and the directional coupling coefficient of two adjacent waveguides. Both these parameters are functions of the optical wavelength. To measure these parameters and compare with numerical calculations, we designed an interferometric test structure (see Fig. 5.5) which can also perform several functions useful in integrated optics such as spectral filtering, interleaving or multiplexing / de-multiplexing for wavelength-division multiplexing (WDM). Such a device does not use microring or standing-wave (e.g., Fabry-Perot) resonators, in which the intensity enhancement (due to the infinite impulse response nature of the transfer function) may cause photorefractive artifacts in LN. The circuit consists of several building blocks where the optical pathway is indicated by the red arrows and consists of four transitions, two directional couplers and twenty 90-degree bends, incurring a cumulative insertion loss of about -15 dB. (The circuit does not need to be so complicated to realize only a Mach-Zehnder interferometer, but showcases some of the capabilities of the platform.)

5.4 Discussion and Analysis

To experimentally show the large difference in the effective modal refractive index between the A and B cross-sections, we measured two distinct MZIs in which the path imbalance of one arm with respect to the other was formed using waveguides of cross-section A and B, of length L_A and L_B , respectively. In each case, the free-spectral range (FSR) of the MZI was approximately 10 nm near the central wavelength of 1550 nm.

Figure 5.5b shows the wavelength variation of the effective refractive index of the A and

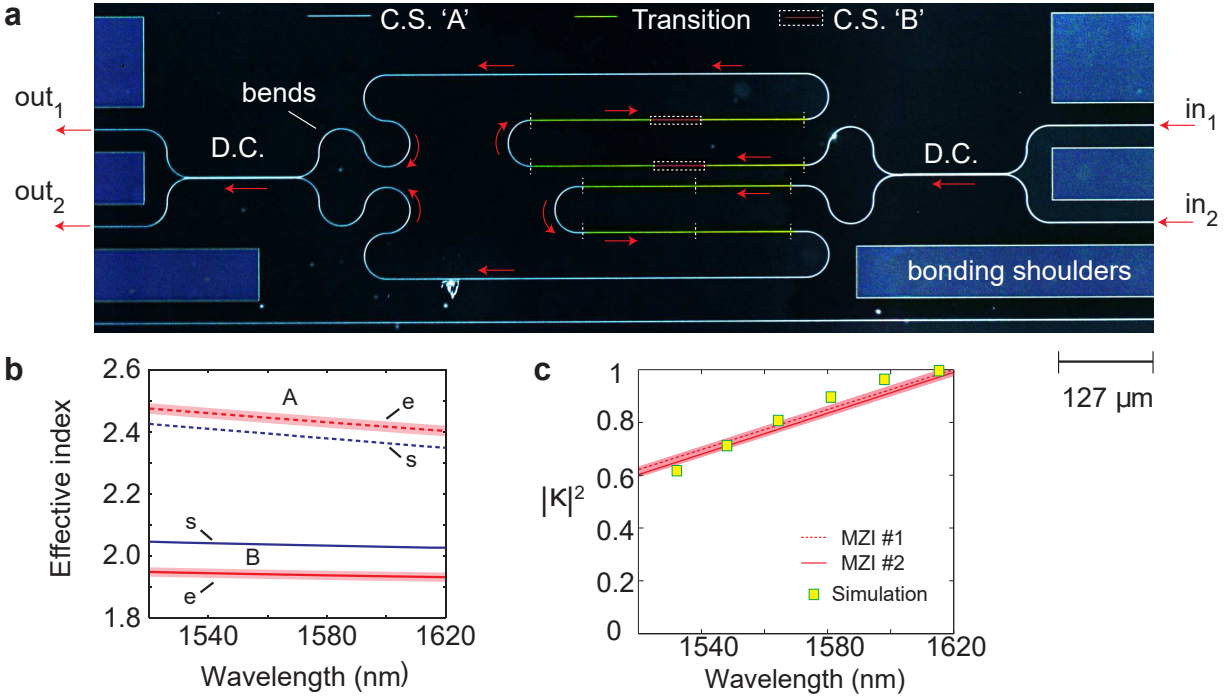


Figure 5.5: Hybrid Si-LN optical circuit. **a** Optical microscope image of an interferometric hybrid Si-LN circuit which uses both waveguide cross-sections (C.S.) A and B, four adiabatic transitions (Transition) in each lightpath, two directional couplers (D.C.), and twenty 90-degree bends in each lightpath. The image is shown using a simulated dark-field colour map for clarity, and with added shading to highlight the different sections. **b** Extracted modal effective index versus wavelength for MZIs with path-length difference (PLD) regions comprised of hybrid waveguides with cross-sections A (dashed lines) and B (solid lines). Simulated values using an eigenmode solver software (A: dotted, and B: solid lines) are also shown, assuming a nominal (design) Si rib waveguide width, and manufacturer-specified LN film thickness. Shaded regions indicate the standard errors provided by the fitting routine. **c** Extracted coupling coefficient of the directional coupler versus wavelength for the MZIs reported here (dashed and solid lines). MZIs with PLD cross-sections A and B use the same type of directional coupler, hence the results are similar. The simulation results shown by the squares were calculated using the supermode equations and a numerical simulation of the eigenmodes. Shaded regions indicate the standard errors provided by the fitting routine.

B waveguides. The two branches (cross-section A and cross-section B) are sufficiently far apart that the results confirm a clear distinction between the A (Si-like) and B (LN-like) guided modes. The group velocity dispersion (GVD) coefficients of the two modes at $\lambda = 1550$ nm are as follows: $D_A \approx -3100$ ps/nm-km for cross-section A, and $D_B \approx -4300$ ps/nm-km for cross-section B, which are of the same order-of-magnitude as that of a typical silicon photonic waveguide whose modal effective area is similar to that of cross-section A, $D_{Si} \approx -1500$ ps/nm-km [38].

Figure 5.5c shows the wavelength variation of the coupling coefficient of a directional coupler which was formed using waveguides of cross-section A, with a gap of $0.4 \mu\text{m}$ between the waveguide edges. As may be expected, the change in the magnitude of the coupling coefficient over the wavelength range of 1520 nm–1620 nm is similar to the behavior seen in all-Si waveguides [39].

On the same chip, outside the LN-bonded region, waveguides and devices may be designed as usual in Si photonics, i.e., with SiO_2 cladding. Because of the high refractive index of Si, light is tightly confined for waveguides of cross-section ‘A’ whether LN or SiO_2 is used as the upper cladding. We designed and measured a Mach-Zehnder interferometer outside of the LN-bonded region, using waveguide with cross-section ‘A’ and with SiO_2 replacing LN as the upper cladding (and with SiO_2 side- and lower-claddings in our fabrication process), as reported in Fig. 5.6. Although our test chip shown in Fig. 5.1 was designed for LN covering nearly all of the Si surface, it is equally possible to design “mixed” chips with smaller-sized LN pieces, which combine traditional Si photonic components with hybrid LN-Si photonic components on a monolithic platform.

We have restricted this fabrication process for reasons of cost and complexity to exclude dopants and electrodes as part of the Si chip, which could be used for electro-optic effects. Simulations show that gold electrodes can be positioned directly on the LN thin-film layer (surface opposite to the bonded interface to Si) at a lateral distance of only $0.4 \mu\text{m}$ from the Si edge for cross-section A and $4 \mu\text{m}$ from the Si edge for cross-section B, for an estimated additional propagation loss of 0.1 dB/cm. Alternatively, electrodes can be fabricated on the LN layer after substrate removal, following the traditional approach [13].

These results show that, even though LN is not a CMOS-compatible material, foundry-

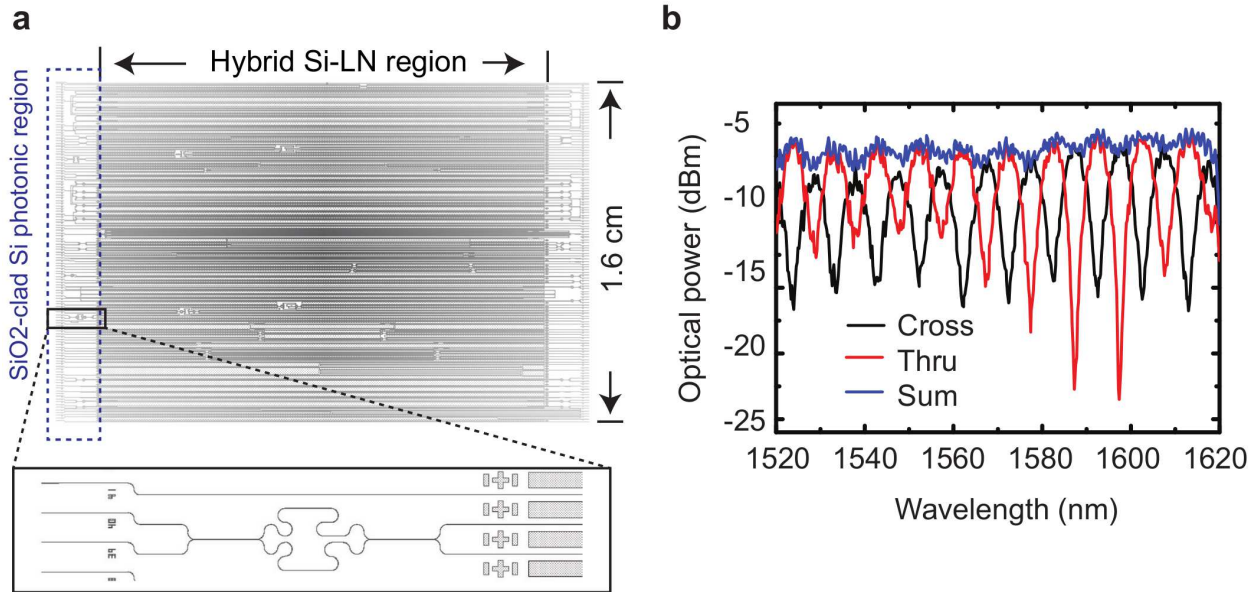


Figure 5.6: Si/SiO₂ Mach-Zehnder interferometer (MZI). **a** An SiO₂-clad Si photonic MZI was fabricated on the same chip but outside the bonded LN region. The input-output waveguides pass under the LN bonded region and emerge on the other facet of the chip. **b** The measured ‘Thru’ (red) and ‘Cross’ (black) characteristics, and their sum (blue) follow the expected behavior for an MZI, and demonstrate that conventional Si photonic devices can be fabricated alongside the hybrid Si-LN ones (the y-axis (dB) is in arbitrary units).

fabrication technologies can play a very useful role in a new generation of LN integrated optics. While LN has always been a desirable material for its nonlinear and electro-optic properties, it has not been possible in the past to make compact and complex waveguide circuits as is possible nowadays in Si photonics using precise and highly-repeatable DUV lithography. We have shown a suite of hybrid building blocks from which optical circuits can be assembled alongside traditional Si photonics components. While improved wafer-scale bonding techniques are being developed by industry for commercial applications, here we have shown chip-scale direct bonding of chips that are a few centimeters squared (the size of a typical field size of a DUV stepper lithography system), with enough bond strength to permit dicing and simple packaging for test and measurement. A similar approach may also be applied to design and investigate optical circuits using other thin-film materials in place of LN, leveraging the advanced foundry fabrication capabilities of Si photonics as a waveguiding template for the hybrid modes without needing to pattern the thin-films.

5.5 Acknowledgments

Chapter 5, in part, is a reprint of the material as it appears in Scientific Reports 2016. Peter O. Weigel, Marc Savanier, Christopher T. DeRose, Andrew T. Pomerene, Andrew L. Starbuck, Anthony L. Lentine, Vincent Stenger & Shayan Mookherjea, Scientific Reports **6**, 22301. The dissertation author, together with his adviser, led the research efforts for this work and co-authored the paper.

Bibliography

- [1] Lawrence M. Lithium niobate integrated optics. *Reports on Progress in Physics*. 1993;56(3):363.
- [2] Smit M, Van der Tol J, Hill M. Moore's law in photonics. *Laser & Photonics Reviews*. 2012;6(1):1–13.
- [3] Hochberg M, Baehr-Jones T. Towards fabless silicon photonics. *Nature Photonics*. 2010;4(8):492.
- [4] Sohler W, Hu H, Ricken R, Quiring V, Vannahme C, Herrmann H, et al. Integrated optical devices in lithium niobate. *Optics and Photonics News*. 2008;19(1):24–31.
- [5] Chiba A, Sakamoto T, Kawanishi T, Higuma K, Sudo M, Ichikawa J. 16-level quadrature amplitude modulation by monolithic quad-parallel Mach-Zehnder optical modulator. *Electronics letters*. 2010;46(3):227–228.
- [6] Levy M, Osgood Jr R, Liu R, Cross L, Cargill III G, Kumar A, et al. Fabrication of single-crystal lithium niobate films by crystal ion slicing. *Applied Physics Letters*. 1998;73(16):2293–2295.
- [7] Rabiei P, Gunter P. Optical and electro-optical properties of submicrometer lithium niobate slab waveguides prepared by crystal ion slicing and wafer bonding. *Applied physics letters*. 2004;85(20):4603–4605.
- [8] Poberaj G, Koechlin M, Sulser F, Günter P. High-density integrated optics in ion-sliced lithium niobate thin films. In: *Integrated Optics: Devices, Materials, and Technologies XIV*. vol. 7604. International Society for Optics and Photonics; 2010. p. 76040U.
- [9] Tamir T, Tomlinson W. Guided-wave optoelectronics. *Applied Optics*. 1989;28:2262.
- [10] Thomas J, Heinrich M, Zeil P, Hilbert V, Rademaker K, Riedel R, et al. Laser direct writing: Enabling monolithic and hybrid integrated solutions on the lithium niobate platform. *physica status solidi (a)*. 2011;208(2):276–283.

- [11] Ulliac G, Guichardaz B, Rauch JY, Queste S, Benchabane S, Courjal N. Ultra-smooth LiNbO₃ micro and nano structures for photonic applications. *Microelectronic Engineering*. 2011;88(8):2417–2419.
- [12] Takigawa R, Higurashi E, Kawanishi T, Asano T. Lithium niobate ridged waveguides with smooth vertical sidewalls fabricated by an ultra-precision cutting method. *Optics Express*. 2014;22(22):27733–27738.
- [13] Guarino A, Poberaj G, Rezzonico D, Degl’Innocenti R, Günter P. Electro–optically tunable microring resonators in lithium niobate. *Nature photonics*. 2007;1(7):407.
- [14] Mookherjea S, Savanier M. Heterogeneous waveguides and methods of manufacture. Google Patents; 2018. US Patent App. 15/550,493.
- [15] Han H, Cai L, Hu H. Optical and structural properties of single-crystal lithium niobate thin film. *Optical Materials*. 2015;42:47–51.
- [16] Takagi H, Maeda R, Hosoda N, Suga T. Room-temperature bonding of lithium niobate and silicon wafers by argon-beam surface activation. *Applied physics letters*. 1999;74(16):2387–2389.
- [17] Howlader M, Suga T, Kim M. Room temperature bonding of silicon and lithium niobate. *Applied physics letters*. 2006;89(3):031914.
- [18] Takigawa R, Higurashi E, Suga T, Shinada S, Kawanishi T. Low-temperature bonding of a LiNbO₃ waveguide chip to a Si substrate in ambient air for hybrid-integrated optical devices. In: *Optomechatronic Micro/Nano Devices and Components II*. vol. 6376. International Society for Optics and Photonics; 2006. p. 637603.
- [19] Lee YS, Kim GD, Kim WJ, Lee SS, Lee WG, Steier WH. Hybrid Si-LiNbO₃ microring electro-optically tunable resonators for active photonic devices. *Optics letters*. 2011;36(7):1119–1121.
- [20] Chen L, Xu Q, Wood MG, Reano RM. Hybrid silicon and lithium niobate electro-optical ring modulator. *Optica*. 2014;1(2):112–118.
- [21] Chiles J, Fathpour S. Mid-infrared integrated waveguide modulators based on silicon-on-lithium-niobate photonics. *Optica*. 2014;1(5):350–355.
- [22] Yoon JG, Kim K. Growth of highly textured LiNbO₃ thin film on Si with MgO buffer layer through the sol-gel process. *Applied physics letters*. 1996;68(18):2523–2525.
- [23] Sakashita Y, Segawa H. Preparation and characterization of LiNbO₃ thin films produced by chemical-vapor deposition. *Journal of applied physics*. 1995;77(11):5995–5999.
- [24] Chen L, Reano RM. Compact electric field sensors based on indirect bonding of lithium niobate to silicon microrings. *Optics Express*. 2012;20(4):4032–4038.
- [25] Hui H, Ricken R, Sohler W. Etching of lithium niobate: from ridge waveguides to photonic crystal structures. *ECIO, Eindhoven*. 2008;.

- [26] Rabiei P, Steier WH. Lithium niobate ridge waveguides and modulators fabricated using smart guide. *Applied Physics Letters*. 2005;86(16):161115.
- [27] Almeida VR, Panepucci RR, Lipson M. Nanotaper for compact mode conversion. *Optics letters*. 2003;28(15):1302–1304.
- [28] Uchida N. Optical waveguide loaded with high refractive-index strip film. *Applied optics*. 1976;15(1):179–182.
- [29] Hu H, Ricken R, Sohler W. Lithium niobate photonic wires. *Optics express*. 2009;17(26):24261–24268.
- [30] Vlasov YA, McNab SJ. Losses in single-mode silicon-on-insulator strip waveguides and bends. *Optics express*. 2004;12(8):1622–1631.
- [31] Bures J. *Guided optics*. John Wiley & Sons; 2009.
- [32] Rao A, Patil A, Chiles J, Malinowski M, Novak S, Richardson K, et al. Heterogeneous microring and mach-zehnder lithium niobate electro-optical modulators on silicon. In: *CLEO: Science and Innovations*. Optical Society of America; 2015. p. STu2F–4.
- [33] Ogusu K, Tanaka I. Optical strip waveguide: an experiment. *Applied optics*. 1980;19(19):3322–3325.
- [34] Cai L, Han SLH, Hu H. Waveguides in single-crystal lithium niobate thin film by proton exchange. *Optics Express*. 2015;23(2):1240–1248.
- [35] Li S, Cai L, Wang Y, Jiang Y, Hu H. Waveguides consisting of single-crystal lithium niobate thin film and oxidized titanium stripe. *Optics express*. 2015;23(19):24212–24219.
- [36] Schmidt R, Cross P, Glass A. Optically induced crosstalk in LiNbO₃ waveguide switches. *Journal of Applied Physics*. 1980;51(1):90–93.
- [37] Mueller CT, Garmire E. Photorefractive effect in LiNbO₃ directional couplers. *Applied optics*. 1984;23(23):4348–4351.
- [38] Turner Amy C, Manolatu C, Schmidt Bradley S, Lipson M, Foster Mark A, Sharping Jay E, et al. Tailored anomalous group-velocity dispersion in silicon channel waveguides. *Opt Express*. 2006;14:4357–4362.
- [39] Aguinaldo R, Shen Y, Mookherjea S. Large dispersion of silicon directional couplers obtained via wideband microring parametric characterization. *IEEE Photonics Technology Letters*. 2012;24(14):1242–1244.

Chapter 6

Characterization of Hybrid Electro-Optic Modulators

6.1 Introduction

Characterizing electro-optic modulators consists of three components: optical, electrical, and electro-optical characterization. Proper characterization requires an understanding of both optical integrated circuits and microwave electronics, and at high frequencies equipment limitations become a nontrivial concern. For this reason, extracting high frequency electro-optic information – namely, the device’s electro-optic response – is an interesting experimental challenge.

6.2 Optical Characterization of an Electro-Optic Modulator

Optically, the full electro-optic modulator consists of a Mach-Zehnder interferometer with a path-length difference in one arm, and several Si waveguide width changes as shown in Fig. 6.1a. Broadband directional couplers are used for 50/50 splitters. Simulated effective mode indices for different low order waveguide modes in the hybrid Si-LN region are shown in Fig. 6.1b, with modes ‘B’ and ‘C’ of Fig. 6.1a shown in Fig. 6.1c. Γ_{Si} is the optical confinement factor in Si, Γ_{LN} is the optical confinement factor in LN, and n_{eff} is the mode’s effective (i.e. phase) index.

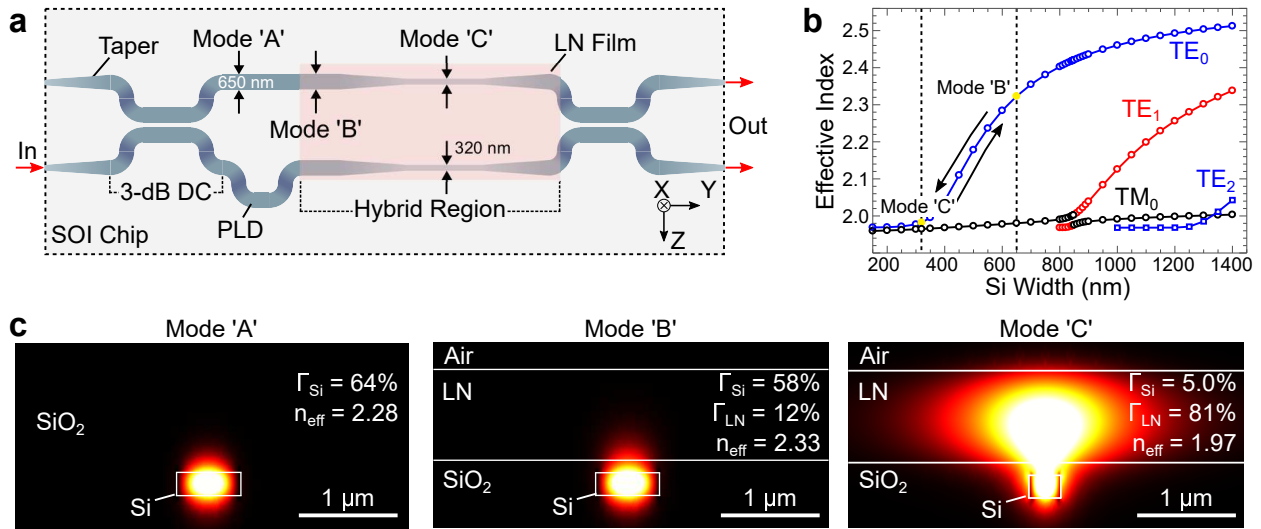


Figure 6.1: **a** Schematic of the EOM (not to scale, not showing electrodes), including two 3-dB directional couplers (DC) and a waveguide segment for path-length difference (PLD). Three optical waveguide modes are used, labeled as A, B, and C. Modes A (Si under SiO₂) and B (Si under LN) have Si rib width $w = 650$ nm whereas mode C has $w = 320$ nm. **b** Dispersion curves (effective index versus w) in the hybrid region; w values for modes B and C are chosen to stay within the single-mode region of operation. An adiabatic waveguide transition (variation in w) is designed to evolve from mode B to C and vice versa. **c** Calculated Poynting vector components along the direction of propagation. Modes A and B are Si-guided and have a similar confinement fraction in Si. Mode C, with LN confinement factor (Γ_{LN}) greater than 80%, is used in the phase-shifter segments.

6.2.1 Optical Transmission through an Electro-Optic Modulator

A fabricated electro-optic modulator has the optical transmission as shown in Fig. 6.2a, with an interferometer pattern caused by the path-length difference in one arm of the EOM. The spacing between nulls, known as the free spectral range (FSR, $\Delta\lambda_{FSR}$) varies from 5.4 nm around 1525 nm to 5.8 nm around 1575 nm. From theory [1],

$$\Delta\lambda_{FSR} \approx \frac{\lambda^2}{n_g L_{FSR}} \quad (6.1)$$

where λ is the wavelength, n_g is the optical group index in the path-length difference region, and L_{FSR} is the path-length difference between the two arms, since it is this path-length difference that is causing a wavelength-dependent phase difference. For $L_{FSR} = 96.26 \mu\text{m}$, n_g is between 4.47 and 4.44. These sorts of relatively high group indices are common for high-index Si waveguides.

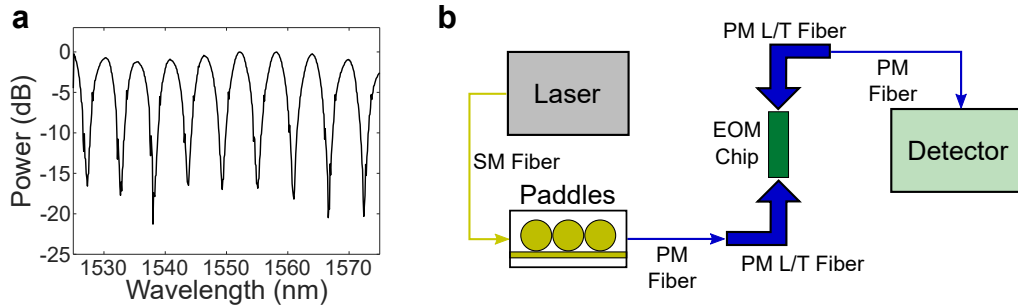


Figure 6.2: **a** Optical transmission through EOM device with greater than 15 dB extinction ratio across the entire measured wavelength range of 1525 nm to 1575 nm. **b** Pictorial representation of optical setup. SM = single mode, PM = polarization maintaining, and L/T = lensed/tapered. Paddles are used to precisely control polarization going onto the chip.

The experimental setup for this measurement is described in Fig. 6.2b. For optical transmission, the measurement is relatively straightforward; a laser source with good linear polarization may not even require additional polarization control. For this work, commercially available optical fiber “paddles” (hollow, adjustable ceramic cylinders designed to hold tightly wound spools of fiber) are used for additional polarization control to ensure that laser light entering the chip is horizontally polarized more details on attaining a high degree of horizontal polarization is described in Section 6.2.4. Lensed/tapered polarization maintaining fibers from Oz Optics, Ltd. were used to

couple on and off the chip using waveguide edge couplers. Lensed tapered fibers have a mode field diameter of $2.5 \mu\text{m}$, small enough to efficiently match the input/output waveguide mode. All fiber after the paddles is PM to ensure the highly linear polarization state is maintained. From the clean spectrum of Fig. 6.2a – which has no ripples that would normally be caused by polarization effects – it is clear that the polarization of the input light is well controlled and horizontally polarized.

6.2.2 Propagation Loss

All waveguides have some of propagation loss. “Propagation loss” refers to a per unit length loss term describing how much of the optical signal is attenuated simply by traveling through the waveguide. Waveguide loss is typically described in dB per centimeter. Optical fibers, for example, have propagation losses of less than 0.5 dB/km, or $5\text{e-}6$ dB/cm.¹ A good Si waveguide, on the other hand, has a propagation loss around 1 dB/cm.

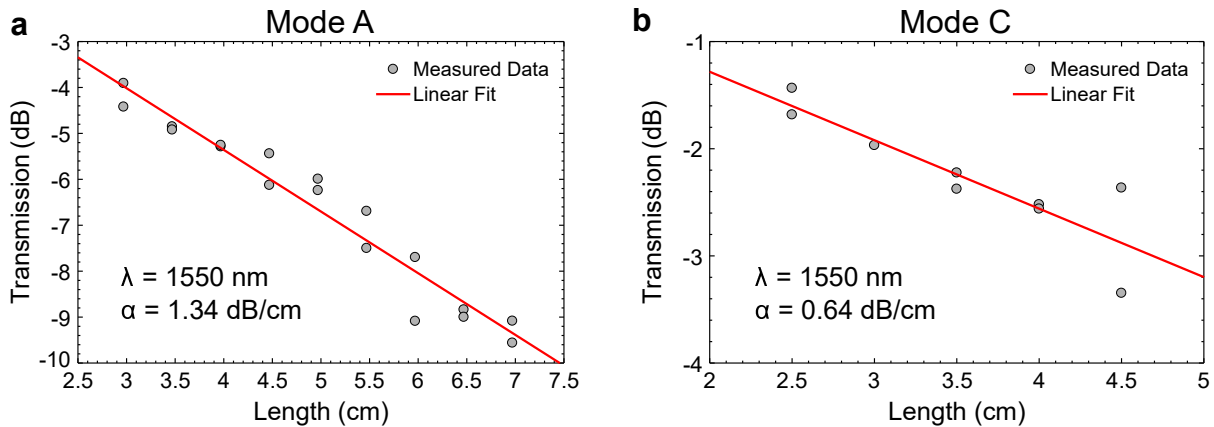


Figure 6.3: Transmission for various waveguide lengths at $\lambda = 1550$ nm is shown for the all-Si mode (a, Mode A) and the Si-LN mode (b, Mode C). Propagation loss is significantly lower for the hybrid, narrow-Si mode, at only 0.64 dB/cm compared with 1.34 dB/cm for the all-Si mode. The y-axes are normalized to be 0 dB for 0 cm length waveguides.

For this Si-LN device, two sets of propagation loss measurements were performed to describe the propagation loss in the non-hybrid region (mode ‘A’ in Fig. 6.1c) and in the hybrid, narrow Si region (mode ‘C’ in Fig. 6.1c). The results at $\lambda = 1550$ nm are shown in Fig. 6.3. Propagation losses in Mode C are only 0.64 dB/cm compared with 1.34 dB/cm in Mode A. These results may seem

¹The extremely low loss of optical fibers has been a significant motivator of research into optics for the last 35 years.

surprising at first, but with some thought they become clear. LN is a highly pure crystalline insulator with intrinsically low propagation loss (as early as the late 1980s, LN waveguide propagation losses were shown to be as low as 0.15 dB/cm [2]), and Mode C is designed with the intention of pushing as much of the optical mode into the LN film as possible while still maintaining a small mode area. By reducing the Si rib width and increasing Γ_{LN} , less light scatters off impurities in the lossier Si and overall propagation loss is significantly reduced.

Still, propagation losses in both cases can be reduced by improving the fabrication process. In particular, Si sidewall roughness can be further reduced with additional oxidation steps. SiO₂ is deposited via plasma-enhanced chemical vapor deposition (PECVD) in a university cleanroom above Mode A only after bonding the LN. Performing this deposition in a industry grade dedicated SiO₂ PECVD chamber would likely reduce optical losses as well. Lastly, it is unclear whether the bonding process somehow reduces the optical quality of the LN film (perhaps simply by handling the sample) or if the bond interface is a source of optical loss caused by, perhaps, strain-induced crystal defects. It is also possible that the propagation loss of Mode C can be optimized by adjusting the Si rib height and width and the LN film thickness (though this would of course impact the performance of the electro-optic device).

6.2.3 Spline Bending Loss

In addition to straight waveguides for propagation, spline bends are used for bent or angled optical routing. As a low-loss waveguide bend, spline functions are mathematically superior to quarter circle bends [3]. The most significant source of loss in a quarter-circle waveguide bend is at the point where the straight waveguide and the quarter-circle bend meet, due to the asymmetric mode supported by a circularly bent waveguide. Spline bends, however, have zero curvature (infinite bending radius) at their inputs and outputs, elegantly avoiding the in/out coupling issue without adding too much additional length to the bend. Based on the results of Fig. 6.4a, 30 μm spline bends are used for all electro-optic modulators (in the broadband directional couplers and path-length difference sections), though 15 μm bends or even 10 μm bends would have been acceptable as well.

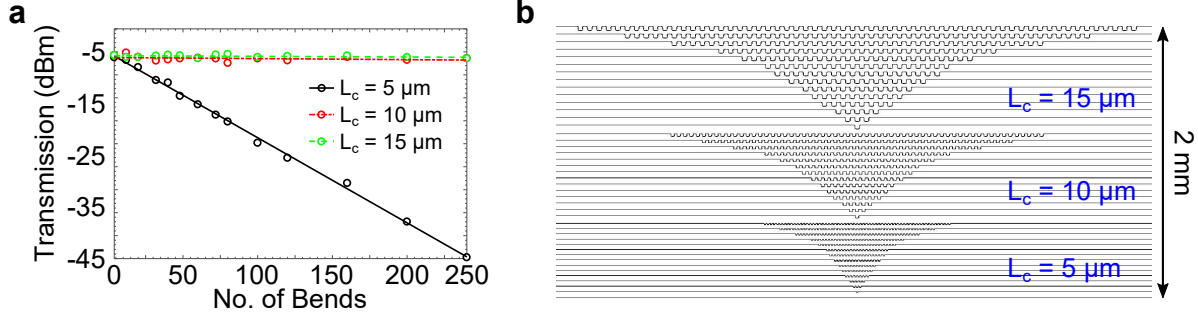


Figure 6.4: **a** Measured (circles) spline bending loss for various characteristic lengths (L_c) at $\lambda = 1550 \text{ nm}$. Lines represent linear fits of transmission measurements for a number of devices with varying amounts of quarter-circle spline bends. For $L_c = 5 \mu\text{m}$, $10 \mu\text{m}$, and $15 \mu\text{m}$, $\alpha_b = 0.18 \text{ dB}/90^\circ$, $0.0023 \text{ dB}/90^\circ$, and $0.0015 \text{ dB}/90^\circ$, respectively. **b** GDS layout of array of spline bends of various characteristic length and number of bends.

In Fig. 6.4, each spline is defined by its characteristic length L_c . As described in Chapter 3, L_c is analogous to the bend radius of a quarter-circle bend. The full length of a $15 \mu\text{m}$ quarter-circle bend is $23.6 \mu\text{m}$, whereas the full length of a $15 \mu\text{m}$ spline bend is $27.0 \mu\text{m}$. Similarly, a $30 \mu\text{m}$ quarter-circle bend has a length of $47.1 \mu\text{m}$ versus $54.1 \mu\text{m}$ for a $30 \mu\text{m}$ characteristic length spline bend. So although the spline bend has a marginally longer path length than a typical quarter-circle bend, this extra length is vastly outweighed by the optical propagation benefits. GDS layout of the various spline bend test structures are included in Fig. 6.4b to show how that despite the large number of devices required for these tests, they can be densely packed without crosstalk due to the high confinement of the Si waveguide, even though the Si waveguide is only 150 nm thick.

6.2.4 Method to Optimize Optical Polarization State

Due to the importance of optical polarization control for high-quality optical transmission measurements, it is worth taking the time to understand how to minimize undesired polarization components.

Typical lasers are designed to output a single, linear polarization state, either horizontal (TE) or vertical (TM). Polarization maintaining (PM) fibers, as the name implies, maintain this polarization state along their length by breaking the symmetry of a single mode (SM) circular fiber core to prevent coupling between TE and TM fundamental modes. Imagine an ideal laser with

100% of its output light polarized horizontally. In such a scenario, PM fiber can connect directly from the laser to the next component in the experiment, without any need for polarization control and stability. However, since realistic lasers can sometimes have a noticeable fraction of light in an orthogonal polarization state (or even a circular or elliptical polarization state, if the laser is poorly designed) polarization control after the laser becomes exceedingly useful.

To minimize undesired polarization components, fiber paddles are used after the laser. As described previously, fiber paddles are simply spools of SM fiber in three adjacent, adjustable ceramic cylinders. Each paddle can have a different number of fiber spools in it. By spooling fiber into the paddles, some polarization rotation occurs in the stressed fiber. By then rotating the paddles, torsional stress on the fiber adds an additional polarization rotation. In this way, the three paddles act as tunable knobs to control the polarization state.

The simplest way of minimizing undesired polarization components is to pass the optical signal through a set of paddles, through a polarization rotator, and into a photodetector. The polarization rotator should be set to pass light linearly polarized orthogonal to the desired linear polarization state; if horizontally polarized light is desired, the polarizer should be set to pass vertically polarized light, and vice versa. Then, the desired polarization state can be obtained by minimizing light at the undesired polarization angle. This is much more accurate than maximizing the desired polarization state, since low power measurements are more sensitive to fine adjustments. When done correctly, a polarization extinction ratio of 30 to 1 or greater can be achieved.

6.3 Electrical Characterization of an Electro-Optic Modulator

Electrical characterization of electro-optic modulators can be extracted from scattering matrix measurements through a vector network analyzer (VNA). The scattering matrix of an electrical network measure incident and reflected voltages through the various ports of the network. In the case of a two-port network (one input and one output), the scattering matrix is defined as

$$\begin{bmatrix} V_1^- \\ V_2^- \end{bmatrix} = \begin{bmatrix} S_{11} & S_{12} \\ S_{21} & S_{22} \end{bmatrix} \begin{bmatrix} V_1^+ \\ V_2^+ \end{bmatrix}; \quad (6.2)$$

S_{11} , S_{12} , S_{21} , and S_{22} are called the S-parameters of the network. Physically, S_{ii} can be thought of as the reflection at port i and S_{ij} as the transmission from port j through port i .

Another useful matrix for two-port analysis is the *ABCD* matrix:

$$\begin{bmatrix} V_1 \\ I_1 \end{bmatrix} = \begin{bmatrix} A & B \\ C & D \end{bmatrix} \begin{bmatrix} V_2 \\ I_2 \end{bmatrix}. \quad (6.3)$$

Block diagrams of (6.2) and (6.3) are shown in Fig. 6.5a-b, respectively. Note that the direction of current flow at port 2 has been redefined for the *ABCD* matrix, following standard convention [4]. Conversions between S-parameters and *ABCD* parameters are well known and are as follows (from [4]):

$$A = \frac{(1 + S_{11})(1 - S_{22}) + S_{12}S_{21}}{2S_{21}} \quad (6.4)$$

$$B = Z_0 \frac{(1 + S_{11})(1 + S_{22}) - S_{12}S_{21}}{2S_{21}} \quad (6.5)$$

$$C = \frac{1}{Z_0} \frac{(1 - S_{11})(1 - S_{22}) - S_{12}S_{21}}{2S_{21}} \quad (6.6)$$

$$D = \frac{(1 - S_{11})(1 + S_{22}) + S_{12}S_{21}}{2S_{21}}. \quad (6.7)$$

Z_0 is the characteristic impedance of the measurement system, and is typically 50 Ω .

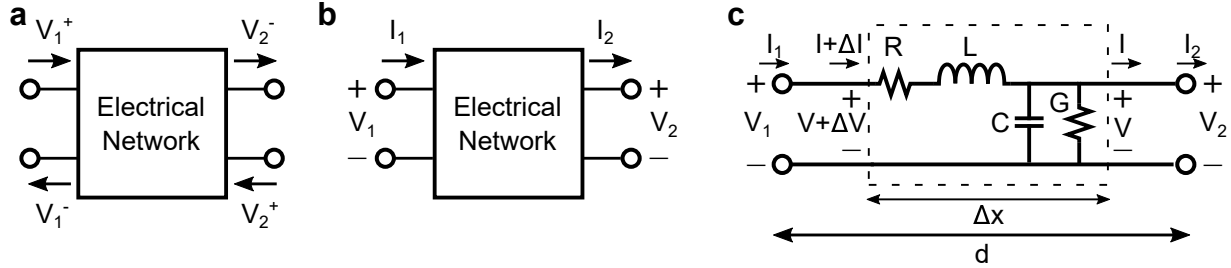


Figure 6.5: **a** Scattering matrix representation of a two-port electrical network. **b** $ABCD$ matrix representation of a two-port electrical network. **c** Circuit schematic for a long, lossy transmission line of length d . R , L , C , and G are the per unit length series resistance, series inductance, shunt capacitance, and shunt impedance of the transmission line. Δx is a short length of the total transmission line. V_1 , $V + \Delta V$, V , and V_2 are various voltages along the length of the line ($V_1 =$ input voltage, $V_2 =$ output voltage), with corresponding currents shown above each voltage.

6.3.1 Lossy Transmission Line Theory

In the case of a long, lossy transmission line (Fig. 6.5c), the $ABCD$ parameters can be related to the transmission line's characteristic impedance and propagation constant. Performing loop analysis (KVL) on Fig. 6.5c results in

$$\Delta V = I_z \Delta x, \quad (6.8)$$

which can be rearranged and taken to the limit as Δx goes to zero to get

$$\frac{dV}{dx} = I_z. \quad (6.9)$$

A similar node analysis (KCL) results in an expression for the differential current in the line:

$$\frac{dI}{dx} = Vy. \quad (6.10)$$

$Z \equiv zd = (R + j\omega L)d$ is the series impedance of the line, and $Y \equiv yd = (G + j\omega C)d$ is the shunt impedance of the line. Variables z and y are the per unit length series and shunt impedances of the line, respectively. (6.9) and (6.10) can be combined and rearranged into

$$\frac{d^2V}{dx^2} - Vzy = 0, \quad (6.11)$$

whose roots are located at $\pm\sqrt{yz}$:

$$V = A_1e^{x\sqrt{yz}} + A_2e^{-x\sqrt{yz}}. \quad (6.12)$$

z and y can be related to the characteristic impedance and propagation constant of the transmission line from the circuit components of Fig. 6.5c [4]. The characteristic impedance is

$$Z_c = \sqrt{\frac{R + j\omega L}{G + j\omega C}} = \sqrt{\frac{z}{y}}, \quad (6.13)$$

and the complex propagation constant is

$$\gamma = \sqrt{(R + j\omega L)(G + j\omega C)} = \sqrt{zy}. \quad (6.14)$$

$\gamma = \alpha + j\beta$, where $\alpha = \frac{2\pi k_m}{\lambda_m}$ and $\beta = \frac{2\pi n_m}{\lambda_m}$; k_m is the imaginary component of the effective index of the electrical signal, n_m is the real part of the effective index of the electrical signal, and λ_m is the wavelength of the electrical signal. The variables y and z can be replaced with Equation (6.13) and Equation (6.14) in Equation (6.12):

$$V = A_1e^{\gamma x} + A_2e^{-\gamma x} \quad (6.15)$$

$$I = \frac{A_1}{Z_c}e^{\gamma x} - \frac{A_2}{Z_c}e^{-\gamma x}. \quad (6.16)$$

If $x = 0$ then $V = V_2$, $I = I_2$, and $A_1 = \frac{V_2 + Z_c I_2}{2}$ and $A_2 = \frac{V_2 - Z_c I_2}{2}$. If $x = d$, $V = V_1$ and $I = I_1$. With some algebra, the following expressions for V_1 and I_1 – the input voltage and current – are obtained in terms of V_2 and I_2 :

$$V_1 = \frac{V_2 + Z_c I_2}{2} e^{\gamma d} + \frac{V_2 - Z_c I_2}{2} e^{-\gamma d} \quad (6.17)$$

$$I_1 = \frac{V_2/Z_c + I_2}{2} e^{\gamma d} - \frac{V_2/Z_c - I_2}{2} e^{-\gamma d}. \quad (6.18)$$

Substituting the exponentials in Equation (6.17) and Equation (6.18) with hyperbolic functions and again performing some simple algebra results in

$$V_1 = V_2 \cosh(\gamma d) + Z_c I_2 \sinh(\gamma d) \quad (6.19)$$

$$I_1 = V_2 \frac{\sinh(\gamma d)}{Z_c} + I_2 \cosh(\gamma d). \quad (6.20)$$

Combining Equation (6.19) and Equation (6.20) with the definition of the *ABCD* matrix in Equation (6.3) finally gives expressions for A, B, C, and D in terms of Z_c and γ :

$$A = \cosh(\gamma d) \quad (6.21)$$

$$B = Z_c \sinh(\gamma d) \quad (6.22)$$

$$C = \frac{1}{Z_c} \sinh(\gamma d) \quad (6.23)$$

$$D = \cosh(\gamma d). \quad (6.24)$$

The *ABCD* values for a transmission line can be experimentally determined by carefully measuring the transmission line's S-parameters and using Equations (6.4)-(6.7). Finally, from Equation (6.21) and Equation (6.22):

$$\gamma = \text{acosh}(A)/d \quad (6.25)$$

$$Z_c = B/\sqrt{A^2 - 1}. \quad (6.26)$$

6.3.2 Electrical Extraction from VNA Measurements

Using the theory developed in Section 6.3, it is relatively straightforward to electrically characterize an electro-optic modulator.

Electrically, an EOM is simply a two-port device; in particular, it is a two-port lossy transmission line that matches the modeling of Fig. 6.5c. This means that Equations (6.21)-(6.26) can be used to determine the characteristic impedance, microwave effective index, and microwave propagation loss of the coplanar waveguide transmission line used for the EOMs in this work.

Measurements were performed in the High Speed Circuits Lab at UC San Diego using an Agilent E8361A vector network analyzer up to 67 GHz, high enough to extract microwave parameters. The measured $|S_{21}|^2$ and $|S_{11}|^2$ curves are shown in Fig. 6.6a and the extracted microwave parameters are shown in Fig. 6.6b.

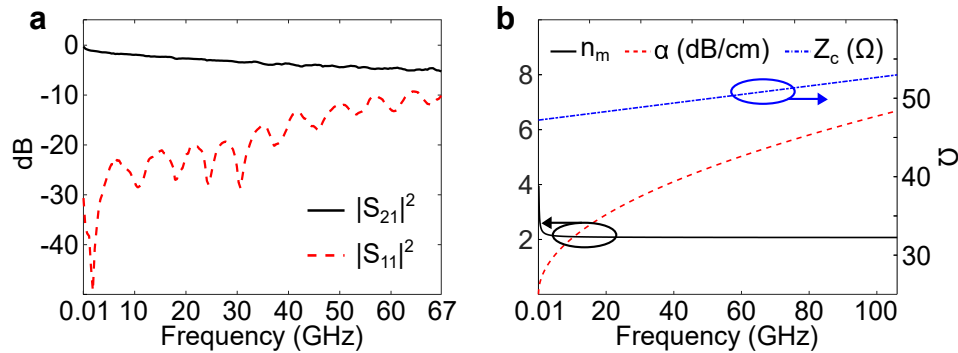


Figure 6.6: **a** Measured electrical S-parameters of the EOM's coplanar-waveguide transmission line. **b** Left y-axis: extracted microwave phase index n_m and microwave loss α_m (units of dB/cm). Right y-axis: characteristic impedance Z_c (Ω).

The data of Fig. 6.6b are fits of the raw extracted data. There are several things to note about the extracted data in Fig. 6.6b. First, the microwave index is nearly flat at high frequencies

(> 10 GHz or so). This is not by accident: since index matching is a critical bandwidth limitation – particularly at higher frequencies – and the optical index does not change with microwave frequency, it is imperative that n_m be as flat as possible so that index matching can occur across a wide range of frequencies. In Fig. 6.6, $n_m \approx 2.08$. Second, the microwave loss, which is in units of dB/cm, has a distinct curvature to it that approximately follows an $x^{1/2}$ shape. This is because microwave losses at high frequencies tend to be dominated by conductor losses, i.e. the losses due to the metal electrodes, which scale as $x^{1/2}$. With this in mind, a commonly used loss value known as the conductor loss can be extracted by dividing α by the square root of frequency, in GHz, to get $\alpha_{cond} = 0.65 \text{ dB}/(\text{cm-GHz}^{1/2})$. This value, along with n_m and Z_c , can be substituted into the equation for the electro-optic bandwidth of a modulator (Equation 1.23) to obtain a theoretical electro-optic response, as long as the optical group index is known as well.

6.3.3 Measuring $V_\pi L$

The $V_\pi L$ term is the product of the halfwave voltage (the voltage required to switch the optical output intensity from a maximum (“one”) to a minimum (“zero”), and the active device length L . Experimentally, electrostatic (dc) data are obtained by applying a dc voltage to one end of the CPW line and measuring the optical intensity at a particular wavelength of interest. By sweeping the voltage and recording the optical intensity for each voltage point, a \sin^2 curve is created of optical power versus applied voltage. The difference (in voltage) between the maximum optical power and minimum optical power is V_π , and multiplying that value by the device’s length (in cm) gives the $V_\pi L$ figure of merit.

The $V_\pi L$ of the device of Fig. 6.7 is 6.7 V-cm. This compares well with the simulated value of 6.1 V-cm. The difference is likely a combination of fabrication imperfections (such as non-constant electrical line widths/heights/gaps) a non-exact LN r_{33} value in the LN film used here, and slight variations to the Si waveguide dimensions. From these relatively minor errors can result the 9.8% error between simulation and measurement. Note that for $V_\pi L$ measurements at zero-frequency, the other end of the CPW can be left as an open circuit since only an electric field is

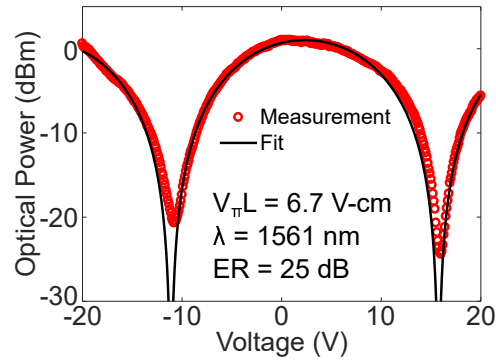


Figure 6.7: A plot of optical power versus applied dc voltage. The dc voltage supply is a Keithley 2420. Device length is 5 mm. ER = extinction ratio. Fitting was performed in MATLAB.

required to induce an optical phase shift in the device. For non-zero frequencies a load is required to prevent reflections and for impedance matching.

6.3.4 Low Frequency Electro-Optic Response

At low frequencies,² a VNA can be used with a photodetector to measure the frequency response of an EOM. Port 1 of the VNA is used as a signal, which gets fed in to the electrical input of the EOM. The electrical output is loaded with a 50 Ω impedance, and the optical output is put directly into a photodetector whose output goes into Port 2 of the VNA. The VNA can then be swept across its frequency range and, as long as proper calibration has been performed to account for all sources of electrical loss (cables, adapters, probes, the photodetector, etc.), the frequency response produced by the VNA will be that of the EOM.

An example of this measurement is shown in Fig. 6.8 for a low-frequency EOM device. The setup is shown in Fig. 6.8a and the measurement is shown in Fig. 6.8b.

6.3.5 High Frequency Electro-Optic Response

At higher frequencies, an optical spectrum analyzer (OSA) can be used to extract the electro-optic response. In this experiment, a signal generator is used to generate a sine wave that is

²Here “low” means 6 GHz, but really this method works at any frequency as long as a VNA and a photodetector are available for the desired frequency range.

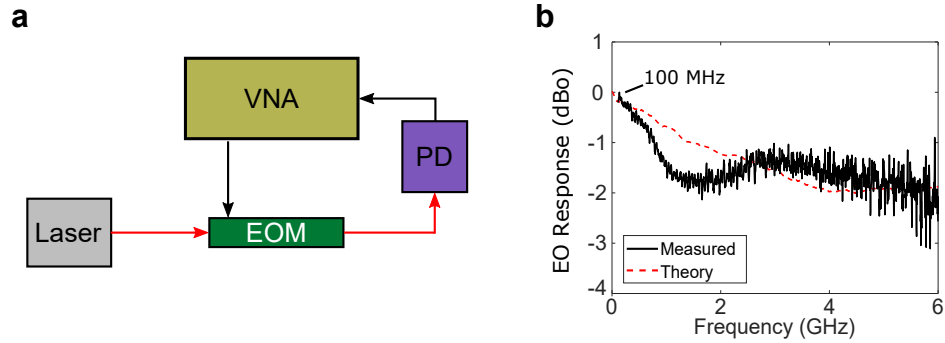


Figure 6.8: **a** Experimental setup for low frequency modulation response. PD = photodetector. Red arrows represent the optical signal, black arrows represent the electrical signal. **b** Measured response of a low frequency EOM from 100 MHz up to 6 GHz (the limit of the VNA). Units of dBo are used to denote that this is the optical modulation response.

launched onto the EOM device through high frequency GSG (ground-signal-ground) probes. The electrical output again is loaded with a 50Ω impedance, just as in the low frequency measurement of Section 6.3.4. However, instead of sending the modulated optical output into a photodetector connected to the second port of the VNA generating the microwave signal, it is sent into an OSA. Due to the nature of phase modulators, the modulated optical signal will have optical sidebands spaced at frequencies corresponding to the electrical frequency of the input sine wave; the power in these sidebands is proportional to the frequency response of the modulator [5]. By carefully measuring these sidebands, high frequency electro-optic measurements can be performed with only a signal generator and an OSA.

6.4 Electro-Optic Characterization of an Electro-Optic Modulator

Electro-optic modulation, the imprinting of a radio-frequency (RF) waveform on an optical carrier, is one of the most important photonics functions, being crucial for high-bandwidth signal generation, optical switching, optical waveform shaping, data communications, ultrafast measurements, sensing and ranging, timing and telemetry, and RF photonics. Although silicon (Si) photonic electro-optic modulators can be fabricated using wafer-scale technology compatible with the semi-

conductor industry, Si depletion-mode phase electro-optic modulators (EOMs) are limited to an electrical 3-dB bandwidth of about 50 GHz [6], whereas applications will benefit by having access to higher RF frequencies. Bulk lithium niobate (LN) modulators [7] and etched LN modulators [8] can scale to 70-100 GHz bandwidths, but are not integrated with the Si photonics toolkit and fabrication process adopted widely over the last decade. Here, we show an ultra-high-bandwidth Mach-Zehnder EOM, based on silicon photonics, made using conventional lithography and wafer-scale fabrication, bonded to an unpatterned LN thin film using a low-temperature (200°C) back-end process without etching or patterning the LN film. Our design allows for compatibility with silicon photonics, with light input/output and optical components, including directional couplers, low-radius bends, and path-length difference segments, realized in a foundry Si photonics process while avoiding high temperature processing [9]. This hybrid LN-Si MZM achieves beyond 100 GHz 3-dB electrical bandwidth.

6.4.1 Fabrication

The fabrication approach for the final devices developed for this thesis work is similar to the general approach of Chapter 4, but with a few changes.

In our fabrication approach, depicted in Fig. 6.9, MZMs were built on a silicon photonics platform, using photolithography on silicon-on-insulator wafers (220 nm Si thickness, 3 μm oxide thickness) and did not require sub-resolution features unlike most plasmonic or polymeric slot modulators [10, 11]. Silicon thinning (down to 150 nm) and feature patterning were followed by oxide deposition and subsequent chemical mechanical polishing and oxide thinning by a timed wet etch (diluted hydrofluoric acid) process. After die segmentation, commercially-procured x-cut thin-film LN on insulator (NanoLN, Jinan Jingzheng Electronics Co. Ltd.) was bonded over a large area (1 cm^2) with a pressure of 45 kPa, but not processed further (e.g., no etching [12, 13] or sawing [14] of LN was performed). Oxide bonding was done at room temperature after surface cleaning and surface plasma activation steps. The bonded sample was thermally annealed at 200°C for one hour under pressure. The bonded stack has been shown to withstand repeated temperature-cycling to

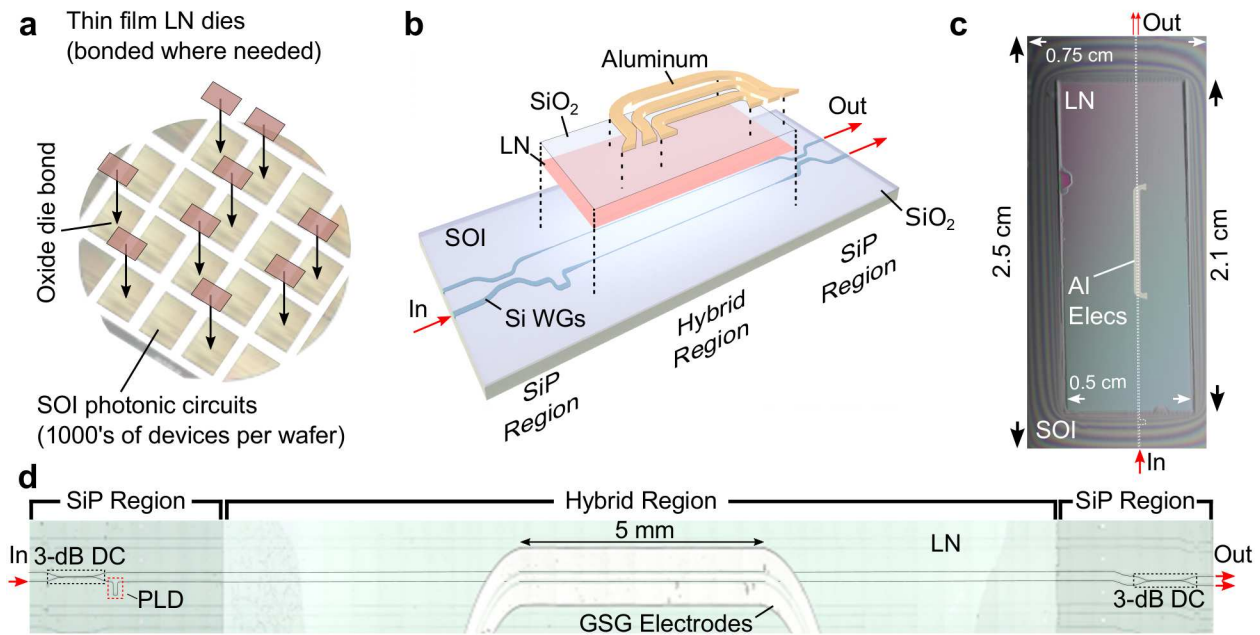


Figure 6.9: **a** Thin film x-cut lithium-niobate (LN) on insulator dies were bonded at room temperature to segmented dies of a patterned and planarized silicon-on-insulator (SOI) wafer which contained fabricated silicon photonic waveguide circuits. No etching or patterning of the LN film was performed. **b** Exploded representation of the EOM, where an unpatterned, un-etched LN thin film was bonded to a Mach-Zehnder interferometer fabricated in Si. Aluminum electrodes were deposited on a 50 nm SiO₂ layer over the LN film. SiP Region denotes the SiO₂-clad region outside the bonded LN film, containing Si waveguide circuits, such as feeder waveguides, bends, directional couplers, and path-length difference segments. **c** Top view of a representative fabricated hybrid Si-LN EOM test chip, which contains 60 EOM waveguide structures in parallel (in the north-south direction); for this report, test electrodes for use in push-pull configuration were only fabricated on one EOM device. **d** Composite microscope image of the EOM. DC: directional coupler, PLD: path-length difference, GSG: ground-signal-ground, SiP: Si photonics.

at least 300°C [15], sufficient for the post-processing required here. In fact, several fabricated chips were repeatedly processed, after bonding, through multiple cycles of electrode formation, removal and re-formation, in search of the optimal dimensions. No debonding or noticeable degradation to the stability or quality of the samples occurred during these additional process steps. The LN die handle was removed, followed by coplanar waveguide electrode formation using aluminum deposition, with total electrode thickness of 1.6 μm . A fully fabricated chip is shown in Fig. 6.9c; a microscope image of the EOM is provided in Fig. 6.9d. The electrodes used here are more than 15 times thinner than those used in Ref. [7], thus improving fabrication practicality. The silicon photonic features were made on a high-resistivity Si handle wafer, potentially mitigating piezoelectric resonances from traditional LN substrates [16]. As described below, the optical input and output from the MZM section were through (crystalline) silicon photonic waveguiding structures.

6.4.2 Electro-Optic Mach-Zehnder Modulator Design

For the MZM reported here, the silicon photonics region outside the bonded LN area included four types of optical waveguide structures: fully-etched tapers for light input and output from the chip (edge couplers), single-mode broadband directional couplers (>15 dB extinction ratio from 1525-1575 nm, maximum of approximately 30 dB), path-length difference (PLD) segment (including spline curve bends), and adiabatic waveguide tapers for inter-layer transitions (Si-to-LN and vice-versa). Precise foundry processing of the Si photonic features results in accurate and repeatable formation of the directional coupler splitting ratio. Since the LN layer is neither patterned nor etched in our design, there was no alignment issue at the bonding step; the Si features alone determine the optical propagation path.

The adiabatic waveguide tapers were designed to achieve a vertical inter-layer transition (from Si to LN, and the reverse). As shown in Fig. 6.1, the design uses the TE-polarized fundamental guided mode, which is also used in conventional silicon photonics at 1.5 μm wavelengths [17]. Since the refractive index of Si at these wavelengths (approximately 3.5) is significantly higher

than that of LN (approximately 2.2), the large index difference enables control of the mode size and location (i.e., mainly in the Si rib or the LN slab) through lithography of the Si layer alone. Thus, only the width of the Si waveguide (w) was varied in our design; when $w > 600$ nm, light at $1.55 \mu\text{m}$ is mostly confined within the Si rib with confinement factor $\Gamma_{Si} = 64\%$ (Mode A) and $\Gamma_{Si} = 58\%$ (Mode B). For $w = 320$ nm, light is guided in Mode C and sees the LN slab layer, with confinement fraction in the LN layer calculated as $\Gamma_{LN} = 81\%$ and $\Gamma_{Si} = 5\%$. Longitudinal Poynting vector simulations of these modes are shown in Fig. 6.1c. The Mode B to Mode C transition loss is estimated as 0.1 dB from simulations and is described in more detail in previous work [18]. A benefit of these high-bandwidth modulators is that Γ_{LN} has less variation with small errors in fabricated waveguide dimensions than plasmonic or polymeric slot waveguide MZMs.

Vertical, inter-layer transitions to and from the hybrid LN-Si region occur only where needed, inside the perimeter of the bonded region. Optical losses between Modes A and B are minimized by keeping the Si waveguide wide ($w = 650$ nm) when crossing into the hybrid region. Thus, the edges of the bonded thin film, even if rough on the scale of the optical wavelength, do not significantly affect optical propagation. This makes the back-end integration of thin-film LN simple and feasible, without requiring precision etching or patterning of either LN or silicon after bonding. Complex waveguiding circuits can be built up with a single bonded layer and multiple vertical transitions, as shown elsewhere [18], but were not required here. A design library of hybrid LN-Si components was created to aid in simulations and design within the Lumerical Interconnect simulation environment [19], of which portions of the design manual are included in Chapter 3.

6.4.3 Electro-Optic Measurements

Light input and output was achieved using tapered single-mode, polarization-maintaining fibers, whose positions were controlled using micro-positioning stages. From test structures, an optical propagation loss of -0.6 dB/cm in the hybrid LN-Si region was measured. The propagation losses in the Si-only regions were about -1.3 dB/cm and are kept short in this design. The edges of the silicon photonic chip were lightly polished, but not fully prepared or packaged; hence, the

edge coupling loss was about -3 dB per edge and the total fiber-to-fiber insertion loss was -13.6 dB. The calculated intrinsic loss of the full MZM (not including edge couplers), based on the measured propagation loss (-0.6 dB/cm in the EOM, -1.3 dB/cm outside the EOM) and the device length (0.5 cm for the EOM, 1.67 cm outside the EOM), simulated inter-layer transition loss estimates (-0.1 dB each), should be about -2.9 dB. However, the actual insertion loss was around -7.6 dB. The extra 4.7 dB is likely due to higher-than-expected loss in the broadband directional couplers and tapers, as well as an estimated (from simulations) additional -0.4 dB loss due to the electrical lines, which pass directly over the optical mode (see Fig. 6.9d). It is also possible that the propagation losses in this particular device are higher than expected due to the multiple re-fabrication performed on this chip in search of the optimum electrode structure. At low speeds, the MZM demonstrated a high extinction ratio (> 20 dB) as shown in Fig. 6.10a, with $V_{\pi}L = 6.7$ V.cm at dc for an $L = 0.5$ cm device.

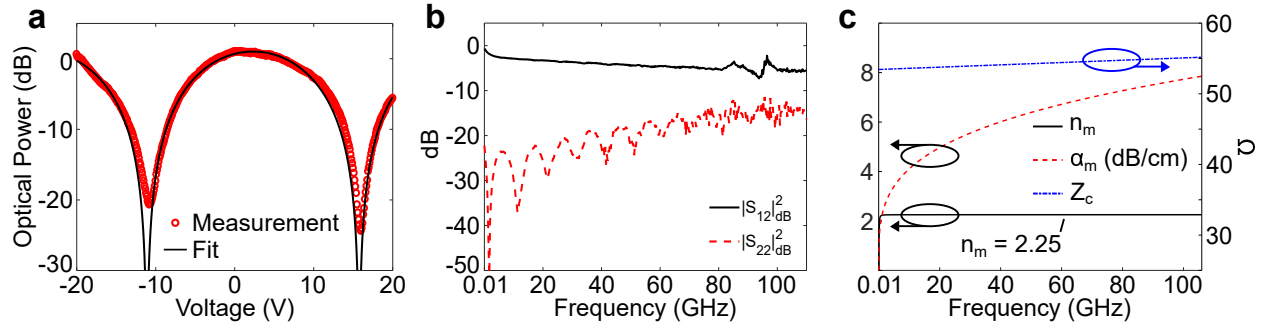


Figure 6.10: **a** Normalized optical transmission of the Mach-Zehnder interferometric electro-optic Modulator (MZM), versus dc voltage at optical wavelength = 1560 nm. Fitted $V_{\pi}L = 6.7$ V.cm for device length $L = 0.5$ cm. **b** Measured electrical S-parameters of the MZM's coplanar-waveguide line used to model the transmission line characteristics. **c** Left y-axis: extracted microwave phase index n_m and microwave loss α_m (dB/cm) over the dc-110 GHz frequency range. Right y-axis: characteristic electrode impedance Z_c (Ω).

RF measurements were performed on a bare-die chip using 50- probes rated to 110 GHz and using laboratory equipment and RF waveguide components also rated and calibrated to about 110 GHz. The RF driving waveform was either from an RF oscillator (up to 67 GHz) or three different frequency multipliers (sequentially covering the range of frequencies up to 106 GHz). GSG probes were used for both launch and termination. Calibration of the signal pathway was performed using

a high-frequency RF power sensor. To inform a computational model of the expected behavior, electrical S-parameters were measured using a Vector Network Analyzer up to 110 GHz, as shown in Fig. 6.10b, and analyzed using standard algebraic transformations and lossy transmission line circuit analysis [4]. The minor artifact near 90 GHz is attributed to repeated testing by contact probes, and does not disrupt the smoothly-varying general trend seen in the data. The microwave refractive index, n_m , was fitted to a power-law equation and the characteristic impedance, Z_c , was fitted to a first-order polynomial of the RF frequency. As shown in Fig. 6.10c, $n_m = 2.25$ and Z_c varied between 53.4 and 55.1 Ω from dc to 110 GHz. The microwave loss, α_m , when fitted to a power-law equation, followed approximately an $f^{1/4}$ dependence, in contrast with the typical $f^{1/2}$ dependence in traditional EOMs [7]. Because we have relatively thin electrodes and a Si substrate, α_m is not due solely to conductor loss, and instead, includes a combination of conductor, substrate, and radiation losses.

Using the electro-optic bandwidth theory derived in Chapter 1 and the extracted parameters of Fig. 6.10c (which used Equations (6.25) and (6.26)), a calculated electro-optic bandwidth curve is shown in Fig. 6.11 (solid black line) along with the measured electro-optic response using the OSA sideband technique of Section 6.3.5. Specifically, the method of Ref. [5] was used to detect signals and modulation sidebands at an optical wavelength of 1560 nm. With the modulator biased at quadrature, the difference (log scale) between the optical intensity of the first sideband and carrier signal was used to extract the modulation index, and thus the frequency response, from 106 GHz down to 2 GHz (providing a safe margin for the 0.18 GHz resolution of the OSA). The peak-to-peak RF drive amplitude was about 1 V. Frequency multipliers were used for the frequency range above 67 GHz up to 106 GHz. The electro-optic response is shown in Fig. 6.11, and an (electrical) 3-dB bandwidth was observed to lie well beyond 106 GHz, the limit of our measurement capabilities. The measurement matches well with the calculated response (solid black line in Fig. 6.11). Electro-optic measurements at frequencies beyond 67 GHz require RF multipliers and time-consuming calibrations using appropriate waveguides, cables, probes and detectors for each frequency band, as observed elsewhere [20]. Some of the scatter in the measurements at the highest frequencies arises

from the calibration of the frequency extenders, which have nonlinear and discontinuous dispersion curves. The measured flat-spectrum modulation response is consistent with our simulation based on electrical S-parameter measurements, which predicts flat frequency response to even higher frequencies.

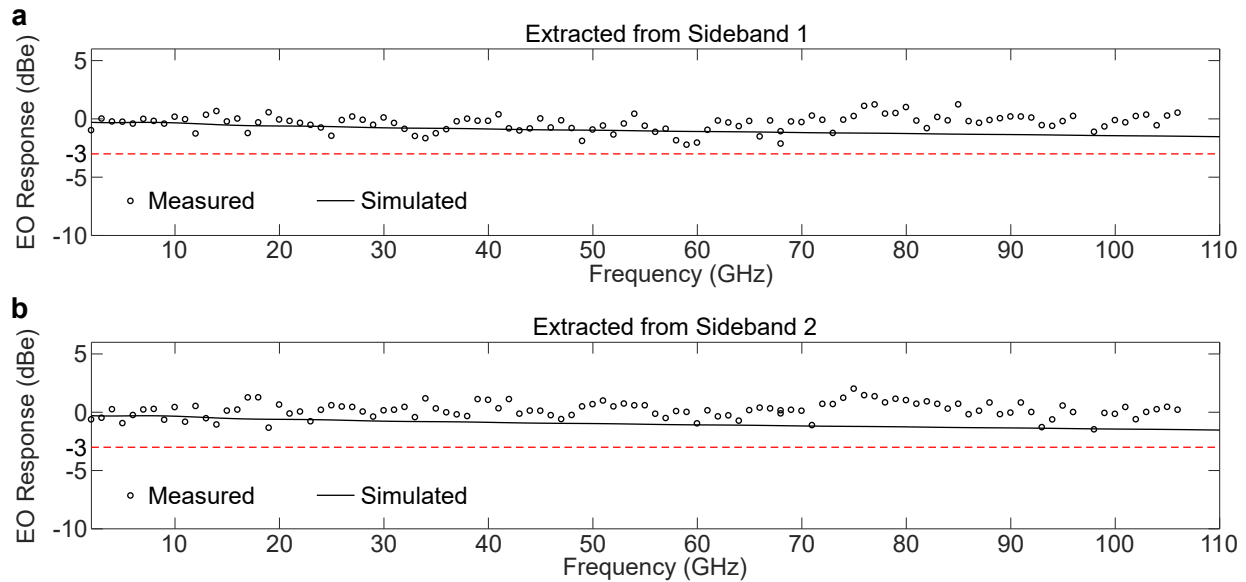


Figure 6.11: Electro-optic response of the EOM for both sidebands (a and b) from the optical spectrum analyzer. Solid black line: calculated response from electrical S-parameters of Fig. 3c; black circles: electro-optic response from sideband OSA measurements.

The product $V_{\pi}L = 6.7$ V.cm (with a 0.5 cm length) in this device compares favorably with other high-bandwidth LN MZIs and commercial technology, but the present devices were not designed to minimize $V_{\pi}L$. Recently, a fully-etched thin-film LN-on-SiO₂ MZM was reported, which achieved low $V_{\pi}L = 2.2$ V.cm [8]. In contrast with our device, that device is not integrated with other integrated photonics components, and relies on etching LN, which may lead to concerns such as heat and pyroelectric charge buildup, structural defect formation and Nb depletion [21, 22]. An order-of-magnitude lower $V_{\pi}L$ product can be achieved using plasmonic [23] or graphene [24] modulators, which are less widely adopted than LN modulators at this time.

6.5 Conclusion

In this thesis work, an un-patterned thin-film of LN was simply bonded at room temperature to the patterned and planarized Si waveguide circuits, with an anneal step at 200°C. In contrast, fabrication of bulk titanium-indiffused LN modulators and doped III-V or Si modulators require at least 600°C and typically 900-1000°C [25, 26], limiting them to either standalone or front-end-of-line device fabrication. Based on our approach, integration of electronic circuits alongside a very-high-bandwidth LN EOM may be envisioned. More complex integrated optics can be realized, which use a wider range of silicon photonic components such as filters, interferometers and detectors alongside one or several ultra-high-bandwidth modulators, formed using single-step bonding. Integration may also avoid the challenges of traditional packaging of LN EOMs: the 70-GHz unpackaged LN modulator of Ref. [7] was reported to achieve a 3-dB bandwidth, when packaged into a stand-alone module, of only about 30 GHz [27].

In summary, an electro-optic Mach Zehnder modulator (MZM) based on single-mode silicon (Si) photonic circuits bonded at low temperature to an unpatterned, un-etched thin-film of lithium niobate (LN) and utilizing the well-known Pockels electro-optic effect has been shown. Both theory and measurements support the performance of this device as a greater-than-100-GHz electrical bandwidth EOM, realized using a new design and fabrication process that brings lithium niobate, the traditional electro-optic material-of-choice in the first few decades of integrated optics, into compatibility with silicon photonics, the more recent platform for more complex integrated optics. The input and output are in silicon photonics and, through the use of inter-layer vertical waveguide transitions, the device is not sensitive to the rough edges, if any, of the LN thin film. The fabrication process, which does not require etching or sawing of LN, is based on a standard silicon photonics foundry fabrication flow. Such a device can bring ultrawide electro-optic bandwidths to integrated silicon photonics, and benefit applications in analog and digital communications, millimeter-wave instrumentation, analog-to-digital conversion, sensing, antenna remoting and phased arrays.

6.6 Acknowledgments

Chapter 6, in part, is currently being prepared for submission for publication of the material. Peter O. Weigel, Jie Zhao, Kelvin Fang, Hasan Al-Rubaye, Douglas Trotter, Dana Hood, John Mudrick, Christina Dallo, Andrew T. Pomerene, Andrew L. Starbuck, Christopher T. DeRose, Anthony L. Lentine, Gabriel Rebeiz and Shayan Mookherjea. Portions of Chapter 6 are reprinted from Conference on Lasers and Electro-Optics (CLEO) 2018. Peter O. Weigel, Jie Zhao, Douglas Trotter, Dana Hood, John Mudrick, Christina Dallo, Andrew T. Pomerene, Andrew L. Starbuck, Christopher T. DeRose, Anthony L. Lentine and Shayan Mookherjea, paper SF2I.4. The dissertation author, together with his adviser, led the research efforts for this work and co-authored the papers.

Bibliography

- [1] Yariv A, Yeh P. Photonics. Oxford University Press Oxford, UK.; 2007.
- [2] Suchoski P, Findakly TK, Leonberger F. Stable low-loss proton-exchanged LiNbO₃ waveguide devices with no electro-optic degradation. *Optics letters*. 1988;13(11):1050–1052.
- [3] Farin G. Curves and surfaces for computer-aided geometric design: a practical guide. Elsevier; 2014.
- [4] Pozar DM. Microwave engineering. John Wiley & Sons; 2009.
- [5] Shi Y, Yan L, Willner AE. High-speed electrooptic modulator characterization using optical spectrum analysis. *Journal of lightwave technology*. 2003;21(10):2358.
- [6] Sun J, Sakib M, Driscoll J, Kumar R, Jayatilleka H, Chetrit Y, et al.. A 128 Gb/s PAM4 Silicon Microring Modulator; 2018. Paper TH4A.7.
- [7] Noguchi K, Mitomi O, Miyazawa H. Millimeter-Wave Ti:LiNbO₃ Optical Modulators. *Journal of Lightwave Technology*. 1998;16:615–619.
- [8] Zhang M, Wang C, Chen X, Bertrand M, Shams-Ansari A, Chandrasekhar S, et al. Ultra-High Bandwidth Integrated Lithium Niobate Modulators with Record-Low V_{pi}. vol. TH4A.5. OFC; 2018. .
- [9] DeRose CT, Gehl M, Long C, Boynton N, Martinez N, Pomerene A, et al. Radio frequency silicon photonics at Sandia National Laboratories. 2016 IEEE Avionics and Vehicle Fiber-Optics and Photonics Conference (AVFOP); 2016. p. 3–4.

- [10] Zhu S, Lo GQ, Kwong DL. Phase modulation in horizontal metal-insulator-silicon-insulator-metal plasmonic waveguides. *Optics Express*. 2013;21:8320–8330.
- [11] Ayata M, Fedoryshyn Y, Heni W, Baeuerle B, Josten A, Zahner M, et al. High-speed plasmonic modulator in a single metal layer. *Science*. 2017;358:630–632.
- [12] Mercante AJ, Yao P, Shi S, Schneider G, Murakowski J, Prather DW. 110 GHz CMOS Compatible thin film LiNbO₃ modulator on silicon. *Optics Express*. 2016;24:15590–15595.
- [13] Ulliac G, Calero V, Ndao A, Baida F, Bernal MP. Argon plasma inductively coupled plasma reactive ion etching study for smooth sidewall thin film lithium niobate waveguide application. *Optical Materials*. 2016;53:1–5.
- [14] Courjal N, Devaux F, Gerthoffer A, Guyot C, Henrot F, Ndao A, et al. Low-loss LiNbO₃ tapered-ridge waveguides made by optical-grade dicing. *Optics Express*. 2015;23:13983–13990.
- [15] Weigel PO, Mookherjea S. Reducing the thermal stress in a heterogeneous material stack for large-area hybrid optical silicon-lithium niobate waveguide micro-chips. *Optical Materials*. 2017;66:605–610.
- [16] Nightingale JL, Becker RA, Willis PC, Vrhel JS. Characterization of frequency dispersion in Ti-indiffused lithium niobate optical devices. *Applied Physics Letters*. 1987;51:716–718.
- [17] Vlasov YA, McNab SJ. Losses in single-mode silicon-on-insulator strip waveguides and bends. *Optics Express*. 2004;12:1622–1631.
- [18] Weigel PO, Savanier M, DeRose CT, Pomerene AT, Starbuck LA, Lentine AL, et al. Lightwave Circuits in Lithium Niobate through Hybrid Waveguides with Silicon Photonics. *Scientific Reports*. 2016.
- [19] Weigel PO, Mookherjea S. Process Design Kit and Modulator Simulation for Hybrid Silicon-Lithium Niobate Integrated Optics. *CLEO*; 2017.
- [20] Hoessbacher C, Josten A, Baeuerle B, Fedoryshyn Y, Hettrich H, Salamin Y, et al. Plasmonic modulator with >170 GHz bandwidth demonstrated at 100 GBd NRZ. *Optics Express*. 2017;25:1762–1768.
- [21] Ren Z, Heard PJ, Marshall JM, Thomas PA, Yu S. Etching characteristics of LiNbO₃ in reactive ion etching and inductively coupled plasma. *Journal of Applied Physics*. 2008;103:034109.
- [22] Kirkby CJ. Low-energy ion-beam processing damage in lithium niobate surface-acoustic-wave optical waveguide devices and its post-manufacture removal. *Journal of Materials Science*. 1992;27:3637–3641.
- [23] Haffner C, Heni W, Fedoryshyn Y, Niegemann J, Melikyan A, Elder DL, et al. All-plasmonic Mach-Zehnder modulator enabling optical high-speed communication at the microscale. *Nature Photonics*. 2015;9:525–528.

- [24] Soriano V, Midrio M, Contestabile G, Asselberg I, Campenhout JV, Huyghebaerts CG, et al. Graphene-silicon phase modulators with gigahertz bandwidth. *Nature Photonics*. 2018;12:40–44.
- [25] Wooten EL, Kissa KM, Yi-Yan A, Murphy EJ, Lafaw DA, Hallemeier PF, et al. A Review of Lithium Niobate Modulators for Fiber-Optic Communications Systems. *IEEE Journal of Selected Topics in Quantum Electronics*. 2000;.
- [26] Stolk PA, Gossman HJ, Eaglesham DJ, Jacobson DC, Rafferty CS, Gilmer GH, et al. Physical mechanisms of transient enhanced dopant diffusion in ion-implanted silicon. *Journal of Applied Physics*. 1997;81:6031–6050.
- [27] Howerton MM, Burns WK. *Broadband traveling wave modulators in LiNbO₃*. Cambridge University Press; 2002.

Chapter 7

Second Harmonic Generation in Hybrid Waveguides

7.1 Introduction

The electro-optic modulation discussed so far in this thesis is a special case of a set of optical phenomena known as nonlinear optics. The “nonlinear” portion of that name refers to the frequency mixing process whereby input signals combine in some way (through addition or subtraction of frequencies; the “mixing” process) to generate one or more output signals at different frequencies. The electro-optic Pockels effect in lithium niobate (LN) can be thought of as a type of nonlinear optical process where a high frequency optical signal, typically on the order of tens or hundreds of THz, interacts with a much lower electrical signal, well below 1 THz, to generate a new electromagnetic wave. Since the frequency of the electrical signal is several orders of magnitude lower than that of the optical signal, the generated electromagnetic wave produced by the electrical-optical interaction is assumed to have the same wavelength as the input optical signal, and the electrical signal is treated as a perturbation. This approximation allows for index matching in electro-optic devices, as opposed to the more precise phase matching required in optical-optical nonlinear interactions.

In particular, LN-based nonlinear optical devices have strict phase matching criteria that have hindered their development from research into useful products. The design discussed in this chapter proposes bonding Si-based circuitry, and silicon carbide waveguides in particular (SiC), to a LN film. With the proper design and further development efforts, it may be possible to monolithically integrate electrical circuitry into a LN-based nonlinear optical device to stabilize the highly-sensitive phase matching conditions.

7.2 Optical Second-Harmonic Generation

In the field of nonlinear optics, there are several types of nonlinear processes. In addition to the aforementioned electro-optic Pockels effect, one of the most commonly used processes is second harmonic generation (SHG). Every nonlinear process must conserve energy in some way, and so each nonlinear process is defined by its energy conservation condition. SHG is the process whereby a pump laser in a second-order nonlinear material, such as LN, generates an electromagnetic wave at twice the input laser's frequency ($\omega + \omega = 2\omega$). This chapter will only consider the SHG process.

7.2.1 Derivation of Power at the Generated Second Harmonic Frequency

To begin this derivation, and as with any derivation, a few assumptions must be made. First, it is assumed that the optical modes are linearly polarized horizontally along the crystal (\hat{z}) axis of the x -cut LN. The form we use for the electric field is

$$\mathbf{E}_i(x, y, z, t) = A_i(y)\mathcal{E}_i(x, z)e^{j(\beta_i y - \omega_i t)} + A_i^*(y)\mathcal{E}_i^*(x, z)e^{-j(\beta_i y - \omega_i t)} \quad (7.1)$$

where i is an index used to number the optical waves (this notation becomes helpful when considering more than one wave), A_i is the longitudinal amplitude, \mathcal{E}_i is the transverse wave function of the mode, β_i is the (real) phase constant ($\beta_i = 2\pi n_i / \lambda_i$ where n_i is the effective mode index and λ_i is the

free space wavelength), and ω_i is the angular frequency of the wave ($\omega_i = 2\pi c/\lambda_i$). Some authors (e.g., [1]) include a factor of 1/2 in this description of \mathbf{E}_i . Admittedly, there is a justified reason for doing so if the wave is defined by the standard definition of a plane wave¹:

$$\begin{aligned}\mathbf{E}_i &= \mathbf{E}_0 \cos(\omega_i t - \beta_i y + \phi) \\ &= \Re[A_i(y)\mathcal{E}_i(x, z)e^{j(\beta_i y - \omega_i t)}] \\ &= \frac{1}{2}A_i(y)\mathcal{E}_i(x, z)e^{j(\beta_i y - \omega_i t)} + \frac{1}{2}A_i^*(y)\mathcal{E}_i^*(x, z)e^{-j(\beta_i y - \omega_i t)},\end{aligned}\tag{7.2}$$

where \mathbf{E}_0 is a real-valued vector describing the amplitude of the wave and all additional phase information is contained in ϕ .

However, when working with optical waves, the exponential form of \mathbf{E}_i is easier to handle algebraically and is commonly used, and so the form of \mathbf{E}_i in Equation (7.1) is used here with the understanding that $\mathbf{E}_i = 2\mathbf{E}_0 \cos(\omega_i t - \beta_i y + \phi)$.

As with most electromagnetic derivations, we begin with Maxwell's equations, which in differential form and in SI units are

$$\nabla \cdot \mathbf{D}_i = \rho\tag{7.3}$$

$$\nabla \cdot \mathbf{B}_i = 0\tag{7.4}$$

$$\nabla \times \mathbf{E}_i = -\frac{\partial \mathbf{B}_i}{\partial t}\tag{7.5}$$

$$\nabla \times \mathbf{H}_i = \mathbf{J}_i + \frac{\partial \mathbf{D}_i}{\partial t}.\tag{7.6}$$

\mathbf{E}_i represents the electric field in free space, while \mathbf{D}_i is used to describe how the electric field behaves in materials (likewise, \mathbf{B}_i describes magnetic fields in free space and \mathbf{H}_i describes magnetic fields in materials). In Gaussian units, $\mathbf{D}_i = \mathbf{E}_i$ in free space, agreeing with the implications of the previous sentence. However, because we choose to work in SI units, we introduce a constant ϵ_0 so

¹Note that for $x = a + jb$: $\frac{x+x^*}{2} = \frac{(a+jb)+(a-jb)}{2} = \Re[x]$.

that $\mathbf{D}_i = \epsilon_0 \mathbf{E}_i$ and $\mathbf{B}_i = \mu_0 \mathbf{H}_i$ in free space. ϵ_0 is the vacuum permittivity and μ_0 is the vacuum permeability. These are constants with known values: $\epsilon_0 = 8.854187817 \dots \times 10^{-12}$ F/m (Farads per meter) and $\mu_0 = 1.256637061 \dots \times 10^{-6}$ H/m (Henries per meter).

For passive optical waveguides in non-magnetic materials: $\rho = 0$ (there are no free charges), $\mathbf{J}_i = 0$ (there is no electrical current), and $\mathbf{B}_i = \mu_0 \mathbf{H}_i$ (the material is non-magnetic). Taking the cross product of Equation (7.5) and knowing that $\nabla \times (\nabla \times \mathbf{V}) = \nabla(\nabla \cdot \mathbf{V}) - \nabla^2 \mathbf{V}$ for some vector \mathbf{V} , we find that

$$\nabla(\nabla \cdot \mathbf{E}_i) - \nabla^2 \mathbf{E}_i = -\mu_0 \frac{\partial^2 \mathbf{D}_i}{\partial t^2} \quad (7.7)$$

by using Equation (7.6). In a material, $\mathbf{D}_i = \epsilon_0 \mathbf{E}_i$ is no longer necessarily valid. An additional term \mathbf{P}_i is added to account for how the material responds to \mathbf{E}_i :

$$\mathbf{D}_i = \epsilon_0 \mathbf{E}_i + \mathbf{P}_i \quad (7.8)$$

where \mathbf{P}_i is called the dielectric polarization density and responds to the electric field \mathbf{E}_i dependent on the material. \mathbf{P}_i can be expanded as a Taylor series:

$$\mathbf{P}_i = a_1 \mathbf{E}_i + a_2 \mathbf{E}_i \mathbf{E}_i + \dots = \mathbf{P}_i^{(1)} + \mathbf{P}_i^{(2)} + \dots \quad (7.9)$$

The expansion of Equation (7.9) goes to infinity, but since we are considering interactions in LN we only care about first-order (linear) and second-order (nonlinear, i.e. the interaction of multiple input waves) – this is why we only look at two teRMS on the right-hand side of Equation (7.9). Because the first term is linear, it is simply a linear response to \mathbf{E}_i . This is true for all optical waves in a material, even when there are multiple optical waves concurrently propagating in the same material. However, when multiple waves concurrently propagate in a material, they can generate new waves under the proper conditions. The second-order nonlinear term in Equation (7.9) represents the behavior of the material when subject to two optical waves. Likewise, a third-order term would represent the material's response to three optical waves, a fourth-order term would

represent the material's response to four optical waves, and so on. These interactions are governed by energy conservation, so that the newly generated wave in second-order nonlinear interactions has a frequency equal to the sum (or difference) of the initial waves. More specifically, \mathbf{E} in Equation (7.9) is the sum of the two input waves \mathbf{E}_1 and \mathbf{E}_2 , where each has the form of Equation (7.1). In that case, we find that

$$\begin{aligned}
\mathbf{P}_i^{(2)} = & a_2 [A_1^2 \mathcal{E}_1^2 e^{2j(\beta_1 y - \omega_1 t)} + A_2^2 \mathcal{E}_2^2 e^{2j(\beta_2 y - \omega_2 t)} \\
& + 2A_1 A_2 \mathcal{E}_1 \mathcal{E}_2 e^{j((\beta_1 + \beta_2)y - (\omega_1 + \omega_2)t)} \\
& + 2A_1 A_2^* \mathcal{E}_1 \mathcal{E}_2^* e^{j((\beta_1 - \beta_2)y - (\omega_1 - \omega_2)t)} + \text{c.c.}] \\
& + 2a_2 [A_1 A_1^* \mathcal{E}_1 \mathcal{E}_1^* + A_2 A_2^* \mathcal{E}_2 \mathcal{E}_2^*].
\end{aligned} \tag{7.10}$$

Equation (7.10) contains every possible second-order nonlinear interaction. They can be organized by the frequencies in the exponential of each term, which have to add up to ω_i by energy conservation. What this means is that $2\omega_1 = \omega_i$ and $2\omega_2 = \omega_i$ in the first two terms describe second harmonic generation (SHG), $\omega_1 + \omega_2 = \omega_i$ in the third term describes sum frequency generation (SFG), $\omega_1 - \omega_2 = \omega_i$ in the fourth term describes difference frequency generation (DFG), and $\omega_1 - \omega_1 = \omega_i = 0$ and $\omega_2 - \omega_2 = \omega_i = 0$ in the last two terms describe optical rectification (OR). We don't consider the complex conjugate terms because they describe the same processes as the first four terms, but with negative frequencies.

Two waves at fixed frequencies will not excite all these interactions. For example, a single wavelength of light can generate a second-order harmonic by SHG. That same single wavelength of light can never meet the energy conservation conditions of SFG or DFG because they require multiple wavelengths. However, the generated signal from SHG could potentially interact with its first harmonic source via SFG or DFG to generate a third wavelength of light. We can determine the efficiencies of these interactions by using coupled mode theory.

First, we will follow standard convention and replace a_1 and a_2 in Equation (7.9) and Equation (7.10) with $a_1 = \epsilon_0(\epsilon_r - 1)$ and $a_2 = \epsilon_0 \chi^{(2)33} = 2\epsilon_0 d_{33}$. ϵ_r is the relative permittivity of

a material, and $\chi_{33}^{(2)}$ is the second-order nonlinear susceptibility of a LN crystal when all three interacting waves are polarized along the \hat{z} -axis of the crystal [1]. Likewise, d_{33} is the nonlinear coefficient and defined (by historical convention) as $d_{33} = \frac{1}{2}\chi_{33}^{(2)}$.

Next, we can reorganize Equation (7.8) so that

$$\mathbf{D}_i = \epsilon_0 \epsilon_r \mathbf{E}_i + \mathbf{P}_i^{(2)}. \quad (7.11)$$

Because of the addition of $\mathbf{P}_i^{(2)}$ in Equation (7.11), $\nabla \cdot \mathbf{E}_i = 0$ is only exactly true for isotropic materials (so that ϵ_r does not change across space) where $\mathbf{P}_i^{(2)}$ is zero and there are no nonlinear interactions. However, $\nabla \cdot \mathbf{E}_i \approx 0$ is a good assumption in most nonlinear cases. Using this assumption and substituting Equation (7.11) into Equation (7.7) gives the nonlinear wave equation:

$$\nabla^2 \mathbf{E}_i - \mu_0 \epsilon \frac{\partial^2 \mathbf{E}_i}{\partial t^2} = \mu_0 \frac{\partial^2 \mathbf{P}_i^{(2)}}{\partial t^2}, \quad (7.12)$$

where $\epsilon = \epsilon_0 \epsilon_r$. Because we are considering SHG, we know from Equation (7.10) that

$$\mathbf{P}_{\text{SH}}^{(2)} = 2\epsilon_0 d_{33} \left[A_{\text{FH}}^2 \mathcal{E}_{\text{FH}}^2 e^{2j(\beta_{\text{FH}} y - \omega_{\text{FH}} t)} + \text{c.c.} \right] \quad (7.13)$$

$$\mathbf{P}_{\text{FH}}^{(2)} = 4\epsilon_0 d_{33} \left[A_{\text{SH}} \mathcal{E}_{\text{SH}} A_{\text{FH}}^* \mathcal{E}_{\text{FH}}^* e^{j((\beta_{\text{SH}} - \beta_{\text{FH}}) y - (\omega_{\text{SH}} - \omega_{\text{FH}}) t)} + \text{c.c.} \right] \quad (7.14)$$

where “c.c.” is used to denote the complex conjugate and the i subscript has been replaced with “SH” for the interaction that would generate a second harmonic wave from the first harmonic (FH) pump and $\omega_{\text{SH}} = 2\omega_{\text{FH}}$. Now Equation (7.12) can be expanded into its three constituent equations – one for each interacting wave:

$$\nabla^2 \mathbf{E}_{\text{SH}} - \mu_0 \epsilon \frac{\partial^2 \mathbf{E}_{\text{SH}}}{\partial t^2} = \mu_0 \frac{\partial^2 \mathbf{P}_{\text{SH}}^{(2)}}{\partial t^2} \quad (7.15)$$

$$\nabla^2 \mathbf{E}_{\text{FH}} - \mu_0 \epsilon \frac{\partial^2 \mathbf{E}_{\text{FH}}}{\partial t^2} = \mu_0 \frac{\partial^2 \mathbf{P}_{\text{FH}}^{(2)}}{\partial t^2} \quad (7.16)$$

$$\nabla^2 \mathbf{E}_{\text{FH}} - \mu_0 \epsilon \frac{\partial^2 \mathbf{E}_{\text{FH}}}{\partial t^2} = \mu_0 \frac{\partial^2 \mathbf{P}_{\text{FH}}^{(2)}}{\partial t^2} \quad (7.17)$$

There are two equations for \mathbf{E}_{FH} because SHG requires two pumps at the FH wavelength to maintain energy conservation.

For now we will only consider Equation (7.16). $\nabla^2 \mathbf{E}_{\text{FH}}$ can be expanded so that

$$\nabla_t^2 \mathbf{E}_{\text{FH}} + \frac{\partial^2 \mathbf{E}_{\text{FH}}}{\partial y^2} - \mu_0 \epsilon \frac{\partial^2 \mathbf{E}_{\text{FH}}}{\partial t^2} = \mu_0 \frac{\partial^2 \mathbf{P}_{\text{FH}}^{(2)}}{\partial t^2} \quad (7.18)$$

where ∇_t is the transverse component of ∇^2 . We can ignore the complex conjugate on each side of the equation and still maintain the equality. In that case, the second-order derivative with respect to \hat{y} can be expanded to get

$$\begin{aligned} \nabla_t^2 \mathbf{E}_{\text{FH}} + \frac{\partial^2 A_{\text{FH}}}{\partial y^2} \mathcal{E}_{\text{FH}} e^{j(\beta_{\text{FH}} y - \omega_{\text{FH}} t)} + j2\beta_{\text{FH}} \frac{\partial A_{\text{FH}}}{\partial y} \mathcal{E}_{\text{FH}} e^{j(\beta_{\text{FH}} y - \omega_{\text{FH}} t)} \\ - \beta_{\text{FH}}^2 \mathbf{E}_{\text{FH}} - \mu_0 \epsilon \frac{\partial^2 \mathbf{E}_{\text{FH}}}{\partial t^2} = \mu_0 \frac{\partial^2 \mathbf{P}_{\text{FH}}^{(2)}}{\partial t^2}. \end{aligned} \quad (7.19)$$

Here we can make a useful observation: the transverse component of \mathbf{E}_{FH} is independent of the transverse component of \mathbf{E}_{SH} . In other words, the mode profile of \mathbf{E}_{FH} is not affected by the presence of \mathbf{E}_{SH} . This means that $\nabla_t^2 \mathbf{E}_{\text{FH}}$ will be the same regardless of whether or not \mathbf{E}_{SH} is present. We can imagine a waveguide that produces exactly the same mode profile but without any nonlinear properties, in which case the right-hand side of Equation (7.18) goes to zero and we are left with the linear wave equation:

$$\nabla_t^2 \mathbf{E}_{\text{FH}} + \frac{\partial^2 \mathbf{E}_{\text{FH}}}{\partial y^2} - \mu_0 \epsilon \frac{\partial^2 \mathbf{E}_{\text{FH}}}{\partial t^2} = 0. \quad (7.20)$$

In a linear waveguide, A_{FH} does not change with propagation length because it does not couple into the SH mode. In this case, $\partial^2 \mathbf{E}_{\text{FH}}/\partial y^2$ simply reduces to $-\beta^2 \mathbf{E}_{\text{FH}}$ and we have

$$\nabla_t^2 \mathbf{E}_{\text{FH}} - \beta^2 \mathbf{E}_{\text{FH}} - \mu_0 \epsilon \frac{\partial^2 \mathbf{E}_{\text{FH}}}{\partial t^2} = 0. \quad (7.21)$$

By substituting Equation (7.21) into Equation (7.19) and using the slowly varying amplitude approximation ($\partial^2 A_{\text{FH}}/\partial y^2 \ll 2\beta_{\text{FH}}\partial A_{\text{FH}}/\partial y$), we have

$$j2\beta_{\text{FH}} \frac{\partial A_{\text{FH}}}{\partial y} \mathcal{E}_{\text{FH}} e^{j(\beta_{\text{FH}}y - \omega_{\text{FH}}t)} = \mu_0 \frac{\partial^2 \mathbf{P}_{\text{FH}}^{(2)}}{\partial t^2}. \quad (7.22)$$

From Equation (7.14) and remembering that $\omega_{\text{SH}} - \omega_{\text{FH}} = \omega_{\text{FH}}$, Equation (7.22) becomes

$$j2\beta_{\text{FH}} \frac{\partial A_{\text{FH}}}{\partial y} \mathcal{E}_{\text{FH}} e^{j\beta_{\text{FH}}y} = -4\omega_{\text{FH}}^2 \mu_0 \epsilon_0 d_{33} A_{\text{SH}} \mathcal{E}_{\text{SH}} A_{\text{FH}}^* \mathcal{E}_{\text{FH}}^* e^{j(\beta_{\text{SH}} - \beta_{\text{FH}})y} \quad (7.23)$$

after taking the second-order derivative of \mathbf{P}_{FH} with respect to time and removing like terms from both sides of the equation. We are interested in learning how A_{FH} changes along the propagation length of the device, so by moving terms around and integrating both sides of Equation (7.23) across the transverse plane, we arrive at an expression for $\partial A_{\text{FH}}/\partial y$:

$$\frac{\partial A_{\text{FH}}}{\partial y} = j \frac{4\pi}{n_{\text{FH}} \lambda_{\text{FH}}} A_{\text{SH}} A_{\text{FH}}^* \Gamma^* e^{-j\Delta\beta y} \quad (7.24)$$

where n_{FH} is the effective mode index of the FH wave, $\Delta\beta = 2\beta_{\text{FH}} - \beta_{\text{SH}}$, and

$$\Gamma = \int_{-\infty}^{+\infty} \mathcal{E}_{\text{SH}}^*(x, z) \cdot \mathbf{d}_{\text{eff}}(x, z) : \mathcal{E}_{\text{FH}}(x, z) \mathcal{E}_{\text{FH}}(x, z) dA \quad (7.25)$$

where $:$ is a double-dot product, the normalization is chosen to be $\int_{-\infty}^{+\infty} |\mathcal{E}_i(x, z)|^2 dA = 1$ and

$$\mathbf{d}_{\text{eff}}(x, z) = \begin{cases} 0 & 0 < x < \infty \\ d_{33} & -h_{\text{LN}} \leq x \leq 0 \\ 0 & -\infty < x < -h_{\text{LN}}. \end{cases} \quad (7.26)$$

In Equation (7.26), h_{LN} is the thickness of the LN film. Equation (7.24) is the coupled mode equation for A_{FH} in SHG in an x -cut LN film-based waveguide.

A similar derivation can be performed with Equation (7.15) to find a coupled mode equation for A_{SH} :

$$\frac{\partial A_{\text{SH}}}{\partial y} = j \frac{4\pi}{n_{\text{SH}}\lambda_{\text{FH}}} A_{\text{FH}}^2 \Gamma e^{j\Delta\beta y} \quad (7.27)$$

In most applications, the assumption that $\partial A_{\text{FH}}/\partial y \approx 0$ is used because the amount of energy transferred into the SH mode is typically much less than the initial energy in the FH mode. This is known as the “undepleted pump” approximation. In that case, A_{FH} in Equation (7.27) does not vary along the propagation length and a simple integration along the propagation direction can be performed to get

$$A_{\text{SH}}(y = L) = \frac{4\pi}{n_{\text{SH}}\lambda_{\text{FH}}\Delta\beta} A_{\text{FH}}^2 \Gamma \left(e^{j\Delta\beta L} - 1 \right) \quad (7.28)$$

where L is the length of the nonlinear region.

While Equation (7.28) is helpful for seeing the relationship between the SH and FH waves, what is more useful is an expression for power in the SH wave. Power in the mode can be found by calculating the Poynting vector \mathbf{S} from $\mathbf{S}_{\text{SH}} = \mathbf{E}_{\text{SH}} \times \mathbf{H}_{\text{SH}}$, finding the time averaged Poynting vector, and integrating the real part along \hat{y} over the transverse plane. Using the definition of \mathbf{E} in Equation (7.1), these operations can be described by

$$P_{\text{SH}} = 2 \int_{-\infty}^{\infty} \Re [\mathbf{E}_{\text{SH}} \times \mathbf{H}_{\text{SH}}^*] \cdot \hat{y} \, dA. \quad (7.29)$$

An expression for \mathbf{H}_{SH} can be found from Equation (7.5). Because we are only interested in the power propagating along the device (i.e. along the \hat{y} -axis) and the electric field is nearly entirely polarized along the \hat{z} -axis, the only component of \mathbf{H}_{SH} that we are concerned with is that which is polarized along the \hat{x} -axis. From Equation (7.5) we have

$$\frac{\partial E_z}{\partial y} = j\omega_{\text{SH}}\mu_0 H_x \quad (7.30)$$

after taking the derivative of H with respect to time. From Equation (7.1) and ignoring the complex conjugate we have

$$E_z = A_{\text{SH}}(y) \mathcal{E}_{\text{SH}}(x, z) e^{j(\beta_{\text{SH}}y - \omega_{\text{SH}}t)}. \quad (7.31)$$

We take the derivative to get

$$\frac{\partial E_z}{\partial y} = \frac{\partial A_{\text{SH}}}{\partial y} \frac{1}{A_{\text{SH}}} E_z + j\beta E_z. \quad (7.32)$$

By substituting Equation (7.27) and Equation (7.28) into Equation (7.32) and replacing “L” in Equation (7.28) with “y,” we get

$$H_x = \frac{\Delta\beta}{\omega_{\text{SH}}\mu_0} \frac{e^{j\Delta\beta y}}{e^{j\Delta\beta y} - 1} E_z + \frac{\beta_{\text{SH}}}{\omega_{\text{SH}}\mu_0} E_z. \quad (7.33)$$

The cross product of \mathbf{E}_{SH} and \mathbf{H}_{SH}^* in Equation (7.29) simplifies to $E_z H_x^*$. The real part of that product is

$$\Re[E_z H_x^*] = \frac{|E_z|^2}{\omega_{\text{SH}}\mu_0} \left(\beta_{\text{SH}} + \frac{\Delta\beta}{2} \right). \quad (7.34)$$

In a device designed for nonlinear optics, $\Delta\beta$ is ideally zero and practically much smaller than β_{SH} , so that in all reasonable cases $\Delta\beta/2 \ll \beta_{\text{SH}}$. In that case we can ignore the second term in Equation (7.34) and can use Equation (7.29) to get

$$P_{SH} = \frac{2\beta_{SH}}{\omega_{SH}\mu_0} |A_{SH}|^2 \int_{-\infty}^{\infty} |E_{SH}|^2 dA, \quad (7.35)$$

but from our normalization condition the integral equals 1 and the power in the SH wave reduces to

$$P_{SH} = 2c\epsilon_0 n_{SH} |A_{SH}|^2. \quad (7.36)$$

In fact, the form of Equation (7.36) is valid for any TE waveguide mode defined by the electric field in Equation (7.1). Thus,

$$P_{FH} = 2c\epsilon_0 n_{FH} |A_{FH}|^2. \quad (7.37)$$

From Equation (7.28) and Equation (7.36), we have

$$P_{SH} = \frac{128\pi^2 c\epsilon_0}{n_{SH}\lambda_{SH}^2 \Delta\beta^2} |\Gamma|^2 |A_{FH}|^4 \sin\left(\frac{\Delta\beta L}{2}\right)^2. \quad (7.38)$$

We will now make two important substitutions. First, we will replace the sine in Equation (7.38) with a sinc: $\sin(x)^2 = x^2 \text{sinc}(x)^2$; second, we will use Equation (7.37) to replace $|A_{FH}|^4$. After making these substitutions, we finally arrive at an expression for power in the SH wave under the undepleted pump approximation:

$$P_{SH} = \frac{8\pi^2 |\Gamma|^2}{n_{SH} n_{FH}^2 c\epsilon_0 \lambda_{FH}^2} P_{FH}^2 L_{NL}^2 \text{sinc}^2\left(\frac{\Delta\beta L}{2}\right) \quad [\text{W}]. \quad (7.39)$$

7.3 Design of Folded Hybrid Silicon Carbide-Lithium Niobate Waveguides for Efficient Second Harmonic Generation

In this section, a design for a highly efficient folded hybrid silicon carbide-lithium niobate (SiC-LN) SHG device is discussed, based on [2]. Although the focus of this thesis has been on electro-optic devices, the theoretical work shown here will hopefully provide a strong case for why

the thin film LN platform should be considered for nonlinear optics, as well as even an idea of how such devices can be fabricated in the not-so-distant future.

7.3.1 A Brief Background of Integrated Photonic Circuits and Nonlinear Optics in LN

Equation (7.39), the power in a SH wave during SHG, consists of leading terms and a $\text{sinc}^2(x)$ term, where x is a function of the phase mismatch $\Delta\beta$. It turns out that for most waveguides designed for SHG, there is significant enough dispersion between λ_{FH} and λ_{SH} that the phase mismatch is prohibitively large, in which case the nonlinear efficiency is negligible and no second harmonic wave is generated. Several solutions to this problem have been investigated and attempted over the years and are documented in [3]. However, for LN photonic circuits, the d_{33} coefficient is desirable due to its size and the fact that two similarly polarized waves at the FH and SH wavelengths can be used efficiently. In this case, the most promising technique for producing high efficiency nonlinear devices is periodic poling of the LN crystal. This is known as periodically poled lithium niobate, or PPLN. PPLN is one of the most well-known and widely used materials, but has not been studied in the proposed configuration: a nonlinear device that can be folded into a compact region without etching PPLN, leveraging the technology to make complex integrated photonic circuits in bonded thin-film lithium niobate [4]. This configuration both minimizes the longest edge of the device on a microchip, and achieves very high conversion efficiency.

High-index-contrast silicon or III-V photonics are used to drive modern integrated optics toward achieving more functionality in a smaller device and energy footprint, and tighter integration with microelectronics. Scaled-up integrated photonic circuits with dozens of electrically-driven or active (e.g., laser or detector) components have been densely integrated within a few squared millimeters [5, 6]. However, nonlinear optical (NLO) devices are difficult to scale-up, for a few different reasons.

Crystalline lithium niobate (LiNbO_3 or LN) has been an attractive material for nonlinear optics (NLO) due to its wide transparency window, low loss, and its large second-order nonlinear

coefficient, d_{33} [7] (five times higher than that of AlN [8], for example). However, NLO devices based on LN (and similar materials) mostly use waveguides with titanium indiffusion or annealed proton exchange to create a relatively weak core-cladding index difference [9, 10, 11], resulting in a large modal effective area, large minimum bending radius and low nonlinear efficiencies. Thus, a long and straight device is typically used to generate appreciable amounts of power by second-harmonic generation or wavelength conversion. Unlike the square footprints achieved in silicon or III-V photonics (which are amenable to microelectronics packaging), LN NLO devices tend to be narrow in one dimension (tens of microns) and very long in the other (several centimeters) [10].

This work presents and studies a way to overcome this limitation. As a representative case study, designs and simulations of an NLO LN device for wavelength conversion from 1550 nm to 775 nm wavelengths are presented and discussed. Two aspects of this approach enable the improved structure: (a) a high-index contrast material, silicon carbide (SiC), is used as a “ridge” to load a thin slab of LN, thus enabling a confined mode with a small effective area A_{eff} at both the fundamental and second-harmonic wavelengths with (simultaneously) low loss, low dispersion, and ease of fabrication; and (b) bends are designed to periodically compensate for walk-off, thus enabling a very compact device with simplified poling and packaging requirements. High conversion efficiencies are predicted even with realistic assumptions for loss, disorder as affecting the periodic poling, and imperfect fabrication of bends.

This design is possible thanks to advances in crystal ion slicing over the past twenty years [12, 13] and the introduction of commercially available LN thin films on handle (abbreviated as LNOI). In fact, a new class of optical waveguides has recently emerged, wherein a semiconductor or glass rib material is bonded or deposited to a LN thin film to form a hybrid waveguide. These hybrid devices have used Si ribs on LN (Si-LN) to make all-optical interferometers [4] and electro-optic modulators [14], and SiN-LN to make nonlinear optical (NLO) waveguides [15] and electro-optic modulators [16]. While SiN-LN hybrid waveguides are useful for nonlinear conversion into the visible regime, the low refractive index of SiN ($n \approx 2$) compared with LN ($n \approx 2.13$ along the crystal

axis) prevents the SiN-LN structure from being used in more complex geometries. Conversely, Si-LN devices are useful because of the high index of Si. By changing the width of the high-index Si rib, the optical mode can be confined in the Si to make low-loss, low-radius bends and complex waveguiding devices that require such bends [4]. Yet the low bandgap of Si (1.1 eV) prevents the hybrid Si-LN waveguide from being used for nonlinear processes in the visible regime.

7.3.2 Overview of the Proposed Structure

Here, we propose a new hybrid waveguide design: amorphous silicon carbide (SiC) which can be deposited by plasma-enhanced chemical vapor deposition (PECVD) onto a LN film, and patterned into waveguides. Such a SiC film has a band gap of $E_{g,\text{SiC}} = 2.18$ eV and a refractive index in the range of 2.9-3.1, as shown in Fig. 7.1. SiC deposition was performed in an Oxford Plasmalab 80+ PECVD at a temperature of 350°C, an RF power of 20 W, a chamber pressure of 1000 mT, a SiH_4 flow rate of 300 sccm, and a CH_4 flow rate of 50 sccm. Under these conditions, we observed a deposition rate of 7.73 nm/min. The SiC used in this work has a much higher refractive index than that of SiN or LN. The n (real refractive index) and k (imaginary refractive index) curves of Fig. 7.1 were fit from ellipsometry over the wavelength range of 200-2000 nm to the Tauc-Lorentz model [17] using the Levenberg-Marquardt non-linear fitting algorithm in Regress Pro, a free spectroscopic ellipsometry fitting software. The fitting parameters and the figure of merit during the fit (χ^2 , not the same as the nonlinear optical susceptibility) are provided in Table. 7.1. The SiC film has a bandgap of $E_g = 2.18$ eV, nearly twice as wide as that of Si.

Recent works in hybrid LN waveguides have used Si ($E_{g,\text{Si}} = 1.1$ eV, $n_{\text{Si}} \approx 3.5$ [18, 19, 4, 14]) and SiN ($E_{g,\text{SiN}} = 5.0$, $n_{\text{SiN}} \approx 2$ [19, 15, 16]). SiC has a wider band gap than Si, and a higher refractive index than both SiN and LN [20]. A wider band gap material allows for nonlinear interactions below 1.1 μm (the band gap of Si), particularly in the visible regime; a higher refractive index than LN allows for a larger variety of hybrid waveguide designs, as well as the potential for high-density

Table 7.1: Fitted parameters of the Tauc-Lorentz model for our PECVD SiC film. See [17] for more details on the Tauc-Lorentz model.

Fit Parameter	Value
A_L	313.795
E_0 (eV)	2.99442
C	2.79093
E_g (eV)	2.1766
ϵ_∞	1.30125
χ^2	71.1215

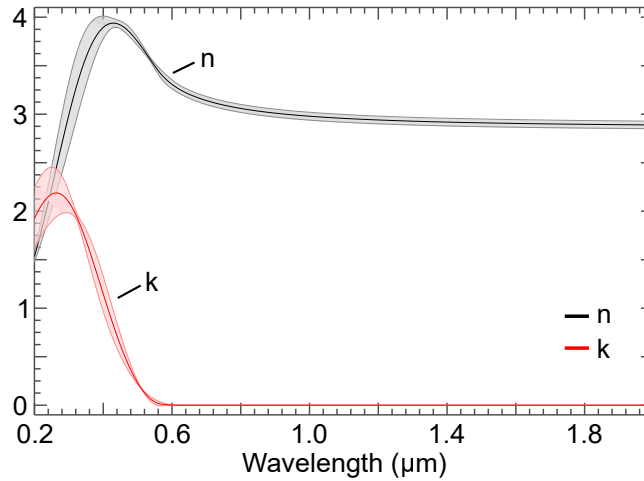


Figure 7.1: Measured n and k curves of PECVD amorphous SiC.

on-chip circuitry similar to what is possible with silicon photonics. SiC is also becoming available through foundry fabrication of devices at wafer-scale, potentially benefiting integrated optics using this material.

The design described in this work consists of two sections with the cross-section of Fig. 7.2a: 1) a traditional straight waveguide NLO section; and 2) several iterations of a straight waveguide NLO section plus a taper plus a 180° bend, as in Fig. 7.2b, to fold the device into a compact footprint and reduce the poling length significantly. Because of the high index of SiC, tight bends can be made in the SiC layer to keep the length of the device short without reducing the total nonlinear interaction length.

As poling length decreases, poling domain width increases based on the number of bends in the device. The design described here has a width of approximately $600 \mu\text{m}$, though wider or

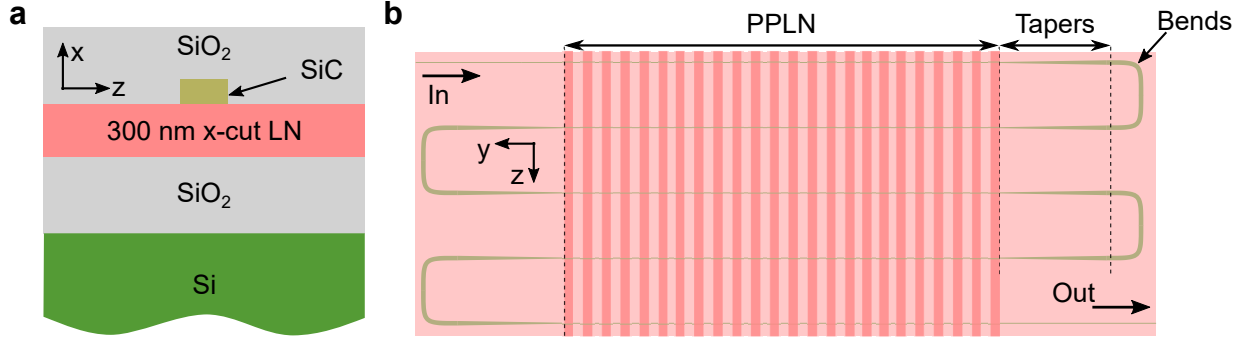


Figure 7.2: **a** Cross-section of hybrid SiC-LN waveguide. **b** Top view of our proposed structure, consisting of a quasi-phase matched region (the “PPLN” section), an adiabatic taper to convert the SiC width from a narrow rib to a wide rib, and two 90° spline bends to wrap the SiC back around into the PPLN section.

narrower folded structures can be designed. This distance is comparable to the poling width of bulk LN devices, which are typically z -cut and poled through the substrate.

7.3.3 Additional Theory of the Nonlinear Interaction Region

As stated earlier, the NLO interaction consider here is second harmonic generation (SHG) from 1550 nm to 775 nm, using fundamental TE-like modes with a cross-section of Fig. 7.2a, where the x -cut LN is a 300 nm film. As will be shown throughout this chapter, choosing such a thin LN film and cladding it with low index SiO_2 increases the efficiency of the SHG process by reducing the optical mode area well below the mode sizes of traditional LN devices.

Because the device of interest here makes use of PPLN, Equation 7.39 is no longer precisely correct. Physically, periodically poling the LN crystal is the act of flipping the sign of the d_{33} nonlinear coefficient, as in Fig. 7.2b. This can be thought of as a square wave, which can be defined mathematically as

$$d(y) = d_{33} \text{sgn} \left[\cos \left(\frac{2\pi y}{\Lambda} \right) \right], \quad (7.40)$$

where $d(z)$ is the value of the nonlinear coefficient d_{33} along the length of the device, sgn is the sign, or signum, function, and Λ is the grating period (the physical period of a single section of poled crystal). By representing $d(y)$ in Equation 7.40 as a Fourier series, we find [3]:

$$d_m = \frac{2}{m\pi} d_{33}, \quad m = \text{odd}. \quad (7.41)$$

In Equation 7.41, m denotes the order of the grating structure. For example, the structure shown in Fig. 7.2b is a first-order grating structure, where each positive and negative section of d_{33} is of equal length. In this case, d_{33} becomes $(2/\pi)d_{33}$, and Equation 7.39 becomes:

$$P_{\text{SH}} = \left(\frac{2}{\pi}\right)^2 \frac{8\pi^2 |\Gamma|^2}{n_{\text{SH}} n_{\text{FH}}^2 c \epsilon_0 \lambda_{\text{FH}}^2} P_{\text{FH}}^2 L_{\text{NL}}^2 \text{sinc}^2\left(\frac{\Delta\beta L}{2}\right) \quad [\text{W}]. \quad (7.42)$$

Higher-order grating structures result in significantly less efficient devices since the $2/\pi$ term is squared in Equation (7.42), though the requirements on poling period length become less strict. It should be noted that even values of m can be used, since an even value of m corresponds to a complete phase mismatch period in one LN domain region, effectively having no impact on the phase matching conditions.

Variations of Equation (7.42) can be derived, and are well cataloged in [3]. Of interest in this chapter is the SH power for a lossy waveguide, which is:

$$P_{\text{SH}} = \left(\frac{2}{\pi}\right)^2 \frac{8\pi^2 |\Gamma|^2 L_{\text{NL}}^2 P_{\text{FH}}^2}{n_{\text{SH}} n_{\text{FH}}^2 \epsilon_0 c \lambda_{\text{FH}}^2} e^{-(\alpha_{\text{FH}} + \alpha_{\text{SH}}/2)L_{\text{NL}}} \times \left[\frac{\sin^2\left(\frac{\Delta\beta L_{\text{NL}}}{2}\right) + \sinh^2\left(\frac{(\alpha_{\text{FH}} - \alpha_{\text{SH}}/2)L_{\text{NL}}}{2}\right)}{\left(\frac{\Delta\beta L_{\text{NL}}}{2}\right)^2 + \left(\frac{(\alpha_{\text{FH}} - \alpha_{\text{SH}}/2)L_{\text{NL}}}{2}\right)^2} \right]. \quad (7.43)$$

α_{SH} and α_{FH} are the SH and FH mode losses, respectively, in units of inverse length. Equation (7.43) is used in Fig. 7.5a. As is commonly done [21], we define the normalized nonlinear conversion efficiency as:

$$\eta_0 = \left(\frac{2}{\pi}\right)^2 \frac{8\pi^2 |\Gamma|^2}{n_{\text{SH}} n_{\text{FH}}^2 c \epsilon_0 \lambda_{\text{FH}}^2} \cdot 100 \cdot 0.01^2 \quad \left[\frac{\%}{\text{W} - \text{cm}^2} \right]. \quad (7.44)$$

In Equation (7.44), only the effective mode indices, wavelength, and Γ can be altered by the designer. In practice, Γ is optimized to improve η_0 , as the mode indices are much less sensitive to changes in the geometry and wavelength is typically pre-determined.

7.3.4 Silicon Carbide-Lithium Niobate Second Harmonic Generation Design

The three variable geometric parameters in the cross-section of Fig. 7.2a are the width (w_{SiC}) and height (h_{SiC}) of the SiC rib, as well as the height (h_{LN}) of the LN film. As stated in the previous section, $h_{\text{LN}} = 300 \text{ nm}$ is chosen to keep the mode area small.

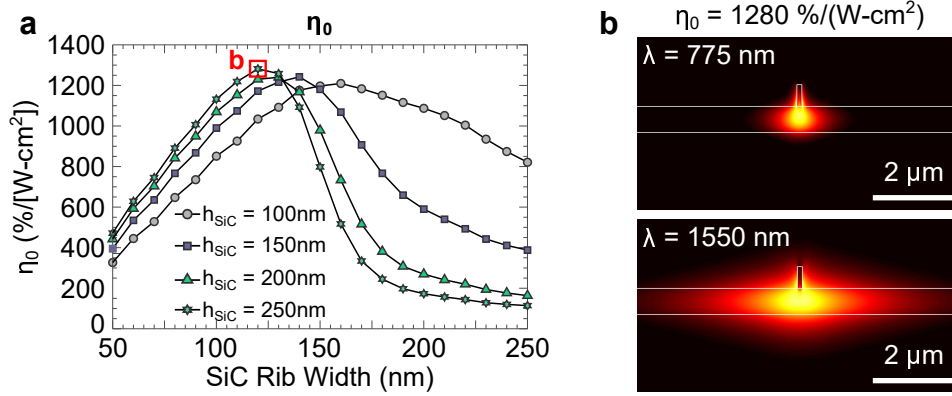


Figure 7.3: **a** Sweep of η_0 versus SiC width for SiC heights of 100 nm, 150 nm, 200 nm, and 250 nm. **b** Mode pictures for $w_{\text{SiC}} = 120 \text{ nm}$ and $h_{\text{SiC}} = 250 \text{ nm}$ for the SH mode (top) and FH mode (bottom).

Lumerical's MODE Solutions was used to simulate the modes of the FH and SH waves for a given waveguide cross-section. η_0 was calculated from Equation (7.44) for a variety of combinations of w_{SiC} and h_{SiC} . These simulated η_0 values are shown in Fig. 7.3a, with modes from the highest η_0 design ($w_{\text{SiC}} = 120 \text{ nm}$, $h_{\text{SiC}} = 250 \text{ nm}$) shown in Fig. 7.3b, where $\eta_0 = 1280 \text{ %/(W-cm}^2\text{)}$. A value of $d_{33} \approx 25 \text{ pm/V}$ was used for these simulations [22].

The local maximum of each curve in Fig. 7.3a exists because of an inherent trade-off between A_{eff} (effective mode area) and LNCF (LN confinement factor) for the two interacting modes; if the modes are too big then η_0 decreases, but the only portion of the modes that contributes to second-order NLO is that which exists in the LN film layer. The ideal waveguide design should result in low A_{eff} values and high LNCF values at both FH and SH wavelengths. However, because the SiC rib has a higher index than that of the LN film, if the SiC is made too large then LNCF will decrease and η_0 will be reduced. For a more detailed analysis of A_{eff} and LNCF, please refer to

sections 7.3.8 and 7.3.9.

Each of the curves in Fig. 7.3a has a maximum over $1200 \text{ \%}/(\text{W}\cdot\text{cm}^2)$ and a grating period Λ between $3.418 \mu\text{m}$ and $3.421 \mu\text{m}$.

7.3.5 Impact of Variations of Design Parameters

The effects of typical fabrication and real-world conditions on the operation of the hybrid SiC-LN SHG NLO device are nontrivial. Some amount of detailed analysis is required not only to understand fabrication tolerances, but also to have a good sense of the amount of post-fabrication tuning (by, for example, varying device temperature or operating wavelength) that is available.

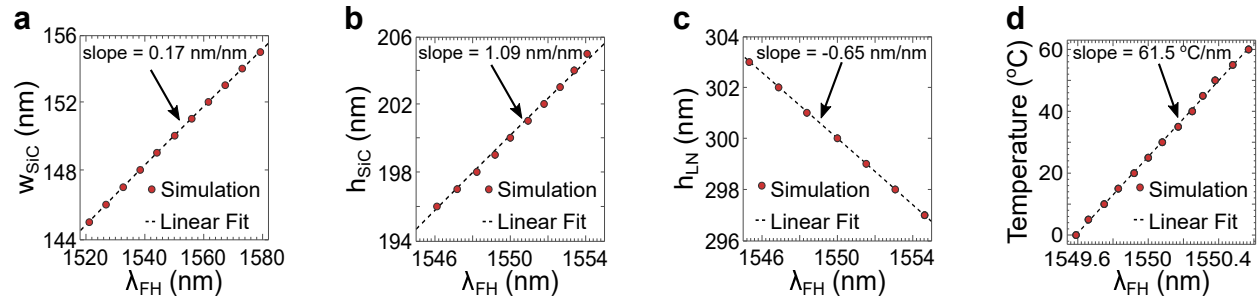


Figure 7.4: How the phase matching FH wavelength shifts as a function of w_{SiC} , h_{SiC} , h_{LN} , and temperature is shown in **a**, **b**, **c**, and **d**, respectively.

The wavelengths of the guided modes which can participate in a quasi-phase matched (QPM; a device that uses periodic poling or some other scheme to force $\Delta\beta = 0$) interaction are determined by the LN grating period Λ , fixed during the design and fabrication. As discussed in Section 7.2.1, $\Delta\beta = \beta_{\text{SH}} - 2\beta_{\text{FH}} - 2\pi/\Lambda$. If we set $\Delta\beta = 0$ (so the device is (quasi)-phase matched) and rearrange this equation we obtain:

$$\Lambda = \frac{2\pi}{\lambda_{\text{FH}}} (n_{\text{SH}} - n_{\text{FH}}), \quad (7.45)$$

where n_{SH} and n_{FH} are the SH and FH mode effective indices and are dependent upon λ_{FH} , w_{SiC} , h_{SiC} , and h_{LN} . Equation (7.45) sets the condition for Λ during the waveguide design at a particular wavelength (in this case, $\lambda_{\text{FH}} = 1550 \text{ nm}$). Ideally, $\Delta\beta = 0$ and second harmonic power is always at

a maximum. In reality, fabrication errors will alter n_{SH} and n_{FH} , and $\Delta\beta \neq 0$ for $\lambda_{\text{FH}} = 1550$ nm. Instead, $\Delta\beta$ will equal zero at some other combination of wavelengths.

This can be thought of as a shift of the $\text{sinc}^2\left(\frac{\Delta\beta_{\text{LNL}}}{2}\right)$ curve in Equation (7.42). In Fig. 7.4a-c, plots are shown of the simulated shift of this peak with fabrication errors for a designed structure of $w_{\text{SiC}} = 150$ nm and $h_{\text{SiC}} = 200$ nm. Each simulated curve was matched with a linear fit (a good approximation for the most part, though there is some quadratic behavior in Fig. 7.4b) to compare the plots. The $\text{sinc}^2\left(\frac{\Delta\beta_{\text{LNL}}}{2}\right)$ peak is most sensitive to the width of the SiC rib in Fig. 7.4a, where a 1 nm deviation causes a nearly 6 nm change in FH wavelength. This is not surprising when one considers Fig. 7.9 in Section 7.3.9: when the SiC rib changes, LNCF – and therefore the mode effective index – will also change, resulting in a shift in the $\text{sinc}^2\left(\frac{\Delta\beta_{\text{LNL}}}{2}\right)$ peak. Because LNCF is less sensitive to changes in the height of the hybrid waveguide (both SiC and LN), h_{SiC} and h_{LN} have less of an impact on the change in the $\text{sinc}^2\left(\frac{\Delta\beta_{\text{LNL}}}{2}\right)$ peak.

The plots of Fig. 7.4a-c assume the device is at 25°C. In Fig. 7.4d, the effect of temperature on the $\text{sinc}^2\left(\frac{\Delta\beta_{\text{LNL}}}{2}\right)$ peak is simulated, where temperature-dependent material refractive indices cause Δk to vary with temperature. The change in refractive index of amorphous SiC as a function of temperature around room temperature is approximately linear, and displays a value of $\frac{dn}{dT} = 9.2 \times 10^{-5} \text{ }^\circ\text{C}^{-1}$ [23]. Similarly, the temperature-dependent refractive index models of [20] and [24] are used for LN and SiO₂, respectively. The simulated device is fairly stable from 0-60°C (Fig. 7.4d). In this range, the FH wavelength varies only by approximately 1 nm, low enough to be tuned with a common semiconductor diode laser to account for thermal drift.

7.3.6 Loss and Disorder

In addition to cross-section geometry fabrication tolerances, one must also consider the impact of a realistic level of propagation loss at the FH and SH wavelengths, and quantify the expected reduction in conversion efficiency that would result. In a real device, there will be some amount of propagation loss that will degrade the generated SH output power. When loss is introduced into the SHG model with Equation (7.43), the peak second harmonic output power is

reduced (Fig. 7.5a). In fabricated waveguides, losses for thin-film LN is 0.3–1.2 dB/cm [25, 26, 15] and around 5 dB/cm for amorphous SiC [27]. For a fairly reasonable hybrid waveguide propagation loss of 2 dB/cm, peak SH power is reduced by 2.98 dB, or approximately a factor of 2. In the case of 5 dB/cm propagation loss – the upper loss limit for this waveguide, since SiC is its most lossy material – peak SH power is reduced by approximately a factor of 5.

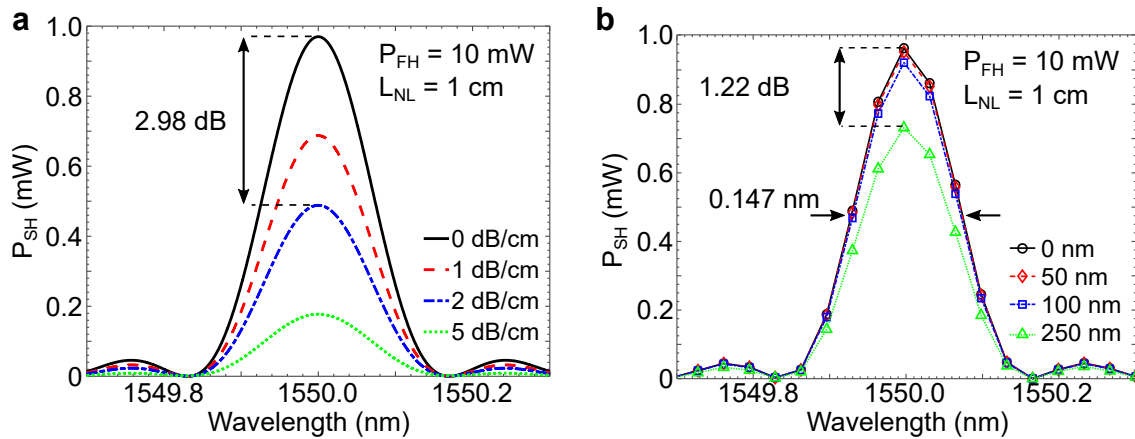


Figure 7.5: Simulated P_{SH} when loss is added to the model (a) and when duty cycle error is added to the model (b). In both cases, the input power (P_{FH}) is 10 mW and the nonlinear interaction length is assumed to be 1 cm. In b, each curve represents a different RMS poling period error, from 0 nm (no error) to 250 nm.

A similar analysis for Fig. 7.5a was performed in Fig. 7.5b, but instead of adding loss to the waveguide it was assumed that the QPM grating period had different amounts of duty cycle error. “Duty cycle error” refers to variations in the periodicity of domain inversion regions of the LN film. For this design, $\Lambda = 2.79 \mu\text{m}$. While these grating periods can be expected to be periodic on average, local disorder is inevitable during poling of the domain inversions. Fig. 7.5b uses direct numerical integration of Equations (7.15)-(7.17) to calculate P_{SH} under the undepleted pump approximation. For realistic values of duty cycle error (0-0.25 μm), there is at most a 1.22 dB drop in maximum P_{SH} . In the case of a 0.1 μm duty cycle error, the drop in maximum power and the FWHM bandwidth reduction are both negligible. For this reason we expect the hybrid SiC-LN waveguide to be quite robust to QPM grating period duty cycle error.

7.3.7 Bent Hybrid Waveguide Region

A high-index contrast hybrid waveguide such as SiC-LN can be formed into low-loss, low-radius bends to connect straight NLO waveguide sections, as shown in Fig. 7.2b. A top view of a single 180° bend with tapers and phase markings is shown in Fig. 7.6a, where an adiabatic linear taper is used to connect the nonlinear mixing section with the bent section. A straight wide SiC waveguide is placed between the adiabatic taper and the bend to account for phase mismatch that occurs between the FH and SH waves in the taper and bend. If the FH and SH waves are out of phase, then the newly generated SH wave in each additional nonlinear mixing section could destructively interfere with the previously generated SH waves. The phases ϕ in Fig. 7.6b are $\Delta\beta L$ radians along the lengths of the tapers, wide straight waveguides, and bends.

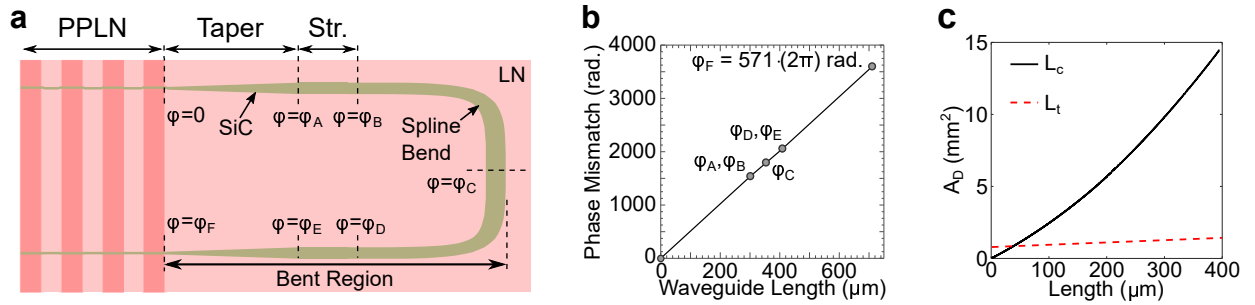


Figure 7.6: **a** Top view of the 180° bend, plus tapers and additional straight waveguides (“Str.”), connecting adjacent QPM NLO sections. The phase along the structure is tracked in **b** to ensure that an integer multiple of $\Delta k = 2\pi$ rad. occurs at the output of the bend. **c** Plot of device area A_D versus L_c (solid black curve) when $L_t = 100 \mu\text{m}$ and L_t (dashed red curve) when $L_c = 40 \mu\text{m}$. For both curves, $L_{NL} = 1 \text{ cm}$ and $n = 10$.

Two 90° spline bends are used in Fig. 7.6 to create the 180° bend. In order to minimize the total footprint of the device, we derive an approximate equation for its area:

$$A_D = w_D \times h_D \approx 2L_c L_{NL} \frac{n}{n+1} + 4L_t L_c n + 4L_c^2 n, \quad (7.46)$$

where A_D is the footprint of the device, $w_D = 2L_c n$, $h_D = L_s + 2L_t + L_c$, L_c is the characteristic length of the 90° spline bend, L_{NL} is the total nonlinear interaction length (the sum of all the straight narrow section lengths), n is the number of 180° turns, and L_t is the length of the adiabatic taper. As one should expect, A_D is proportional to the square of L_c , meaning that L_c , not L_t , is more

critical when considering a compact design. This behavior is shown in Fig. 7.6c. For this reason, an important design consideration for this structure is minimization of the characteristic spline bend without incurring significant optical losses. In addition, reducing L_c reduces the width of the device, resulting in a narrower poling width.

Simulated spline bending losses are shown in Fig. 7.7a,b at 775 nm and 1550 nm, respectively. These simulations were performed in Lumerical's FDTD Solutions software. Losses are higher for the 1550 nm wave because the modes are larger and less confined in the SiC rib for a given rib width. For our design, we chose a characteristic length of $30 \mu\text{m}$ and a SiC rib width of 700 nm. From Fig. 7.7a,b, this is a good compromise between low losses and short L_c .

Since the narrow (nonlinear section, width of 150 nm) and wide (spline bend, width of 700 nm) SiC rib widths – see Fig. 7.6a – are now determined for this design, connecting them with a linear taper is simply a matter of determining L_t . Taper losses for various L_t at both the FH and SH wavelengths, also simulated with Lumerical's FDTD Solutions software, are provided in Fig. 7.7c. We chose a value of $L_t = 300 \mu\text{m}$.

Using the device parameters chosen in this work, and for $L_{NL} = 1 \text{ cm}$ and $n = 10$, $A_D = 0.94 \text{ mm}^2$. This means a 1 cm long device can be reduced to less than a 1 mm^2 area with a maximum dimension of less than 1.6 mm. The loss penalty for such a device is 2.4 dB for the FH wave and 0.4 dB for the SH wave, and are almost entirely due to taper losses. These losses can be reduced by choosing a longer taper length, though this would increase the footprint of the device.

The waveguiding components in the bent region (see Fig. 7.6a) are subject to fabrication tolerances, and these fabrication tolerances can impact the SH output power because of interference between separately generated SH waves. In Fig. 7.7d, direct numerical integration was used to calculate P_{SH} versus wavelength for several waveguide width errors, similar to what was done in Fig. 7.5b with duty cycle error. In Fig. 7.7d, P_{SH} is calculated for RMS waveguide width errors between 0 nm and 10 nm along the length of each linear waveguide component for a structure with 10 bent regions and 1 mm nonlinear sections, for a total nonlinear interaction length of 1 cm. The input FH power is 10 mW.

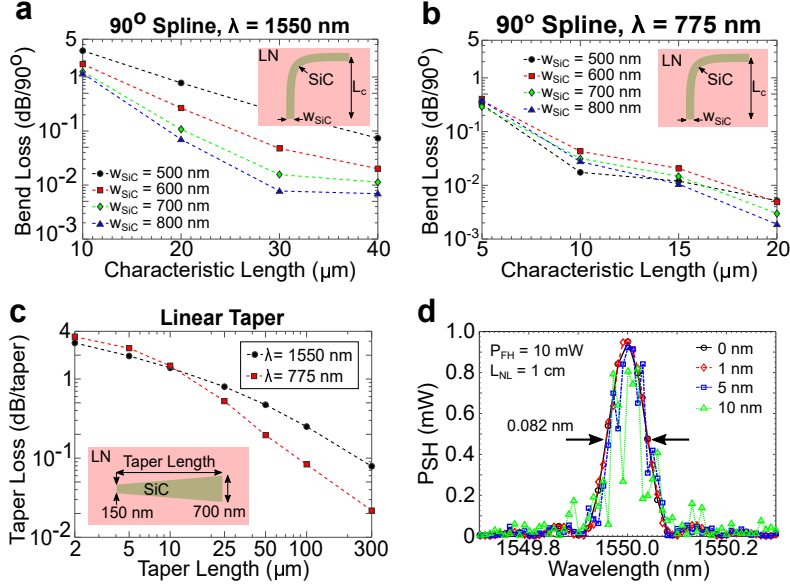


Figure 7.7: Simulated spline bending losses for the SH and FH waves are shown in parts **a** and **b**, respectively. Losses are significantly lower for the SH wave because of its reduced mode size. Simulated taper losses are shown in part **c** for both SH and FH waves. **d** Simulated SH output power in a bent hybrid SiC-LN NLO, SHG device with 10 bends and 10 nonlinear sections 1 mm in length each. Different RMS waveguide width errors between 0 nm (no error) and 10 nm in the bent region (Fig. 7.6a) were simulated.

The full width half max (FWHM) of the curves in Fig. 7.7d – even with 0 nm RMS waveguide width error – is 0.082 nm compared with the FWHM of 0.147 nm in Fig. 7.5. This reduction in FWHM can be explained by the additional phase matching requirements of the bent region: in the bent region, a particular device geometry has been carefully chosen so that the phase difference between the SH and FH waves at the output of the bent region is precisely a multiple of 2π (Fig. 7.6b). As wavelength changes, that phase matching condition is no longer met and separately generated SH waves partially interfere to reduce the SH output power at wavelengths other than 1550 nm. However, the device is tolerant to RMS waveguide width errors up to 5 nm. At a 10 nm waveguide width RMS error the curve of Fig. 7.7d loses its shape, though certain wavelengths still generate sizable output SH power.

Because the phase-matching curve of the device narrows with the addition of waveguide bends, fabrication of this device will be slightly more challenging than standard nonlinear optical device fabrication. However, unlike traditional LN devices which are made by indiffusion or

implantation, features in the SiC rib can be fabricated with photolithography or electron beam lithography, in which case the ribs width and height can be made accurate down to fewer than 10 nm - within the range of fabrication errors considered in Fig. 7.4. A tunable pump laser will likely be required to offset any fabrication error in a practical device. At a pump wavelength of 1550 nm, tunable lasers are commercially available.

If these fabrication challenges can be overcome, it may be possible to use this platform in diverse applications such as, for example, maintaining the phase matching condition as is done with adiabatically-chirped poling periods [28], but with a long sequence of carefully designed waveguide bends for rephasing instead of poling.

7.3.8 Effective Mode Area (A_{eff})

In typical non-hybrid NLO waveguide geometries, a reduced A_{eff} (effective mode area) is analogous to a more efficient device since the intensity of each mode for a given amount of power is increased in the NLO material. The definition of A_{eff} used here is:

$$A_{\text{eff}} = \frac{\left(\int_{-\infty}^{+\infty} |\mathbf{E}|^2 dA\right)^2}{\int_{-\infty}^{+\infty} |\mathbf{E}|^4 dA} \quad [\text{m}^2]. \quad (7.47)$$

In this hybrid SiC-LN waveguide, optical modes are vertically confined by both the SiC rib and the LN film, and horizontally confined by the SiC rib. By reducing the thickness of the hybrid waveguide (the combined thickness of the SiC rib and LN film), a lower A_{eff} can be obtained.

Since amorphous SiC does not display a $\chi^{(2)}$ nonlinearity, any portion of the optical mode that is not in the LN will not contribute to SHG. This is apparent in Fig. 7.8, where although A_{eff} decreases as w_{SiC} and h_{SiC} increase for both the SH and FH modes in Fig. 7.8a and Fig. 7.8b, respectively, η_0 (calculated with (7.44)) is actually higher in the geometry of Fig. 7.8d ($w_{\text{SiC}} = 150$ nm, $h_{\text{SiC}} = 250$ nm) than in Fig. 7.8c ($w_{\text{SiC}} = 250$ nm, $h_{\text{SiC}} = 250$ nm), despite the modes of Fig. 7.8c having lower A_{eff} values. This is because the SH mode is almost entirely contained in the SiC rib in Fig. 7.8c, whereas in Fig. 7.8d it has expanded enough into the LN to offset the efficiency penalty

incurred for increasing the mode sizes.

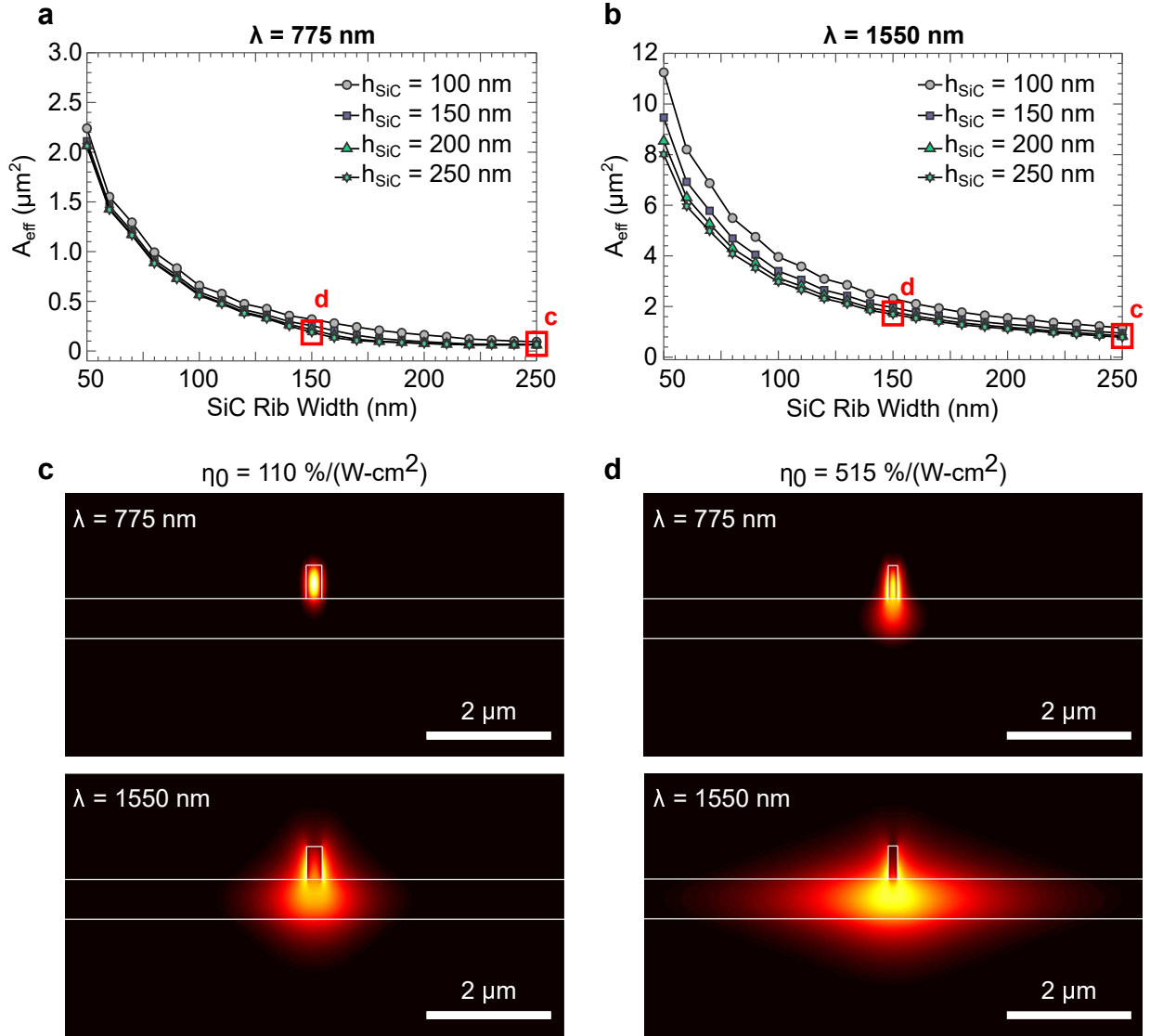


Figure 7.8: Sweep of A_{eff} versus SiC width at $\lambda = 775$ nm (part a) and $\lambda = 1550$ nm (part b) for SiC heights of 100 nm, 150 nm, 200 nm, and 250 nm. c and d show mode pictures for $w_{\text{SiC}} = 250$ nm and $h_{\text{SiC}} = 250$ nm (part c) and $w_{\text{SiC}} = 150$ nm and $h_{\text{SiC}} = 250$ nm (part d) for the SH mode (top) and the FH mode (bottom). Despite the reduced mode areas of the design of c, the design of d has a higher normalized conversion efficiency due to the locations of the modes.

7.3.9 Lithium Niobate Confinement Factor (LNCF)

The outcome of Section 7.3.8 is that a hybrid waveguide for NLO needs to be designed so that the interacting modes do not only overlap in the smallest area possible, but that they do so

specifically in the LN region.

To track the portion of each mode that is in the LN film, we introduce a parameter called the LN confinement factor (LNCF):

$$\text{LNCF} = \frac{\int_{-\infty}^{+\infty} \int_{-h_{LN}}^0 |\mathbf{S}_y|^2 dx dz}{\int_{-\infty}^{+\infty} \int_{-\infty}^{+\infty} |\tilde{\mathbf{S}}|^2 dx dz} \cdot 100 \quad [\%], \quad (7.48)$$

where \mathbf{S} is the total time-averaged Poynting vector and \mathbf{S}_y is the time-average Poynting vector parallel to the propagation axis y . We only consider the y -component of the Poynting vector in the numerator because we are only interested in knowing how much TE-like light resides in the LN film for a given mode, and only the longitudinal component of the Poynting vector is non-zero in the case of an optical mode that is 100% TE-polarized.

Simulated sweeps of LNCF versus w_{SiC} for various h_{SiC} in Fig. 7.9 reveal that the LNCF is fairly stable for the FH mode across the SiC rib geometries we consider, but is sensitive to changes in both w_{SiC} and h_{SiC} for the SH mode. We know from Fig. 7.8 that too narrow of a SiC rib will dramatically increase the mode areas and reduce conversion efficiency, but we also know from Fig. 7.9a-b that if we do not pick a narrow enough SiC rib then too much of the mode, especially the SH mode, will be confined in the SiC rib. Knowing this, we select two reasonable choices for the SiC geometry and show their interacting modes in Fig. 7.9c ($w_{SiC} = 100$ nm, $h_{SiC} = 100$ nm) and Fig. 7.9d ($w_{SiC} = 200$ nm, $h_{SiC} = 100$ nm). Indeed, in both cases η_0 is higher than in the designs chosen in Fig. 7.8. However, the more efficient of the two designs is not the one where LNCF is at a maximum (Fig. 7.9c), but when it is well below its maximum for the SH wave (Fig. 7.9d).

7.4 Concluding Thoughts

Despite the more than 50 years of research and discovery in the field of nonlinear optics, it still remains a significant challenge to routinely design and fabricate highly efficient, integrated nonlinear optical devices. This is in large part due to a combination of deviations from designs

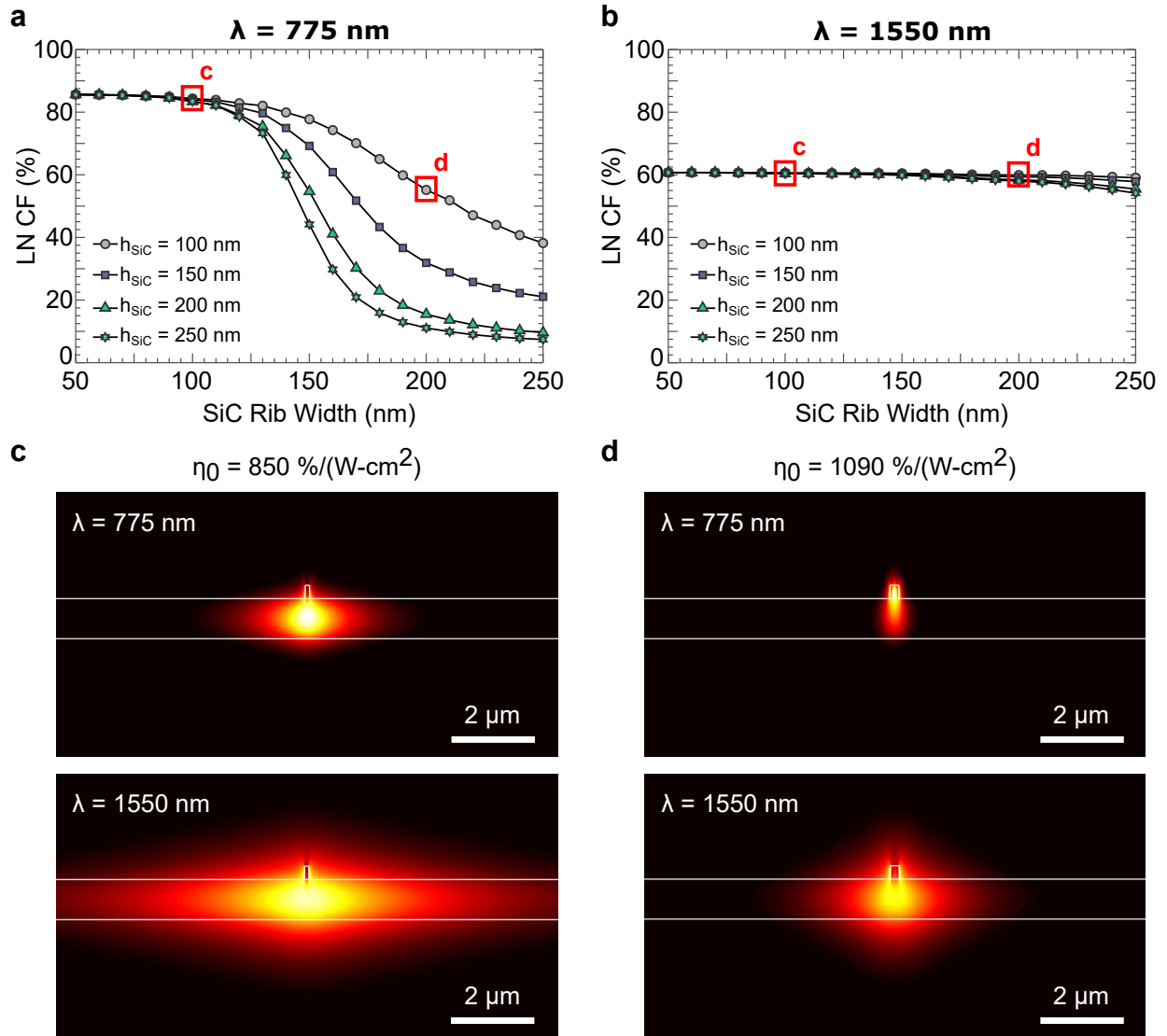


Figure 7.9: Sweep of LNCF versus SiC width at $\lambda = 775 \text{ nm}$ (part **a**) and $\lambda = 1550 \text{ nm}$ (part **b**) for SiC heights of 100 nm, 150 nm, 200 nm, and 250 nm. **c** and **d** show mode pictures for $w_{\text{SiC}} = 100 \text{ nm}$ and $h_{\text{SiC}} = 100 \text{ nm}$ (part **c**) and $w_{\text{SiC}} = 200 \text{ nm}$ and $h_{\text{SiC}} = 100 \text{ nm}$ (part **d**) for the SH mode (top) and the FH mode (bottom). **d** has a higher η_0 than **c** because of its reduced A_{eff} , despite having a lower LNCF for the SH wave.

during fabrication and the strict design tolerances of integrated nonlinear optical devices. Much of the work in this chapter on hybrid thin film LN-based devices has been done with the hope that it may be useful as a foundation for the study of fabricating nonlinear optical devices in a foundry-compatible process (as with the electro-optic modulators discussed in previous chapters), where tolerances are tighter and feedback devices can be integrated on-chip. Perhaps in the not-so-distant future foundry-fabricated, highly efficient, compact nonlinear optical devices will be developed that feature monolithic integration with electrical circuits to monitor and perhaps eventually stabilize the device for continuous, repeatable nonlinear mixing.

7.5 Acknowledgments

Chapter 7, in part, is a reprint of the material as it appears in *Journal of the Optical Society B* 2018. Peter O. Weigel & Shayan Mookherjea, *JOSA B* 35(3), 593-600 and in *Conference on Lasers and Electro-Optics (CLEO) 2017*. Peter O. Weigel, Marc Savanier and Shayan Mookherjea, paper SW4M.5. The dissertation author, together with his adviser, led the research efforts for this work and co-authored the papers.

Bibliography

- [1] Yariv A, Yeh P. *Photonics: optical electronics in modern communications*. Oxford Univ.; 2006.
- [2] Weigel PO, Mookherjea S. Design of folded hybrid silicon carbide-lithium niobate waveguides for efficient second-harmonic generation. *JOSA B*. 2018;35(3):593–600.
- [3] Sutherland RL. *Handbook of nonlinear optics*. CRC press; 2003.
- [4] Weigel PO, Savanier M, DeRose CT, Pomerene AT, Starbuck AL, Lentine AL, et al. Lightwave circuits in lithium niobate through hybrid waveguides with silicon photonics. *Scientific reports*. 2016;6:22301.
- [5] Lee BG, Rylyakov AV, Green WM, Assefa S, Baks CW, Rimolo-Donadio R, et al. Monolithic silicon integration of scaled photonic switch fabrics, CMOS logic, and device driver circuits. *Journal of Lightwave Technology*. 2014;32(4):743–751.

- [6] Sun J, Timurdogan E, Yaacobi A, Hosseini ES, Watts MR. Large-scale nanophotonic phased array. *Nature*. 2013;493(7431):195.
- [7] Nikogosyan DN. *Nonlinear optical crystals: a complete survey*. Springer Science & Business Media; 2006.
- [8] Jung H, Guo X, Zhu N, Papp SB, Diddams SA, Tang HX. Phase-dependent interference between frequency doubled comb lines in a $\chi(2)$ phase-matched aluminum nitride microring. *Optics letters*. 2016;41(16):3747–3750.
- [9] Schreiber G, Suche H, Lee Y, Grundkötter W, Quiring V, Ricken R, et al. Efficient cascaded difference frequency conversion in periodically poled Ti: LiNbO₃ waveguides using pulsed and cw pumping. *Applied Physics B*. 2001;73(5-6):501–504.
- [10] Schreiber G, Hofmann D, Grundkoetter W, Lee YL, Suche H, Quiring V, et al. Nonlinear integrated optical frequency converters with periodically poled Ti: LiNbO₃ waveguides. In: *Integrated Optics Devices V*. vol. 4277. International Society for Optics and Photonics; 2001. p. 144–161.
- [11] Amin J, Pruneri V, Webjörn J, Russell PSJ, Hanna D, Wilkinson J. Blue light generation in a periodically poled Ti: LiNbO₃ channel waveguide. *Optics communications*. 1997;135(1-3):41–44.
- [12] Levy M, Osgood Jr R, Liu R, Cross L, Cargill III G, Kumar A, et al. Fabrication of single-crystal lithium niobate films by crystal ion slicing. *Applied Physics Letters*. 1998;73(16):2293–2295.
- [13] Rabiei P, Gunter P. Optical and electro-optical properties of submicrometer lithium niobate slab waveguides prepared by crystal ion slicing and wafer bonding. *Applied physics letters*. 2004;85(20):4603–4605.
- [14] Chen L, Xu Q, Wood MG, Reano RM. Hybrid silicon and lithium niobate electro-optical ring modulator. *Optica*. 2014;1(2):112–118.
- [15] Chang L, Li Y, Volet N, Wang L, Peters J, Bowers JE. Thin film wavelength converters for photonic integrated circuits. *Optica*. 2016;3(5):531–535.
- [16] Jin S, Xu L, Zhang H, Li Y. LiNbO₃ thin-film modulators using silicon nitride surface ridge waveguides. *IEEE Photonics Technology Letters*. 2016;28(7):736–739.
- [17] Jellison Jr G, Modine F. Parameterization of the optical functions of amorphous materials in the interband region. *Applied Physics Letters*. 1996;69(3):371–373.
- [18] Edwards DF, Ochoa E. Infrared refractive index of silicon. *Applied optics*. 1980;19(24):4130–4131.
- [19] Semiconductor V. General properties of Si, Ge, SiGe, SiO₂ and Si₃N₄; 2002. Online. Available from: www.virginiasemi.com/pdf/generalpropertiesSi62002.pdf.

- [20] Edwards G, Lawrence M. A temperature-dependent dispersion equation for congruently grown lithium niobate. *Optical and quantum electronics*. 1984;16(4):373–375.
- [21] Fejer MM, Magel GA, Lim E. Quasi-phase-matched interactions in lithium niobate. In: *Nonlinear Optical Properties of Materials*. vol. 1148. International Society for Optics and Photonics; 1990. p. 213–225.
- [22] Shoji I, Kondo T, Kitamoto A, Shirane M, Ito R. Absolute scale of second-order nonlinear-optical coefficients. *JOSA B*. 1997;14(9):2268–2294.
- [23] Della Corte FG, Montefusco ME, Moretti L, Rendina I, Rubino A. Study of the thermo-optic effect in hydrogenated amorphous silicon and hydrogenated amorphous silicon carbide between 300 and 500 K at 1.55 μm . *Applied Physics Letters*. 2001;79(2):168–170.
- [24] Leviton DB, Frey BJ. Temperature-dependent absolute refractive index measurements of synthetic fused silica. In: *Optomechanical Technologies for Astronomy*. vol. 6273. International Society for Optics and Photonics; 2006. p. 62732K.
- [25] Volk MF, Sunstov S, Rüter CE, Kip D. Low loss ridge waveguides in lithium niobate thin films by optical grade diamond blade dicing. *Optics express*. 2016;24(2):1386–1391.
- [26] Cai L, Wang Y, Hu H. Low-loss waveguides in a single-crystal lithium niobate thin film. *Optics letters*. 2015;40(13):3013–3016.
- [27] Shoji Y, Nakanishi K, Sakakibara Y, Kintaka K, Kawashima H, Mori M, et al. Hydrogenated amorphous silicon carbide optical waveguide for telecommunication wavelength applications. *Applied Physics Express*. 2010;3(12):122201.
- [28] Leshem A, Meshulam G, Porat G, Arie A. Adiabatic second-harmonic generation. *Optics letters*. 2016;41(6):1229–1232.

Appendix A

A.1 Alternative $V_\pi L$ Derivation

As an alternative to the $V_\pi L$ equation derived in Chapter 1, the following definition may be used. This definition may be more useful depending on the simulation tool and method. Many thanks to Dr. Ryan Aguinaldo for his discussions regarding this and many other mathematical proofs.

From well-known electro-optic theory (see, for example, [1]), we know that:

$$\Delta n_e \approx -\frac{1}{2}n_e^3 r_{33} E_z \quad (\text{A.1a})$$

$$\Delta n_o \approx -\frac{1}{2}n_o^3 r_{13} E_z \quad (\text{A.1b})$$

Equation (A.1a) describes an index change along the extraordinary axis of the crystal, and Equation (A.1b) describes an index change along the ordinary axes of the crystal; in both equations it is assumed the RF electric field is polarized entirely along the extraordinary axis. We can rewrite the RF field in its most general form as:

$$E_{RF}(\vec{r}) = V_{RF} \cdot \Psi(\vec{r}) \quad (\text{A.2})$$

where V_{RF} is the voltage of the RF signal and $\psi(\vec{r})$ is some space-dependent function. Because the changes in indices described by Equation (A.1) are linear with respect to the RF field, we expect the change in the effective index to also be linear with respect to the RF field:

$$\Delta n_{\text{eff}} = C \int E_{\text{RF}}(\vec{r}) \cdot f(\vec{r}) d^2r = CV_{\text{RF}} \int \psi(\vec{r}) \cdot f(\vec{r}) d^2r = CV_{\text{RF}}\gamma. \quad (\text{A.3})$$

Here we use C to represent some combination of constants, $f(\vec{r})$ to denote some spatial function related to the normalized optical field, and γ to constitute a two-dimensional summation of the space-dependency attributed to the RF field and the optical field. Note that n_{eff} is the effective index of the propagating optical signal *before* an external field is applied. Now, if we rearrange (A.3) to be in terms of the constants C and γ , we can say:

$$\frac{\Delta n_{\text{eff}}}{V_{\text{RF}}} = C\gamma. \quad (\text{A.4})$$

Δn_{eff} can be related to the phase by observing the space-dependent phase. For a fixed modulator length L , the space-dependent phase shift is written as:

$$\Delta\phi = \Delta\beta L = \frac{2\pi}{\lambda} \Delta n_{\text{eff}} L \quad (\text{A.5})$$

In the desired case where $\Delta\phi = \pi$, Equation (A.5) becomes:

$$\Delta n_{\text{eff},\pi} = \frac{\lambda}{2L}, \quad (\text{A.6})$$

where $\Delta n_{\text{eff},\pi}$ is the change in the effective index required to achieve a π radian phase shift. Using the form of Equation (A.4) along with Equation (A.6), we have:

$$\frac{\lambda}{2LV_{\text{RF}}} = C\gamma. \quad (\text{A.7})$$

Noticing that the right-hand side of Equation (A.4) is identical to the right-hand side of Equation (A.7), we equate the left-hand sides of the respective equations and rearrange to obtain a

final equation for $V_{\pi}L$ that is in terms of the applied RF voltage and the change in effective index, Δn_{eff} :

$$V_{\pi}L = \frac{\lambda}{2} \frac{V_{\text{RF}}}{\Delta n_{\text{eff}}}. \quad (\text{A.8})$$

Equation (A.8) allows for the calculation of $V_{\pi}L$ from any single V_{RF} point. With this expression, the $V_{\pi}L$ value for a given device structure can be computed by, for example, computing the optical mode with and without an applied voltage. Coupling an electrostatic model with an optical model is fairly straightforward in COMSOL Multiphysics, in which case this expression for $V_{\pi}L$ is beneficial.

Lastly, the change in optical effective index can be written in a more obvious form:

$$\Delta n_{\text{eff}} = n_{\text{eff}}(V_{\text{RF}}) - n_{\text{eff}}(0). \quad (\text{A.9})$$

A.2 Deriving the Electro-Optic Response from Coupled Mode Theory

Although the electro-optic bandwidth equation in Chapter 1 is accurate, it is possible to arrive at a similar expression with coupled mode theory. In fact, several works over the years have provided partial explanations of how to arrive at an accurate bandwidth model for a lossy electro-optic modulator, but a complete derivation is difficult to find in the literature ([2, 3, 4]). We take this opportunity to provide a complete derivation from coupled-mode theory, beginning with the wave equation in a nonlinear medium (see [5] for details of how to arrive at this step):

$$\nabla^2 \mathbf{E}_j - \frac{1}{c^2} \frac{\partial^2 \mathbf{E}_j}{\partial t^2} = \frac{1}{\epsilon_0 c^2} \frac{\partial^2 \mathbf{P}_j}{\partial t^2}, \quad (\text{A.10})$$

where $j = 1, 2$, or 3 , corresponding respectively to the input optical signal, the input electrical signal, and the output modulated optical signal; c is the speed of light in a vacuum, ϵ_0 is the free space

permittivity, \mathbf{E} is the electric field, and \mathbf{P} is the polarization density field in the medium. For this derivation, we will take our guided optical mode to be propagating along the \hat{x} -axis in a LN crystal. Our RF electric field and optical electric field components are assumed to be polarized along the \hat{z} -axis (extraordinary axis) of the crystal, and therefore we can assume the electric field to be of the form:

$$\mathbf{E}_j = A_j(x)e^{i(k_jx - \omega_j t)}\hat{z}. \quad (\text{A.11})$$

$A_j(x)$ is the longitudinal-dependent amplitude of the electric field, k_j is the propagation constant of the field, and ω_j is the frequency of the field. By examining the particular case where $j = 3$ (output field), we can replace “j” in (A.11) with “opt,” and by standard coupled-mode theory we arrive at the lossless differential equation for A_{opt} :

$$\frac{\partial A_{\text{opt}}}{\partial x} = \frac{2i\omega_{\text{opt}}}{cn_{\text{opt}}}d_{33}A_{\text{opt}}A_{\text{elec}}e^{i\Delta kx}. \quad (\text{A.12})$$

d_{33} is the component of the nonlinear susceptibility tensor which corresponds to our crystal and applied field orientations. An important difference between Equation (A.12) and standard coupled-mode equations (again, see [5]) is our assumption herein that the frequency of the input optical signal is approximately the same as the frequency of the output optical signal. Truly, $\omega_3 = \omega_1 + \omega_2$, but the RF frequency ω_2 (in the GHz frequency regime) is on the order of 1000 times less than the optical input frequency ω_1 (in the THz frequency regime). Thus the electrical signal is nearly constant, with respect to an optical wavelength, along the length of the LN crystal, and so we can make the assumption that $A_1 \approx A_3$. For this reason, we are able to place A_{opt} in the right-hand side of Equation (A.12).

Though it is tempting to then say $k_1 \approx k_3$, this assumption will result in a static phase mismatch Δk , which is defined as:

$$\Delta k = k_1 + k_2 - k_3. \quad (\text{A.13})$$

Specifically, if $k_1 \approx k_3$, then Δk would always be equal to k_2 , making us unable to minimize our phase mismatch. Instead, we will expand this phase mismatch equation and realize that the refractive index in the waveguide core at a frequency ω_1 will be, in practicality, identical to the refractive index in the waveguide core at a frequency ω_3 . Thus:

$$\Delta k = k_1 + k_2 - k_3 = \frac{2\pi n_1}{\lambda_1} + \frac{2\pi n_2}{\lambda_1} - \frac{2\pi n_3}{\lambda_1}, \quad (\text{A.14})$$

where $\frac{1}{\lambda_3}$ exactly equals $\frac{1}{\lambda_1} + \frac{1}{\lambda_2}$ under the second-order nonlinear effect, and n_j is the effective index of the corresponding signal in the waveguide. As mentioned earlier, we can now say with great accuracy that $n_1 \approx n_3$ to obtain:

$$\Delta k = \frac{2\pi}{\lambda_2}(n_2 - n_3) = \frac{2\pi}{\lambda_{\text{RF}}}(n_{\text{RF}} - n_{\text{opt}}). \quad (\text{A.15})$$

This immediately tells us that we can minimize our phase mismatch (i.e. the phase difference between the RF field and the optical field) by designing our modulator such that n_{RF} is as close to n_{opt} as possible. If loss were not a factor, then the theory up to this point could be used to maximize optical bandwidth (such as in [1]). Since we are considering loss as well – both optical loss and RF loss – we must adjust Equation (A.12). This is done simply by phenomenologically subtracting a loss term from (A.12), so that we have ([6]):

$$\frac{\partial A_{\text{opt}}}{\partial x} = \frac{2i\omega_{\text{opt}}}{cn_{\text{opt}}}d_{33}A_{\text{opt}}A_{\text{elec}}e^{i\Delta kx} - \alpha_{\text{opt}}A_{\text{opt}}. \quad (\text{A.16})$$

We make one final assumption before solving this differential equation. Since our pump (the RF signal) is much stronger than the optical signal, we can take advantage of the undepleted pump approximation and say that $A_{\text{RF}}(x)$ is only affected by material absorption:

$$A_{\text{RF}}(x) = A_{\text{RF}}(x=0)e^{-\alpha_{\text{RF}}x}. \quad (\text{A.17})$$

Finally, we are able to solve Equation (A.16) from the beginning of the modulation region

($x = 0$) to the end of the modulation region ($x = L$), thereby obtaining an expression for the output optical signal:

$$A_{\text{opt}}(x = L) = A_{\text{opt}}(x = 0)e^{-\alpha_{\text{opt}}L}e^{i\Delta\phi}, \quad (\text{A.18})$$

where:

$$\Delta\phi = \frac{2\omega_{\text{opt}}d_{33}}{n_{\text{opt}}c}LA_{\text{RF}}(x = 0)e^{-\frac{\alpha_{\text{RF}}L}{2}}e^{i\frac{\Delta kL}{2}} \left[\frac{\cos(\frac{\Delta kL}{2}) \sinh(\frac{\alpha_{\text{RF}}L}{2}) - i \sin(\frac{\Delta kL}{2}) \cosh(\frac{\alpha_{\text{RF}}L}{2})}{\frac{\alpha_{\text{RF}}L}{2} - i\frac{\Delta kL}{2}} \right]. \quad (\text{A.19})$$

Our next step is to consider the output of the MZM in terms of optical intensity, since any practical use of the EOM requires data conversion back to the electrical domain by use of a photodetector. The MZM output is a linear combination of the signal passing through the unmodulated arm and the signal passing through the modulated arm. Using Equation (A.18) as our description of the modulated signal, we can obtain an output amplitude A_{out} :

$$A_{\text{out}}(x) = A_{\text{opt}}(x = 0)e^{-\alpha_{\text{opt}}L}e^{i\Delta\phi} + A_{\text{opt}}(x = 0)e^{-\alpha_{\text{opt}}L} = A_{\text{opt}}(x = 0)e^{-\alpha_{\text{opt}}L}(1 + e^{i\Delta\phi}), \quad (\text{A.20})$$

And thereby calculate the proportional value of I_{out} :

$$I_{\text{out}} \propto |A_{\text{out}}|^2 = A_{\text{out}}A_{\text{out}}^* = 2A_{\text{out}}(x = 0)^2e^{-2\alpha_{\text{opt}}L}[1 + \cos(\Delta\phi)]. \quad (\text{A.21})$$

From the right-hand side of Equation (A.21), we can see that I_{out} is proportional to a cosine function of the phase change of Equation (A.19). Because we desire high-speed modulation, we want to modulate about a voltage that resides in the linear region of this cosine function; this is done to maximize the output intensity difference between an applied voltage of V_{RF} and an applied voltage of zero. Since the linear region of a cosine wave has the highest magnitude slope of the cosine function, the linear region is where we will obtain the greatest high/low output intensity

difference. Therefore, we can make the assumption that $\Delta\phi$ is small about $\pi/2$ radians (where $\pi/2$ is the halfway point between the maximum and minimum values of the $\cos(\Delta\phi)$ function), and $\cos(\Delta\phi) \approx \pi/2 - \Delta\phi$.

We now have the relationship:

$$I_{\text{out}} \propto (1 + \pi/2 - \Delta\phi). \quad (\text{A.22})$$

To relate Equation (A.22) to the optical bandwidth, we first need to define the bandwidth in terms of the output intensity. For an EOM, we would like to know how I_{out} changes as V_{RF} varies between its high and low values at different electrical frequencies. Mathematically, we can write this as:

$$\text{normalized EO response} = \frac{\text{change in optical output intensity}}{\text{change in RF voltage}} = \frac{\frac{\Delta I_{\text{out}}|_{\text{RF}}}{\Delta V_{\text{RF}}}}{\frac{\Delta I_{\text{out}}|_{\text{dc}}}{\Delta V_{\text{dc}}}}. \quad (\text{A.23})$$

Here we normalize our EO response to the dc case to determine how our output degrades, as a function of frequency, from the best-case scenario of sub-Hz frequency (which is what we are calling dc). In Equation (A.23), ΔV_{RF} and ΔV_{dc} are identical, since the value of the high and low voltages are the same regardless of the electrical frequency at which the device is being operated. We can use Equation (A.22) to say:

$$\Delta I_{\text{out}}|_{\text{RF}} = (1 + \pi/2 - \Delta\phi_{\text{high}})|_{\text{RF}} - (1 + \pi/2 - \Delta\phi_{\text{low}})|_{\text{RF}} = -(\Delta\phi_{\text{high}} - \Delta\phi_{\text{low}})|_{\text{RF}} = -\Delta\phi|_{\text{RF}} \quad (\text{A.24a})$$

$$\Delta I_{\text{out}}|_{\text{dc}} = (1 + \pi/2 - \Delta\phi_{\text{high}})|_{\text{dc}} - (1 + \pi/2 - \Delta\phi_{\text{low}})|_{\text{dc}} = -(\Delta\phi_{\text{high}} - \Delta\phi_{\text{low}})|_{\text{dc}} = -\Delta\phi|_{\text{dc}}. \quad (\text{A.24b})$$

From Equation (A.19), we define $\Delta\phi|_{\text{dc}}$ as:

$$\Delta\phi|_{\text{dc}} = \frac{2\omega_{\text{opt}}d_{33}}{n_{\text{opt}}c} L_{\text{RF}}(x=0), \quad (\text{A.25})$$

And, taking the magnitude of the EO response, we obtain:

$$|m(f_{\text{RF}})| = e^{-\frac{\alpha_{\text{RF}}L}{2}} \left[\frac{\sinh^2(\frac{\alpha_{\text{RF}}L}{2}) + \sin^2(\frac{\Delta kL}{2})}{(\frac{\alpha_{\text{RF}}L}{2})^2 + (\frac{\Delta kL}{2})^2} \right]^{1/2}, \quad (\text{A.26})$$

Where $m(f_{\text{RF}})$ is the electro-optic response of the device, and f_{RF} is the RF electrical frequency. By converting Equation (A.26) into dB, one can choose whether to use the optical bandwidth definition ($10\log_{10}(m)$) or the electrical bandwidth definition ($20\log_{10}(m)$). From Equation A.26, it is clear that two of the limiting factors of the bandwidth for a traveling-wave EOM structure in a MZM configuration are the optical-electrical index mismatch and the electrical losses.

Bibliography

- [1] Yariv A, Yeh P. Photonics: Optical Electronics in Modern Communications. Oxford University Press; 2007. Print.
- [2] D Janner MB D Tulli, Pruneri V. Waveguide Electro-Optic Modulation in Micro-Engineered LiNbO₃. Journal of Optics A: Pure Applied Optics. 2008;10(104003).
- [3] Haeyang Chung WSCC, Adler EL. Modeling and Optimization of Traveling-Wave LiNbO₃ Interferometric Modulators. IEEE Journal of Quantum Electronics. 1991;27(3):608–617.
- [4] Donnelly JP, Gopinath A. A Comparison of Power Requirements of Traveling-Wave LiNbO₃ Optical Couplers and Interferometric Modulators. IEEE Journal of Quantum Electronics. 1987;QE-23(1):30–41.
- [5] Boyd RW. Nonlinear Optics, 3rd ed. Academic Press; 2008. Print.
- [6] Sutherland. Handbook of Nonlinear Optics. Marcel Dekker, Inc.; 2003. Print.